Cryo-gravure de couches atomiques par plasma : mécanismes et procédés

Gaëlle Antoun

UNIVERSITÉ D'ORLÉANS

ÉCOLE DOCTORALE N°552
Energie, Matériaux, Sciences de la Terre et de l'Univers (EMSTU)

Laboratory: UMR 7344
Groupe de Recherches sur l'Energétique des Milieux Ionisés (GREMI)

PhD thesis presented by:

Gaëlle ANTOUN

defended on : **December 18th 2020**

to obtain the degree of : **Doctor of University of Orleans**

Discipline/ Speciality : Physics / Nano electronics

Cryo-Atomic Layer Etching by plasma: mechanisms and processes

PhD directed by:

Mr DUSSART Rémi	Professor, GREMI, University of Orleans
Mr TILLOCHER Thomas	Associate Professor, HDR, GREMI, University of Orleans

Referees :

Mrs BOUCHOULE Sophie	Research Director, C2N, CNRS
Mr OEHRLEIN Gottlieb	Professor, University of Maryland

JURY :

Mrs BOUCHOULE Sophie	Research Director, C2N, CNRS
Mr CARDINAUD Christophe	Research Director, IMN, CNRS
Mr CHABERT Pascal *(President)*	Research Director, LPP, CNRS
Mrs DESPIAU-PUJO Emilie	Assistant Professor, LTM, University of Grenoble Alpes
Mr DUSSART Rémi	Professor, GREMI, University of Orleans
Mr FAGUET Jacques *(invited)*	Director, Tokyo Electron Ltd
Mr OEHRLEIN Gottlieb	Professor, University of Maryland
Mr TILLOCHER Thomas	Associate Professor, HDR, GREMI, University of Orleans
Mrs WANG Mingmei *(invited)*	Etch manager, Tokyo Electron Ltd

"Theory is when you know everything and nothing works; practice is when everything works and nobody knows why. Here we combine theory with practice: nothing works and nobody knows why."

Albert Einstein

Acknowledgments

This thesis was carried out in the french laboratory *GREMI* based in Orleans and Bourges. It is a joint research unit belonging to both the *University of Orleans* and the *CNRS*. The Cryo-ALE project was funded by the Japanese company *TEL.* In this paragraph I would like to thank all the people who were in one way or another involved in this thesis and who made it a memorable experience.

First, I would like to thank all the jury members for their valuable comments and help to improve this work. It was a great honor for me to have them as members of the jury.
Thanks to *Sophie Bouchoule, Research Director at C2N laboratory* and to *Gottlieb Oehrlein*, *Professor at Maryland University* for reviewing my manuscript, and for their feedback despite all the issues encountered.
I would like to thank *Pascal Chabert, Research Director at LPP laboratory* for being the president of the PhD defense jury. I also thank *Emilie Despiau-Pujo, Associate Professor at Grenoble Alpes University*, *Christophe Cardinaud, Research director at IMN laboratory, Rémi Dussart, Professor at Orleans University* and *Thomas Tillocher, Associate Professor at Orleans University* for being part of the jury and their helpful comments.
Finally, I thank *Mingmei Wang* and *Jacques Faguet,* both from *TEL* who agreed to be part of my jury as guest members.

Once again, I would like to express my sincere gratitude to my thesis directors: *Rémi Dussart,* and *Thomas Tillocher*. First for accepting me in the “etching group”, and secondly for all their time, support and discussions. I learned a lot from them, both about science and culture. By their concern for the well-being of their PhD students, and by offering many opportunities, they help making this experience greater than expected. I was lucky to have such supervisors even though I caught *TT (bad luck) syndrome*☺.
I also would like to thank *Philippe Lefaucheux* without whom I could not have done this thesis. In addition to all his advice and support, he truly contributed to ensure that this work was done in good conditions with always functional equipment.

I would like to acknowledge all TEL members with whom I worked on this subject. First, thanks to *Jacques Faguet, Shigeru Tahara* and *Kaoru Maekawa* for all the discussions and advices that helped improve this work during these three years. I would also like to thank *Mingmei Wang, Du Zhang* and *Hojin Kim* for all the fruitful discussions. Finally, I thank *Kumiko Yamazaki* and *Nagisa Sato* for all their kindness and help during those three years.

During the thesis, I had the opportunity to perform experiments at IMN laboratory. Therefore, I would like to thank *Aurélie Girard* and *Christophe Cardinaud* for hosting me so kindly and for sharing their expertise in XPS with me.

Again I would like to thank all of them for trusting me in this project.

In addition, I would like to thank the GREMI director *Anne-Lise Thomann* for her support. Also, for their help in all the administrative procedures, I would like to thank *Sylvie Jauffrion* and *Corinne Delhaye* and *Olivier Chazard.*

For their technical support, as well as their personal support, a special thanks to *Arnaud Stolz, Sylvain Iseni, Thomas Lecas* and *Nicolas Dumuis.*

I would also like to acknowledge all the other GREMI researchers for those years.

Thanks to the best office colleagues ever: *Ronan, Robin, Edouard* and *William*. In so many ways, including ducks and fishes, they were of great support.

Thanks also to all the shared work with the J²C organizing committee and especially to *Ludivine* and *Marianna.*

Aside from the work, this thesis was full of great memories, from coffee breaks to events such as Bowling, Escape game, Laser game, Raclette, Game nights.. and so on! For all those shared moments thanks to *Rim, Lamiae, Azadeh & Payam, Sotheara, Andréa, Erik & Mathilde, Vinni, Fadi, Cédric*, *Martin, Antoine* and all the other PhD students and Post-docs. With special thanks to *Vanessa, Ronan* and *Augusto !*

I also would like to thank *Agathe*, *Hippolyte,* (and again *Ronan* and *Augusto)* for making this last year easier, despite the sanitary crisis, with Skype meetings for sport and games.

I also thank my friends *Nina, Mélanie* and *Pierre-Adrien* who supported me with so much enthusiasm.

And last but not least, I would like to thank my parents and sisters for their endless support in all my projects. Also thanks to *Lucas* who was there for me throughout the thesis and cheered me up whenever I needed it. Thanks for all the support <3

Table of contents

Index of abbreviations and acronyms

3D IC	Three Dimensional Integrated Circuit
ALD	Atomic Layer Deposition
ALE	Atomic Layer Etching
AR	Aspect Ratio
ARDE	Aspect Ratio Dependent Etching
ARIE	Aspect Ratio Independent Etching
AOI	Angle Of Incidence
a-Si	Amorphous silicon
BEOL	Back-End-Of-Line
CCP	Capacitively Coupled Plasma
CMOS	Complementary Metal-Oxide Semiconductor
CVD	Chemical Vapor Deposition
DUV	Deep Ultraviolet
EPC	Etch Per Cycle
EQP	Electrostatic Quadrupole Plasma
ER	Etch rate
FC	Fluorocarbon
FET	Field Effect Transistor
FWHM	Full Width at Half Maximum
GAAFET	Gate-All-Around Field Effect Transistor
GREMI	Groupe de Recherches sur l'Energétique des Milieux Ionisés
GWP	Global Warming Potential
HAR	*High Aspect Ratio*
HARC	*High Aspect Ratio Contact*
HJY	Horiba Jobin Yvon
IC	Integration Circuits
ICP	Inductively Coupled Plasma
IMEC	Institut de Microélectronique Et Composants
IMN	Institut des Matériaux Jean Rouxel de Nantes
IMFP	Inelastic Mean Free Path
IUPAC	International Union of Pure and Applied Chemistry
LPCVD	Low Pressure Chemical Vapor Deposition
MBCFET	Multi-Bridge Channel Field Effect Transistor
MEMS	Microelectromechanical Systems

MFC	Mass Flow Controller
MID	Multiple Ion Detection
Mono	Monochromator
MOSFET	Metal Oxide Semiconductor Field Effect Transistor
MWL	Multiwavelength
NIR	Near Infrared
NIST	National Institute of Standards and Technology
OES	Optical Emission Spectroscopy
OML	Orbital Motion Limited
OPTIMIST	Opening of a Technical Platform for the Investigation of the Mechanisms of Interaction between plasma and Surface on a large Temperature range
p-Si	Polycrystalline silicon
PEM	Photoelastic Modulator
PID	Plasma Induced Damage
PID	Proportional Integral Derivative
PLC	Programmable Logic Controller
PME	Polarization Modulation Ellipsometer
PR	Photoresist
RF	Radio Frequency
RGA	Residual Gas Analysis
RIE	Reactive Ion Etching
SADP	Self-Aligned Double Patterning
SAQP	Self-Aligned Quadrupole Patterning
SE	Spectroscopic Ellipsometry
SEM	Scanning Electron Microscopy
SAC	Self-Aligned Contact
SIMS	Secondary Ion Mass Spectrometry
SiO_2	Silicon dioxide
SLE	Self-Limiting Etching
TCP	Transformer Coupled Plasma
TEL	Tokyo Electron Limited
TSV	Through-Silicon-Via
QMS	Quadrupole Mass Spectrometry
XPS	X-ray Photoelectron Spectroscopy

Introduction

In 1965, Gordon E. Moore, at that time director of research and development department at Fairchild Semiconductor and later co-founder of Intel, published an article in Electronics on the future of electronics. He claimed that the future would rely on the development of the semiconductor integrated circuits to build more powerful and cheaper machines. For him, the number of components on integrated circuits would double every two years, and at the same time the cost of production would be minimized and the yield increased [1].

Since that time, the electronics industries have managed indeed to follow this so-called "Moore's Law" until reaching the "More than Moore" or the "Beyond Moore's law" areas, as components are now designed at nanometric and atomic scales [2]–[4].

Nowadays, the semiconductor industries are focusing on improving the components by creating new configurations and reducing their size to the atomic scale. Fig. I. 1 illustrates the Field Effect Transistors (FET) evolution. The planar FET, since its first introduced by W. Shockley [5] in 1952 has seen its configuration evolving. Indeed, once its size has shrinked close to 20 nm in 2014, its performance has reached its limits. Consequently, three-dimensional configurations have been designed to keep improving transistors. By adding a fin, hence creating the FinFET, the current leakage has been reduced and performances enhanced. Since the invention of FinFET, even more complex configurations have been imagined and designed, such as the Gate-All-Around FET (GAAFET) [6], [7]. With their complexity and performance increased, the FET have seen their critical dimensions decreasing to very challenging sizes (close to 3-5 nm). Recently, in 2019, Samsung presented a new configuration of FET, the Multi-Bridge Channel FET (MBCFET) that would possibly be etched to 3 nm [8], [9].

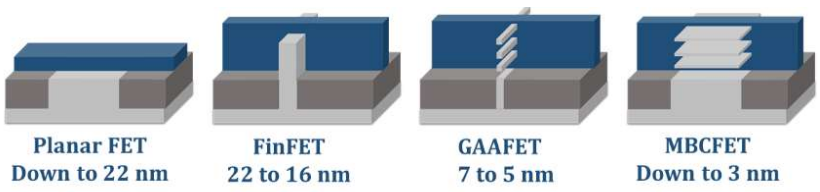

Fig. I. 1. FET evolution, adapted from [8]

FinFET manufacturing is very challenging already. Indeed, to build the fins at the nanoscale, Self-Aligned Double Patterning (SADP) and Self-Aligned Quadruple Patterning (SAQP) methods are used. In brief, those methods consist in creating the fins by first etching spacers using a mandrel element, that is then be etched at his turn [10], [11]. So, several steps of deposition and etching are used for FinFET manufacturing, and each of them may lead to

defects that could cause failures in the devices. Some of those defects are presented in Fig. I. 2, adapted from [10]. If the processing is not clean enough, some residual particles may stay on the surface, mentioned as 1 in Fig. I. 2. During the etching processes, the ion energy and direction have to be perfectly controlled with a high selectivity, or some defects may appear. As observed in Fig. I. 2. 3, there may still be some residual particles from the etching of the corner. Also, Line Edge and width roughness may appear on the fins (Fig. I. 2. 4). Or, even, the fin size may not be equal (Fig. I. 2. 5). Also, some voids may appear (Fig. I. 2. 2) during the deposition step of the metal for the gate formation.

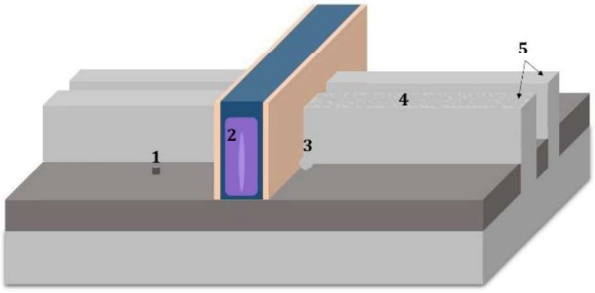

Fig. I. 2. Problems encountered in FET manufacturing, adapted from [10], with 1. residual particle, 2. void, 3. corner residue, 4. surface roughness, 5. unequal fins

To address these issues and prevent defects, Atomic Layer Etching (ALE) has been proposed such as a promising technique to achieve nanoscale patterns.

In 1988, the first patent and publication on Atomic Layer Etching was published. The inventor was M. Yoder who proposed ALE such as a new technique to etch one atomic layer of diamond [12]. Since that time, the studies on ALE have never stopped increasing, as it is shown in Fig. I. 3 with a real gain of interest since 2010 [13], [14].

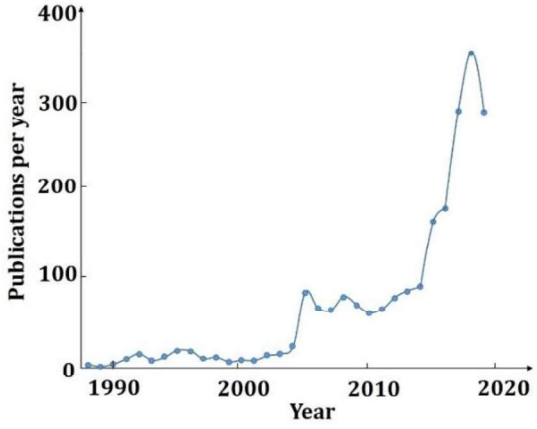

Fig. I. 3. Number of ALE publications per year, adapted from [13], [14]

In parallel, in 1986, Bensaoula *et al.* published an article on the etching of tungsten films at low-temperature (~ -100°C) [15]. Two years later, in 1988, Tachi *et al.* published the first article on silicon (Si) deep etching using cryogenic temperatures (-130°C to -100°C). In this article, they showed some benefits of low temperature processing, such as a high selectivity between Si and photoresist and anisotropic etching profiles of Si, only using an SF_6

plasma [16]. Again, two years after, in 1990, ALE was proposed on Si by Horiike *et al.* [17], [18]: Si was cooled to low temperature, down to -180°C, and according to the authors, it was hence possible to limit spontaneous etching while fluorine was physisorbed on the surface. Then, Ar^+ ion bombardment was performed on the surface to enable the etching [18]. However, low temperature processing has some constraints such as the need of using liquid nitrogen to cool, and consequently the use of particular equipment which has cooling means and are designed to withstand low temperatures. Therefore, room temperature processes have prevailed.

Nevertheless, over the years, new interests have been discovered for cryogenic processes such as limitation of reactor walls contamination [19] and reduction of material damage, for example for low-K materials etching [20].

In fact, in 2012, a study on low-k materials etching at low temperature was run during a collaboration between three entities. A French laboratory named *Groupe de Recherches sur l'Energétique des Milieux Ionisés* (GREMI), a Belgium institute *Institut de Microélectronique Et Composants* (IMEC) and *Tokyo Electron Limited* (TEL) a japanese supplier for semiconductor production equipment.

After this first collaboration, a new project was developed between GREMI and TEL, on the investigation of Atomic Layer Etching at cryogenic temperatures. Hence, this thesis is part of this collaboration as it has been supported by TEL and accomplished in GREMI.

Atomic Layer Etching and cryogenic etching have been combined and will be referred to as "cryo-ALE" in this manuscript.

The first chapter is a general state of the art of silicon-based material etching and cryogenic etching processes, which provides a database to develop cryo-ALE and for the understanding of this thesis work. The second chapter presents the reactor and diagnostics used to achieve this work. The third chapter is dedicated to the ALE of silicon dioxide (SiO_2) based on the physisorption of C_4F_8 at low temperature. The purpose of this chapter is to prove the feasibility of the process, understand the involved mechanisms and discuss the effect on the selectivity towards silicon and silicon nitride. In the fourth chapter, cryo-ALE of Si is investigated with a different approach. It relies on the chemisorption of a SiO_xF_y layer after a plasma of SiF_4 / O_2. Even though this work was first dedicated to Si etching, it revealed interesting results also for Si_3N_4 etching. Finally, a general conclusion will sum up all the main results obtained during this thesis.

Chapter I.

Introduction to plasma etching

I. Etching generalities

I.1. Principle of plasma etching

Etching techniques have no longer to prove their usefulness in the nanotechnology manufacturing industries. Regardless of the etching method and the material used, the general principle is the same. Patterns are transferred through a mask deposited at the surface of the substrate. The material of the mask is chosen so that the substrate is etched selectively by a plasma created from reactive gases. This means that the mask has to resist to the etching, or at least be etched much more slowly than the substrate (Fig. I. 4).

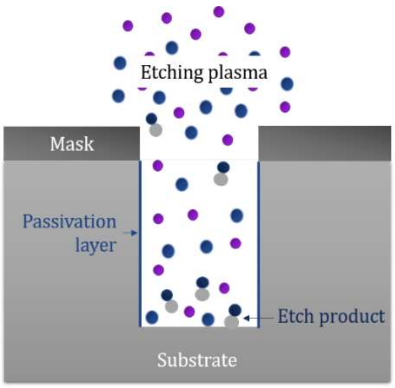

Fig. I. 4. Etching principle for anisotropic etching

The reactive gases are generally halogen-based gases (Fluorine, Chlorine or Bromine). The reactive gas is chosen based on its ability to react with the substrate (chemical affinity) and create stable and volatile etching by-products [21].

Radicals produced from the reactive plasma will adsorb to the surface according to reaction probability, the substrate temperature and the residence time on the surface.

Then the adsorbed species react with the substrate surface and form a new molecule. This molecule is the etching by-product. Once formed, it will desorb from the surface and be evacuated by the pumping system. If the product is not volatile, there will be a risk of redeposition on the substrate or on the reactor walls instead of being pumped [6]. The evaporation rate (R_V) of the etching product can be expressed as followed in Eq. I. 1.

$$R_V = \frac{p_0\, exp(-\Delta H/RT)}{\sqrt{2\pi m k_B T}} \qquad \text{I. 1}$$

With, p_0 an integration constant from Clausius-Clapeyron equation (Pa), ΔH the heat of vaporization (J.mol^{-1}), R the gas constant (J.mol^{-1}.K^{-1}), T the temperature (K), m the molar mass (g.mol^{-1}) and k_B the Boltzmann constant (J.K^{-1}) [6].

Then, the desorption rate (k_d) is given by the Frenkel-Arrhenius equation (Eq. I. 2)

$$k_d = k_d^0 \exp(-E_d/k_B T) \qquad \text{I. 2}$$

With k_d^0 the attempt frequency of the particle for desorption (s^{-1}) and E_d the desorption energy, or the energy needed for desorption (kJ.mol-1). It is expected for volatile etching products to have a high desorption rate [22]. To enhance it, the energy needed to enable the desorption can be supplied by the ions present in the plasma and accelerated in the sheath above the substrate [21], [23]. However, if the ion energy is too high, etching may occur by sputtering, and non-volatile species may redeposit on the reactor walls or on the substrate surface, or even create surface damage.

A study conducted by Coburn and Winters in 1979, on Si etching by XeF_2 gas and Ar^+ ion beam has shown the benefit of coupling both chemical and physical etching. Indeed, as shown in Fig. I. 5, it has been demonstrated that some small chemical etching (~ 5 Å/min) occurs when exposing Si to a XeF_2 flow, due to reaction between fluorine and silicon. Also, a small physical etching is observed in Ar^+ ion beam (~ 2 Å/min). However if both, XeF_2 flow and Ar^+ ion beam are coupled, the etch rate is dramatically increased (> 50 Å/min) [21], [23], [24].

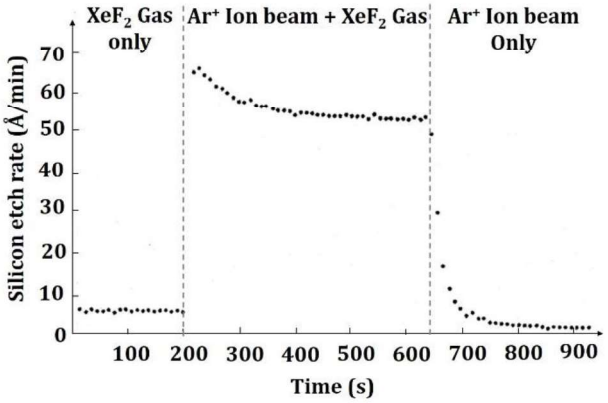

Fig. I. 5. Silicon etch rate depending on the gas and ion chemistry used, adapted from [24]

Reactive Ion Etching (RIE) takes advantage of the synergy between chemical etching and physical etching to realize anisotropic profiles [6]. The ratio of neutral flux and ion energy flux is very important and needs to be controlled to ensure optimal etching [21]. The energy of the ions will depend on the ion sheath width, the acceleration voltage, the ion mass and the RF frequency supplied [23]. Processing at low pressure increases ion mean free path and enhance the directionality and hence the efficiency of the ions for profiles etching [25]. A high plasma electron density will enhance the dissociation and favor the creation of reactive species

[21], [23]. In addition, the substrate may be negatively biased in order to provide energy to the positive ions and direct them to promote anisotropic etching. At the same time, in this case, the ion flux on the sidewalls is reduced and is much lower compared to the ion flux reaching the bottom of the features [21]. Consequently, the bottom of the hole will be etched by creating volatile and stable products, whereas at the same time, the sidewalls will be passivated by the non-volatile products creating a thin modified layer.

Finally, the substrate temperature may also play a role in the etching, as it may affect the adsorption of radicals and the reactions at the surface [21]. Hence, decreasing the substrate temperature is expected to decrease sidewalls etching but not the bottom etching [26].

Fig. I. 6 summarizes the main parameters of interest presented to control well the etching.

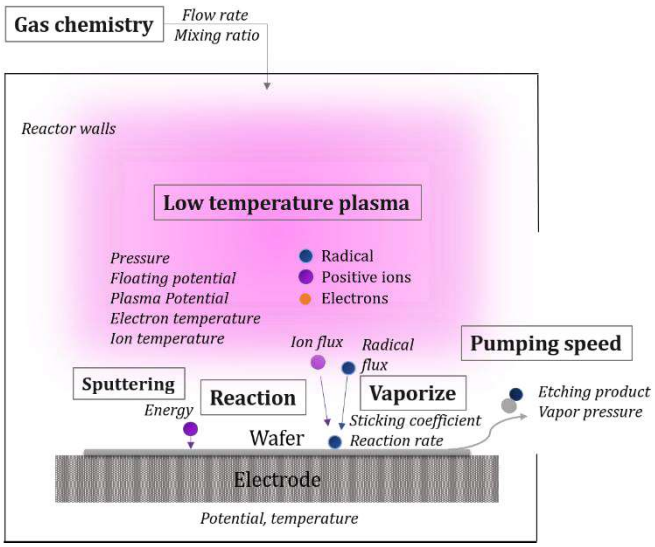

Fig. I. 6. General parameters of interest in a plasma etcher, adapted from [23]

I.2. Main etching parameters

Regardless of the etching method used, some dimensions and parameters are relevant to characterize the etching.

Some of them are represented in Fig. I. 7.

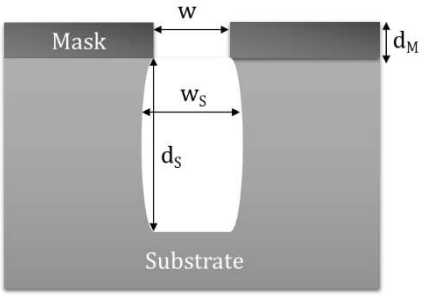

Fig. I. 7. Etch profile with dimensions of interest

- Etch rate

The etch rate (ER) is the etched thickness per time unit. It is usually expressed in nm/min or µm/min. In Atomic Layer Etching (ALE), where several steps exist sequentially, the ER can also be expressed as Etch Per Cycle (EPC) in nm/cycle or Å/cycle. During an etching process, the ER may vary over time. Consequently, it is useful to differentiate between the ER at a particular time of the process and the average etch rate during all the process.
The expression for average ER is simply:

$$ER = \frac{d_S}{Process\ time} \qquad I.\ 3$$

With d_S the etched depth (nm), and the process time in min or s.

- Selectivity

As represented in Fig. I. 7, a mask is needed to etch the samples. Usually, the patterns are transferred in a photoresist mask by photolithography. This mask can then be used to etch directly the substrate or to open a hard mask deposited on the substrate.
The choice of the mask material is usually performed according to the etching selectivity between the substrate and the mask. In other words, the mask needs to resist to chemical and physical etching. The selectivity of the mask (M) over the substrate (S_b) is evaluated using the Eq. I. 4 below:

$$S_{M/S_b} = \frac{ER_M}{ER_{Sb}} \qquad I.\ 4$$

- Uniformity

Nowadays, the diameter of the wafers etched in production is 300 mm. The etching uniformity all over the wafer is very important to control.
To evaluate the uniformity, the etched thickness is measured across the wafer and compared to the average value.
The relative variation should be as low as possible. An acceptable uniformity is about < ± 3% [27].

- Profile

Profiles are characterized by their degree of anisotropy (A) given in Eq. I. 5 below and presented in Fig. I. 8. When the etch rate is the same in all directions, it is referred to as "isotropic etching" (A close to 1). If the etching occurs in the vertical direction only, it will be considered as infinitely anisotropic [27].

$$A = \frac{d_s}{0.5(w_s - w)} \qquad I.\ 5$$

a. Isotropic profile b. Anisotropic profile

Fig. I. 8. Etch profiles

- Aspect ratio

The aspect ratio (AR) is another important parameter since it may affect the etch rate. It is the ratio between the etched depth (d_S) and the opening width (w) of the pattern (Eq. I. 6)

$$AR = \frac{d_S}{w} \qquad I.\ 6$$

I.3. Defects possibly encountered

During the etching processes, many defects may appear in the etching profile or on the material surface. Some main defects are presented in this section.

- Aspect Ratio Dependent Etching (ARDE) or Reactive Ion Etching lag (RIE lag)

ARDE also called RIE lag, is one of the main undesired phenomena for high aspect ratio features. As illustrated in Fig. I. 9, it corresponds to the etch rate decrease when the aspect ratio gets bigger. This is due to a lack of neutrals transport to the etch front [28]–[30]. To estimate the ratio between the neutral flux arriving at the bottom of a microstructure and depending on the aspect ratio, $F(AR)$, and the neutral flow present in the plasma and arriving to the top of the pattern, $F(0)$, Eq I. 7 has first been proposed by Coburn and Winters [30] and represented in [23], [28].

$$\frac{F(AR)}{F(0)} = \frac{K}{K + S_n - KS_n} \qquad I.\ 7$$

With S_n the reaction probability at the bottom surface, and K assimilated to the Knudsen or Clausing coefficient for vacuum systems. It corresponds to the probability of transmission through a tube in a molecular flow. In other words, to the probability for a molecule in a chamber A entering a tube to go out from another opening to chamber B. With here, the bottom of the profile linked to the second exit [28], [30]–[32]. Hence, as K decreases when the AR is bigger, the Eq. I. 7 confirms that $F(AR)$ is decreased when AR increases.

Also, the ion transport to the bottom of a hole is decreased when the AR is increased [21], [29], [33].

To decrease this effect, it is proposed to increase the neutral flux arriving to the etch front, for example by increasing the pressure [6], [28].

Fig. I. 9. Aspect Ratio Dependent Etching

Fig. I. 10 displays other main defects that can be observed in the etch profiles [6], [21], [26].

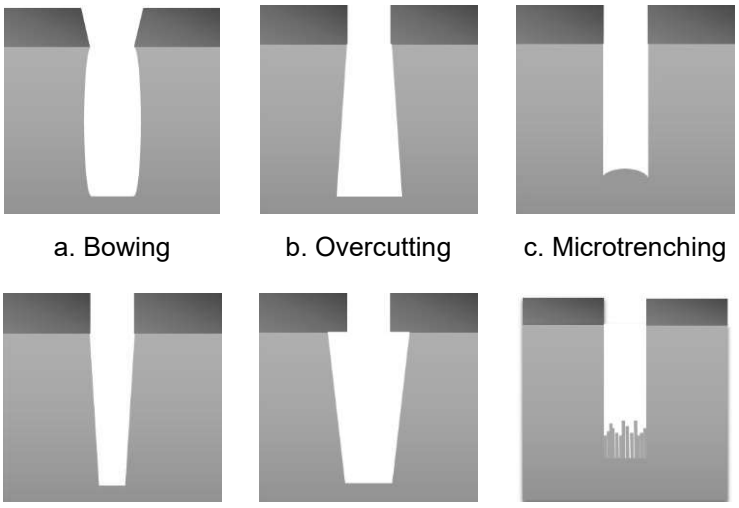

Fig. I. 10. Different types of observed defects, adapted from [6]

- Faceting

Mask faceting is observed when sputtering occurs on the corners of the mask, inducing a slope of the mask profile as in Fig. I. 10. a.

- Bowing (Fig. I. 10. a)

The mask faceting explained above, can induce the bowing of the trenches sidewalls. Several effects may cause it as ions deflection or charge effect from the mask. It can also be due to collisional sheath.

- Overcutting (Fig. I. 10. b)

Overcutting corresponds to a negative slope of the etch profile. It can be due to ion scattering or less efficient passivation.

- Microtrenching (Fig. I. 10. c)

Microtrenching is obtained when ions are deflected toward the bottom of the feature, causing an over etch.

- Tapered profile (Fig. I. 10. d)

Tapered profiles are formed when the etched trenches have a positive slope. They are due to redeposition on the sidewalls of polymers from the reactive gas, or of etching products from sputtering, or to an increasing passivation layer.

- Undercutting (Fig. I. 10. e)

The undercutting corresponds to the etching occurring under the mask. This is due to chemical isotropic etching. To reduce this effect, good passivation of the sidewalls would reduce and even suppress this phenomenon.

- Micrograssing (Fig. I. 10. f)

Micrograssing corresponds to micro columns at the bottom of the profile. This phenomenon is due to residual polymer at the bottom during the etching process.

Some surface damages can also appear due to sputtering by ion bombardment, inducing a surface roughness increase [23].

II. Deep etching of silicon

Deep silicon etching is used for many microelectronic components such as Microelectromechanical Systems (MEMS), Complementary Metal-Oxide semiconductor (CMOS), Through-Silicon-Via (TSV).

Specific demands are required for each component. For example, a typical value of the average etch rate for MEMS devices is at least about 3 µm/min, and an aspect ratio of about 30:1 could be requested [26], [34]. For Through-Silicon-Via, the etch depth is over 100 µm and high etch rate of the order of 3-4 µm/min is also desired, with an aspect ratio of at least 15:1. Smooth sidewalls are also needed for TSV, to optimize the filling with conductive materials.

In brief, to manufacture those components, high etch rate, high aspect ratio and high selectivity are required. In addition, ideally smooth sidewalls and low dependency to aspect ratio processes are also recommended [26].

Therefore, specific deep etch processes were designed to meet these needs: one at room temperature, the Bosch process and one requiring a low substrate temperature, the cryogenic process.

II.1. Processes at room temperature

II.1.i. *The Bosch process, an alternating process*

In 1996, Laemer and Schilp published a patent on Si deep etching. It is an alternating process that is now known as the "Bosch process". In this method, it is proposed to first perform isotropic etching using a reactive plasma of SF_6 with Ar. Typically, 2 to 3 µm are removed during the etch step with an etch rate between 2 and 20 µm/min. Then the sidewalls of the trenches are passivated using a polymerizing plasma chemistry such as CHF_3 with Ar. During this step, around 50 nm of Teflon-like (CF_x) film is deposited. Again, during the etch step, low ion energy (5 to 30 eV) is sufficient to break through the deposited film at the bottom of the trench, and etch the silicon (Fig. I. 11). Thus, deep anisotropic profiles can be obtained. As the ion energy is low, erosion of the mask is prevented, which provides a high selectivity to the mask [35].

However, alternating those steps creates scallop shapes in the etch profile as observed in Fig. I. 11.

Since then, CHF_3 was replaced by C_4F_8 as it has a better ability for creating CF_2 radicals that are needed for passivation. The steps of the mechanism during the process are as follows with examples of possible reactions [26], [36]:

1. Dissociation of SF_6 in plasma phase

$$SF_6 + e^- \rightarrow SF_5^+ + F + 2\,e^- \qquad \textit{I. 8}$$

2. Reaction with Si surface and etch

$$Si_{(s)} + 4\,F_{(g)} \rightarrow SiF_{4(g)} \qquad \textit{I. 9}$$

3. Dissociation of C_4F_8 in plasma phase

$$C_4F_8 + e^- \rightarrow C_3F_6 + CF_2 + e^- \qquad \textit{I. 10}$$

4. Passivation of the trench surface by adsorption of n(CF_2)

From this, it is clear that the polymerization rate as well as the resistance of the polymer to the etching are essential parameters for the good control and the improvement of the process.

The deposition rate is dependent of parameters like pressure, flow rate and Radio Frequency (RF) power. The molecule needed for the deposition is CF_2 [25], [26]. Therefore, the F/C ratio is very important. Ideally, a ratio of 1.45 is needed, and C_4F_6 has also been proposed for the passivation step, as it has a higher deposition rate and a higher ability to create CF_2 than C_4F_8 and hence presents a better resistance to etching.

However, if the deposition is not efficient enough, generalized undercut may appear by etching isotropically the sidewalls. On the contrary, if the deposition is too high, it may induce

micrograssing effect. The latter appears when all the polymer is not removed from the bottom of the trench during the etching, inducing the formation of micro columns.

The etch step is also important. The etch rate needs to be high enough and can be optimized for example by adjusting the pressure or increasing the RF power. Indeed, at the optimum pressure, the fluorine concentration as well as the ion energy are high enough to increase the etch rate. Also increasing, for example, the bias may suppress the micrograssing effect. However, the ion energy should not be too high to prevent mask erosion.

In brief, a balance should be found between the etch and the deposition steps. Also, to reduce the scalloping effect, it is proposed to reduce the duration of each step [26].

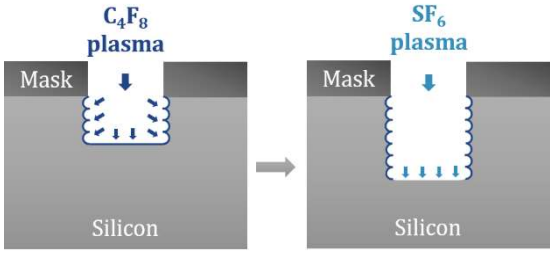

Fig. I. 11. Bosch process principle, adapted from [26]

Despite the promise of high aspect ratio, the Bosch process is sensitive to ARDE effect and to large open areas (loading effect) [25].

Other defect mechanisms were also studied by Choi *et al.* in [37]. They present three mechanisms responsible for defect appearance during a Bosch process.

The first defect is due to residual C_4F_8 in the chamber during the etch step. It induces surface roughening on the feature sidewalls. Then, once the residual gas is pumped out of the chamber, the sidewalls get smoother. The second defect possibly observed is sponge-like surface. It corresponds to voids appearing on the sidewalls of the trench. They are due to voids in the CF_x passivation layer or if the latter is not thick enough. Finally, they also identified surface defects due to fluorine attacking the interface between Si and the passivation layer. This appears if the etch step is too long.

II.1.ii. *Monocyclic processes*

It is also possible to etch Si in one single step. The gas chemistry used is generally fluorine based, but can also be chlorine or bromine based. However, etching Si using chlorine based chemistry leads to a lower etch rate and the etch by-products are less volatile. Selectivity to SiO_2 is also decreased. Etching using bromine is even worse and needs even more ion assistance. Hence, gas mixture of a halogen-based gas with a neutral gas such as Ar brings the energy needed to desorb the product species from the surface by using Ar^+ bombardment energy. Nevertheless, anisotropy with those chemistries is better than with fluorine [21], [26].

Globally, regardless of the chemistry used, the main volatile etching products are SiX_4 like, with X being the halogen element used for etch.
Winters [38] has shown the importance of chemisorption in the etching, more precisely that radicals as CF_3 from dissociated gases play a more important role in the etching than the stable gases. Indeed, they provide, during dissociative adsorption, the fluorine needed to create SiF_4 product and etch Si.
In fluorine based feed gas cases, SF_6 is one of the main gases used to etch Si, however other fluorine based gases are also used, as NF_3 and also fluorocarbon gases like CF_4, C_4F_8, etc. [23], [26]. The gas is first dissociated in the plasma to release fluorine radicals. Then, as expressed in Eq. I. 9, fluorine reacts with Si to form the etching volatile product SiF_4 that is the main etch product in fluorine-based etching. This reaction is possible as the binding energy of Si-F is 5.62 eV and is higher than the binding energy of Si-Si that is 3.39 eV [23], [39]. The formation of SiF_2 as another etching product and being one of the etch limiting factor was claimed in [40]. However, this remains a subject of controversy [41].
When using fluorocarbon-based chemistries, CF_x deposition can easily occur and stop the etching. To etch the CF_x layer, fluorine atoms are needed to diffuse into the CF_x layer and react with it. To enable the etching, a steady state with a balance between the adsorption and desorption of carbon fluxes has to be found, as well as the balance with fluorine supply to enable Si etching. Ions may play two roles in the etching. They help the diffusion of fluorine in the CF_x layer, but also promote the dissociation of CF_x molecules in the deposited layer [42].
In the case of etching by chlorine chemistry, the main gases used are Cl_2 and Ar. Si-Cl binding energy is 4.2 eV which is also higher than Si-Si bond [39].

II.1.iii. *Selectivity*

Most of time, selectivity is a necessary condition in etching. Bosch process enables a selectivity of Si over SiO_2 up to 200:1 and 75:1 over PR [25]. The high etch rate of Si over SiO_2 in fluorine chemistry is possible because fluorine spontaneously reacts with Si and etches it. Whereas SiO_2 and Si_3N_4 would need both ion assistance and fluorine atoms to be etched [24]. Etching Si by using chlorine at controlled energy, also enables good selectivity of Si over SiO_2 [23]. Matsuura *et al.* [43] presented even a perfect selectivity of Si anisotropic etching over SiO_2 when using an ultraclean equipment and under chlorine plasma. If SiO_2 is not activated by Ar plasma before, it is possible to etch Si about 0.7 µm in 8 min, without etching SiO_2.

II.2. Cryogenic etching

II.2.i. *Continuous deep etching*

Si deep etching at low substrate temperature has first been presented by Tachi *et al.* in 1988. They proposed a one-step process where SF_6 is used as an alternative for Si deep etching anisotropically. Although it was well-known that SF_6 plasma isotropically etches Si at room temperature, they showed that, by decreasing the temperature between -130°C and -100°C, it was possible to get highly anisotropic profiles with a high etch rate, between 500 to 1000 nm/min, and a selectivity of 30 over PR.

The mechanism suggested by the authors was that fluorine radicals, that have random incidence, spontaneously etch Si isotropically. However, as the reaction rate depends on temperature, as shown in Eq. I. 1 and Eq. I. 2, decreasing temperature was assumed to suppress sidewall reactions. Especially that, by decreasing the temperature, the amount of physisorbed species and their residence time are increased, so there are less products desorption. Consequently, ion bombardment is required to provide the energy to assist the etching reactions at the bottom of the features [16]. However, if both the temperature and the ion energy are too low, the etching is stopped, as a too thick layer of species from SF_6 plasma, adsorbs to the surface [21].

Later, it was demonstrated that anisotropy at cryogenic temperature was in fact due to the presence of oxygen in the plasma [44]. This enables partial oxidation of the Si trenches sidewalls, by creating a thin SiO_xF_y passivation layer with a thickness of 10 to 20 nm. More precisely, SiF_4 etch product has a longer residence time at low temperature, which enables the reaction with oxygen and hence the passivation layer formation. This silicon oxyfluoride layer is however, sensitive to ion bombardment. Therefore, although this layer grows over the entire Si trench, it will be easily removed at the bottom of the trench by ion bombardment. However, given that the bombardment is lower at the trenches sidewalls, the SiO_xF_y layer accumulates and prevents lateral etching. Hence, high aspect ratio features can be achieved with low sidewall surface roughness [26]. Then, after heating, part of this passivation layer desorbs [45]. The details on the formation and enhancement of the SiO_xF_y passivation layer will be discussed in more details in Chapter IV.

With process enhancement, and temperature decreasing, it is possible to achieve very high selectivity, as Si etching increases, while PR and SiO_2 etching decreases [3], [25], [26]. Indeed, the PR resistance to etching increases [26]. Hence, selectivity of Si over SiO_2 is up to 1000:1 and >100:1 over PR.

Also, processing at low temperature does not always require a high bias to etch. Consequently, it enables etching at a lower bias, which prevents mask sputtering and hence

increase the selectivity [25]. It was also demonstrated that decreasing temperature enables to reduce damages on SiO_2 / Si interface induced by plasma [46].
However, as each technique, standard cryoetching presents some defects. Undercut effect can be observed if the passivation is not effective enough, going up to a hundred of nanometers [47]. Also, if the PR is too thick and the temperature too low, some cracking can occur on the PR. Standard cryoetching can also present ARDE as well as the other defects presented in Fig. I. 10. Nevertheless, this process is considered as a clean process. Indeed, the passivation of the trenches sidewalls is achieved by the formation of a SiO_xF_y layer on a cooled surface, and of which the majority of the layer desorbs after warming the substrate. Therefore, unlike the Bosch process there is no polymer deposition, hence no need for chamber cleaning. Indeed, most of the time the chamber walls are kept at room temperature [25].

II.2.ii. *STiGer process*

In 2008, a new cryogenic alternating process, the STiGer process, has been proposed and patented, following a collaboration between STMicroelectronics and GREMI [48]. It is quite similar to the Bosch process as it consists in alternating an etching plasma and a passivation (deposition) plasma. The feed gas for etching is SF_6, but the passivation layer is deposited at very low substrate temperature (between -110°C and -70°C) by SiF_4 / O_2 plasma. Indeed, relying on several studies performed at the GREMI to understand the mechanisms of the passivation layer formation, they have shown that SiO_xF_y layer can be efficiently formed by SiF_x and O_2 [49]. So the idea of the STiGer process is to enhance the passivation by directly supplying SiF_4 / O_2 [19], [50]. Consequently, alternating both plasmas also leads to scalloping effect on the sidewalls. However, the process is cleaner than the Bosch process for the reactor walls. Indeed, it does not require any cleaning steps and hence wafers manufacturing can go faster [19], [50].
The main advantage of the STiGer process in comparison to the cryogenic standard process is its better robustness. Indeed, as shown in Fig. I. 12, it has a lower sensitivity to temperature: it is possible to keep the same width for trench bottom for a larger range of temperatures, whereas, in standard cryoetching, the bottom width (related to the slope of the sidewalls) strongly depends on the temperature [25], [50].
However, while in standard cryoetching, the main defect is the undercut, in the STiGer process, the main defects are scalloping (Fig. I. 13) and “extended scalloping” that occur at the top of the trench. The latter defect is due to ion reflection at the sharp edge of the first isotropic cavities. To decrease this effect, it is proposed to add O_2 to SF_6 plasma during the first etching

step to help the passivation. Also, as in the Bosch process, the scalloping can be decreased by switching faster the two steps [47].

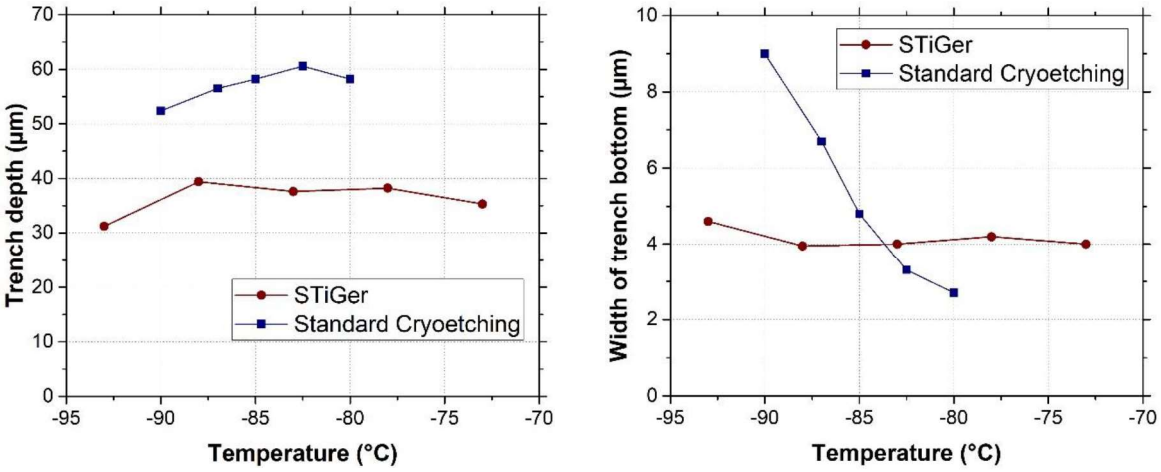

(a) (b)

Fig. I. 12. Comparison between the STiGer process and standard Cryoetching of (a) the trench depth and (b) the width of the bottom of 4 µm wide trenches, adapted from [50]

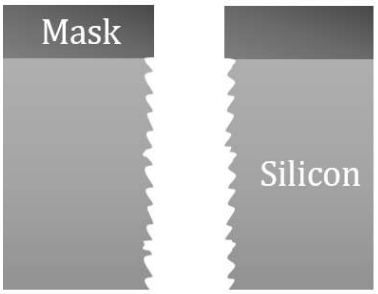

Fig. I. 13. Scalloping in STiGER process

II.2.iii. *Comparison between Bosch and cryogenic etching processes*

A comparison between the three methods presented above for silicon deep etching (Bosch process, standard cryoetching and STiGer process) is presented in Table. I. 1 [19], [25].

Table. I. 1 Comparison between three different Si deep etching processes

	Bosch	**Standard cryoetching**	**STiGer**
Process type	Time-multiplexed	Steady state etch	Time-multiplexed
Temperature	Room temperature	-130°C to -100°C	-110°C to -70°C
Feed gas	Etch step: SF_6 Depo step: C_4F_8	SF_6 (+ O_2)	Etch step: SF_6 (+ O_2) Depo step: SiF_4 + O_2
Bias voltage	~ -50 V	~ -15 V to -50 V	~ -50 V
Sidewall passivation	CF_x	SiO_xF_y	SiO_xF_y
Sidewall roughness	High	Low	High
Main defect	Scalloping	Undercut, Bowing	Scalloping
Sensitivity to temperature	Low	High	Medium
Equipment specifications	Fast equipment (MFC, pumps, etc.)	Liquid nitrogen Good clamping	Liquid nitrogen Good clamping Fast equipment
Selectivity (Si/PR)	75:1	> 100:1	
Selectivity (Si/SiO_2)	200:1	Up to 1000:1	
Application	MEMS	TSV	TSV

In conclusion, those three methods use SF_6 as etch gas for Si deep etching. Each of them has its advantages and drawbacks. Hence, the choice of using one of those methods will depend on the desirable etching characteristics.

II.2.iv. *Cryogenic etching of low-k materials*

Low-k materials are of interest for interconnects in Back-End-Of-Line (BEOL) manufacturing. They are dielectrics that have a dielectric constant k below 4.2, lower than that of SiO_2. There are mainly two types of low-k materials; hybrid silica-based materials and organic polymers. The main ones are presented in [51]. Hybrid silica-based materials have

Si-O bonds but also Si-CH_3 bonds providing them hydrophobic properties. However, when those low-k are etched by plasma processes, the Si-CH_3 bonds may be removed, transforming the material into hydrophilic. This causes water adsorption in the material's pore and consequently increases its dielectric constant to 80. This undesired phenomenon is one of the Plasma Induced Damages (PID) reported for low-k materials [51]. Several studies have therefore managed to get rid of it, and cryogenic processing appeared as one of the solutions. It has been proposed during the collaboration mentioned in the introduction, between IMEC, TEL, GREMI, and Air Liquide. The principle is to protect the low-k from PID by condensing a polymer into its pores ("capillary condensation"). The process principle is presented below in Fig. I. 14.

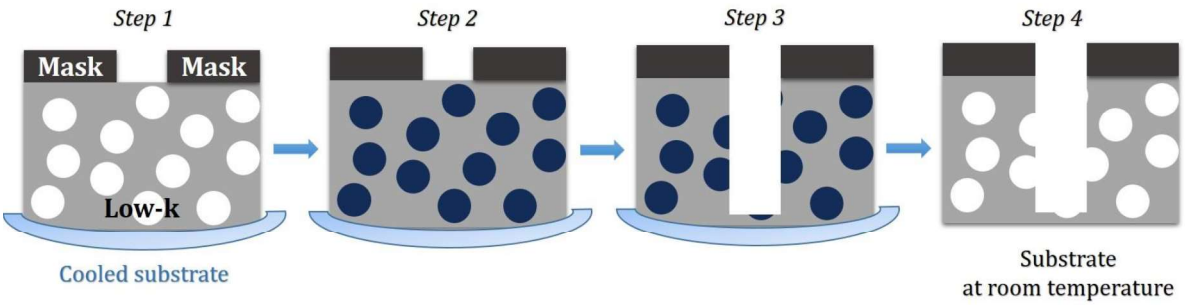

Fig. I. 14. Principle of low-k cryogenic etching

First, the low-k material is cooled. The temperature is determined according to the gas to use in step 2. Indeed, in this second step a fluorocarbon gas is injected in order to condense it in the low-k pores. So the cooling temperature is chosen in order to enable condensation. The gases studied were C_4F_8 with a process temperature at -120°C, and a high boiling point organic gas (undisclosed gas) that enables to increase the process temperature to -50°C.
Then, in step 3, the densified material is etched by SF_6 + FC mix plasma.
Finally, in step 4, the sample is annealed for 10 min at 400°C under N_2 atmosphere to remove all remaining FC from the films.
This process prevents the diffusion of active radicals through the interconnected pores of the low-k material and hence prevents the depletion of methyl groups. In this way, cryogenic etching of low-k offers very low material damage [20], [52]–[55].

In this past few years, cryogenic processes have regained interest among many large companies in the field of microelectronics, and many patents have been filed proposing cryogenic etching methods [56]–[61].

III. Etching mechanisms for silicon based materials

III.1. Silicon dioxide etching

SiO_2 is used for multilevel interconnects in via manufacturing [62]. The etching mechanisms and processes to enhance selectivity will be presented in this section.

III.1.i. *Mechanism*

The most used gases for SiO_2 etching are fluorocarbon-based gases, such as C_4F_8 and CF_4. They are injected in plasma phase in order to create CF_x that deposit and react on the surface. The F/C ratio plays an important role in the etching. High F/C ratio is obtained with gases such as C_4F_8 or C_5F_8. Ideally, CF_2 radical production is desired, as they react with SiO_2 and etch it at lower ion energy assistance than the one needed to etch Si; while CF_3 radicals have small reaction probabilities (less than 10^{-6}) [63]. A simplified global reaction, between the FC gas and SiO_2 is presented in Eq. I. 11 [23].

$$CF_x + SiO_2 \rightarrow SiF_x + CO_2 \qquad I.\ 11$$

However, FC gases are polymerizing gases that deposit on the surface. Therefore, sufficient ion assistance is required to break through the FC layer and enable the reaction presented in Eq. I. 11. The etching occurs by using the fluorine from the deposited layer that diffuses to SiO_2 surface by ion assistance that can be supported by Ar^+ ion bombardment [63]. It is consequently possible to obtain anisotropic etch. A balance has to be found between the etching and the deposition by tuning the bias power [64].

To increase the etching of SiO_2, O_2 may be mixed with C_4F_8. The oxygen enhances the production of radicals such as CF, CF_2 and C_2 and hence prevents CF build-up on the substrate surface [33].

III.1.ii. *Selectivity depending on FC deposition*

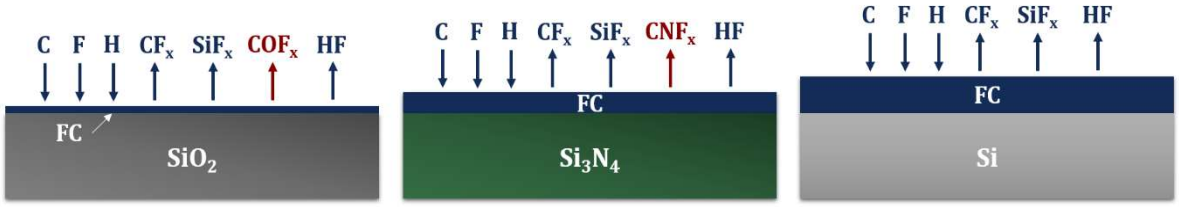

Fig. I. 15. Surface reactions of FC layer depending on the surface material, adapted from [65]

Fig. I. 15. represents the behavior of a deposited FC layer depending on the substrate material. In this figure, the FC deposited layer is formed from hydrogenated fluorocarbon based gases, such as CHF_3, so it is considered that carbon, fluorine and hydrogen species arrive to the

substrate surface to form the polymer layer. However, for a same plasma exposure, the layer thickness is not the same for the three materials. It is thinner for SiO_2 and thicker for Si. This is due to the different consumption of each element.

Fig. I. 16. presents the ER of different Si based materials depending on the thickness of the deposited FC layer. This figure was adapted from [64], where the authors performed the etching using different FC based gases as CHF_3, C_2F_6/ C_3F_6 and C_3F_6/ H_2. This figure confirms what is presented in Fig. I. 15 above. The deposited FC layer does not exceed 2 nm on SiO_2 regardless of the parameters applied, while the deposited thickness increases up to 7 nm on Si surface. It also shows the influence of this thickness on the etching, as the thinner the FC layer is, the higher the ER is.

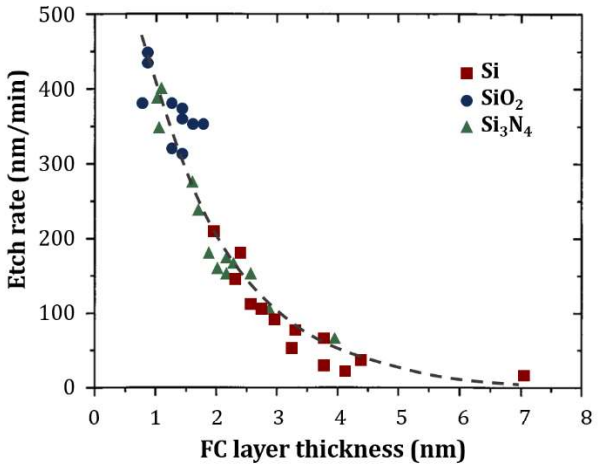

Fig. I. 16. Etch rate of Si, Si_3N_4 and SiO_2 depending on the deposited FC thickness when using different FC gases chemistries, adapted from [64]

The surface chemistries are as follows on the different materials. In the case of SiO_2, each element brought reacts with the surface and is consumed. Fluorine reacts with silicon to create volatile SiF_x products. Carbon is consumed by effective reactions with the oxygen from the substrate, creating volatile species, such as CO, CO_2 and COF_2. For example, COF_2 appeared to be weakly bonded to SiO_2 surface, making it easy to desorb. Finally, HF is also created and evacuated.

Same reactions occur on Si_3N_4, with the formation of SiF_x etch products, but also desorption of HF. In the case of carbon, it is consumed by reactions with the nitrogen from the substrate, creating volatile CNF_x products. However, this reaction is less effective than the formation of COF_x for SiO_2. Consequently, less carbon is consumed in this layer and the FC layer is hence thicker.

In the case of Si substrate, the absence of elements to react with carbon makes its consumption drastically reduced. So, the FC layer is much thicker than on the other substrates. The etching of Si is thus, more dependent on the deposition rate than the other materials.

However, even if the deposited thickness varies for one material to another, the FC film is always present, and its thickness stays constant for the same material during the etching process.

Once the FC layer is deposited, it reacts with the substrate surface, creating a modified layer to be etched. Ions are then used to bring energy for the layer defluorination and substrate etch. However, if the FC layer thickness is too high, the modified layer thickness decreases and the ion energy is dissipated in the FC layer, without reaching the substrate for etching. The FC layer becomes an etch-inhibiting film. This phenomenon more likely occurs if very polymerizing gases are used and if the bias is not high enough [21], [62], [63], [65].

In summary, controlling the thickness of the FC deposited layer and the bias enables to achieve high etching of SiO_2 over Si and Si_3N_4.

To keep enhancing the selectivity between SiO_2 and Si, hydrogen may be added to the process. For example, hydrogenated fluorocarbon based gases as CHF_3 can be used as well as gas mixtures as CF_4 with H_2. As presented above, fluorine spontaneously reacts with silicon. By adding hydrogen, the latter will help consuming fluorine by creating HF, and hence the etch rate of Si will decrease [23], [42]. Selectivity can be multiplied by 3 using CHF_3 instead of CF_4 due to even thicker FC deposited layer on Si [66].

Finally, to achieve selectivity of SiO_2 over Si_3N_4, gas mixture as C_4F_6 / Ar / O_2 can be used [67]. As the FC deposited layer thickness is higher on Si_3N_4 than on SiO_2, using C_5F_8 instead of C_4F_8, will increase the SiO_2 etching over Si_3N_4, as the polymerization is even higher [68].

III.1.iii. *Process defects and drifts*

Even if the process mechanisms seem to be now well-known, ARDE phenomenon is often reported. Indeed, when the aspect ratio of the feature to etch is increased, the ion flux incident to the bottom decreases as well as the neutral flux while the ion energy increases [33], [69].

Also, drifts due to reactor wall contamination when using fluorocarbon based chemistries have been reported in several articles.

It was noticed in [70] the influence of CF_2 concentration on the selectivity of SiO_2 over Si_3N_4. However, it was shown that the CF_2 concentration depends on the process pressure and the reactor wall conditions. This was then also discussed in [71], where the contribution of low pressure on the species mean free path and the heating of the chamber walls were underlined. Indeed, they showed that by decreasing the pressure, the probability of collisions between two molecules in the gas (gas / gas collisions) are reduced and so the mean free path is increased. Consequently, the probability of a molecule arriving from the chamber wall to the substrate after a gas / chamber collision is higher. Thus, the authors conclude that decreasing pressure

increases the influence of species at the reactor walls. They also showed that at the process beginning, the chamber walls are at lower temperature. Consequently, there is an accumulation of carbon on the chamber walls. Then, the reactor walls heat up during the process. Therefore, this induces a redeposition of carbon on the wafer, causing a decrease in the etch rate and so process drifts.

In [72], it was also noticed that the etch rates of Si_3N_4 and Si decrease over time during the process, due to the heating of the reactor walls. The authors also attributed it to the temperature of the reactor walls that increases after a certain time to a value where the fluorocarbon does not deposit on it anymore. However, as the species density remains the same in the plasma, since deposition decreases on the reactor walls, according to them, deposition hence increases on the substrate surface kept cold, inhibiting the etching on Si_3N_4 and Si.

III.2. Silicon nitride etching

Si_3N_4 is used for various applications, as mask in Integrated Circuits (IC) fabrication, spacer for Metal Oxide Semiconductor Field Effect Transistor (MOSFET), but also as an encapsulating layer, or called passivation film for the device protection and as an etch stop layer [6], [62], [73]–[77]. The main etching mechanisms of Si_3N_4 with high selectivity to other materials, are presented in this section.

III.2.i. *Chemistries used and mechanisms*

A large choice of gases exists to etch Si_3N_4. However, same elements as for Si and SiO_2 etch, are typically used such as fluorine, oxygen, carbon and nitrogen. H.F. Winters, in [78], proposed to etch Si_3N_4 using XeF_2 as fluorine source coupled to Ar^+ ion bombardment. The latter helped the desorption of the etching products such as SiF_4, but also SiF and SiF_2. Nitrogen from the plasma reacts with nitrogen of the surface and desorbs as N_2 from the surface.

In another example, B.E.E Kastenmeier and his coworkers proposed in [74] to etch Si_3N_4 using CF_4, O_2 and N_2. By mixing a certain amount of O_2 with CF_4, the amount of free fluorine in the plasma is increased. As oxygen reacts with the carbon from CF_4, it limits the deposited thickness of the FC layer on Si_3N_4 and consequently increases its etch rate.

Adding N_2 to the plasma did not affect the amount of free fluorine but it helped creating new radicals and metastables, like NO and NO*, that reacted with Si_3N_4. They played two different roles. First, NO*, with its excitation energy between 4.8 eV and 6.4 eV, brought the energy needed to break Si-N bonds that have a binding energy of about 4.5 eV. Secondly, NO from the plasma can possibly react with nitrogen from the substrate surface and desorb as N_2. Then

an oxygen or fluorine atom takes the place of nitrogen on Si dangling bond. So the addition of N_2 to CF_4 and O_2 mix increases Si_3N_4 etch rate by a factor of 7 [74].
Si_3N_4 etching is also possible using NF_3 mixed to O_2 [79]. However, the selectivity over SiO_2 is not high enough. Consequently, B.E.E Kastenmeier and his coworkers proposed again in [80] to use high flows of O_2 and N_2 and adding just a little flow of CF_4 and NF_3. Indeed, fluorine easily etched Si, so there was no need for high amount, while O_2 and N_2 also helped removing nitrogen from the surface.

III.2.ii. *Selectivity over other materials*

Etching Si_3N_4 by fluorine based chemistries, as SF_6 at 70°C, offers a small selectivity between 1.0 and 1.7 over SiO_2 [73]. To increase it, patents were published to anisotropically and selectively etch Si_3N_4 by using CHF_3 mixed with SF_6 and some Ar [73], [81].
Another way to achieve high selectivity over SiO_2 using fluorocarbon based gases was proposed by Lee *et al*. in [75]. In the previous section, it was demonstrated that a hydrogenated fluorocarbon based plasma enables to selectively etch SiO_2 over Si_3N_4 and Si, due to the formation of a FC layer protecting the latter two materials. However, Lee *et al.* [75] demonstrated the possibility to reverse the thickness behavior of the deposited FC layer between SiO_2 and Si_3N_4 in order to selectively etch Si_3N_4 over SiO_2 (Fig. I. 17). To do so, the authors proposed to mix a fluorine-based gas as CF_4 or NF_3 or SF_6 with CH_4. Beyond a certain amount of CH_4 injected, the etching of SiO_2 stopped, while the etching continued on Si_3N_4. They showed that a 2 nm thick fluorocarbon deposited layer is enough to stop the etching. The reactions taking place at the surface are the same as the one shown in section III.1.ii. However, the addition of a sufficient amount of hydrogen provided by CH_4, affects the etch rate behavior of each material. As hydrogen helps consuming fluorine from the deposited layer, it favors deposition instead of etching on the materials. However, hydrogen also reacts with Si_3N_4 surface to create HCN and NH_x volatile etch products. So the optimal amount of CH_4 depends on the other mixed gas. As the purpose is to create FC layers on the other materials to prevent the etching, more CH_4 amount is needed when mixed with NF_3 or SF_6 than with CF_4.
Following this reasoning, other gas mix using hydrogenated fluorocarbon gases were also proposed in [73] as CHF_3-SF_6, CHF_3-O_2 or CHF_3-C_2F_6 to etch silicon nitride. It was also shown in [76] that Si_3N_4 etching was enhanced when using radicals as CHF_2 and fluorine atoms rather than CHF_2^+ ions.

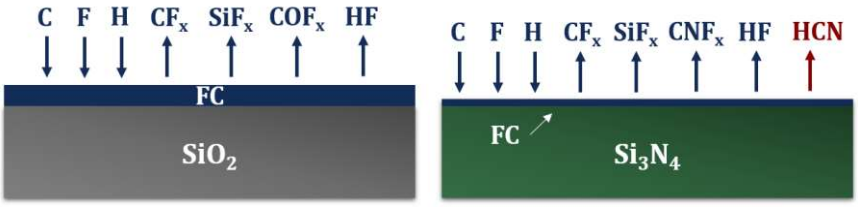

Fig. I. 17. FC deposited layer in CF_4 / CH_4 plasma mixture depending on the material

Whereas in [79], it is proposed to etch Si_3N_4 by using NF_3 / O_2 mix, in [82], it was also proposed to add NH_3 in a certain amount and so create a mix NF_3 / O_2 / NH_3 to obtain a selectivity over SiO_2 higher than 100:1. Indeed, doing so increased the formation of NO, as observed in [74], and decreased the fluorine amount, so Si_3N_4 was more etched, while SiO_2 was less etched.
Also, using a CF_3I / O_2 / H_2 neutral beam, it was possible to etch Si_3N_4 with a selectivity of 6.2 and 18.6 for Si and SiO_2 respectively. In addition to the reactions occurring and presented above, oxygen helped oxidizing the Si surface, inducing the stop of the etching. They explain that the energy threshold to break Si-O bonds is higher than for breaking Si-N bonds. Consequently, adjusting the bias to only break Si-N bonds helps increasing the selectivity [77].

IV. Conclusion and limitations of (deep) etching

The deep etching of silicon-based materials has been studied extensively. Nevertheless, it is still under investigation. Indeed, most of the processes presented above suffer from ARDE effects, with the limitation of ions and neutrals arriving to the bottom of the trenches. Also, time-multiplexed alternating processes as Bosch and STiGer present surface damages and scalloping effects, that are sometimes not acceptable for the application. While steady state etch processes offer smoother trenches sidewalls, their control is less efficient, as same energy is provided and used for deposition and etching reactions, which prevents from obtaining optimal conditions for both mechanisms [13].
Finally, those processes present several limits for today components requirements, such as for the manufacturing at nanoscale and atomic scale with as less defects as possible.
Therefore, a new process called Atomic Layer Etching (ALE) has been recently introduced to answer today manufacturing demands.

V. Atomic Layer Etching

As explained in the introduction, Atomic Layer Etching has seen a gain of interest since 2010, and is considered today as the most advanced etching method [83]. The requirements of the micro and nano technology industries do not stop getting stringent with the design of smaller components without defects, smoother surfaces and greater aspect ratios [84], [85]. Process control ability is tested more than ever, and ALE seems to be the most promising technique to meet all those requests.

V.1. General information

V.1.i. *Principle*

Atomic Layer Etching (ALE) is a cyclic process of several self-limiting sequences to remove one to few monolayers per cycle. In order to improve the control of the etching process, reaction steps have been separated compared to standard etching. Fig. I. 18 shows the different steps of an ALE cycle.

The first step of the cycle consists in exposing the substrate surface to a reactive gas, generally in plasma phase, in order to adsorb radicals at the surface, creating a modified layer. The purpose of this step is to create bonds between the gas species and the substrate (E_{ML}) that need less energy to be broken than the bonds between the atoms of the substrate itself (E_S), hence $E_{ML} < E_S$. So, the main objective of this step is just to modify the substrate surface, with no etching at all. Hence, the ion energy in this plasma should be low, or at least lower than E_{ML} [83], [86], [87].

Once the whole surface is covered by the formed modified layer, no more species adsorb at the surface: it is why this step is qualified as “self-limiting”. A purge or pumping step may be performed after to ensure the evacuation of all the species that did not adsorb at the surface, and hence control the amount of reactive species in the reactor.

The third step is the etch step. An inert plasma, usually Ar, is applied with a low ion energy (E_i) to prevent sputtering, but high enough to provide the energy needed to remove the modified layer [86].

$$E_{ML} < E_i < E_S \qquad \text{I. 12}$$

It was shown in [88], that Ar^+ does not only contribute to ion bombardment assistance but also helps the creation of new active sites for the next adsorption step. Depending on the application, this step can be controlled to provide either isotropic or anisotropic etching [89]. As in continuous etching, the etch products need to be stable and volatile in order to prevent

any redeposition on the substrate and limit any ARDE effect [90]. This step is also self-limited, since, once the modified layer has been depleted and $E_i < E_S$, the etch stops.
Finally, there is another purge or pumping step in order to remove all the etch products from the chamber before restarting a new cycle [4], [7], [85], [89], [91], [92].

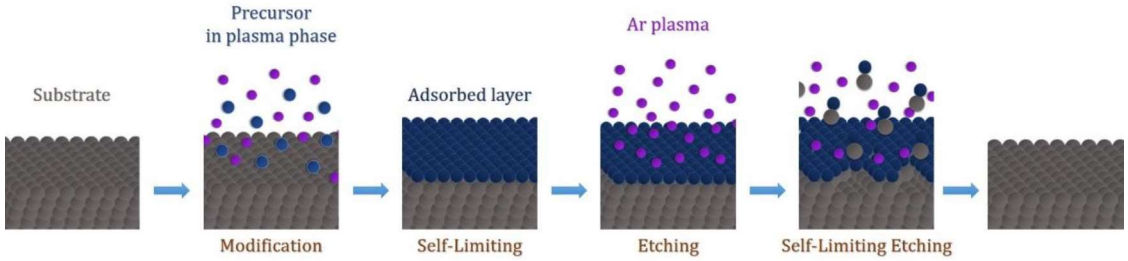

Fig. I. 18. Steps in one cycle of Atomic Layer Etching, adapted from [13]

V.1.ii. *Main parameters for ALE evaluation*

Three parameters, the saturation curve, the energy scan and the synergy test are presented in this section. They are the main parameters used to qualify an ALE process and characterize it.

V.1.ii.a. Saturation curve

In contrast to continuous etching, in ALE, etching occurs at the beginning of the etching step in each cycle. Once the modified layer is depleted, the etch stops. Quasi ALE is an intermediate process where the etch rate decreases significantly through time but does not stop. Fig. I. 19 illustrates the evolution of the EPC for ALE, quasi ALE and continuous etching. It shows that the etch saturates versus time for ALE because of self-limiting etching. This is why such a plot is called “saturation curve”. This self-limiting behavior of the etching is the one to consider to qualify the process as ALE, rather than the etch amount per cycle [13].

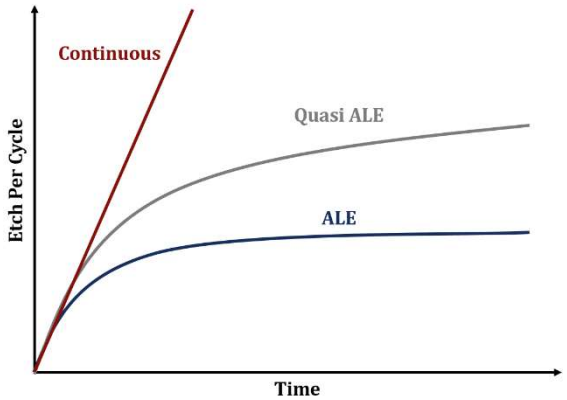

Fig. I. 19. Saturation curve

V.1.ii.b. Energy scan test

As mentioned in section V.1.i, the ion energy during the etch plasma has to be well defined to perform ALE. If the ion energy is too low, only partial removal occurs creating roughness and uncontrolled etching as the amount of the modified layer increases. On the other hand, if the ion energy is too high, sputtering occurs by ion bombardment. The surface may hence be damaged with surface roughness increase and SLE is not reached. Therefore, as displayed in Fig. I. 20, this defines an ALE window where the energy of the ions is, as expressed in Eq. I. 12, in the desirable range to assist the complete removal of the modified layer with no sputter etch [13], [86], [87].

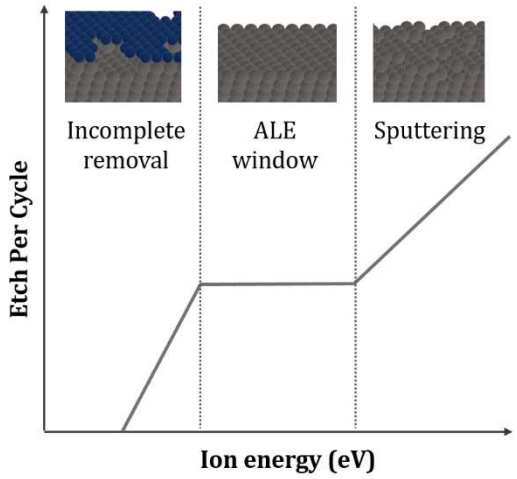

Fig. I. 20. Etching behavior as a function of energy, adapted from [13]

V.1.ii.c. Synergy test

To improve the control of etching during the process, synergy tests may be performed. The purpose of those tests is to identify any undesired etching. In other words, as reactive species are used in the deposition step, some chemical etching may occur even without ion bombardment assistance. In addition, as explained in the previous paragraph, during the etch plasma, some sputtering may occur. Both phenomena are undesired, as they prevent etch amount control, and they should be avoided. Hence, to identify their influence, these steps are performed separately and independently (either etching or deposition). Their resulting EPC are then compared to the EPC obtained when combining both reactions in a global process [13], [84], [93]:

$$ALE\ synergy\ \%\ (S) = \frac{EPC-(\alpha+\beta)}{EPC} \times 100\% \quad [93] \qquad \textit{I. 13}$$

With α, the EPC during only the modification step, β, the EPC during only the etching step and EPC is when both steps are combined. All three entities are in nm/cycle [93]. ALE is considered as ideal when its synergy is close to 100% [84].
If chemical etching is identified during the deposition step, one way, suggested in [13], to get rid of it consists in decreasing the substrate temperature to inhibit the chemical reactions and spontaneous etching. Parameters of this plasma also have to be reviewed and optimized.
On the other hand, if physical etching is detected during the etching plasma without having previously modified the surface, ion energy has to be reduced below the sputtering threshold of the etched material [13]. However, Berry *et al.* [90] showed, using a Monte Carlo model, that it is possible to obtain a synergy close to 100% even with high ion energy if the exposure time is reduced. This enables to perform faster controlled processes with etch steps of less than 5 s.

ALE can also be achieved in other ways. Thermal ALE for example, modifies the substrate surface and uses ligand exchange or heat to help the desorption of volatile etch products [84]. Coupling both plasma and thermal method for higher selectivity and directionality has been proposed in [94]. It has been chosen to not further discuss those types of ALE, but only plasma assisted ones in the next sections.

V.2. ALE of silicon

Silicon was the main material studied to understand, develop and enhance ALE process. Consequently, different chemistries were proposed in order to understand the role of each step of the process. Mainly, silicon was etched by chlorine or fluorine based plasmas, as presented in a non-exhaustive list in Table. I. 2.

Table. I. 2. References for some of the main studies on Si ALE

Modification gas	Etching gas	Ion energy (eV)	EPC (Å/cycle)	References
CF_4 / O_2	Ar	20	1.3 - 2.5	[17], [18]
NF_3 / N_2, F_2 / He	Ar	20	0.5 - 8	[18]
Cl_2 (+Ar)	Ar	20 - 40	0.6 - 15	[13], [86], [95]–[97]
C_4F_8 / Ar	Ar	20-30	3	[98], [99]
CHF_3 / Ar	Ar	20-30	6	[98], [99]

Y. Horiike's team [17], [18] was the first to propose Si ALE to reduce sidewall damages compared to continuous etching processes. According to them, decreasing the substrate temperature to a value between -70°C and -170°C reduces spontaneous etching of silicon by fluorine. Thus, the modification step to supply fluorine was performed testing several gases like CF_4 / O_2, NF_3 / N_2 and F_2 / He discharges. Ar ions were used to supply the energy for

desorption of the etching products. They succeeded in showing that, in those conditions, fluorine physisorbs to the silicon surface and that only a small amount of fluorine is needed to perform the etching. They also succeeded in performing self-limiting and anisotropic etching, while reducing the micro loading effect.

Since those publications, instead of a fluorination of Si surface, Si ALE has been proposed using Cl_2 / Ar to chlorinate the surface by Matsuura *et al*. [95]. Indeed, chlorine would chemisorb on Si surface but would not form volatile $SiCl_x$. Hence, as chlorine does not spontaneously etch Si, it is an easier chemistry to prevent etching during the modification step [97]. Cl_2^+ and Cl^+ can also collide to the surface and break Si-Si bonds. Then, they react with Si to passivate the surface by creating $SiCl_x$, and finally form volatile products as $SiCl_2$ and $SiCl_4$. Consequently, this chlorination step is self-limiting, as it stops once the whole silicon surface area is covered by a monolayer, following Langmuir theory on adsorption [95], [100]. While the binding energy of Si-Si is about 2.4 eV, the energy given by Ar^+ ions is close to 50 eV in the experiments. Such a high energy of Ar^+ can be required, as they lose some energy by collisions in the plasma before reaching the substrate. Consequently, around ten Ar^+ ions are needed to remove one $SiCl_x$. However, it should not be forgotten that the Si physical sputtering threshold is about 20 eV, which makes ALE more complicated to be achieved in an efficient way and without sputtering [98]. So Ar^+ energy needs to be well controlled during the etch step. Knowing that one monolayer of Si is about 1.4 Å [83], one to few monolayers could be etched per cycle by Cl_2 / Ar chemistry. Surfaces remained smooth, while performing anisotropic etching at a synergy close to 90% [13], [83], [85], [87], [92], [93].

In [89], whereas the purpose of the article was initially the study of the process equipment for ALE, the authors showed that Si coupon EPC in chlorine based etching chemistry depends on the carrier wafer material. More etching is observed when using SiO_2 carrier wafer than a Si one. Indeed, during the deposition step, the surface coverage is not the same on both materials. A multilayer deposits on SiO_2, and species from that layer contribute then to the etching of Si.

Metzler *et al.* in [98] and [99] also tried fluorocarbon based gases like C_4F_8 and CHF_3, for Si ALE. During the process, the silicon surface may react with oxygen coming from undesired erosion of the quartz window in the reactor, and with fluorine from the FC gas, creating a modified layer, between the FC deposited layer and the silicon substrate surface. Fig. I. 21 shows the etch behavior as a function of the deposited FC amount. The stacking layers are clearly separated in the figure, however, in reality, these layers can be mixed. In Fig. I. 21. a, about 0.5 nm of FC are deposited on Si surface, whereas in Fig. I. 21. b, about 1.1 nm are deposited. Then, it shows that after etching, a higher amount of Si is removed when a higher amount of FC was deposited. They explain that during the FC layer deposition, Si surface is fluorinated. Hence, the thicker the layer, the deeper the etching per cycle is. However, this is

valid for relatively small deposited thicknesses (0.5 to 1.5 nm). The modified layer also plays a major role by supplying reactants for Si etching. Although the deposition step is not self-limiting, the etching step is self-limiting: as soon as the deposited layer is depleted, the etch stops. This behavior is opposite to what is usually observed in continuous etching. Even if the growth rate of the CF_x layer is more efficient on Si, it actually enhances the etching of Si compared to SiO_2 instead of stopping it. In continuous etching, the FC amount deposited on the surface is in a steady state, whereas in ALE, the deposited amount is globally but not exactly the same at each cycle. A small variation in the substrate surface chemistry due to oxidation or contamination affects the deposited amount and consequently the etched thickness. The F/C ratio is higher when using CHF_3 than C_4F_8, which increases the deposition rate, but it also brings more fluorine to etch Si. The etch step duration as well as the ion energy affects the selectivity between Si and SiO_2. Increasing the etch step length or the ion energy ensures the consumption of fluorine while possibly oxidizing Si surface. Consequently, SiO_2 is etched selectively to Si. On the other hand, reducing the etch step length or the ion energy enables to etch Si selectively to SiO_2.

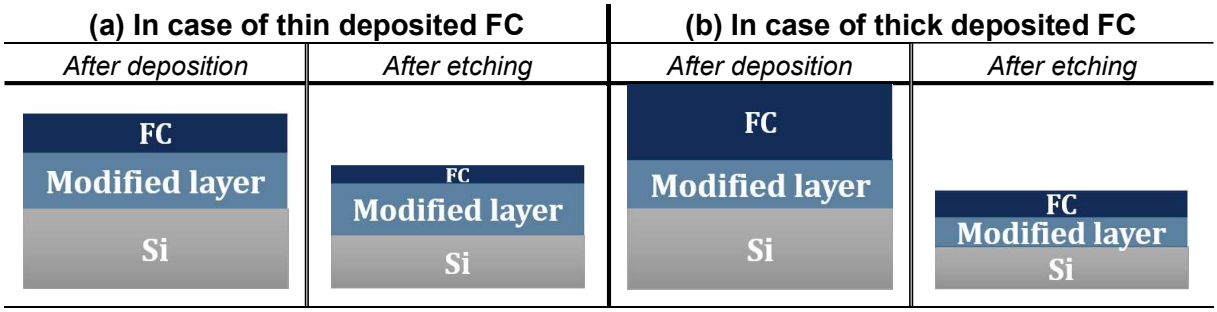

Fig. I. 21. Thickness evolution along steps adapted from [99], with (a) a deposited amount of about 0.5 nm and (b) a deposition of about 1.1 nm

In [101], Metzler *et al.* tried to remove the native oxide from Si substrate by adapting ALE of SiO_2. They mixed CF_4 with Ar for the modification step followed by Ar sputtering. Then they removed the residual CF_x from the surface by using a H_2 / Ar plasma. Even if they succeeded in removing 50% of oxygen from the surface, by doing so, they also demonstrated how much the silicon surface can be reactive and easily oxidized. Especially, Ar sputtering, even at low ion energy, helps the oxidation of the surface due the residual oxygen present in the chamber.

V.3. ALE of silicon dioxide

SiO_2 ALE has generated a lot of interest and studies. The plasma chemistries used for the modification step were generally fluorocarbon based [92]. Table. I. 3 sums up some of those studies.

Table. I. 3. References for some main studies on SiO_2 ALE

Modification gas	Etching gas	Ion energy (eV)	EPC (Å/cycle)	Reference
C_4F_8/Ar	Ar	20-35	2-4	[98], [102]–[104]
C_4F_8	Ar	90-130	2	[105]
CHF_3/Ar	Ar	20-35	4	[98], [103], [106]
$C_3F_7OCH_3$	O_2 or Ar		1.1 to 2.1	[107]

During the modification step, SiO_2 is exposed to a CF_x plasma in order to deposit a thin FC layer. Between the FC layer and the SiO_2 substrate, a thin modified layer CF_x-SiO_2 of about 4 Å is created as illustrated in Fig. I. 22. It is then etched by Ar^+ ion bombardment. Ar flow can also serve as a purge between each step.

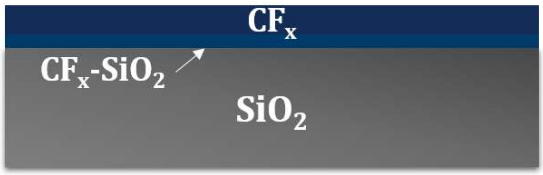

Fig. I. 22. SiO_2 surface after exposure to CF_x plasma

Although Rauf *et al.* simulated in [108] the possibility to have self-limiting deposition when using low CF_2^+ and CF_3^+ ions energy, experiments showed that the deposition step is not self-limited. Hence it needs to be accurately controlled to only deposit around a monolayer of CF_x [67]. As in continuous etching, in the etching step, fluorine from the deposited and modified layer reacts with silicon to form volatile SiF_4, while carbon reacts with oxygen creating volatile CO and CO_2 [93]. At the end of Ar plasma step, some residual fluorine can be detected on the substrate surface [104], [108].

Metzler *et al*. were the first to demonstrate the possibility of controlling the etch rate of SiO_2 by depositing a thin FC layer by C_4F_8 / Ar mix, and then applying an Ar plasma with an ion energy of less than 30 eV to achieve self-limiting etching [104]. C. Li *et al*. showed in [103] that, depending on the FC layer thickness, the etching selectivity between SiO_2 and Si_3N_4 can be tuned. Two cases are possible while etching Si_3N_4 and SiO_2 using a CF_x plasma. They are presented in Fig. I. 23. If the fluorine radicals in the FC layer are depleted and if the ion energy is higher than the physical sputtering threshold of Si_3N_4 (≈ 20 eV) but lower than SiO_2 physical sputtering threshold (≈ 45 eV), Si_3N_4 keeps etching by sputtering while SiO_2 etching is stopped. Hence, it is possible to obtain an etching selectivity between Si_3N_4 and SiO_2. But, if the FC

layer accumulates due to both low ion energy and longer step time, the FC layer deposited on Si_3N_4 is much thicker and protect it from etching, and only SiO_2 is etched, achieving high selectivity over Si_3N_4.

Huard *et al.* demonstrated in [109] by computational investigation that Si_3N_4 is etched during the first ALE cycles before the FC layer is significantly thick to inhibit the etching. This behavior can limt the selectivity when only few ALE cycles are needed. They hence propose to start with a longer deposition step to build up a thicker FC layer from the first cycle.

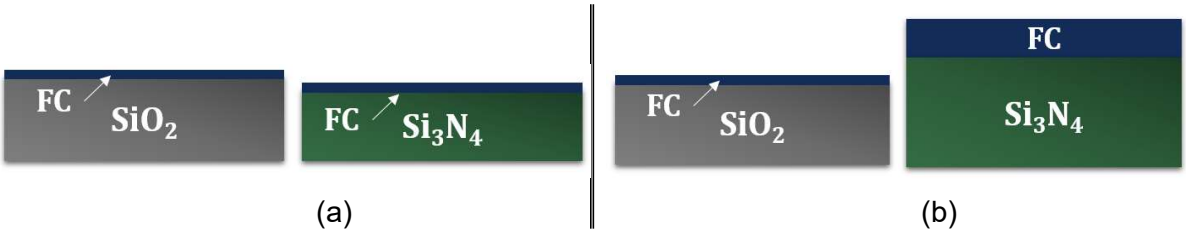

Fig. I. 23. SiO_2 and Si_3N_4 after etching in (a) FC depleted conditions and (b) FC accumulated conditions

As already mentioned, in order to create a modified layer, CF_x radicals are supplied in plasma phase. Deposition occurs not only on the substrate, but also on the reactor walls. Consequently, some drifts can be observed during the etching with an increase of the EPC along cycles, due to fluorine release from the deposited layer on the reactor walls and also from reactions between CF_x and the quartz window [102], [110].

In order to limit those drifts that can affect the reproducibility of the process, reactor walls cleaning and conditioning can be performed. It was suggested for example in [102], to first clean the reactor walls by a plasma of O_2, SF_6 and Ar mix for 10 min, followed by 75 min of SF_6 / Ar plasma, then deposit about 12 nm of SiO_2 using a SiH_4 / Ar / O_2. And finally, clean again the reactor for 75 min.

Dallorto *et al.* in [106] studied the influence of fluorine deposited on the reactor walls and the substrate temperature during the etching of SiO_2. They fluorinated the reactor chamber walls and then performed an Ar plasma on SiO_2 at different temperatures and checked the etching. When SiO_2 was at 20°C, 9 Å/min were etched. Whereas the etch rate was only 0.5 Å/min when decreasing the temperature to -10°C, and no etching at all was observed if decreasing the substrate to -40°C. They hence concluded that the effect of fluorine from the chamber walls is significantly decreased if the substrate is cooled to -10°C. They suggest that the reactivity between fluorine / FC films from the chamber walls and SiO_2 decreases with temperature decrease. Thus by decreasing SiO_2 temperature to -10°C, they succeeded to obtain quasi-self-limiting etching behavior.

However, they also showed that varying the process temperature from room temperature to -40°C increases the deposition amount per cycle, but the EPC remains about the same, meaning that this ALE process is not thermally dependent. It also enables to reduce loading

effect while increasing the aspect ratio independent etching (ARIE) behavior. However, they also showed the importance of controlling the pressure for anisotropic etching. Indeed, by decreasing the pressure, they obtain high ion energy and reduce the density of fluorine and carbon. Consequently, the contribution of fluorine radicals in isotropic etching is also reduced [106], [111].

While most of the publications propose the use of C_4F_8 or CHF_3 for etching, Y. Kim *et al*. [107] propose the use of a bigger molecule $C_3F_7OCH_3$, that is more ecofriendly as its Global Warming Potential (GWP) is lower than the usual gases. Indeed, the GWP for 100 years time horizon of C_4F_8 and CHF_3 are respectively of about 8700 and 11700, whereas it is about 499 for $C_3F_7OCH_3$ [112], [113]. They were able to etch SiO_2 with some selectivity over Si using $C_3F_7OCH_3$ / O_2 plasma. However, the study showed that the etching rate using this molecule is lower than with C_4F_8 or CHF_3. This is due to the F/C ratio that is lower using $C_3F_7OCH_3$.

To also increase selectivity of SiO_2 over Si and Si_3N_4, Lin *et al.* propose in [114] to use $C_3H_3F_3$ that enables to etch SiO_2 while building a passivation HFC layer on Si and Si_3N_4 that is less rich in fluorine than when using C_4F_8.

As in continuous etching, selectivity of SiO_2 etching over Si_3N_4 is a main concern and is needed for example for self-aligned contacts (SAC) application [13], [67], [109], [115]. As SiO_2 physical sputtering threshold is around 45 eV, it is higher than for Si or Si_3N_4 [104]. Therefore lowering the ion energy helps increasing selectivity over Si or Si_3N_4 as undesired etching is prevented.

V.4. ALE of silicon nitride

ALE of silicon nitride can be useful for gate spacers manufacturing. Consequently, selectivity over other materials is very important. Contrary to Si or SiO_2, Si_3N_4 cannot be etched by chlorine based materials because Si-N bonds are stronger than Cl-N bonds [13]. Instead, fluorine and hydrogen based chemistries are used for its etching. Table. I. 4 presents some references for different gases used for Si_3N_4 ALE [3], [92].

Many studies presented in the previous sections used fluorocarbon based gases to etch Si_3N_4 as well as SiO_2. As for SiO_2, fluorine from the FC layer contributes in the etching of Si in Si_3N_4. However, a too thick FC deposited layer prevents the etching of Si_3N_4, therefore a higher bias is required than for SiO_2 etching to prevent the layer build-up. As for SiO_2, the FC deposited layer has not a self-limited behavior on Si_3N_4 [115]. However, by using $C_3H_7OCH_3$, Kim *et al.* [107] managed to achieve a high selectivity of 26.6 of Si_3N_4 over Si.

Table. I. 4. References for some main studies on Si_3N_4 ALE

Modification gas	Etching gas	Ion energy (eV)	EPC (Å/cycle)	Reference
SF_6	Ar		4-5	[116]
C_4F_8 / Ar	Ar	20-35	4-5	[103]
CHF_3/Ar	Ar	20-35		[103]
$C_3H_7OCH_3$	Ar or O_2			[107]
H_2 or He	Ar^+ / H_2	20-100	20-60	[117], [118]
H_2	SF_6 or NF_3 / Ar	40	60-90	[119], [120]
H_2	NF_3-NH_3		50-100	[121]
H_2	SF_6		20-50	[122]
CHF_3 / O_2	Annealing		21-27	[123]

Otherwise, many studies aimed to use H_2 for H^+ ion implantation in order to first modify SiN surface. Hydrogen helps removing nitrogen from the surface by creating NH_3 as etch by-product, leaving Si as a modified layer [13], [92], [117]. It is also explained, in Bouchilaoun *et al.* [124] work that after hydrogen plasma, Si-H bonds and N-H bonds are created. By creating those bonds, the energy of the back-bonds is affected. Si-N-H back-bond energy is lower than for Si-N-Si. Therefore, it becomes easier to etch SiN after hydrogen plasma treatment. Then, Si can be removed from the surface by fluorine, as SiF_x and / or SiF_xH_y etch-products.

The energy used for the ion implantation helps controlling the depth of the modified layer and consequently the etch depth [119].

To remove the modified layer after hydrogen treatment, several techniques were proposed. In [117], Matsuura *et al.* propose to simply bombard the modified layer using Ar^+ and H^+ ions to remove Si.

Posseme *et al.* [118] proposed an alternative way to etch the modified layer. In their approach, the modified surface is removed by chemical wet etch using HF solution. This technique allowed to reduce damages on silicon germanium during spacer etching. However, this led to other defects on SiN surface. Consequently, in [121], they use NF_3 and NH_3 plasma to remove the modified layer. They showed that the surface chemistry of this intermediate product is the salt $(NH_4)_2SiF_6$. Etching it enables a selectivity of 8 on modified SiN over the pristine SiN. However, there is no selectivity over SiO_2.

In [119] and [120], Sherpa *et al.* use a slightly different approach to achieve SiN etching with a selectivity over SiO_2 higher than 100. First, they also modify the surface by H^+ ion bombardment. However, in these articles, they present the possibility to choose the directionality of the etching during the modification step. If the hydrogen implantation is processed at low pressure, the modification occurs using ions, which then enables anisotropic etching. If the pressure is increased, the modification occurs in radicals regime, inducing

isotropic etching. Then, they suggest using SF_6 or NF_3 with Ar to supply fluorine radicals for Si modified layer removal.

In [122], after surface modification by hydrogen plasma, the layer is etched by a SF_6 plasma. They obtain a high selectivity over SiO_2 which is due to the difference needed to dissociate Si-O in comparison to Si-N bonds.

Finally, the approach proposed by Shinoda *et al.* [123] is a cyclic process, where first, SiN is exposed to CHF_3 / O_2 downstream plasma in order to create a thin modified layer $(NH_4)_2SiF_6$. Then, the sample is simply annealed at around 100°C-120°C by infrared irradiation in order to sublimate the layer. The modified layer desorbs by producing the volatile etch-products SiF_4, NH_3 and HF. They also observe a great selectivity over SiO_2 as the latter does not contain any nitrogen from the formation of the modified layer.

VI. ALE, advantages and enhancements possibilities

Atomic Layer Etching consists of self-limiting sequential reactions to remove atomically thin layers of a material. When ideal ALE is performed, with self-limiting steps for modification and etching, respecting the saturation curve, it can enable uniform etching on the sample surface, and become less dependent on the reactant fluxes uniformity [83], [85]. Moreover, as the reactions are self-limiting, it helps limiting the loading effect observed in continuous etching [13]. Therefore, it gives the opportunity of achieving etching on larger wafers. Nevertheless, an over exposure to ions may be necessary, which can induce mask erosion [87].

Moreover, ALE appeared to be a smooth process as surface roughness is decreased after it. It is due to the low ion energy in the etching step that helps the diffusion of the surface atoms and consequently smooth the surface. ALE also enables to achieve higher selectivity than in continuous etching, high aspect ratio and surface damage decrease [83], [84], [100]. Ideal ALE also enables ARIE due to its self-limiting properties. However, a small amount of residual reactant in the etching step may compromise this advantage [100].

One of the reasons why ALE is not yet commonly used in industry is because it is still considered as a slow process. However, a real gain in time enhancement has already been performed since its introduction [83]. Some equipment enhancements are sometimes recommended to perform controlled and precise steps and achieve precise and reproducible ALE. For example, the installation of fast response valves enables a better control of the reactant injection dose. Also the possibility of a precise control of the plasma source helps adjusting the ion energy [91].

However, the more advances are made, the more the demand for even smaller components increases, reaching new limits. More specifically, such atomic scale processes may experience drifts through time, due to reactor wall contamination, especially when using FC chemistries [98], [102], [106], [110], [125], [126]. To prevent those drifts and ensure reproducibility, long cleaning steps and reactor wall conditioning of around two hours may be needed.

To overcome this particular drift issue, cryo-ALE has been proposed and is the research topic of this thesis. In addition to reducing drifts, it is required by this process to limit material damage and ensure high selectivity between the materials studied.

VII. References

[1] G. E. Moore, “Cramming More Components Onto Integrated Circuits,” *Electronics*, vol. 38, no. 8, pp. 82–85, 1965.

[2] C. G. N. Lee, K. J. Kanarik, and R. A. Gottscho, “The grand challenges of plasma etching: a manufacturing perspective,” *J. Phys. D: Appl. Phys.*, vol. 47, no. 27, p. 273001, 2014.

[3] K. Ishikawa *et al.*, “Progress and prospects in nanoscale dry processes: How can we control atomic layer reactions ?,” *Jpn. J. Appl. Phys.*, vol. 56, no. 6S2, p. 06HA02, 2017.

[4] F. Roozeboom, F. Van Den Bruele, Y. Creyghton, P. Poodt, and W. M. M. Kessels, “Cyclic Etch/Passivation-Deposition as an All-Spatial Concept toward High-Rate Room Temperature Atomic Layer Etching,” *ECS J. Solid State Sci. Technol.*, vol. 4, no. 6, pp. N5067–N5076, 2015.

[5] W. Shockley, “A Unipolar ‘Field-Effect’ Transistor,” *IEEE*, vol. 40, no. 11, pp. 1365–1376, 1952.

[6] V. M. Donnelly and A. Kornblit, “Plasma etching: Yesterday, today, and tomorrow,” *J. Vac. Sci. Technol. A*, vol. 31, no. 5, p. 050825, 2013.

[7] C. T. Carver, J. J. Plombon, P. E. Romero, S. Suri, T. A. Tronic, and R. B. Turkot, “Atomic Layer Etching: An Industry Perspective,” *ECS J. Solid State Sci. Technol.*, vol. 4, no. 6, pp. N5005–N5009, 2015.

[8] I. Cutress, “Samsung Announces 3nm GAA MBCFET PDK, Version 0.1,” *AnandTech*, 2019. https://www.anandtech.com/show/14333/samsung-announces-3nm-gaa-mbcfet-pdk-version-01 (accessed Mar. 26, 2020).

[9] Y. Jeon, “[Editorial] Making Semiconductor History: Contextualizing Samsung’s Latest Transistor Technology,” *News.samsung*, 2019. https://news.samsung.com/global/editorial-making-semiconductor-history-contextualizing-samsungs-latest-transistor-technology (accessed Apr. 03, 2020).

[10] N. Draeger, “Tech Brief: FinFET Fundamentals,” *Lam Research*, 2016. https://blog.lamresearch.com/tech-brief-finfet-fundamentals/ (accessed Mar. 26, 2020).

[11] L. Yuan, J. Zeng, Y. Woo, and J. Kye, “Self-aligned double patterning process for two dimensional patterns,” US20160163584A1, 2016.

[12] M. N. Yoder, “Atomic layer etching,” US4756794A, 1988.

[13] K. J. Kanarik *et al.*, “Overview of atomic layer etching in the semiconductor industry,” *J. Vac. Sci. Technol. A*, vol. 33, no. 2, p. 020802, 2015.

[14] E. Kessels, “Atomic layer etching turns 32.5 years old! – A good occasion to share an ALE timeline and an animated version of the ALE periodic table,” *Atomic Limits*, 2020. https://www.atomiclimits.com/2020/03/02/atomic-layer-etching-turns-32-5-years-old-a-good-occasion-to-share-an-ale-timeline-and-an-animated-version-of-the-ale-periodic-table/ (accessed Mar. 26, 2020).

[15] A. Bensaoula, A. Ignatiev, J. Strozier, and J. C. Wolfe, “Low-temperature ion beam enhanced etching of tungsten films with xenon difluoride,” *Appl. Phys. Lett.*, vol. 49, no. 24, pp. 1663–1664, 1986.

[16] S. Tachi, K. Tsujimoto, and S. Okudaira, “Low-temperature reactive ion etching and microwave plasma etching of silicon,” *Appl. Phys. Lett.*, vol. 52, no. 8, pp. 616–618, 1988.

[17] Y. Horiike *et al.*, “Digital chemical vapor deposition and etching technologies for semiconductor processing,” *J. Vac. Sci. Technol. A*, vol. 8, no. 3, pp. 1844–1850, 1990.

[18] H. Sakaue, S. Iseda, K. Asami, J. Yamamoto, M. Hirose, and Y. Horiike, “Atomic Layer Controlled Digital Etching of Silicon,” *Jpn. J. Appl. Phys.*, vol. 29, no. Part 1, No. 11, pp. 2648–2652, 1990.

[19] R. Dussart, T. Tillocher, P. Lefaucheux, and M. Boufnichel, “Plasma cryogenic etching of silicon: from the early days to today’s advanced technologies,” *J. Phys. D: Appl. Phys.*, vol. 47, no. 12, p. 123001, 2014.

[20] F. Leroy *et al.*, “Cryogenic etching processes applied to porous low-k materials using SF_6/C_4F_8 plasmas,” *J. Phys. D: Appl. Phys.*, vol. 48, no. 43, p. 435202, 2015.

[21] C. Cardinaud, M.-C. Peignon, and P.-Y. Tessier, “Plasma etching: principles, mechanisms, application to micro- and nano-technologies,” *Appl. Surf. Sci.*, vol. 164, no. 1–4, pp. 72–83, 2000.

[22] H. J. Kreuzer and Z. W. Gortel, *Physisorption kinetics*, vol. 1. Springer-Verlag Berlin Heidelberg, 1986.

[23] H. Abe, M. Yoneda, and N. Fujiwara, “Developments of Plasma Etching Technology for Fabricating Semiconductor Devices,” *Jpn. J. Appl. Phys.*, vol. 47, no. 3, pp. 1435–1455, 2008.

[24] J. W. Coburn and H. F. Winters, “Ion- and electron-assisted gas-surface chemistry—An important effect in plasma etching,” *J. Appl. Phys*, vol. 50, no. 5, pp. 3189–3196, 1979.

[25] M. J. Walker, “Comparison of Bosch and cryogenic processes for patterning high-aspect-ratio features in silicon,” 2001, pp. 89–99, [Online]. Available: http://proceedings.spiedigitallibrary.org/proceeding.aspx?articleid=883583.

[26] B. Wu, A. Kumar, and S. Pamarthy, “High aspect ratio silicon etch: A review,” *J. Appl. Phys*, vol. 108, no. 5, p. 051101, 2010.

[27] F. F. Chen and J. P. Chang, *Lecture Notes on Principles of Plasma Processing*. Springer US, 2003.

[28] C. M. Huard, Y. Zhang, S. Sriraman, A. Paterson, and M. J. Kushner, “Role of neutral transport in aspect ratio dependent plasma etching of three-dimensional features,” *J. Vac. Sci. Technol. A*, vol. 35, no. 5, p. 05C301, 2017.

[29] R. A. Gottscho, C. W. Jurgensen, and D. J. Vitkavage, “Microscopic uniformity in plasma etching,” *Journal of Vacuum Science & Technology B: Microelectronics and Nanometer Structures Processing, Measurement, and Phenomena*, vol. 10, no. 5, pp. 2133–2147, 1992.

[30] J. W. Coburn and H. F. Winters, “Conductance considerations in the reactive ion etching of high aspect ratio features,” *Appl. Phys. Lett.*, vol. 55, no. 26, pp. 2730–2732, 1989.

[31] P. Clausing, “The Flow of Highly Rarefied Gases through Tubes of Arbitrary Length,” *J. Vac. Sci. Technol.*, vol. 8, no. 5, pp. 636–646, 1971.

[32] J. Kiihamäki, “Deceleration of silicon etch rate at high aspect ratios,” *J. Vac. Sci. Technol. A*, vol. 18, no. 4, pp. 1385–1389, 2000.

[33] K. Nishikawa, H. Ootera, S. Tomohisa, and T. Oomori, “Transport mechanisms of ions and neutrals in low-pressure, high-density plasma etching of high aspect ratio contact holes,” *Thin Solid Films*, vol. 374, no. 2, pp. 190–207, 2000.

[34] M. A. Blauw, T. Zijlstra, and E. Van Der Drift, “Balancing the etching and passivation in time-multiplexed deep dry etching of silicon,” *J. Vac. Sci. Technol. B*, vol. 19, no. 6, p. 2930, 2001.

[35] F. Laermer and A. Schilp, “Method of anisotropically etching silicon,” US5501893A, 1996.

[36] R. Nagarajan, K. Prasad, L. Ebin, and B. Narayanan, “Development of dual-etch via tapering process for through-silicon interconnection,” *Sens. Actuators A Phys*, vol. 139, no. 1–2, pp. 323–329, 2007.

[37] J. W. Choi, W. L. Loh, S. K. Praveen, R. Murphy, and E. T. K. Swee, “A study of the mechanisms causing surface defects on sidewalls during Si etching for TSV (through Si via),” *J. Micromech. Microeng.*, vol. 23, no. 6, p. 065005, 2013.

[38] H. F. Winters, “The role of chemisorption in plasma etching,” *J. Appl. Phys*, vol. 49, no. 10, pp. 5165–5170, 1978.

[39] L. Sha and J. P. Chang, “Plasma etching of high dielectric constant materials on silicon in halogen chemistries,” *J. Vac. Sci. Technol. A*, vol. 22, no. 1, pp. 88–95, 2004.

[40] D. L. Flamm, V. M. Donnelly, and J. A. Mucha, “The reaction of fluorine atoms with silicon,” *J. Appl. Phys*, vol. 52, no. 5, pp. 3633–3639, 1981.

[41] V. M. Donnelly, “Review Article: Reactions of fluorine atoms with silicon, revisited, again,” *J. Vac. Sci. Technol. A*, vol. 35, no. 5, p. 05C202, 2017.

[42] T. E. F. M. Standaert, M. Schaepkens, N. R. Rueger, P. G. M. Sebel, G. S. Oehrlein, and J. M. Cook, “High density fluorocarbon etching of silicon in an inductively coupled plasma: Mechanism of etching through a thick steady state fluorocarbon layer,” *J. Vac. Sci. Technol. A*, vol. 16, no. 1, pp. 239–249, 1998.

[43] T. Matsuura *et al.*, “Directional etching of Si with perfect selectivity to SiO_2 using an ultraclean electron cyclotron resonance plasma,” *Appl. Phys. Lett.*, vol. 56, no. 14, pp. 1339–1341, 1990.

[44] J. W. Bartha, J. Greschner, M. Puech, and P. Maquin, “Low temperature etching of Si in high density plasma using SF_6/O_2,” *Microelectron. Eng.*, vol. 27, no. 1–4, pp. 453–456, 1995.

[45] G. Antoun *et al.*, “The role of physisorption in the cryogenic etching process of silicon,” *Jpn. J. Appl. Phys.*, vol. 58, no. SE, p. SEEB03, 2019.

[46] T. Mizutani, T. Yunogami, and K. Tsujimoto, “Lower plasma-induced damage in SiO_2/Si at lower temperatures,” *Appl. Phys. Lett.*, vol. 57, no. 16, pp. 1654–1656, 1990.

[47] T. Tillocher *et al.*, “Optimization of submicron deep trench profiles with the STiGer cryoetching process: reduction of defects,” *J. Micromech. Microeng.*, vol. 21, no. 8, p. 085005, 2011.

[48] R. Dussart *et al.*, “Deep anisotropic silicon etch method,” US20080293250A1, 2008.

[49] R. Dussart *et al.*, “Passivation mechanisms in cryogenic SF_6/O_2 etching process,” *J. Micromech. Microeng.*, vol. 14, no. 2, p. 190, 2003.

[50] T. Tillocher *et al.*, “Two Cryogenic Processes Involving SF_6/O_2, and SiF_4 for Silicon Deep Etching,” *J. Electrochem. Soc.*, vol. 155, no. 3, p. D187, 2008.

[51] M. R. Baklanov *et al.*, “Plasma processing of low-k dielectrics,” *J. Appl. Phys*, vol. 113, no. 4, p. 041101, 2013.

[52] T. Tillocher, “Cryogravure et gravure profonde par plasma pour la microélectronique et les MEMS,” 2018.

[53] L. Zhang *et al.*, “Damage Free Cryogenic Etching of a Porous Organosilica Ultralow-k Film,” *ECS Solid State Lett.*, vol. 2, no. 2, pp. N5–N7, 2012.

[54] L. Zhang *et al.*, “Low damage cryogenic etching of porous organosilicate low-k materials using $SF_6/O_2/SiF_4$,” *ECS J. Solid State Sci. Technol.*, vol. 2, no. 6, pp. N131–N139, 2013.

[55] R. Chanson *et al.*, “Damage-free plasma etching of porous organo-silicate low-k using micro-capillary condensation above −50°C,” *Sci. Rep.*, vol. 8, no. 1, 2018.

[56] G. Antoun *et al.*, “Plasma etching method and plasma etching apparatus,” WO2019117130A1, 2019.

[57] I. S. Byun, D. S. Han, S. H. Jeong, M. S. Kim, C. K. Lee, and C. W. Song, “Method of etching in low temperature and plasma etching apparatus,” KR20190142107A, 2019.

[58] A. J. Annunziata, C. Kothandaraman, N. P. Marchack, and H. Miyazoe, “Cryogenic patterning of magnetic tunnel junctions,” US10170697B2, 2019.

[59] K. J. Kanarik, J. Marks, Y. Pan, and S. S.-H. Tan, “Plasma Etching Chemistries of High Aspect Ratio Features in Dielectrics,” WO2019178030A1, 2019.

[60] T. Lill, I. L. Berry, and A. Ricci, “Ion beam etching utilizing cryogenic wafer temperatures,” US20170250087A1, 2017.

[61] J. Kudo, W. Takayama, and M. Tomura, “Etching process method,” US20170372916A1, 2017.

[62] T. E. F. M. Standaert, C. Hedlund, E. A. Joseph, G. S. Oehrlein, and T. J. Dalton, “Role of fluorocarbon film formation in the etching of silicon, silicon dioxide, silicon nitride, and amorphous hydrogenated silicon carbide,” *J. Vac. Sci. Technol. A*, vol. 22, no. 1, pp. 53–60, 2004.

[63] J. W. Butterbaugh, “Plasma–surface interactions in fluorocarbon etching of silicon dioxide,” *J. Vac. Sci. Technol. B*, vol. 9, no. 3, p. 1461, 1991.

[64] M. Schaepkens and G. S. Oehrlein, “A Review of SiO_2 Etching Studies in Inductively Coupled Fluorocarbon Plasmas,” *J. Electrochem. Soc.*, vol. 148, no. 3, pp. C211–C221, 2001.

[65] M. Schaepkens, T. E. F. M. Standaert, N. R. Rueger, P. G. M. Sebel, G. S. Oehrlein, and J. M. Cook, “Study of the SiO_2 -to- Si_3N_4 etch selectivity mechanism in inductively coupled fluorocarbon plasmas and a comparison with the SiO_2-to-Si mechanism,” *J. Vac. Sci. Technol. A*, vol. 17, no. 1, pp. 26–37, 1999.

[66] G. S. Oehrlein, Y. Zhang, D. Vender, and O. Joubert, “Fluorocarbon high-density plasmas. II. Silicon dioxide and silicon etching using CF_4 and CHF_3,” *J. Vac. Sci. Technol. A*, vol. 12, no. 2, pp. 333–344, 1994.

[67] M. Honda *et al.*, “Benefits of atomic-level processing by quasi-ALE and ALD technique,” *J. Phys. D: Appl. Phys.*, vol. 50, no. 23, p. 234002, 2017.

[68] H. Motomura, S. Imai, and K. Tachibana, “Difference between C_4F_8 and C_5F_8 plasmas in surface reaction processes for selective etching of SiO_2 over Si_3N_4,” *Thin Solid Films*, vol. 374, no. 2, pp. 243–248, 2000.

[69] E. J. Capdos Tinacba, M. Isobe, K. Karahashi, and S. Hamaguchi, “Molecular dynamics simulation of Si and SiO_2 reactive ion etching by fluorine-rich ion species,” *Surface and Coatings Technology*, vol. 380, p. 125032, 2019.

[70] J. A. O’Neill and J. Singh, “Role of the chamber wall in low-pressure high-density etching plasmas,” *J. Appl. Phys*, vol. 77, no. 2, pp. 497–504, 1995.

[71] S. C. McNevin, “Chemical challenge of submicron oxide etching,” *J. Vac. Sci. Technol. B*, vol. 15, no. 2, p. 214, 1997.

[72] M. Schaepkens, R. C. M. Bosch, T. E. F. M. Standaert, G. S. Oehrlein, and J. M. Cook, “Influence of reactor wall conditions on etch processes in inductively coupled fluorocarbon plasmas,” *J. Vac. Sci. Technol. A*, vol. 16, no. 4, pp. 2099–2107, 1998.

[73] J. L. Cain, “Selective dry-etching of bi-layer passivation films,” US5433823A, 1995.

[74] B. E. E. Kastenmeier, P. J. Matsuo, J. J. Beulens, and G. S. Oehrlein, “Chemical dry etching of silicon nitride and silicon dioxide using $CF_4/O_2/N_2$ gas mixtures,” *J. Vac. Sci. Technol. A*, vol. 14, no. 5, pp. 2802–2813, 1996.

[75] S. Lee, J. Oh, K. Lee, and H. Sohn, “Ultrahigh selective etching of Si_3N_4 films over SiO_2 films for silicon nitride gate spacer etching,” *J. Vac. Sci. Technol. B*, vol. 28, no. 1, p. 8, 2010.

[76] Y. Kondo *et al.*, “Silicon nitride etching performance of CH_2F_2 plasma diluted with argon or krypton,” *Jpn. J. Appl. Phys.*, vol. 54, no. 4, p. 040303, 2015.

[77] D. Nakayama *et al.*, “Highly selective silicon nitride etching to Si and SiO_2 for a gate sidewall spacer using a $CF_3I/O_2/H_2$ neutral beam,” *J. Phys. D: Appl. Phys.*, vol. 46, no. 20, p. 205203, 2013.

[78] H. F. Winters, “Etch products from the reaction of XeF_2 with SiO_2, Si_3N_4, SiC, and Si in the presence of ion bombardment,” *J. Vac. Sci. Technol. B*, vol. 1, no. 4, p. 927, 1983.

[79] B. E. E. Kastenmeier, P. J. Matsuo, G. S. Oehrlein, and J. G. Langan, “Remote plasma etching of silicon nitride and silicon dioxide using NF_3/O_2 gas mixtures,” *J. Vac. Sci. Technol. A*, vol. 16, no. 4, pp. 2047–2056, 1998.

[80] B. E. E. Kastenmeier, P. J. Matsuo, and G. S. Oehrlein, “Highly selective etching of silicon nitride over silicon and silicon dioxide,” *J. Vac. Sci. Technol. A*, vol. 17, no. 6, pp. 3179–3184, 1999.

[81] N. Gellrich and R. Kirchmann, “Method for anisotropic plasma-chemical dry etching of silicon nitride layers using a gas mixture containing fluorine,” US6569773B1, 2003.

[82] Y. Wang and L. Luo, “Ultrahigh-selectivity silicon nitride etch process using an inductively coupled plasma source,” *J. Vac. Sci. Technol. A*, vol. 16, no. 3, pp. 1582–1587, 1998.

[83] K. J. Kanarik, S. Tan, and R. A. Gottscho, “Atomic Layer Etching: Rethinking the Art of Etch,” *J. Phys. Chem. Lett.*, vol. 9, no. 16, pp. 4814–4821, 2018.

[84] K. Ishikawa *et al.*, “Rethinking surface reactions in nanoscale dry processes toward atomic precision and beyond: a physics and chemistry perspective,” *Jpn. J. Appl. Phys.*, vol. 58, no. SE, p. SE0801, 2019.

[85] T. Faraz, F. Roozeboom, H. C. M. Knoops, and W. M. M. Kessels, “Atomic Layer Etching: What Can We Learn from Atomic Layer Deposition?,” *ECS J. Solid State Sci. Technol.*, vol. 4, no. 6, pp. N5023–N5032, 2015.

[86] A. Agarwal and M. J. Kushner, “Plasma atomic layer etching using conventional plasma equipment,” *J. Vac. Sci. Technol. A*, vol. 27, no. 1, pp. 37–50, 2009.

[87] C. M. Huard, S. J. Lanham, and M. J. Kushner, “Consequences of atomic layer etching on wafer scale uniformity in inductively coupled plasmas,” *J. Phys. D: Appl. Phys.*, vol. 51, no. 15, p. 155201, 2018.

[88] S. D. Sherpa, P. L. G. Ventzek, M. Lee, G. S. Hwang, and A. Ranjan, “New insight into desorption step by Ar^+ ion-bombardment during the atomic layer etching of silicon,” *J. Vac. Sci. Technol. A*, vol. 36, no. 3, p. 031303, 2018.

[89] M. J. Cooke, “Impact of Atomic Layer Etching on Process Tool Design,” *ECS J. Solid State Sci. Technol.*, vol. 4, no. 6, pp. N5001–N5004, 2015.

[90] I. L. Berry, K. J. Kanarik, T. Lill, S. Tan, V. Vahedi, and R. A. Gottscho, “Applying sputtering theory to directional atomic layer etching,” *J. Vac. Sci. Technol. A*, vol. 36, no. 1, p. 01B105, 2018.

[91] A. Goodyear and M. Cooke, “Atomic layer etching in close-to-conventional plasma etch tools,” *J. Vac. Sci. Technol. A*, vol. 35, no. 1, p. 01A105, 2017.

[92] G. S. Oehrlein, D. Metzler, and C. Li, “Atomic Layer Etching at the Tipping Point: An Overview,” *ECS J. Solid State Sci. Technol.*, vol. 4, no. 6, pp. N5041–N5053, 2015.

[93] K. J. Kanarik *et al.*, “Predicting synergy in atomic layer etching,” *J. Vac. Sci. Technol. A*, vol. 35, no. 5, p. 05C302, 2017.

[94] X. Sang and J. P. Chang, “Physical and chemical effects in directional atomic layer etching,” *J. Phys. D: Appl. Phys.*, vol. 53, no. 18, p. 183001, 2020.

[95] T. Matsuura, J. Murota, Y. Sawada, and T. Ohmi, “Self-limited layer-by-layer etching of Si by alternated chlorine adsorption and Ar^+ ion irradiation,” *Appl. Phys. Lett.*, vol. 63, no. 20, pp. 2803–2805, 1993.

[96] B.-J. Kim, S. Chung, and S. M. Cho, “Layer-by-layer etching of Cl-adsorbed silicon surfaces by low energy Ar^+ ion irradiation,” *Appl. Surf. Sci.*, vol. 187, no. 1–2, pp. 124–129, 2002.

[97] S. D. Athavale and D. J. Economou, “Realization of atomic layer etching of silicon,” *J. Vac. Sci. Technol. B*, vol. 14, no. 6, pp. 3702–3705, 1996.

[98] D. Metzler, C. Li, S. Engelmann, R. L. Bruce, E. A. Joseph, and G. S. Oehrlein, “Fluorocarbon assisted atomic layer etching of SiO_2 and Si using cyclic Ar/C_4F_8 and Ar/CHF_3 plasma,” *J. Vac. Sci. Technol. A*, vol. 34, no. 1, p. 01B101, 2016.

[99] D. Metzler, C. Li, S. Engelmann, R. L. Bruce, E. A. Joseph, and G. S. Oehrlein, “Characterizing fluorocarbon assisted atomic layer etching of Si using cyclic Ar/C_4F_8 and Ar/CHF_3 plasma,” *J. Chem. Phys.*, vol. 146, no. 5, p. 052801, 2017.

[100] C. M. Huard, Y. Zhang, S. Sriraman, A. Paterson, K. J. Kanarik, and M. J. Kushner, “Atomic layer etching of 3D structures in silicon: Self-limiting and nonideal reactions,” *J. Vac. Sci. Technol. A*, vol. 35, no. 3, p. 031306, 2017.

[101] D. Metzler, C. Li, C. S. Lai, E. A. Hudson, and G. S. Oehrlein, “Investigation of thin oxide layer removal from Si substrates using an SiO_2 atomic layer etching approach: the importance of the reactivity of the substrate,” *J. Phys. D: Appl. Phys.*, vol. 50, no. 25, p. 254006, 2017.

[102] R. J. Gasvoda, A. W. Van De Steeg, R. Bhowmick, E. A. Hudson, and S. Agarwal, “Surface Phenomena During Plasma-Assisted Atomic Layer Etching of SiO_2,” *ACS Appl. Mater. Interfaces*, vol. 9, no. 36, pp. 31067–31075, 2017.

[103] C. Li, D. Metzler, C. S. Lai, E. A. Hudson, and G. S. Oehrlein, “Fluorocarbon based atomic layer etching of Si_3N_4 and etching selectivity of SiO_2 over Si_3N_4,” *J. Vac. Sci. Technol. A*, vol. 34, no. 4, p. 041307, 2016.

[104] D. Metzler, R. L. Bruce, S. Engelmann, E. A. Joseph, and G. S. Oehrlein, “Fluorocarbon assisted atomic layer etching of SiO_2 using cyclic Ar/C_4F_8 plasma,” *J. Vac. Sci. Technol. A*, vol. 32, no. 2, p. 020603, 2014.

[105] S. S. Kaler, Q. Lou, V. M. Donnelly, and D. J. Economou, “Atomic layer etching of silicon dioxide using alternating C_4F_8 and energetic Ar^+ plasma beams,” *J. Phys. D: Appl. Phys.*, vol. 50, no. 23, p. 234001, 2017.

[106] S. Dallorto *et al.*, “Atomic layer etching of SiO_2 with Ar and CHF_3 plasmas: A self-limiting process for aspect ratio independent etching,” *Plasma Process Polym*, vol. 16, no. 9, p. 1900051, 2019.

[107] Y. Kim, S. Lee, Y. Cho, S. Kim, and H. Chae, “Plasma atomic layer etching of SiO_2 and Si_3N_4 with heptafluoropropyl methyl ether ($C_3F_7OCH_3$),” *J. Vac. Sci. Technol. A*, vol. 38, no. 2, p. 022606, 2020.

[108] S. Rauf *et al.*, “A molecular dynamics investigation of fluorocarbon based layer-by-layer etching of silicon and SiO_2,” *J. Appl. Phys*, vol. 101, no. 3, p. 033308, 2007.

[109] C. M. Huard, S. Sriraman, A. Paterson, and M. J. Kushner, “Transient behavior in quasi-atomic layer etching of silicon dioxide and silicon nitride in fluorocarbon plasmas,” *J. Vac. Sci. Technol. A*, vol. 36, no. 6, p. 06B101, 2018.

[110] M. Kawakami, D. Metzler, C. Li, and G. S. Oehrlein, “Effect of the chamber wall on fluorocarbon-assisted atomic layer etching of SiO_2 using cyclic Ar/C_4F_8 plasma,” *J. Vac. Sci. Technol. A*, vol. 34, no. 4, p. 040603, 2016.

[111] S. Dallorto *et al.*, “Balancing ion parameters and fluorocarbon chemical reactants for SiO_2 pattern transfer control using fluorocarbon-based atomic layer etching,” *J. Vac. Sci. Technol. B*, vol. 37, no. 5, p. 051805, 2019.

[112] United Nations Climate Change, “Global Warming Potentials (IPCC Second Assessment Report) | UNFCCC.” https://unfccc.int/process/transparency-and-reporting/greenhouse-gas-data/greenhouse-gas-data-unfccc/global-warming-potentials (accessed Oct. 02, 2020).

[113] I. Bravo, Y. Díaz-de-Mera, A. Aranda, K. Smith, K. P. Shine, and G. Marston, “Atmospheric chemistry of $C_4F_9OC_2H_5$ (HFE-7200), $C_4F_9OCH_3$ (HFE-7100), $C_3F_7OCH_3$ (HFE-7000) and $C_3F_7CH_2OH$: temperature dependence of the kinetics of their reactions with OH radicals, atmospheric lifetimes and global warming potentials,” *Phys. Chem. Chem. Phys.*, vol. 12, no. 19, p. 5115, 2010.

[114] K.-Y. Lin *et al.*, “Achieving ultrahigh etching selectivity of SiO_2 over Si_3N_4 and Si in atomic layer etching by exploiting chemistry of complex hydrofluorocarbon precursors,” *J. Vac. Sci. Technol. A*, vol. 36, no. 4, p. 040601, 2018.

[115] M. Wang, P. L. G. Ventzek, and A. Ranjan, “Quasiatomic layer etching of silicon oxide selective to silicon nitride in topographic structures using fluorocarbon plasmas,” *J. Vac. Sci. Technol. A*, vol. 35, no. 3, p. 031301, 2017.

[116] S. G. Walton *et al.*, “Electron beam generated plasmas: Characteristics and etching of silicon nitride,” *Microelectron. Eng.*, vol. 168, pp. 89–96, 2017.

[117] T. Matsuura, Y. Honda, and J. Murota, “Atomic-order layer-by-layer role-share etching of silicon nitride using an electron cyclotron resonance plasma,” *Appl. Phys. Lett.*, vol. 74, no. 23, pp. 3573–3575, 1999.

[118] N. Posseme, O. Pollet, and S. Barnola, “Alternative process for thin layer etching: Application to nitride spacer etching stopping on silicon germanium,” *Appl. Phys. Lett.*, vol. 105, no. 5, p. 051605, 2014.

[119] S. D. Sherpa and A. Ranjan, “Quasi-atomic layer etching of silicon nitride,” *J. Vac. Sci. Technol. A*, vol. 35, no. 1, p. 01A102, 2017.

[120] S. D. Sherpa, P. L. G. Ventzek, and A. Ranjan, “Quasiatomic layer etching of silicon nitride with independent control of directionality and selectivity,” *J. Vac. Sci. Technol. A*, vol. 35, no. 5, p. 05C310, 2017.

[121] N. Posseme, V. Ah-Leung, O. Pollet, C. Arvet, and M. Garcia-Barros, “Thin layer etching of silicon nitride: A comprehensive study of selective removal using NH_3/NF_3 remote plasma,” *J. Vac. Sci. Technol. A*, vol. 34, no. 6, p. 061301, 2016.

[122] K. Nakane, R. H. J. Vervuurt, T. Tsutsumi, N. Kobayashi, and M. Hori, “*In Situ* Monitoring of Surface Reactions during Atomic Layer Etching of Silicon Nitride Using Hydrogen

Plasma and Fluorine Radicals," *ACS Appl. Mater. Interfaces*, vol. 11, no. 40, pp. 37263–37269, 2019.

[123] K. Shinoda *et al.*, "Self-limiting reactions of ammonium salt in CHF_3/O_2 downstream plasma for thermal-cyclic atomic layer etching of silicon nitride," *J. Vac. Sci. Technol. A*, vol. 37, no. 5, p. 051002, 2019.

[124] M. Bouchilaoun *et al.*, "A Hydrogen Plasma Treatment for Soft and Selective Silicon Nitride Etching," *Phys. Status Solidi A*, vol. 215, no. 9, p. 1700658, 2018.

[125] M. Matsui, T. Usui, and T. Ono, "Effect of plasma dissociation on fluorocarbon layers formed under C_4F_8/Ar pulsed plasma for SiO_2 etching," *J. Appl. Phys*, vol. 56, no. 6S2, p. 06HB03, 2017.

[126] T. Tsutsumi *et al.*, "Atomic layer etching of SiO_2 by alternating an O_2 plasma with fluorocarbon film deposition," *J. Vac. Sci. Technol. A*, vol. 35, no. 1, p. 01A103, 2017.

Chapter II.

Experimental techniques

This chapter aims to present the different substrates and equipment used during this project.

I. Substrates

All substrates for this thesis work were supplied by TEL. All the samples provided are coatings made on p-type Si wafers of 775 ± 25 µm thick and 300 mm in diameter. For testing, they were cleaved into coupons of 20x20 mm² to 30x30 mm² and glued on a 150 mm wafer, usually an oxidized silicon wafer.

The glue used is a special glue that resists to low temperatures and that has a good thermal conductivity.

(a) SiO_2 (b) a-Si (c) Si_3N_4

Fig. II. 1. Studied samples configuration (not to scale)

I.1. Silicon dioxide

The SiO_2 used for this project is a thermal oxide of about 100 ± 5 nm thick (Fig. II. 1. a.). Thermal oxidation technique consists in heating the wafer between 700°C and 1200°C, then exposing it to oxygen atmosphere to let it diffuse through the surface and oxidize the substrate surface. This technique allows the creation of very pure oxide films [1].

I.2. Amorphous silicon

The amorphous silicon (a-Si) used were 50 ± 3 nm thick with a 100 ± 5 nm undercoat of SiO_2 formed before the silicon deposition layer, as presented in Fig. II. 1. b.

I.3. Silicon nitride

In the case of silicon nitride, there was no undercoat. The Si_3N_4 deposited layer is about ~250 ± 13 nm as represented in Fig. II. 1. c. The Si_3N_4 was deposited by Low Pressure Chemical Vapor Deposition (LPCVD). This method is therefore based on the Chemical Vapor Pressure (CVD) technology, where a precursor is injected in gas phase and will react chemically with the substrate to form the thin film layer. Processing at low pressure ensure a better uniformity of the coating and prevent contaminations (compared to atmospheric pressure deposition) [1].

II. Reactors

Etching tools were developed and enhanced through years to meet, among other things, the electronics industry expectations. Most of the etch tools are Inductively Coupled Plasma (ICP) reactors that provide high density plasmas (about 10^{11} cm^{-3}) and the Capacitively Coupled Plasma (CCP) reactors, that provide medium density plasmas (1.10^9 to 1.10^{10} cm^{-3}). Both of them use generally Radio Frequency (RF) generators of 13.56 MHz. And they operate at low pressure, which helps limiting any exterior contamination [2].
For ALE, same kind of tools can be used, however, some additional adjustments are required, as the ability of gas and plasma pulsing or also, fast pumping equipment [3].
The reactors used in the project are both ICP reactors and are presented below.

II.1. Alcatel 601 E

II.1.i. *General configuration*

The ICP reactor used in this project is an Alcatel 601E located at GREMI (Fig. II. 2). The reactor was designed by Alcatel Micro Machining Systems for industrial use, with the possibility of using it for cryogenic processes. Even though this company does not exist anymore since 2010, the reactor is quite easy to handle, which is why it has been possible to modify it for research use also.
Since its acquisition by the GREMI in 1997, several optimizations were performed on it. New flanges were machined on the diffusion chamber so that a spectroscopic ellipsometer as well as an Energy Quadrupole Plasma Mass Spectrometer could be coupled to it. Also, to enable its use for cryo-ALE, fast valves lines were added. Those modifications will be discussed later in this chapter.

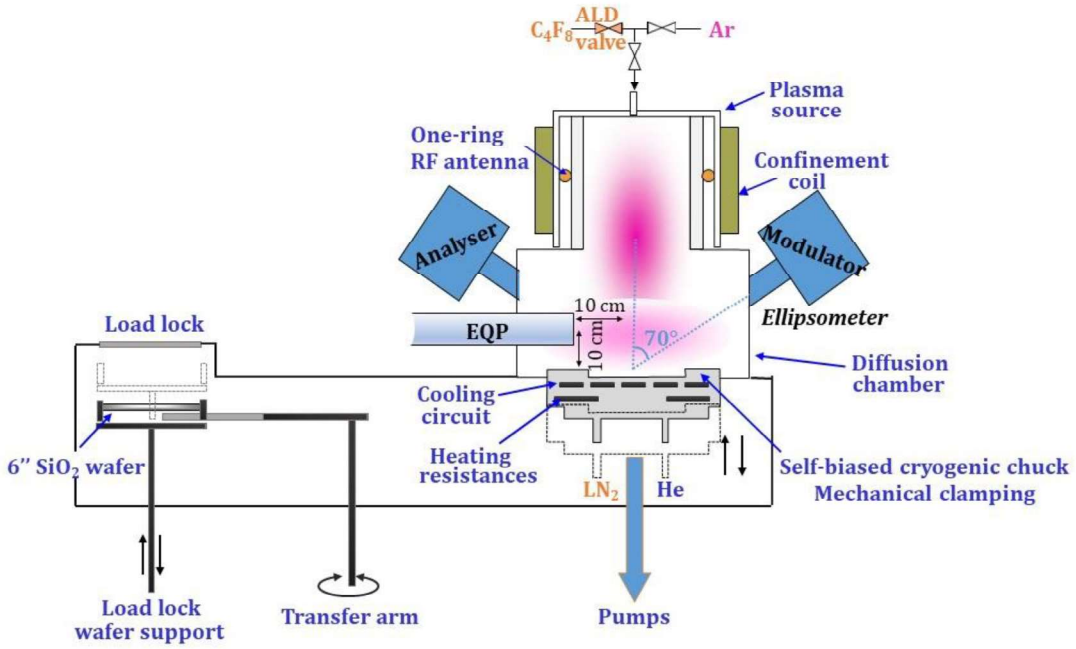

Fig. II. 2. Sketch of Alcatel 601E

The reactor can be presented as the association of several modules presented below.

- Transfer module

The first module is the transfer module of 50 L. As the system is under vacuum, a load lock was designed to load the sample into the chamber without breaking the vacuum. The samples size supported is 100 mm to 150 mm, but only 150 mm wafers were used during the thesis. That is why a small sample cannot be loaded alone and that carrier wafer is necessary for the experiments. The wafer is loaded manually into the load lock, then a pumping system decreases the pressure in the load lock before the transfer to the chamber. The transfer is carried out automatically by a transfer arm fixed to a thumb wheel. By using rotational and vertical translation movements, the arm can move the wafer from the substrate holder in the load lock to the substrate holder of the chamber and vice versa. The transfer arm is designed to limit the contact with the backside of the wafer the most possible.

- Process module

The second module is called the process module. It includes the reactor chamber with the substrate holder, but also the plasma source as well as RF power supplies and the pumping. Once the sample is loaded to the reactor chamber, it is placed on a substrate holder and secured by mechanical clamping. In cryogenic processes, the wafer is cooled through the substrate holder cooling. To ensure the thermal conductivity between both, a helium flow is injected at the backside of the wafer, with a constant pressure kept at 10 mbar.
To cool the chuck, a liquid nitrogen cooling circuit is mounted inside the substrate holder. To prevent any water condensation in the system and electronic problems, a pumping package is

used to ensure the vacuum in the substrate holder system. A heating system, consisting of electrical resistances, associated to a self-adaptive Proportional Integral Derivative (PID) controller is used to regulate the temperature. It is hence possible to cool substrates at temperatures between -150°C and 30°C. However, the temperature is measured inside the chuck below the substrate. It has to be considered that the substrate is in fact slightly warmer than the set point and the measured temperature.

The substrate holder can also be biased using an independent RF generator at 13.56 MHz and an automatic matching box. Finally, the position of the substrate holder can be adjusted vertically to get closer to the plasma source if needed. The distance from the source is between 10 and 20 cm [4].

The plasma source is composed of a single turn RF antenna, with an automatic matching box and separated from the plasma by an alumina tube of 175 mm diameter and 260 mm high (6.2 L). The maximum power is about 3 kW. A confinement coil is wound around the source to generate an axial magnetic field and hence limit electrons loss [5], [6]. And a water circuit is connected to ensure the cooling of the antenna.

Once the plasma is ignited, it diffuses in the so-called diffusion chamber. The latter, made of anodized aluminum, is 400 mm in diameter and 245 mm high (30.8 L).

The process module also includes the pumping system of the chamber. A throttle valve separates the chamber from the turbomolecular pump. It offers the possibility of regulating the pressure in the reactor by defining the set point pressure as a pressure command or as an opening percentage (position) of the valve. The pressure in the chamber during a process is measured using a Baratron gauge, enabling a measurement range between 0.1 and 100 Pa. However, it is recommended to use the reactor between 0.1 and 13 Pa for the processes. A valve enables to separate, if needed, the turbomolecular pump and the primary pump. The base pressure of the chamber is about 2.10^{-4} Pa.

- Gas module

The reactor is equipped with 6 gas lines installed close to the reactor and joining to the same inlet at the top of the source. Those lines include the Mass Flow Controllers (MFC) as well as the valves.

The basic lines installed and used in etching processes are:

- Ar, installed on two lines of 28 sccm and 280 sccm maximum flow
- O_2, one line with 200 sccm maximum flow
- SF_6, one line with 500 sccm maximum flow

For those gas lines, the time needed to reach the set point flow is about one second, which is too long for ALE process. Therefore, two fast lines have been added. They are presented further in this section.

- Control module

The control module enables to use the reactor and execute the process recipes. It is composed of a Programmable Logic Controller (PLC) that can be managed through a user interface. With this interface, it is possible to command the transfer of the wafer, but also start a process manually or program an etching process to be performed automatically. This module also refers to the front control panel of the reactor as well as to temperature, plasma and pressure indicators and regulators.

- Service module

This module includes all the electrical connections, as well as the connections needed for the proper functioning of the reactor. For example, the compressed air for the valves operation, water for cooling and helium for clamping. But also gaseous nitrogen for venting and liquid nitrogen for the chuck cooling.

II.1.ii. *Fast valves lines*

As presented above, the original gas sticks, including valves and MFC's, installed on the reactor have a response time of the order of a second. During this second, the gas flow entering the chamber is not well known and controlled, which can be problematic for ALE processes. Therefore, at the beginning of the thesis, two new gas lines were installed at the top of the source. The installation of these fast injection system at this location, enables to reduce the length of the gas lines downstream of the last inlet isolation valve and hence the time needed to enter the reactor or to be purged. Those new lines were designed and assembled by the GREMI. They include fast Atomic Layer Deposition (ALD) valves and fast MFC.
The ALD Diaphragm valves are very fast valves (response time < 15 ms), manufactured by Swagelok and designed for ALD applications. The MFC, GF 125 type from Brooks Instrument, have a response time of about 300 ms.
The lines were configured in a way where very precise amount of gas is injected into the reactor and is well-known. The ALE gas injection system is composed of a MFC and 3 valves. Their assembly is presented in Fig. II. 3.
Once the gas flow set-point is entered, (Input in Fig. II. 3. b), the MFC enables to fix the gas flow, and the ALD valve right after the MFC is opened (V_i). However, as about 300 ms are needed to reach the maximum flow, during this time, the amount of gas is not perfectly controlled (Output in Fig. II. 3. b). Therefore, a second valve (V_v) enables to pump the lines until the gas flow is stabilized. Then the pumping valve (V_v) is closed, and at the same time, the valve close to the reactor (V_o) opens to let the gas enter the reactor. And, once the gas flow needs to be stopped, the opposite occurs. The valve V_o and V_i close and only V_v is opened

to pump the gas line. As can be observed in Fig. II. 3. b, the pressure stays very stable during the gas injection.

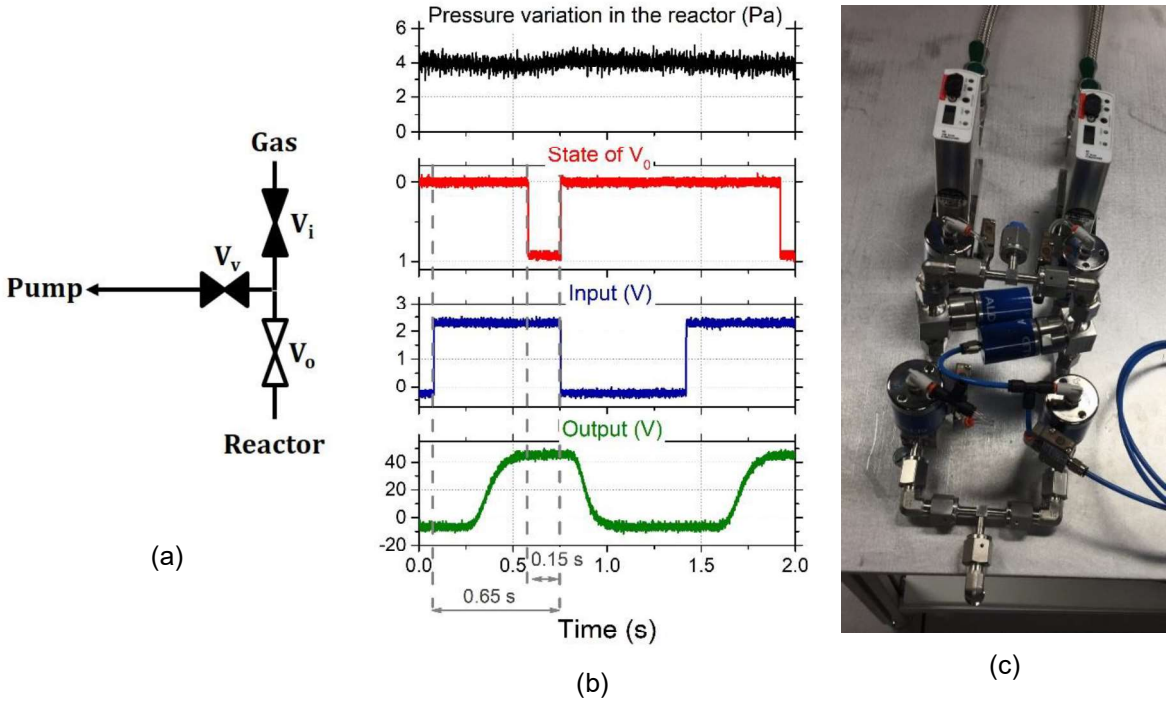

Fig. II. 3. Presentation of the fast gas lines, (a) sketch of the valves configuration, (b) Signals measured by oscilloscope, (c) photo of the 2 lines of gas injection

During the thesis, three gases were used on those lines. First SiF_4 was installed permanently on one of the lines, providing a maximum flow of about 104 sccm. C_4F_8 and O_2 were switched on the second line. Indeed, for C_4F_8 cryo-ALE tests, a fast line was used, with a maximum C_4F_8 flow of 14 sccm. In this configuration, the O_2 was provided by a "standard" gas line from the Alcatel. However, during SiF_4 / O_2 tests, C_4F_8 was disconnected and O_2 was linked to the fast gas line with a maximum flow of 90 sccm.

II.2. OPTIMIST

During this thesis, it appeared relevant to characterize the surface of the samples by X-ray Photoelectron Spectroscopy (XPS). Since the samples of interest are processed at cryogenic temperature, XPS should also be performed by keeping them at the same temperature, which is made possible by the platform OPTMIST from the laboratory IMN in Nantes. It is a platform where an ICP reactor is linked to an XPS (Fig. II. 4). The acronym OPTIMIST comes from the name in French, translated here, "Opening of a Technical Platform for the Investigation of the Mechanisms of Interaction between plasma and Surface on a large Temperature range".

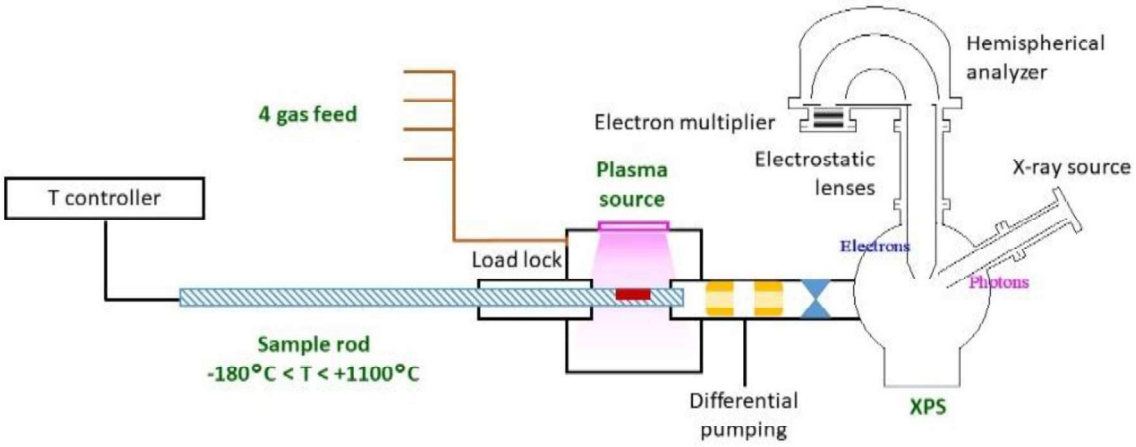

Fig. II. 4. Sketch of OPTIMIST platform

It is a homemade Transformer Coupled Plasma (TCP) reactor. However, the difference is that the coil has a planar shape and the plasma source and the diffusion chamber are one. The power supply is at 13.56 MHz, and the matching box is manual [7]. The ultimate vacuum that can be reached in the reactor is 10^{-5} Pa. 4 gas lines are installed on this reactor. For measurements presented in Chapter IV, a new gas line of SiF_4 has been expressly installed for the project.

One specificity of this platform is the sample holder. The latter is in fact a moving sample rod specifically designed and made for the reactor. The rod is indeed equipped with a temperature regulator, that can heat the rod, and so the sample, up to 1100°C. Two pipes are also added to this rod. The first one allows liquid nitrogen to circulate in the rod. And the second pipe is used to evacuate the gaseous nitrogen. Hence, it is possible to cool the rod and the sample down to -180°C. Also, this rod can be moved from the reactor to the XPS chamber while maintaining the substrate temperature and keeping it under vacuum, preventing any contamination. Therefore XPS analyses are performed quasi in-situ.

III. Surface diagnostics

III.1. Spectroscopic Ellipsometry

Spectroscopic Ellipsometry (SE) has been the main tool of characterization for this project. The basis of this technique is due to P. Drude in 1887 [8]. It is a non-destructive method that helps to determine the thickness of the studied film, as well as its optical constants, (refractive index *n* and extinction coefficient *k*). Two UVISEL spectroscopic ellipsometers from Horiba Jobin Yvon (HJY) have been used. One is coupled to the reactor for in-situ measurements, and the second one is ex-situ to perform measurements at different places of the wafer.

III.1.i. *SE principle*

III.1.i.a. Generic principle information

The used spectroscopic ellipsometers are Polarization Modulation Ellipsometers (PME). The principle of operation is shown in Fig. II. 5. First, a 75 W Xenon arc lamp is used to create a light beam with a spectral range from the infrared (IR), about 826 nm (1.5 eV), to the ultraviolet (UV), about 248 nm (5 eV). Then, UV optical fibers, that are able to cover the spectral range desired (1.5 eV to 5 eV), are used to couple the light to the polarizer. In the polarizer, the light is transformed into a linearly polarized light, before striking the sample. The light is then reflected or transmitted from the sample as an elliptically polarized light and captured by a photoelastic modulator (PEM).

As its name can indicates, it's a modulator based on the photoelastic effect, discovered by Sir David Brewster in 1816 [9]. The modulator is composed of a fused SiO_2 bar that is considered optically isotropic as it has one refractive index. However, it becomes birefringent when a stress is applied to it. Therefore, a piezo electric transducer that can oscillate at the resonance frequency (50 KHz) is installed on the bar. When applying the stress, a modulation of the light is induced. And so the modulated phase shift $\delta(t)$ of the electric field is expressed as follow in Eq. II. 1:

$$\delta(t) = \frac{2\pi d(n_1 - n_0)}{\lambda}\sin(\omega t) \qquad \textit{II. 1}$$

As shown in the equation (Eq. II. 1), the modulated phase shift will be dependent on the studied wavelength. If the electric field is parallel to the plane of incidence, the modulated phase shift will be reported as δ_p. And, when it is perpendicular to the plane of incidence, $\delta(t)$ will be referred as whereas δ_s which comes from the german "senkrecht" meaning perpendicular. However, it enables to get rid of the noises and hence provides accurate results and also fast acquisitions.

After the modulator, the light goes through the analyzer, that transforms the elliptical light back into a linear light.

Then the light goes again through an optical fiber to the monochromator that will separate the light into several components. Finally, the light goes into the detector. The latter is made of photomultipliers for the detection of wavelength in the UV and the visible spectral range. And for the detection in the IR, it is equipped with a InGaAs detector.

After all those steps, the data can be acquired as the measured ellipsometric angles Δ and Ψ. Δ corresponds to the difference in the phase, and Ψ is the amplitude ratio between the polarized lights after reflection from the sample (Fig. II. 5) [10].

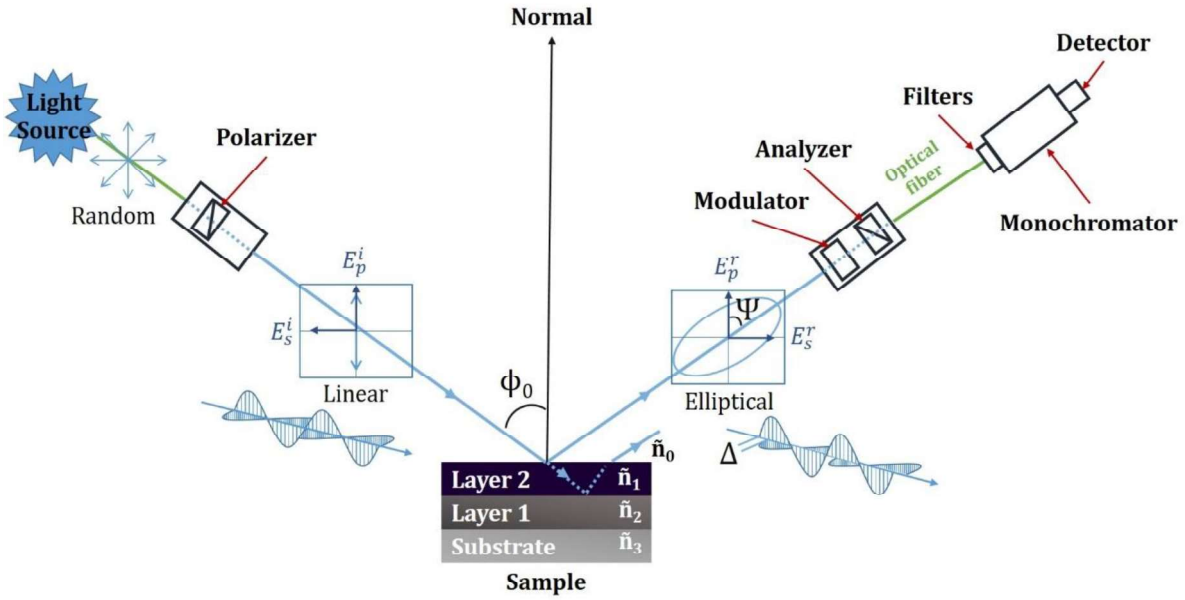

Fig. II. 5. Principle of a SE

The basic ellipsometry equation is:

$$\rho = \frac{r_p}{r_s} = tan\Psi e^{i\Delta} \qquad \textit{II. 2}$$

With r_p and r_s Fresnel coefficients, expressed as:

$$r_p = \frac{E_p^r}{E_p^i} = |r_p|\exp(i\delta_p) \qquad \textit{II. 3}$$

$$r_s = \frac{E_s^r}{E_s^i} = |r_s|\exp(i\delta_s) \qquad \textit{II. 4}$$

And,

$$tan\Psi = \frac{|r_p|}{|r_s|}\ for\ 0° \leq \Psi \leq 90° \qquad \textit{II. 5}$$

$$\Delta = \delta_p - \delta_s\ for\ 0° \leq \Delta \leq 360° \qquad \textit{II. 6}$$

From this variation of polarization, it will be possible to determine the optical properties of the studied layer as well as its thickness with very high precision (± 5 Å) [11].

The relation between Fresnel coefficients and the material properties is given by relying on Snell-Descartes equation:

$$\tilde{n}_0 sin\theta_0 = \tilde{n}_1 sin\theta_1 \qquad \textit{II. 7}$$

With θ_0 and θ_1 respectively the angle of incidence and refraction and $\tilde{n}_0$ the refractive index of the surrounding material:

$$\tilde{n}_0 = n_0 \qquad \textit{II. 8}$$

And $\tilde{n}_1$ the refractive index of the sample:

$$\tilde{n}_1 = n_1 - ik_1 \qquad \textit{II. 9}$$

From those equations, Fresnel coefficients can be expressed for reflection as:

$$r_p = \frac{\tilde{n}_1 \, cos\theta_0 - \tilde{n}_0 \, cos\theta_1}{\tilde{n}_0 \, cos\theta_0 - \tilde{n}_1 \, cos\theta_1} \qquad \textit{II. 10}$$

$$r_s = \frac{\tilde{n}_0 \, cos\theta_0 - \tilde{n}_1 \, cos\theta_1}{\tilde{n}_0 \, cos\theta_0 - \tilde{n}_1 \, cos\theta_1} \qquad \textit{II. 11}$$

By using Eq. II. 2, Eq. II. 10 and Eq. II. 11, the dielectric permittivity can be calculated as:

$$\tilde{\varepsilon} = {\tilde{n}_1}^2 = {\tilde{n}_0}^2 \sin^2\theta_0 \left[1 + \left(\frac{1-\rho}{1+\rho}\right)^2 tan^2\,\theta_0\right] \qquad \textit{II. 12}$$

The reflectance R_e can be then calculated from Fresnel coefficients for reflection with:

$$R_e^s = |r_s| \text{ and } R_e^p = |r_p| \qquad \textit{II. 13}$$

Depending on the angle of incidence (AOI), R_e^p decreases, presenting a minimum at the *principle angle.* When dielectric materials are studied, R_e^p is equal to zero as well as k at an AOI called the *Brewster angle.* Whereas R_e^s always increases with AOI increase.

In our measurements, the AOI was always set at 70°, in order to get the closest to the Brewster angle where sensitivity is the highest.

III.1.i.b. Acquisition mode

Three different methods were used during the thesis to perform SE measurements. Spectroscopic monochromator (Mono) and spectroscopic multiwavelength (MWL) modes were performed for instant measurement. And for process real-time monitoring, kinetic MWL has been used.

For the three acquisition modes, the spectral range can be defined as a function of the material to analyze.

In this work, all tests were performed in a spectral range between 1.5 and 5 eV and in reflection mode.

- Spectroscopic Mono acquisition mode

In the spectroscopic Mono acquisition mode, the measurements are taken with a scanning monochromator. It enables very accurate readings performed between 826 and 248 nm.

- Spectroscopic MWL acquisition mode

The spectroscopic MWL is a multichannel acquisition mode that is very similar to the Spectroscopic Mono acquisition mode. However, in this mode, the measurements are taken at defined multiple wavelengths, using 32 photomultipliers. Hence the measurement can be acquired much faster than in mono, but the result will be less accurate in the IR range due to the reduced number of acquisitions.

- Kinetic MWL acquisition mode

The kinetic mode simply enables to gather data on the sample in real time. Acquisition are made versus time using the MWL configuration presented above. The integration time for each spectrum as well as the time duration of the acquisition can be set by the user.
The spectroscopic ellipsometer offers also other type of acquisitions. However, they will not be presented in this paragraph as they have not been used.

III.1.i.c. Configuration setting

The configuration of the ellipsometer corresponds to the angles set for the modulator M and the analyzer A. Three configurations exist:
Configuration I corresponds to $M = 0°$ and $A = 0°$ and is used for test position.
Configuration II is one of the most common configurations employed, and was used for our measurements. It corresponds to $M = 0°$ and $A = \pm 45°$. It enables to determine accurately Δ on the whole range except around 45°.
In this case Is and Ic are plotted and used for fitting, with:

$$Is = \sin 2\Psi \sin \Delta \qquad \textit{II. 14}$$

$$Ic = \sin 2\Psi \cos \Delta \qquad \textit{II. 15}$$

However, configuration III can also be used and corresponds to $M = \pm 45°$ and $A = \pm 45°$. In this case, it is Ψ that is determined with accuracy on the whole range, except at 90° and 270°. Is is the same as for configuration II, but Ic will be calculated as:

$$Ic = \cos 2\Psi \qquad \textit{II. 16}$$

III.1.ii. *Models used for the studied materials*

As presented in section I. of this chapter, four different silicon based materials were used to conduct this study. The ellipsometry model for each of these materials is presented in this paragraph.
The software used to analyze the acquisitions is DeltaPsi2 from HJY.

III.1.ii.a. Silicon dioxide

Based on information presented in Fig. II. 1, the ellipsometric model for SiO_2 was as follows:

Table. II. 1. Fit model for SiO_2

Layer N°	***Fit***	***Thickness (nm)***	***Fit***	***Material***
Layer 1	F	100.00	F	SiO_2.dsp
Substrate				c-Si_HJY.ref

The substrate used for all the materials is c-Si_HJY.ref from the application library provided by the software. The database of this material is taken from [12] and enhanced by HJY for Near Infrared (NIR) and Deep Ultraviolet (DUV).

The SiO_2 material has been created by HJY using a classical dispersion formula. This formula includes four oscillator models, and is as follows:

$$\varepsilon = \varepsilon_\infty + \frac{(\varepsilon_s - \varepsilon_\infty)\omega_t^2}{\omega_t^2 - \omega^2 + i\Gamma_0\omega} + \frac{\omega_p^2}{-\omega^2 + i\Gamma_D\omega} + \sum_{j=1}^{2} \frac{f_j\omega_{0j}^2}{\omega_{0j}^2 - \omega^2 + i\gamma_j\omega} \qquad \textit{II. 17}$$

With:

$\frac{(\varepsilon_s-\varepsilon_\infty)\omega_t^2}{\omega_t^2-\omega^2+i\Gamma_0\omega}$: The Lorentz oscillator, single oscillator used when re fit on SiO_2 parameters

$\frac{\omega_p^2}{-\omega^2+i\Gamma_D\omega}$: The drude term

$\sum_{j=1}^{2}\frac{f_j\omega_{0j}^2}{\omega_{0j}^2-\omega^2+i\gamma_j\omega}$: The double oscillator

And where: ε_∞ is the dielectric constant for high frequencies, ε_s the static dielectric constant, Γ_0 , Γ_D and γ the damping constants, ω the light energy, ω_t and ω_0 the transition energy of the absorption process, ω_p the plasma energy of the free electron gas and finally f the oscillator strength.

However, for each new coupon of SiO_2 used, a new material was created, based on the configuration presented above in Table. II. 1. The creation of a new material consists on using a material file where the optical properties are defined by the user. It is possible, to start with a reference material file close to the one used and provided by the SE supplier. And then ask to recalculate only some of the optical parameters. In our case, only parameters of SiO_2 were fitted again using single oscillator formula to recalculate ε_∞ and ε_s. With, before the fit, for a classic SiO_2, ε_∞ equal to 1, εs ~ 2.12 and ω_t ~ 12 eV.

In kinetic mode, same material parameters are kept, but with SiO_2 thickness varying through time.

III.1.ii.b. Silicon

- a-Si

The model used to fit measurements on a-Si is presented below in Table. II. 1. The dispersion material used for SiO_2 was also used for the SiO_2 under layer of the a-Si sample, but without making any fit on its parameters.

For the a-Si top layer, a new amorphous dispersion formula (a-Si_nam) has been used. It will be explained below in Eq. II. 18. As on SiO_2, the a-Si_nam parameters were also fitted for each new coupon used.

However, a-Si being rougher than SiO_2, it appeared that adding a third layer to model the surface roughness helps improving the fit. So roughness is modelled with a mixed layer comprising 50% a-Si and 50 % void. Void is modeled using the referenced material from the software library. Table. II. 2 presents the model used.

Table. II. 2. Fit model for a-Si

Layer N°	***Fit***	***Thickness (nm)***	***Fit***	***Material***
Layer 3	F	3.00	F	a-Si_nam.dsp + Void.ref
Layer 2	F	50.00	F	a-Si_nam.dsp
Layer 1		100.00		SiO_2.dsp
Substrate				c-Si_HJY.ref

The new amorphous dispersion formula is used a lot for amorphous surfaces. It corresponds to a single oscillator, including the following parameters:

$$n(\omega) = n_\infty + \frac{B(\omega - \omega_j) + C}{(\omega - \omega_j)^2 + \Gamma_j^2} \qquad \textit{II. 18}$$

$$k(\omega) = \frac{f_j(\omega - \omega_g)^2}{(\omega - \omega_j)^2 + \Gamma_j^2} \; if \; \omega > \omega_g \qquad \textit{II. 19}$$

$$k(\omega) = 0 \; if \; \omega \leq \omega_g$$

With: n_∞ the refractive index at low energy, ω_j the energy when the absorption is the highest and Γ_j the broadening factor, ω_g the band gap energy and $f_j$the oscillator strength. And B and C expressed as follows:

$$B = \frac{f_j}{\Gamma_j}(\Gamma_j^2 - (\omega_j - \omega_g)^2) \qquad \textit{II. 20}$$

$$C = 2 f_j \Gamma_j (\omega_j - \omega_g) \qquad \textit{II. 21}$$

As for SiO_2, when using a new coupon, the parameters of the material are fitted again. However, for an a-Si sample, from HJY, n_∞ is about 1.75, ω_g ~ 1.25 eV, f_j ~ 0.75 eV, ω_j ~ 3.5 eV and Γ_j ~ 1.30 eV.

III.1.ii.c. Silicon nitride

Unlike a-Si sample, the Si_3N_4 sample does not include a SiO_2 undercoat. Hence it is modeled as follow:

Table. II. 3. Fit model for Si_3N_4

Layer N°	***Fit***	***Thickness (nm)***	***Fit***	***Material***
Layer 2	F	2.00	F	SiNx_nam.dsp + Void.ref
Layer 1	F	240.00	F	SiNx_nam.dsp
Substrate				c-Si_HJY.ref

Again, as for silicon, a new amorphous formula is used to build the material folder, and a layer to model the roughness is added.

Before the fit on the coupon used, the SiN_x parameters are as follows: n_∞ is about 1.75, ω_g ~ 3.42 eV, f_j ~ 0.16 eV, ω_j ~ 7.31 eV and Γ_j ~ 1.70 eV.

III.2. X-Ray Photoelectron Spectroscopy

As explained above in the chapter, the reactor OPTIMIST has been used as an XPS is linked to it. This technique is non-destructive and enables to investigate the surface composition of a studied material through a depth of approximately 10 nm. All elements can be detected except for hydrogen and helium.

And thanks to OPTIMIST platform, it is possible to make the measurements while keeping the sample at low temperature. This is very helpful for cryogenic processes where most of the species involved in the mechanisms desorb at room temperature. In this section, the principle of XPS is detailed as well as the equipment used in IMN.

III.2.i. *Principle*

In 1887, H. Hertz discovered the photoelectric effect that will be explained in 1905 by A. Einstein. Later, in 1981, K. Siegbahn received the Physics Nobel Prize after developing this effect for the use of the XPS technique.

The photoelectric effect is observed when sending an electromagnetic radiation X with photons of energy $h\upsilon$ onto an atom with core electrons. This will hence allow one of these electrons to acquire enough energy to be ejected from its core level. This ejected electron will be called as photoelectron (Fig. II. 6). Therefore, the law of conservation of energy can be expressed as follows:

$$h\upsilon = E_B + E_k + \phi_e \qquad \textit{II. 22}$$

With: E_B the binding energy of the considered core level, E_k the kinetic energy of the photoelectron and $\phi_e$the output work needed to remove the photoelectron from the surface and corresponding to the difference between the Fermi level of the material and the vacuum level (Fig. II. 6).

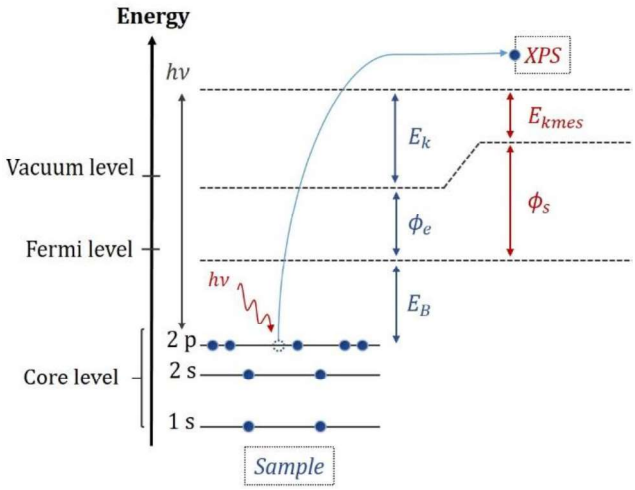

Fig. II. 6. Energy levels involved in XPS measurements

From this law, XPS technique was developed. In this case, the law of conservation of energy would rather be expressed as:

$$h\upsilon = E_B + E_{kmes} + \phi_s \qquad \textit{II. 23}$$

With: E_{kmes} the kinetic energy measured by the spectrometer and ϕ_s the spectrometer work function, corresponding to the removal of the photoelectron from the surface and reaching the spectrometer.

Once the photoelectron is ejected, reaching the sample surface and then the spectrometer will depend on its inelastic mean free path (IMFP). Indeed, the electron may undergo elastic collisions with other electron shells during its trajectory to the surface. So the IMFP corresponds to the average distance covered before collision. Some electrons may reach the surface without any collision and will therefore contribute to the intensity of the peak identified. Other electrons will interact with other shells and loose some energy, so they will only contribute to the background acquisition. And finally, due to too much collisions, some electrons will loose too much energy and hence won't be able to reach the surface. This explains why the analysis is limited in depth, as it will depend on the IMFP of the photoelectrons and on their E_k.

95% of the analyzed photoelectrons contributing to the intensity of the peaks, come from a depth equal to three times the wavelength of analysis [13].

As E_B is specific to each element, measuring E_{kmes} will therefore help identifying the chemical composition of a material's surface [13]–[17].

III.2.ii. *Composition of an XPS*

Basically, the XPS is composed of X-ray source, lenses to focalize the photoelectrons emitted by the surface and an analyzer.

III.2.ii.a. X-ray source

Different types of X-ray sources can be used. In this section, only the non-monochromatic X-Ray tube is presented.

To provide X-rays, a cathode (usually made of tungsten) is heated in order to release electrons. After acceleration, those electrons then induce the ionization of atoms from the anodes (made usually of aluminum and magnesium). In turn, it causes the displacement of an electron from shell 2p to shell 1s, while emitting at its turn a photon $h\upsilon$.

III.2.ii.b. Hemispherical analyzer

The mostly used analyzer type in XPS is hemispherical at 180°. It is composed of two glass hemispheres having the same center for their radius, noted R_1 and R_2 for respectively the smallest and the biggest hemisphere radius (Fig. II. 7). The photoelectrons will be able to enter from an adjustable slot noted W_1 at a solid angle of acceptance Ω and exit from a slot of width W_2. The surfaces of the hemispheres are coated with gold in order to be able to bias them, with a potential $-V_1$ for the small sphere and $-V_2$ for the biggest.

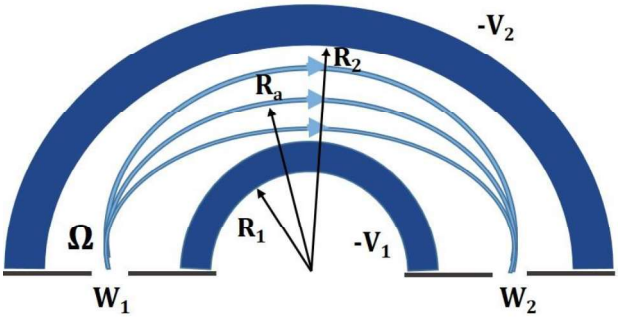

Fig. II. 7. Sketch of an hemispherical analyzer

Therefore, the analysis energy E_a for trajectory of radius R_a is noted as:

$$E_a = k_s\, q\, (V_2 - V_1) \qquad \textit{II. 24}$$

With: q the electron charge and k_s the spectrometer constant, equal to:

$$k_s = \frac{1}{\left(\frac{R_2}{R_1} - \frac{R_1}{R_2}\right)} \qquad \textit{II. 25}$$

If E_k is lower than E_a, the electrons are strongly deviated and stopped by the smallest hemisphere. At the opposite, if E_k is too high in comparison to E_a, the electrons are stopped

by the biggest hemisphere. Therefore, only electrons with $E_k \approx E_a$ will be able to go through the analyzer and be detected.

Hence, the energy resolution of the analyzer (ΔE) can be expressed as:

$$\Delta E = E_a \left(\frac{W}{R_a} + \Omega^2 \right) \qquad \text{II. 26}$$

It depends on the slots opening sizes W and on E_a, so an optimum should be find to obtain the best resolution with the highest intensity [16].

III.2.iii. Characteristics of the XPS used at IMN

The XPS used at the IMN is from Specs. The X-ray source used is Specs XR50 M equipped with Al and Ag anodes and coupled to the monochromator Focus 500. It can hence provide two monochromatic sources, the Al Kα at 1486.7 eV and Ag Lα at 2984.3 eV.

The analyzer mounted is a high performance hemispherical energy analyzer Specs PHOIBOS HR-150 with 1D-DLD detector.

The ultimate vacuum in the XPS chamber is about 10^{-7} Pa.

The software used for the analyses is Casa-XPS.

III.2.iv. Expression of peak intensity

Once the spectrum is acquired, the first thing to do for the identification of the peaks is the subtraction of the background due to secondary electrons. Then, the peaks are decomposed according to their position, Full Width at Half Maximum (FWHM) and spin-orbital splitting.

The intensity of a detected peak is proportional to the density of the species in the analyzed area and can be expressed as [14], [18]:

$$dI(\theta) = \Phi . \frac{A_0}{\cos\theta} . \Omega . L . D(E_a) . T(E_k E_a) . \left(\frac{d\sigma}{d\Omega} \right) . N . exp\left(\frac{-z}{\lambda \cos\theta} \right) . dz \qquad \text{II. 27}$$

With: θ The angle of the photoelectron emission in comparison to the surface normal, Φ the photon flux, Ω the solid angle of acceptance of the hemispherical analyzer, L the emission anisotropy, $D(E_a)$ the detector efficiency, $T(E_k E_a)$ the transmission function of the spectrometer depending on E_k and E_a, N the atomic density, z the depth from the surface, dz the thickness of the studied layer, λ the inelastic mean free path of electrons, $\frac{A_0}{\cos\theta}$ the analyzed surface and $\frac{d\sigma}{d\Omega}$ the differential cross section per atom.

After integration, the intensity expression becomes:

$$I(\theta) = I^{\infty} \left[1 - exp\left(\frac{-z}{\lambda \cos\theta} \right) \right] \qquad \text{II. 28}$$

With I^{∞} the intensity for a uniform material all over its surface, and expressed as:

$$I^{\infty} = \Phi . A_0 . \Omega . L . N . \lambda . D(E_a) . T(E_k E_a) . \left(\frac{d\sigma}{d\Omega}\right) \qquad \text{II. 29}$$

The studied XPS scans in this work present the intensity measured as detected counts per second and plotted as function of the binding energy. Each element at a core level has a specific energy that slightly changes according to the bonds with other elements (chemical shift). Therefore, depending on the position of the measured peak it is possible to determine the species present on the surface.

III.3. Scanning Electron Microscopy

M. Von Ardenne developed the Scanning Electron Microscopy (SEM) in 1938. It enables to acquire surface images at nanometer scale.

It consists in creating a primary electron beam by thermionic effect. Then, the surface is scanned using several electrostatic lenses. The sample will therefore emit secondary electrons of low energy as well as backscattered electrons and X-rays that will be detected by the device (Fig. II. 8) [19]. The pear shape presented in Fig. II. 8 corresponds to the interaction volume.

The SEM used at GREMI is a SUPRA 40 (Zeiss), equipped with a Schottky effect gun.

The images were acquired by only detecting the secondary electrons, with InLens detector. The vacuum in the column was usually about 10^{-7} Pa and the chamber vacuum was about 10^{-5} Pa. The electron high voltage set for the images was 3 kV, and the focusing distance was between 8 and 9 mm.

The SEM was used to look at the etching profiles displayed in Chapter IV, which helped to understand the efficiency of a passivation layer.

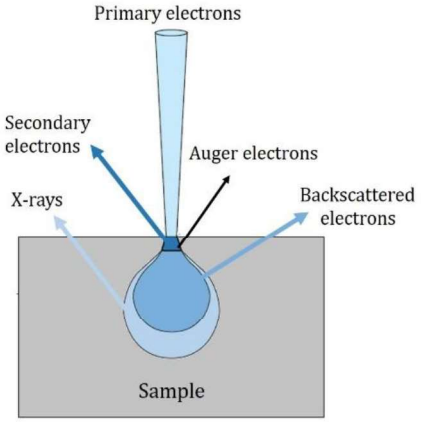

Fig. II. 8. Involved interactions between a primary electron beam with a sample surface during a SEM measurement

III.4. Atomic Force Microscopy

In 1985, many years after the SEM, G. Binning, C. Gerber and C. Quate developed the first Atomic Force Microscope (AFM) [20]. It consists on scanning the surface using the interactions between a probe and the surface to plot back the surface shape.

During this project, AFM measurements were performed to investigate the surface roughness before and after cryo-ALE cycles using C_4F_8 physisorption (Chapter. III). The used AFM is a Bruker Scanning Probe Microscope (SPM) Dimension Icon. The analysis were performed using the ScanAsyst dynamic mode developed by Bruker, and is very similar to the PeakForce Tapping mode. The difference, however, between both is that the ScanAsyst mode is developed with further algorithms to automatically adjust some of the acquisitions parameters, using a feedback loop, in order to take into account the variation in the quality of the sample surface and ensure high resolution and uniform images.

These two dynamic modes are preferred to the contact mode because the latter could be destructive. Indeed, as the tip is always in contact with the surface, depending on the sample investigated, damage would occur to the tip point or to the sample if it is too soft.

The PeakForce Tapping mode is similar to the tapping mode where the tip is into contact with the surface periodically and for a short time. This helps avoiding the effect of lateral forces of the sample. At the same time, this technique enables fast imaging. But unlike the tapping mode, the cantilever is oscillated at frequencies lower than its resonance, enabling a better control of the different forces. Indeed, a sine wave is in this case used to modulate the z-position.

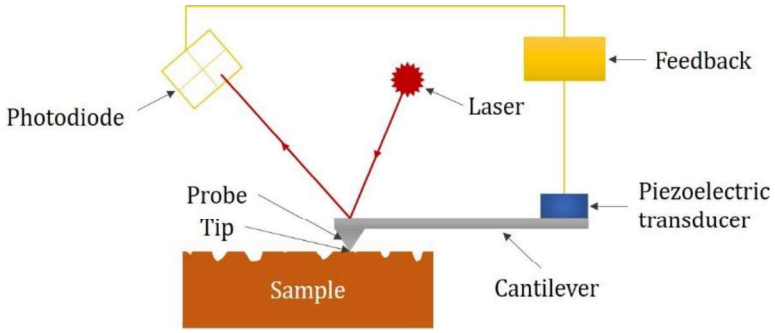

Fig. II. 9. Sketch of an AFM

As shown in Fig. II. 9, the probe and its cantilever are made of a single silicon piece. The end of the cantilever, at the opposite side of the probe, is fixed to a ceramic piezoelectric transducer as a lever arm. The latter will make the tip oscillate at very high frequency near the sample surface. At the same time, a laser beam is sent to the backside of the tip, which reflects the beam towards a photodiode. During measurements, the oscillations of the cantilever and reflection variations are detected by the photodiode and processed using a feedback loop.

When the tip is close to the surface, it is attracted thanks to long-range Van Der Waals forces (Fig. II. 10) until getting into contact with the surface. At that moment, when getting too close to the surface, the tip will undergo short range repulsive forces (peak point of the curve in Fig. II. 11), before it gets off the surface. Those interaction forces are of the order of pN and are measured by the deflection of the cantilever. In this PeakForce Tapping mode, when each peak point is detected, it will force the tip to retract. Therefore, it favors a better resolution on soft surfaces, as it is more sensitive to the forces and can hence operate at low controlled forces [21], [22].

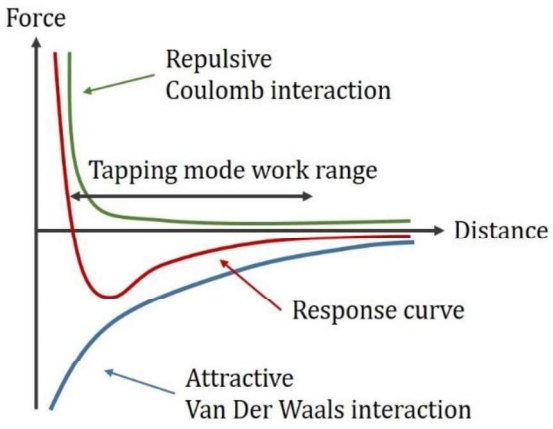

Fig. II. 10. Involved forces in tapping mode

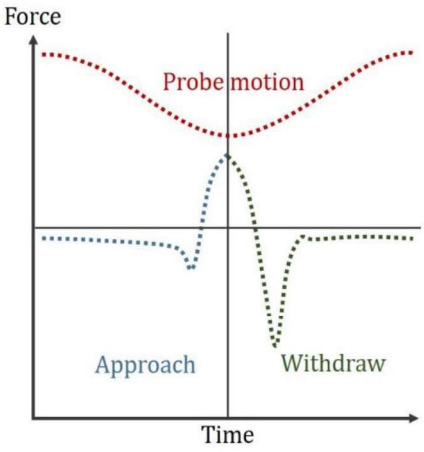

Fig. II. 11. Force response curve during measurement

During the thesis, the images were acquired using ScanAsyst-air probes with a spring constant of 0.4 $N.m^{-1}$, having a tip radius of 2 nm. The image scan size is 500 nm, with 512 points per line, and 512 lines per image. In addition, the scan rate was 1 Hz.

IV. Plasma diagnostics

Finally, in order to know more about the species present in the chamber during the processes, several characterization techniques were used and are presented below.

IV.1. Langmuir probe

IV.1.i. *Principle*

The Langmuir probe was first developed by Irving Langmuir in 1924. It is an intrusive technique, where a biased probe is introduced into the reactor. The applied voltage is varied and the collected current is measured. The resulting Current-Voltage (I-V) characteristic, exhibits three regions, as shown in Fig. II. 12:

- The first region A is observed when applying negative potentials and corresponds to the ion region. It helps measuring the ion density (N_i), as only the positive ions reach the probe and not the electrons.
- The region B is called the electron retardation region. It starts at the floating potential (V_f) and finishes at the plasma potential (V_p). At V_f, the total collected current is equal to zero because the ion and electron currents compensate each other. Then, when increasing the voltage a sheath around the probe is formed. There is a repulsive potential for the electrons, and the electrons density n_e can be described by the Boltzmann equation below:

$$n_e = n_0 exp^{\frac{-q(V_s - V_p)}{k_B T_e}} \quad \text{II. 30}$$

With: V_s the surface potential, n_0 the density of charged species in the plasma and q the electron charge

In this case, only electrons with enough energy will go through the potential barrier and reach the probe. Therefore, the current increases exponentially with the increase of the applied voltage. The electrons current is expressed as follows:

$$I_e = \frac{1}{4} n_0 \, q \, A_s \sqrt{\frac{8 k_B T_e}{\pi m_e}} exp^{\frac{-q(V_s - V_p)}{k_B T_e}} \quad \text{II. 31}$$

And the repulsive current of the ions is considered negligible. When the applied voltage is high enough that no sheath is formed near the probe, an inflection is observed in the I-V curve. The measured current is observed due to thermal difference between electrons and ions in the plasma. It corresponds to V_p. To determine it more precisely, the second derivative of I-V curve can be plotted, and V_p will correspond to the point where the second derivative is equal to zero (Fig. II. 12).

- The region C, as the probe is biased positively, both negative ions and electrons are attracted. This region corresponds to the electron region.

From the region B of the curve and V_p, the Langmuir probe software will calculate the electron temperature (T_e) using the following equation [23]:

$$k_B T_e = \frac{\int_{V_f}^{V_p} I(V) dV}{I(V_p)} \quad \text{II. 32}$$

Then, by knowing T_e, the electron density n_e can also be calculated:

$$n_e = \frac{I(V_p)}{A_p} \sqrt{\frac{2\pi m_e}{q^2 k_B T_e}} \quad \text{II. 33}$$

With: A_p the probe area, m_e the electron mass.

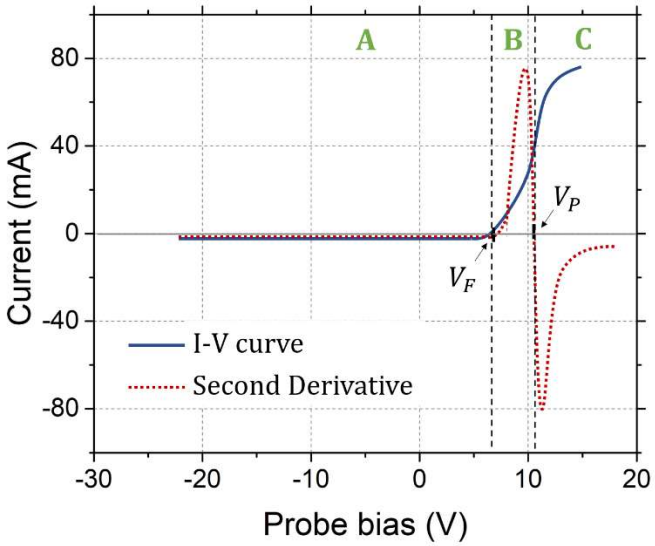

Fig. II. 12. Typical Current-Voltage curve

As mentioned above, a sheath is created at some applied bias. To take it into account in the plasma parameters calculation and in the variation of the measured current, the Laframboise theory has been used. It enables to calculate the currents in the ion region (Eq. II. 34) and in the electrons region (Eq. II. 35) for ions and electrons having a Maxwellian distribution. The results were obtained by Laframboise by resolving Poisson equation and presenting the results as charts. However, Peterson and Talbot expressed it the analytical form presented below:

$$I_{i\,sat} = A_s\, q\, n_i \sqrt{\frac{2k_B T_i}{\pi m_i}} (\beta + |\chi|)^{\alpha} \qquad \text{II. 34}$$

$$I_{i\,sat} = A_s\, q\, n_e \sqrt{\frac{2k_B T_e}{\pi m_e}} (\beta + |\chi|)^{\alpha} \qquad \textit{II. 35}$$

With:

$$\alpha = g(a, b, c, \dots, T_e, n_i) \qquad \textit{II. 36}$$

$$\beta = h(a, b, c, \dots, T_e, n_i) \qquad \textit{II. 37}$$

a, b and c are tabulated coefficients which depend on T_e/T_i ratio.

$$|\chi| = exp^{\frac{q(V_p - V_s)}{k_B T_e}} \qquad \textit{II. 38}$$

However, this theory is only valid when the probe radius is between 5 and 100 times the Debye length. For other cases, for example if the radius is smaller than 3, the Orbital Motion Limited (OML) can be applied [6], [23], [24].

IV.1.ii. *Probe used*

The Langmuir probe used in the thesis is the SmartProbe from Scientific Systems. The filament shape is cylindrical and made of NiCr with a radius of 50 µm.

The probe is also equipped with a reference unbiased probe and that, hence, is at the floating potential. As the plasma potential is affected by the sheath created by the presence of the filament, the reference probe helps correcting the measurements.
A compensation electrode of 3.5 cm² is also added to compensate the fluctuations at the plasma at RF frequency which can distort the I-V curve.
The shaft is made of alumina and is 470 mm length. Finally, because the reactor walls are insulated, a metal ring has been mounted inside the reactor, at the bottom part of the source, and grounded in order to close the circuit. A sketch of the probe is presented in Fig. II. 13.

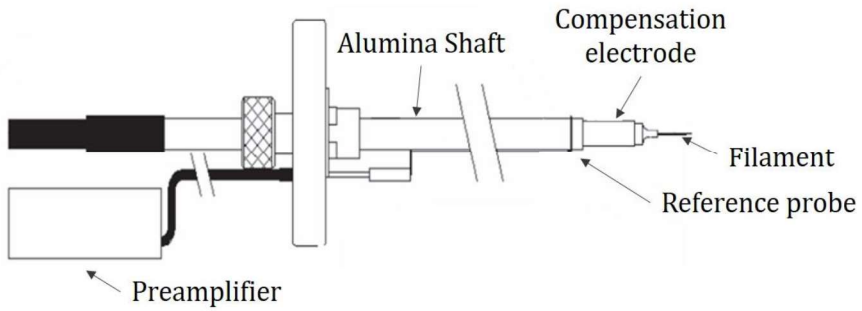

Fig. II. 13. Sketch of the SmartProbe, adapted from [6]

The software used for the acquisitions is Smartsoft [23].
The Langmuir probe was installed at about 100 mm above the samples, at the center of the reactor diffusion chamber. Then, other tests were also performed at same height, but 40 mm and 100 mm away from the center.
Only Ar plasma was characterized at different pressures and source powers.

IV.2. Electrostatic Quadrupole Plasma Mass Spectrometry

Analysis by mass spectrometry were often performed during the thesis for both processes using C_4F_8 and SiF_4 / O_2. This technique enables to identify the species present in the reactor during a process, according to their mass m to charge z ratio.

IV.2.i. *Equipment presentation*

The equipment used is an Electrostatic Quadrupole Plasma Mass Spectrometer (EQP Analyzer or simply QMS) Series 1000 from Hiden Analytical, presented in Fig. II. 14. To simplify the notation, it will be referenced by “QMS” for the rest of the manuscript.

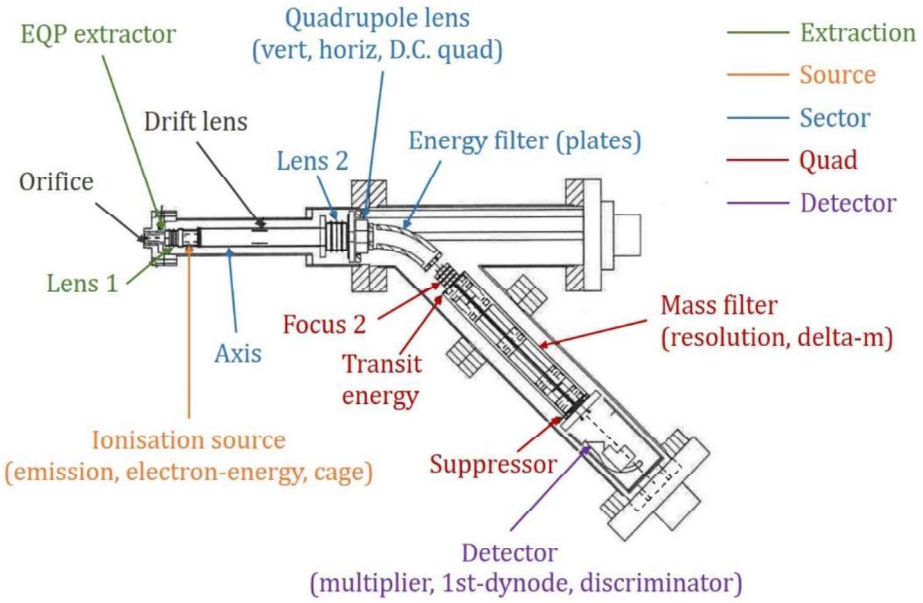

Fig. II. 14. Sketch of a QMS electrodes, adapted from [25]

This type of spectrometers offers several types of acquisitions. It enables to identify either radicals and neutrals or ions (positive or negative) and measures the ion energy, depending on the defined mode, presented below.

The QMS is provided with a Manual Gate Valve and an Adapter Nipple, allowing to isolate the QMS or to vary its horizontal position (length entered into the reactor). It is pumped differentially from the reactor, thus, the ultimate vacuum that can be reached inside the QMS is generally between 4.10^{-7} Pa and 1.10^{-6} Pa. Usually, the orifice was entered until 100 mm far from the center of the reactor and about 100 mm above the samples. The sampling orifice size is 0.1 mm. As presented in Fig. II. 14, the EQP extractor and the first lens help attracting or rejecting ions depending on the analysis mode.

In the case of neutrals and radicals detection, the species enter the orifice, the extractor and finally the ionization source by diffusion. The latter is composed of two filaments made of oxide coated iridium and a cage. A current is applied to the filament to emit electrons. The emitted electrons are then accelerated from the filaments to the cage. The electron energy range for the species dissociation can be set from 1 eV to 100 eV. Neutrals are hence ionized and go out of the cage as ions.

Once out of the ionization chamber, the ionized species go through the sector field where they are filtered according to their energy. This enables to provide information on the energy distribution of the ions.

The Quad then allows mass filtering. It is composed among others of the quadrupole mass filter. The latter is made of four electrodes of 9 mm diameter, where the opposite electrodes are connected with the same RF potential sign. For it, a RF generator is mounted separately and provides the electrical field necessary to separate the ions as a function of their mass m

to charge z ratio. The mass range is 1 to 510 amu. Finally, the ions are directed to the detector, a Secondary Electron Multiplier pulse-counting detector. The detector should not endure more than 5.10^6 counts per second, or it would induce an accelerated aging of the detector. The multiplier voltage can be set between 1600 V and 2700 V.

Analysis can be performed using one of the two main type of scans: the Residual Gas Analysis (RGA) mode and the Secondary Ion Mass Spectrometry (SIMS) mode. The RGA mode enables the detection of radicals and neutrals in the reactor. It can be used during a plasma as well as for simply a gas flow. During this mode, as explained above, the radicals and neutrals enter the spectrometer by diffusion and are directed to the ionization chamber. Usually in literature, and in our measurements, the electron energy was set at 70 eV, in order to dissociate the molecules into several other molecules or species before m/z filtering. On the other hand, the Secondary Ion Mass Spectrometry (SIMS) mode is dedicated only to plasma processes as it detects ions. Both positive and negative ions can be detected with our equipment by applying a voltage to the extractor to attract the desired ions. In this mode, the filament is off, as there is no need for ionization. So the ions only go through m/z analysis.

IV.2.ii. *QMS use*

Only the Residual Gas Analysis (RGA) mode has been used during the thesis. For it, the acquisitions were performed in profile and / or in Multiple Ion Detection (MID) mode. The profile mode enables to perform a scan on a range of masses that can be defined by the user with choice of the pitch. The resulting scan plots the number of detected counts as a function of m/z of the ions of fragmentation of the analyzed neutrals. It is very useful for the detection of species in a constant process, or to identify in a preliminary way the ion to monitor the species of interest. Then, the MID mode can be used to monitor the evolution of the species of interest through time. For it, the user defines the mass of the species to monitor on the software.

The software used to control the QMS is MASsoft application [25].

V. Conclusion

This chapter presented the substrates of interest for this work, which were SiO_2, a-Si, and Si_3N_4. They were etched using an ICP reactor on which a SE, a QMS, an OES and a Langmuir probe were mounted for respectively thickness monitoring and plasma characterization. Extras tests were performed as AFM for characterization of surface roughness and SEM for observation of features. Finally, some tests were conducted using OPTIMIST platform at Nantes in order to make quasi in-situ XPS measurements, for the mechanisms understanding.

VI. References

[1] W. Kern and K. K. Schuegraf, "1 - Deposition Technologies and Applications: Introduction and Overview," in *Handbook of Thin Film Deposition Processes and Techniques (Second Edition)*, K. Seshan, Ed. Norwich, NY: William Andrew Publishing, 2001, pp. 11–43.

[2] C. Cardinaud, M.-C. Peignon, and P.-Y. Tessier, "Plasma etching: principles, mechanisms, application to micro- and nano-technologies," *Appl. Surf. Sci.*, vol. 164, no. 1–4, pp. 72–83, 2000.

[3] M. J. Cooke, "Impact of Atomic Layer Etching on Process Tool Design," *ECS J. Solid State Sci. Technol.*, vol. 4, no. 6, pp. N5001–N5004, 2015.

[4] High Vacuum Technology Alcatel, "User guide, etching tool 601E." 1999.

[5] R. Dussart, T. Tillocher, P. Lefaucheux, and M. Boufnichel, "Plasma cryogenic etching of silicon: from the early days to today's advanced technologies," *J. Phys. D: Appl. Phys.*, vol. 47, no. 12, p. 123001, 2014.

[6] T. Tillocher, "Gravure profonde du silicium par le procédé cryogénique. Application à la réalisation de trous traversants. Optimisation du procédé, mécanismes réactionnels en phase gazeuse et interaction plasma / silicium," Université d'Orléans, 2006.

[7] J. Pereira *et al.*, "In situ x-ray photoelectron spectroscopy analysis of SiO_xF_y passivation layer obtained in a SF_6/O_2 cryoetching process," *Appl. Phys. Lett.*, vol. 94, no. 7, p. 071501, 2009.

[8] P. Drude, "Ueber die Gesetze der Reflexion und Brechung des Lichtes an der Grenze absorbirender Krystalle," *Annalen der Physik*, vol. 268, no. 12, pp. 584–625, 1887.

[9] B. Wang and J. List, "Basic optical properties of the photoelastic modulator: Part I. Useful aperture and acceptance angle," 2005, p. 58881I.

[10] K. Dorywalski, I. Maciejewski, and T. Krzyzynski, "Spectroscopic ellipsometry technique as a materials characterization tool for mechatronic systems - The case of composition and doping concentration monitoring in SBN crystals," *Mechatronics*, vol. 37, pp. 33–41, 2016.

[11] Horiba Jobin Yvon, "Spectroscopic Ellipsometry, User guide." 2008.

[12] G. E. Jellison, "Optical functions of silicon determined by two-channel polarization modulation ellipsometry," *Optical Materials*, vol. 1, no. 1, pp. 41–47, 1992.

[13] T. Meyer, "Gravure du verre de chalcogénure GeSbSe en plasma fluoré ou à base de méthane," Université de Nantes, Nantes, 2019.

[14] L. Fauquier, "Nouvelles approches d'utilisation de la spectroscopie de photoélectrons à rayons X (XPS) pour le développement et le contrôle des technologies FDSOI avancées," p. 245.

[15] O. Mourey, "Développement de nouvelles technologies de gravure : mise en évidence de la stochasticité du bombardement ionique lors de procédés plasma industriels," Université de Grenoble Alpes, 2017.

[16] T. M. Duc, “Analyse de surface par ESCA - Principe et instrumentation,” p. 36, 1998.

[17] J. F. Moulder, W. F. Stickle, P. E. Sobol, and K. D. Bomben, *Handbook of X-ray Photoelectron Spectroscopy*. Perkin-Elmer Corporation, 1992.

[18] G. Hollinger, “Spectroscopies de photoélectrons: XPS ou ESCA et UPS,” p. 21, 1986.

[19] J. Ruste, “Microscopie électronique à balayage - Principe et équipement,” *Techniques de l’ingénieur*, no. P865, p. 24, 2013.

[20] G. Binnig, C. F. Quate, and C. Gerber, “Atomic Force Microscope,” *Phys. Rev. Lett.*, vol. 56, no. 9, pp. 930–933, 1986.

[21] S. B. Kaemmer, “Introduction to Bruker’s ScanAsyst and PeakForce Tapping AFM Technology.” Bruker Nano Surfaces Division.

[22] “PeakForce Tapping.” Bruker Nano Surfaces Division.

[23] Scientific Systems, “SmartProbe manual.” 2002.

[24] S. Béchu, A. Bès, L. Bonny, and A. Lacoste, “Mesures des paramètres électrostatiques d’un plasma par sondes de Langmuir,” presented at the Atelier Diagnostics Plasma, Orléans, 2014.

[25] Hiden Analytical, “EQP/EQS Analyser Operator’s Manual.” 2007.

Chapter III.

Cryo-ALE based on C_4F_8 physisorption

In this chapter, it is proposed to perform ALE by injecting the precursor in gas phase instead of plasma phase. The process of cryo-ALE consists in etching one to few mono-atomic layers per cycle by decreasing the substrate temperature, for example below -40°C. Its principle is presented in Fig. III. 1 and can be compared to the general principle of ALE presented in Fig. I. 18. The first step of this process is the injection of liquid nitrogen to cool the chuck and cool the wafer by injecting He at its backside to ensure the thermal conductivity (1 in Fig. III. 1). Once the wafer temperature has been stabilized, a CF-based gas is injected in order to physisorb on the cooled surfaces (2 in Fig. III. 1). As the reactor walls are kept at room temperature, no adsorption occurs on them. The third step (3 in Fig. III. 1) is the pumping or the purge of the chamber by Argon in order to remove all the surplus of C_4F_8 that did not physisorb. An argon plasma with a low bias is then initiated in order to supply enough energy to the ions to make CF_x radicals react with SiO_2 and etch one to few monolayers of the substrate (4 in Fig. III. 1). This step is self-limited, as once all the CF_x radicals are consumed, the etching stops (5 in Fig. III. 1). It is the so-called SLE (Self-Limiting Etching) [1], [2].

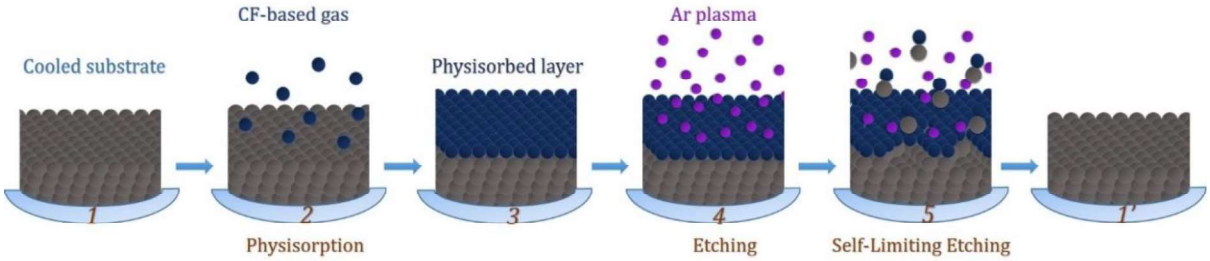

Fig. III. 1. Scheme of cryo-ALE principle

This chapter is focused on the etching of SiO_2 using C_4F_8 physisorption. C_4F_8 was chosen as precursor to conduct this study, as it can physisorb under conditions (pressure and temperature) achievable with our equipment. Moreover, many studies were already carried out using it for SiO_2 ALE as it provides the CF_x needed for SiO_2 etching.

The physisorption step is very critical and important to control the ALE process. Therefore, the first section of this chapter is dedicated to it.

I. Study of physisorption

Physisorption corresponds to physical adsorption, and describes the interaction when a gas molecule enters in contact with an outgassed solid. The solid is qualified as *the adsorbent*, the gas is called *the adsorptive*, and once the adsorptive is in contact with the adsorbent, the gas molecule in contact will be named *the adsorbate* [3] (Fig. III. 2).

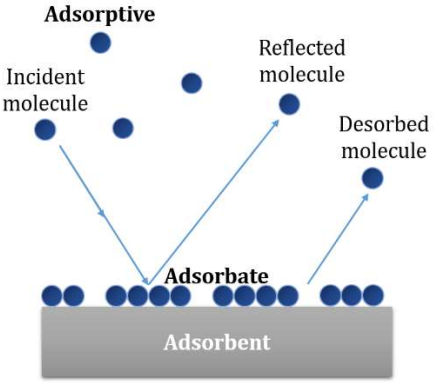

Fig. III. 2. Sketch of molecules adsorption

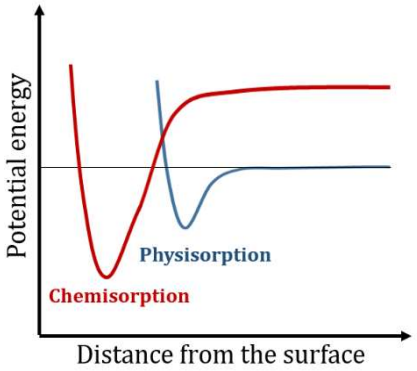

Fig. III. 3. Surface potential energy

When the adsorptive enters in contact with the adsorbent, it may stick to the surface thanks to electromagnetic interactions with the atoms at the adsorbent surface. Fig. III. 3 represents the surface potential energy based on the work of Lennard-Jones. The sketch helps to point out the difference between chemisorption and physisorption. It is considered as chemisorption when there is a chemical reaction with electron transfer between the gas molecule and the solid. In this case, bonds of the adsorbed molecule may break in order to create new ones with the adsorbent. Covalent bonds at short distance are hence created between the adsorbate and the adsorbent. The potential well in this case is deep of about one hundred of $kJ.mol^{-1}$. A temperature increase favors chemisorption, as it will bring the energy needed to create surface chemical reactions.

At the opposite, physisorption occurs at longer distance using Van Der Waals interactions, and the larger the molecule is, greater is the distance. There is no chemical reactions in physisorption. The potential well is shallow with an energy of few $kJ.mol^{-1}$. Decreasing temperature enhances physisorption, whereas a temperature increase would induce molecules desorption [4], [5].

Therefore, Fig. III. 3 summarizes these two cases, indicating that the interactions in physisorption occur at longer distances and lower binding energy than for chemisorption.

I.1. Adsorption parameters

In physisorption, several parameters have to be taken into account, and are expressed below.

I.1.i. *Rate of incident molecules*

Eq.III. 1 describes the rate of molecules entering in contact with the solid surface, noted m *(kg.m^{-2}.s^{-1})* [6]:

$$m = \sqrt{\frac{M}{2\pi RT}} P \qquad \textit{III. 1}$$

With: M the molecular weight (kg.mol^{-1}), R the ideal gas constant (J.mol^{-1}.K^{-1}), T the temperature (K) and P the pressure (Pa).

I.1.ii. *Surface coverage*

When the surface is not yet totally covered by adsorbates, the surface coverage can be identified and estimated as follows.

It corresponds to the number of adsorbate molecules (N_a) compared to the number of sites of the adsorbent surface, available, for example, for a monolayer full coverage (N_s) (Eq. III. 2) [5]. Both N_a and N_s are per unit area of the surface (m^{-2}).

$$\theta = \frac{N_a}{N_s} \qquad \textit{III. 2}$$

Then, as some molecules may adsorb and other desorb at equilibrium, the surface coverage rate can be expressed through time, by taking into account the rate of incident molecules, the sticking probability and the residence time on the surface. Eq. III. 3 below gives the coverage through time [5].

$$\frac{d\theta}{dt} = \frac{SP}{N_s(2\pi m k_B T)^{1/2}} - \frac{\theta}{t_d} \qquad \textit{III. 3}$$

With: S the sticking probability, t_d the surface residence time (s), k_B the Boltzmann constant (eV.K^{-1}).

I.1.iii. *Surface residence time*

The gas molecule needs a certain energy to adsorb to the surface (E_a). However, once it is in contact with the surface, it tends to desorb from it. The energy needed for that can be brought by the adsorbent surface or from an external source. Therefore, decreasing the adsorbent temperature reduces the energy supplied by it, and hence the physisorbed molecule stays longer on the surface.

The Frenkel Arrhenius equation below presents the residence time [5], [7].

$$t_d = t_d^0 exp^{E_d/k_B T} \quad \textit{III. 4}$$

With: t_d the residence time (s), t_d^0 the attempt time of the particle for desorption (s), E_d the desorption energy, or the energy needed for desorption (eV), k_B the Boltzmann constant (eV.K^{-1}) and T the temperature of the substrate (K).

I.2. Langmuir model for monolayer adsorption

In 1918, Langmuir published his study on the adsorption of gases on several materials. He claimed that the surface residence time of an adsorbate was depending on the intensity of the bonds with the adsorbent. Hence, as the bonds are weak in physisorption, desorption occurs quite quickly, and consequently, it is difficult to achieve a total coverage of the adsorbent surface. Also, if the adsorbing molecules are bigger than the elementary spaces to occupy, steric hindrance may occur, preventing the saturation of the adsorbent surface. However, depending on the molecule size and their elastic properties, the molecules will be able to crowd each other to occupy more adjacent spaces [6].

The Langmuir model can be applied for monolayer coverage, when the surface is considered as homogeneous, which means that all the adsorption sites have identical energy, and that no interaction occurs between the adsorbed molecules [8].

Thus, the model equation can be expressed as follows in Eq. III. 5 for $\theta \leq 1$ [8]:

$$n = \frac{n_m bc}{1 + bc} \quad \textit{III. 5}$$

With: n the adsorbed amount per adsorbent mass unit (mol.m^{-3}), n_m the maximum adsorption amount in a monolayer (mol.m^{-3}), b the Langmuir constant (m^3.mol^{-1}), c the concentration of the adsorptive in the gas phase (mol.m^{-3}).

I.3. BET model for multilayer physisorption

As the Langmuir model is only valid for a surface coverage equal or lower than one, Brunauer, Emmett and Teller suggested the BET model in 1938 to extend the theory in case of multilayer coverage. The model equation is expressed below in Eq. III. 6 [9].

$$\frac{x}{\upsilon(1-x)} = \frac{C-1}{\upsilon_m C} x + \frac{1}{\upsilon_m C} \quad \textit{III. 6}$$

With: υ the adsorbed thickness (Å), υ_m the adsorbed amount for a coverage of one monolayer (Å), C the ratio of desorption frequency factor between layers (expressed in Eq. III. 7), x the relative pressure (pressure normalized by vapor pressure, Eq. III. 8).

The ratio C is expressed in Eq. III. 7 below:

$$C = e^{\frac{E_{desorb.1} - E_{desorb.i}}{RT}} \quad \textit{III. 7}$$

With: $E_{desorb.1}$ the desorption energy of the 1st layer (eV), $E_{desorb.i}$ the desorption energy of the ith layer (eV), R the ideal gas constant (eV.mol^{-1}.K^{-1}), T the temperature (K).

Some values of $E_{desorb.1} - E_{desorb.i}$, also expressed as ΔE, have been calculated in [9] and were of the order of 0.03 to 0.06 eV. This shows that $E_{desorb.1}$ is always higher than $E_{desorb.i}$.

The relative pressure, x is expressed as:

$$x = \frac{P}{P_0} \qquad \textit{III. 8}$$

With: P the process pressure (Pa), P_0 the vapor pressure of the molecules to be physisorbed (Pa)

I.4. Adsorption isotherms

International Union of Pure and Applied Chemistry (IUPAC) has identified six base physisorption isotherms to explain physisorption behavior as a function of the adsorbent microstructure and pores [10]. Those isotherms are presented in Fig. III. 4 below.

Isotherms of type I are observed on microporous solids. The adsorbed amount increases with the relative pressure, until reaching a limiting value. If the solid pores are narrower than 1 nm, saturation is quite fast as in I (a) in Fig. III. 4. If they are larger (up to ~ 2.5 nm), the adsorbed amount will reach a limiting value at higher relative pressure and so isotherms will be as I (b) in Fig. III. 4. Those curves correspond to the Langmuir model and are reversible, which means that desorption occurs in the perfectly opposite way.

Isotherms of type II and III are also reversible and occur on macroporous solids (pores larger than 50 nm width) and on nonporous materials. In the case of Isotherms of type II, adsorption is not limited, and so does not stop. The first part of the curve, point B in II in Fig. III. 4, situated at low relative pressure (P/P_0), gives information on monolayer coverage. If the curve at point B has a sharp shape, it means that the monolayer coverage is completed at the end of the knee and the beginning of the almost linear curve. In this case, *C* parameter from BET model is close to 80 [10]. However, if the curve at point B is more gradual and the knee harder to identify, it means that the monolayer coverage is already achieved, and some multilayer physisorption is also occurring. In this case, *C* is lower than 50.

After the point B, the adsorbed amount increases slowly when x (the relative pressure) is still below 1. And if x = 1, adsorption increases faster which induces a change in slope of the curve. In case of a small *C* parameter (*C* < 2), isotherms will be of type III and so the BET model cannot be applied. The bonds between the adsorbate and the adsorbent are weak. There is no knee shape at low relative pressure, which makes more complicated to identify when the

monolayer coverage is achieved. Also, at x = 1, the adsorbed amount is lower than in the case of type II isotherms.

Isotherms of type IV are observed for mesoporous solids (pores with a width between 2 nm and 50 nm). It is possible to identify on it the point B as for isotherms of type II, and the BET model can be applied to it. However, in this configuration of mesoporous solids, after the adsorption, some pore condensation may occur, even at a pressure below the vapor pressure of the gas. However, the adsorption saturates for high relative pressures. The difference between type IV (a) and IV (b) depends on the size of the pores. If they are small (for example less than 4 nm), the adsorption is reversible (type IV (b)). However, if the pores are too big, a hysteresis is observed as in IV (a).

Isotherms of type V are observed for microporous and mesoporous materials with a small *C* (*C* < 2) and in this case the BET model cannot be applied. At low relative pressure, the bonds between the adsorbate and the adsorbent are also weak as in isotherms III. However, a hysteresis is observed at higher relative pressure due to pore filling.

Finally, isotherms of type VI are reversible and are observed for nonporous materials, when the adsorption is achieved layer by layer, as evidenced by the stepwise increase of the adsorbed amount [10].

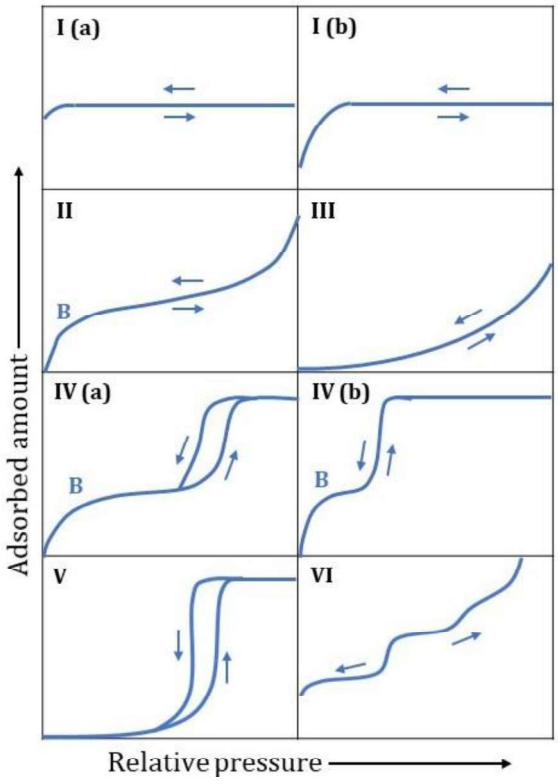

Fig. III. 4. Physisorption isotherms plotting the adsorbed amount of a gas as a function of the relative pressure, adapted from [10]

I.5. Antoine equation

Usually, the residence time of a molecule physisorbing on an adsorbate, is very short compared to the residence time of the adsorbate on the adsorbent. However, when conditions are close to the vapor pressure of the molecule, the residence time at the surface is increased, and more than one layer can adsorb to the surface. As the adsorbent has to be cooled to enhance the residence time of the adsorbate on its surface, Antoine equation has served to get close to condensation parameters of the adsorptive, but still without reaching condensation.

The Antoine equation is obtained by integrating the Clausius-Clapeyron equation that gives the relation between the vapor pressure of a component and temperature [11].

Eq. III. 9 below presents Antoine equation:

$$Log\ (P) = A - \frac{B}{T + C} \qquad \textit{III. 9}$$

With: P the pressure (Pa), A, B and C the Antoine parameters, T the temperature (K).

From this Eq. III. 9, three constants (A, B and C) are given that will help calculating the vapor pressure of a component. The values of those Antoine parameters can be easily found for many gases in National Institute of Standards and Technology (NIST) database [12].

I.6. Water physisorption in the reactor Alcatel 601E

I.6.i. *Effect of water physisorption on spectroscopic ellipsometry signal*

Some water may be present in the reactor chamber due to reactor leakage. When the substrate and the chuck are cooled, this water may condense on the cooled surfaces. So, before the study of C_4F_8 physisorption, water physisorption has been investigated. To do so, a cryo-ALE cycle has been simulated. A SiO_2 coupon has been glued on a 6" SiO_2 carrier wafer and cooled to -120°C. Then, an Ar flow was injected for 70 s, before starting an Ar plasma during 3 min. Details of the process are presented below in the table in Fig. III. 5. Ar flow and Ar plasma steps were alternated 8 times, and the thickness variation was monitored using Spectroscopic Ellipsometry (SE). The test was repeated 3 times after some enhancement to decrease the leakage. The results are plotted in Fig. III. 5. The black curve, qualified as "old", corresponds to the configuration at the beginning of the thesis, where Ar was delivered through facilities lines supplying all the laboratory. The red curve, qualified as "New", corresponds to the installation of an Ar bottle dedicated (and close) to the reactor. And the curve labeled as "New enhanced" corresponds to the sealing enhancement of the new Ar line, by installing metal hard pipes instead of plastic tubes to reduce all leakage sources.

During the injection of the Ar flow, a thickness increase was observed with a deposition rate of about 2.8 Å.s^{-1} using the old configuration. Once the bottle was replaced, the deposition rate was reduced to 0.35 Å.s^{-1} only.

According to [13], it is clear that Ar cannot physisorb at the conditions used (temperature around -120°C and pressure below 10 Pa). So the thickness increase can only be explained by water physisorption due to the reactor leakage.

Hence, the observed thickness increase during the Ar flow in the curve "Old" shows that water was present in the facilities Ar lines and was adsorbing on the cooled SiO_2 surface. Then, once the plastic tubes connecting the Ar bottle to the reactor were replaced by metal hard pipes ("New enhanced" in Fig. III. 5), no thickness variation was observed anymore during the Ar injection. This confirms that the facilities Ar line installation was not sealed correctly. The thickness increase was due to water adsorption. Note that a large part of the water adsorbed layer was removed during the step of Ar plasma with a low bias (-20 V) without etching SiO_2.

-120 °C	***Time (s)***	***Flow (sccm)***	***Pressure (Pa)***	***P_{source} (W)***	***V_{bias} (V)***
Ar flow	70	100	3.0	0	0
Ar plasma	180	100	3.0	400	- 20

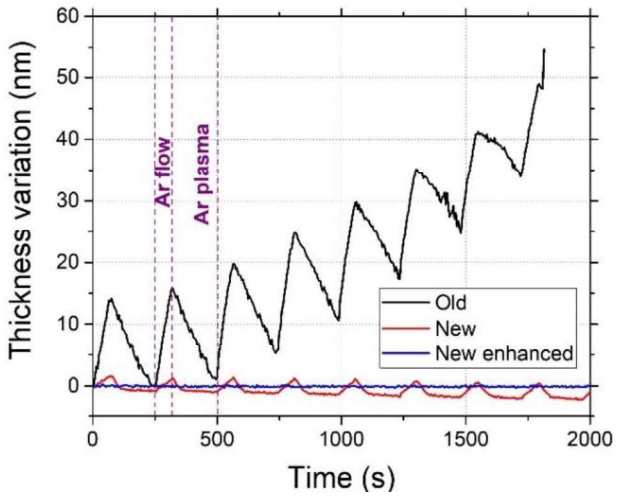

Fig. III. 5. Thickness variation on SiO_2 during ALE simulated processes with only Ar

This test shows the importance of the reactor leakage, which needs to be reduced and controlled, in order to minimize the effect of water physisorption in a cryo-ALE process.

I.6.ii. *Reactor leakage*

As explained above, the reactor leakage can be a determining factor during a cryogenic process. Indeed, due to the reactor leakage, water molecules get inside the reactor and may play a role during the cryo-ALE process if conditions are gathered to let it condensate.

In Fig. III. 6, the reactor leakage was measured in the "new enhanced" configuration. The throttle valve has been closed and then, the pressure has been measured every minute.

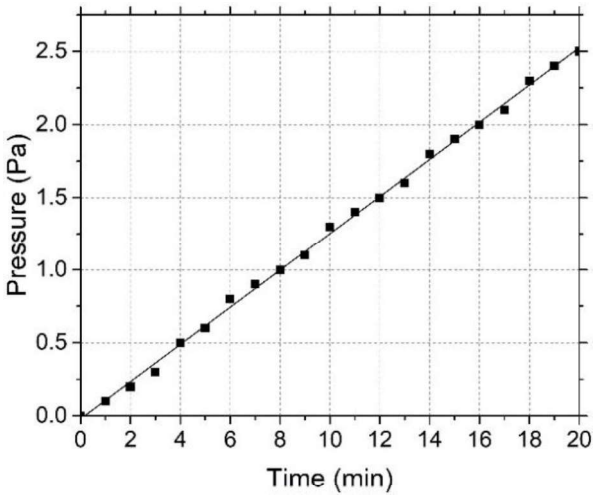

Fig. III. 6. Pressure increase through time for reactor leakage evaluation

The leakage is linear through time and an increase of 2.5 Pa was noticed after 20 min, which is equivalent to 0.125 Pa per minute.

Knowing that the reactor volume is 0.08 m^3, the leak rate in the reactor is 1.67×10^{-4} $Pa.m^3.s^{-1}$. Which means that the air flow (f_{Air}) constantly entering the reactor is equal to 0.10 sccm.

I.6.iii. *Estimation of water partial pressure*

In Fig. III. 7, the vapor pressure curves of C_4F_8 and water have been plotted versus temperature. The continuous part of the curves corresponds to the values from the literature [14], [15], and are showed in Table. III. 1. As those data cover a temperature range above -40°C, an extrapolation using the same values for Antoine's parameters has been performed for each molecule and plotted with squares.

The stripped area corresponds to the water partial pressure operating range during the cryo-ALE processes. The water partial pressure has been evaluated using the leak air flow calculated above. Considering 100 % of moisture, the flow of water is estimated at 2.0×10^{-3} sccm. Knowing that the pressure in the reactor chamber is about 5.0×10^{-4} Pa without any gas injection, it is possible to deduce that the water partial pressure in the reactor chamber is about 1.0×10^{-5} Pa, in just pumping conditions. However, when C_4F_8 is injected at 3.0 Pa with a gas flow of 14 sccm, the water partial pressure may increase to 4.0×10^{-4} Pa.

So, the curves plotted in Fig. III. 7 show that there is no water condensation above -110°C for process pressures between 5.0×10^{-4} Pa and 3.0 Pa. However, below this temperature, water starts to condense on the substrate surface, and may affect the process.

Table. III. 1. Antoine parameters used for C_4F_8 and H_2O, from [14], [15]

	C_4F_8	H_2O
A	4.248	4.6543
B	1007.399	1435.264
C	-30.205	-64.848

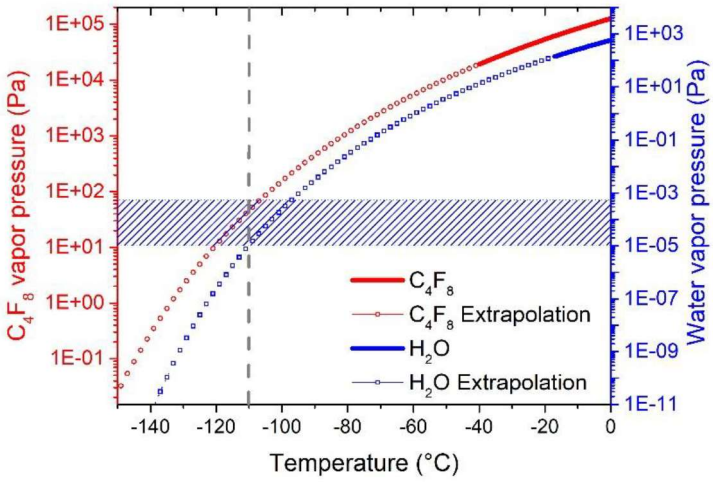

Fig. III. 7. C_4F_8 and H_2O vapor pressure curves [16]

I.6.iv. *Estimation of water deposition rate*

Following the same method, the water deposition rate was estimated when injecting 100 sccm of Ar flow at 3.4 Pa, as in the purge step of a cryo-ALE process. In this case, the partial pressure of water is estimated at 6.8×10^{-5} Pa. At 20°C, the water density can hence be estimated at 1.68×10^{16} m^{-3}, and the water flow density at 2.5×10^{18} $m^{-2}.s^{-1}$. From all those values, the water deposition rate was estimated to be around 0.74 $Å.s^{-1}$ for 100% of moisture and so equal to 0.37 $Å.s^{-1}$ for 50% of moisture. This is of the order of the measured deposition rate in section I.6.i.

I.7. C_4F_8 physisorption

As presented in chapter I, C_4F_8 plasmas are well-known to etch SiO_2. This is the first reason why this gas has been chosen as a test gas for the proof of principle of cryo-ALE.

The second reason is that C_4F_8 condensation conditions are easier to reach than for other etching gases such as SiF_4 or CHF_3 [15], [17].

The processes that will be presented later in this chapter have a temperature range between -120°C and -90°C, and a C_4F_8 pressure range between 1.0 Pa and 6.0 Pa. At those pressures and temperatures, although the conditions are close to the condensation curve, C_4F_8 is still in gas phase when adsorbing on the substrate surface (Fig. III. 7).

Nevertheless, more detailed studies were necessary to better understand C_4F_8 physisorption and its surface residence time, in the conditions used in our processes.

I.7.i. *Characterization of temperature influence on C_4F_8 physisorption using QMS and SE*

I.7.i.a. C_4F_8 mass spectrum

Before performing tests to characterize C_4F_8 physisorption, a mass spectrum of C_4F_8 has been first acquired in profile mode of Residual Gas Analysis (RGA) to identify the main species from the fragmentation of C_4F_8. To obtain Fig. III. 8, C_4F_8 was injected in the reactor at 1.0 Pa. Species were analyzed using an electron energy of 70 eV. The main fragmentation species are CF^+ (31 amu), CF_3^+ (69 amu), $C_2F_4^+$ (100 amu) and $C_3F_5^+$ (131 amu). This result is consistent with what is observed in literature [5], [6]. For the following tests, $C_2F_4^+$ was monitored in Multiple Ion Detection (MID) mode as it is the most intensive line from C_4F_8 fragmentation.

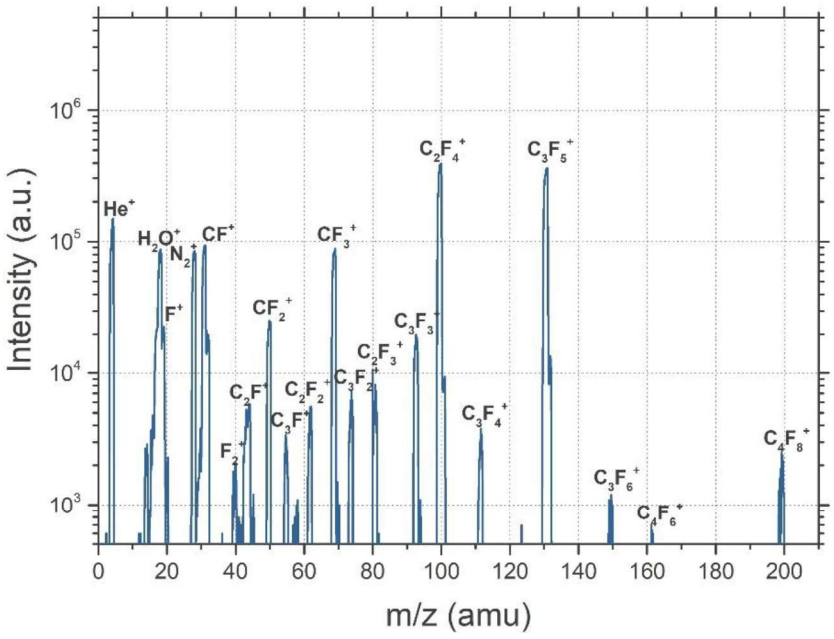

Fig. III. 8. C_4F_8 mass spectrum
(Experimental conditions: C_4F_8 flow: 14 sccm, 1 Pa
QMS 100 mm far from the center of the reactor, Electron energy : 70 eV)

I.7.i.b. C_4F_8 surface residence time

It is clear from Antoine's curve in Fig. III. 7 and from the expression of the surface residence time Eq. III. 4 that temperature has a real influence on the physisorption of C_4F_8 and its residence time. To evaluate this influence, a series of tests has been run. First a 100 nm thick SiO_2 on Si coupon has been glued at the center on a SiO_2 6" carrier wafer. The wafer was then loaded into the reactor and cooled. After that, C_4F_8 was injected at 3.0 Pa for one minute and then stopped. The signal of C_4F_8 in the reactor has been monitored by QMS. Acquisitions were

performed in MID in RGA mode, recording the $C_2F_4^+$ (100 amu) signal. At the same time, the thickness evolution of SiO_2 was monitored by in-situ SE in kinetic mode. The results are presented in Fig. III. 9.

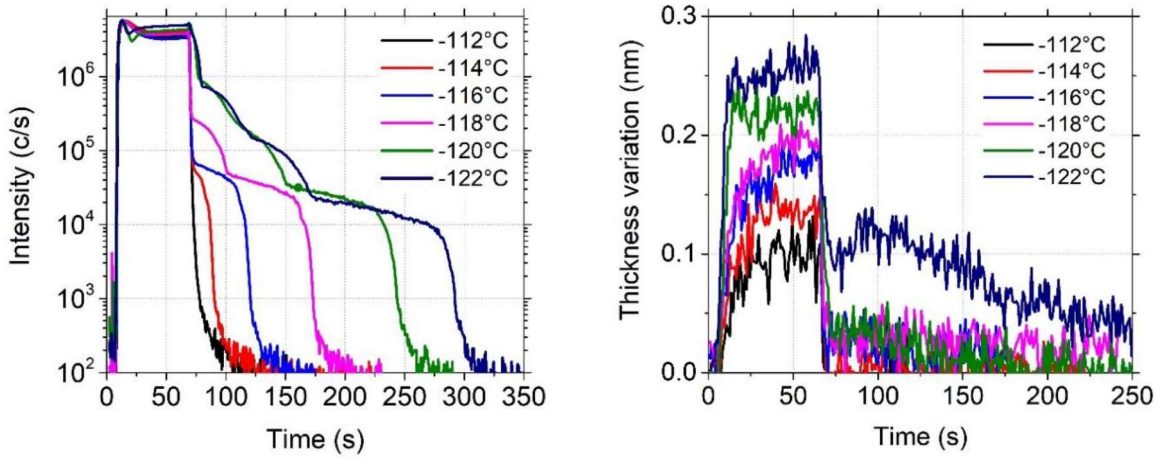

(a) (b)

Fig. III. 9. C_4F_8 physisorption on cooled surfaces depending on temperature, with (a) $C_2F_4^+$ signal monitored by QMS and (b) the thickness variation on SiO_2 monitored by SE (Experimental conditions: C_4F_8 flow: 14 sccm, 3 Pa, 1 min, followed by pumping) [16]

From -112°C to -122°C, when C_4F_8 is injected, the $C_2F_4^+$ signal first increases (Fig. III. 9. a) until reaching a plateau. This is due to the time that it takes to reach 3.0 Pa in the reactor. Then as the pressure and the injected C_4F_8 flow are stable, the $C_2F_4^+$ signal becomes stable as well. The same trend is observed in Fig. III. 9. b showing the thickness variation measured by SE. The layer thickness first increases due to the physisorption of the C_4F_8 molecules. However, when decreasing the temperature, the amount of physisorbed species increases and so does the thickness.

At -112°C, when the C_4F_8 flow is stopped, a sharp decrease of $C_2F_4^+$ signal is observed, as C_4F_8 is pumped from the reactor. This same drop appears for all temperatures. However, it becomes shorter when decreasing temperature as other slopes appear from surface desorption. On Fig. III. 9. b, the measured thickness increases a little bit and decreases when C_4F_8 flow is stopped.

When cooling the substrate to -114°C, a tail appears after the first drop. It corresponds to C_4F_8 molecules desorbing from the cooled surfaces.

When decreasing the sample to -118°C, another slope appears. The first one corresponds to the desorption of species from the wafer surface, whereas the second slope is due to the desorption of C_4F_8 from the chuck that is also cooled. This is confirmed with a complementary test performed in Fig. III. 10. In this test, the chuck was cooled to -120°C and its principle is almost the same as in Fig. III. 9. C_4F_8 is injected for 1 min and then stopped. QMS was used to follow $C_2F_4^+$ signal evolution and SE the thickness variation. In the first case (red curve), He was injected to ensure efficient backside cooling. Once the wafer temperature was stabilized

close to -120°C, C_4F_8 was injected. However, in the second case (black curve), He was not injected beneath the wafer and C_4F_8 was injected without waiting for the wafer to cool down. So here, the wafer temperature was close to room temperature when C_4F_8 was injected. In this later case, without He, only one tail was observed by QMS and no thickness increase has been measured by SE. Whereas the test with He presented the same trend as in Fig. III. 9, with two tails. The end of the second tail coincides with the end of the tail without He. In addition, it is shown by SE that the thickness increases when injecting the C_4F_8 for the wafer with He backside cooling. Then, once C_4F_8 was stopped, a small tail (defined by dash lines in Fig. III. 10. b) confirms that few seconds are needed before desorbing all the molecules from the surface. This time corresponds to the first tail observed by QMS (also indicated in dash lines in Fig. III. 10. a). In absence of He backside cooling, no physisorption is detected by SE. Thereby, it is possible to conclude that the first slope corresponds to species desorbing from the wafer surface and the second slope is from species desorbing from the chuck surface.
At -122°C, the curves obtained by QMS and SE are similar to the one obtained at -120°C, except that C_4F_8 molecules take few more seconds to desorb from the cooled surfaces, as it can be observed in Fig. III. 9. a.

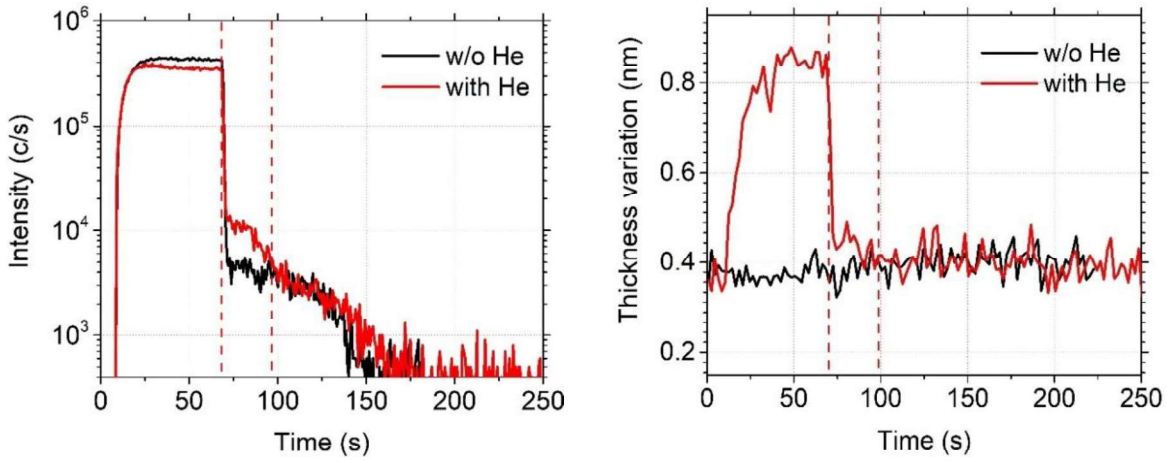

Fig. III. 10. C_4F_8 physisorption on SiO_2 depending on He injection for backside cooling, with (a) $C_2F_4^+$ signal monitored by QMS and (b) the thickness variation on SiO_2 monitored by SE (Experimental conditions: T= -120°C, C_4F_8 flow: 14 sccm, 3 Pa, 1 min, followed by pumping) [16]

From the curves in Fig. III. 11, focusing on the desorption part of the graphs already shown in Fig. III. 9, it was possible to measure the residence time of physisorbed C_4F_8 molecules on the cooled surfaces (SiO_2 and the chuck). First, the time was measured between the moment at which C_4F_8 injection was stopped and the end of the last drop. This time corresponds to the residence time and is noted t_d. The measured times with estimated errors are presented in Table. III. 2. A small error on the measured temperature also exists. Indeed, the temperature indicated in the graph is the set temperature that is reached on the chuck. However, a slight thermal resistance can be induced by the He film, inducing a slightly higher temperature of the

wafer. In the case of multilayer adsorption, since molecules from upper layers desorb faster than molecules directly physisorbed on the substrate surface, it was assumed that the existence of a second (or more) adsorbed layer is negligible as it would desorb much faster than the first layer in direct contact with the surface [6].

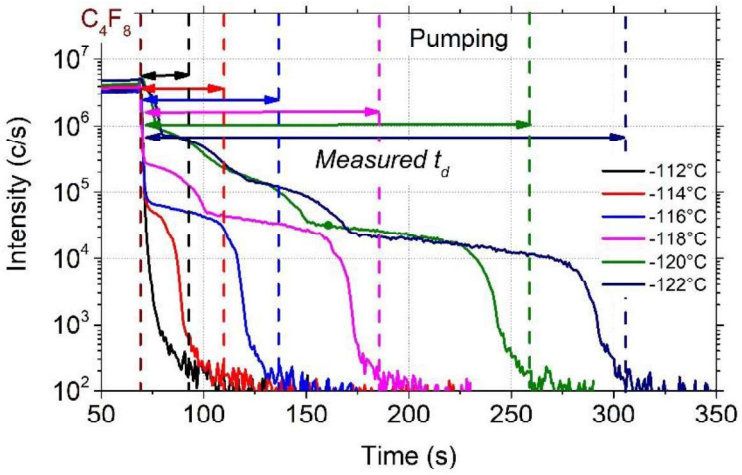

Fig. III. 11. Residence time measurement as a function of temperature on QMS signals from Fig. III. 9

Table. III. 2: Measured residence time and errors as a function of temperature

T (°C)	Measured t_d (s)	Error (s)
-112	38	±10
-114	49	±15
-116	72	±15
-118	120	±20
-120	192	±35
-122	239	±35

Then, relying on the Frenkel Arrhenius equation (Eq. III. 4) presented in section I.1 of this chapter, $\log(t_d)$ was plotted in Fig. III. 12 as a function of 1000/T in order to determine t_d^0 and E_d. To do so, a linear fit was applied to the measurements. Then, the intercept enabled to determine t_d^0 as 1x10^{-11} s. As the slope is equal to E_d/k_B, it enabled to calculate E_d which is 0.17 eV. Those results are consistent with the values given in [3] and [4]. Indeed, when the surface is covered by one monolayer or more, it is expected that t_d^0 gets above 1x10^{-10} s. Also, as it has been measured by SE, there is at least a coverage of one monolayer on the SiO_2 surface in our conditions.

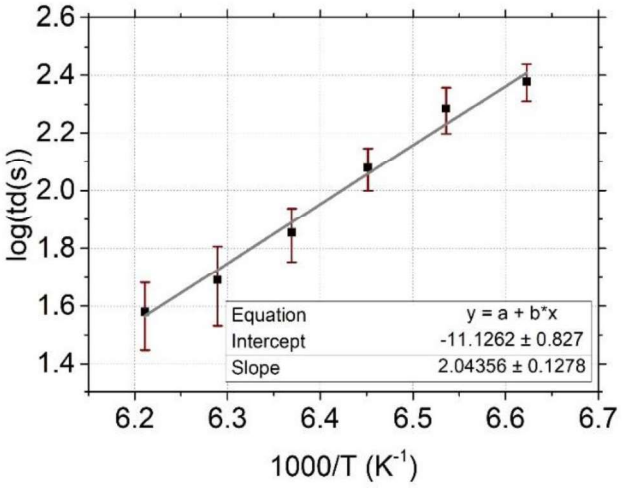

Fig. III. 12. Logarithm of the residence time of the adsorbed C_4F_8 molecules as a function of the inverse of the temperature [16]

I.7.ii. *Characterization of temperature influence on C_4F_8 physisorption using XPS*

C_4F_8 physisorption was also investigated by XPS measurements. Same tests have been performed as previously in Fig. III. 9, with the injection of C_4F_8 flow for one minute on a cooled SiO_2 substrate at different temperatures. C_4F_8 flow was 15 sccm and the pressure set point was 3.0 Pa. However, due to the adsorption of C_4F_8 species on the cold surfaces, the set point pressure was not reached at the lowest temperatures.

After the gas injection, the pressure in the chamber was close to 3.0 Pa, therefore, the sample was kept in the chamber several minutes, waiting for the pressure decrease until $6.0x10^{-4}$ Pa. This is necessary as the pressure must be the lowest possible in the XPS chamber during the measurements (ideally about $1.0x10^{-6}$ Pa). The sample was then transferred to the XPS chamber with the transfer rod and maintained at the process temperature. For each acquisition, a wide scan was performed followed by specific accurate scans for fluorine, oxygen, carbon and silicon components. Between each test, the sample was brought back to room temperature to ensure the desorption of all the adsorbed species from the surface before cooling it back for the next test.

I.7.ii.a. SiO_2 reference sample

Before starting the tests, a reference acquisition was performed on a raw SiO_2 coupon. The wide spectrum is presented in Fig. III. 13. Three expected components are identified. The peak at 103.4 eV corresponds to Si 2p when it is bonded with oxygen in a SiO_2 substrate. Hence in parallel, the peak at 532.6 eV is the oxygen peak O 1s corresponding to a bond with silicon to form SiO_2. The peak around 285 eV corresponds to C 1s when creating C-C or C-Si bonds, and is due to surface contamination. Fluorine peak can be expected around 687 eV, however no fluorine is detected on the raw sample [20].

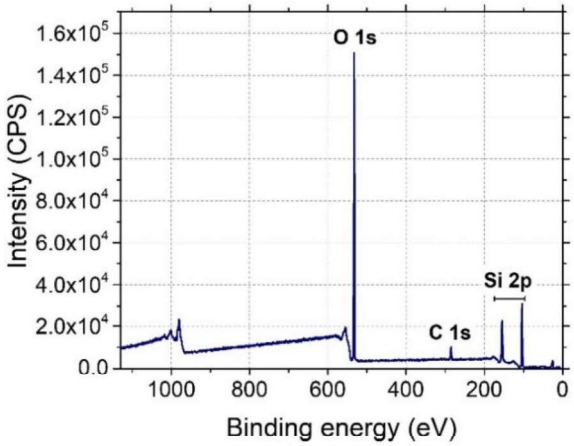

Fig. III. 13. SiO_2 XPS reference spectrum

I.7.ii.b. Adsorption of C_4F_8 at different temperatures

In order to check the influence of the substrate temperature on the physisorption of C_4F_8 on SiO_2, the sample was cooled at different temperatures (20°C, -90°C, -110°C and -120°C) and then exposed to C_4F_8 atmosphere for 1 min at a pressure between 1.5 Pa and 2.6 Pa. This difference in the pressure at same throttle valve opening and C_4F_8 flow is due to C_4F_8 adsorbing more at low temperature and consequently, decreasing the pressure in the chamber. The sample is then transferred to the XPS chamber while keeping it at low temperature. Fig. III. 14 shows the XPS spectra results for the different temperatures. In Fig. III. 14. a, the wide spectrum of the sample shows one main change, which is the appearance of fluorine peaks when the temperature is decreased.
Each component has then been investigated separately. Fig. III. 14. b shows the peaks for Si 2p. Only one peak at 103.4 eV is observed, corresponding to Si-O bonds from SiO_2. The intensity of the peak at 25°C is slightly higher than for the other peaks. This is due to the substrate coverage by the C_4F_8 adsorbed layer, hiding the substrate, at lower temperatures. Same behavior is observed in Fig. III. 14 for O 1s. Only one peak is observed at 532.6 eV for Si-O bonds. For the C 1s component in Fig. III. 14. c, a peak at around 285.0 eV is observed for all the temperatures, corresponding to C-C bonds and due to surface contamination. However, when decreasing the temperature, a second peak clearly appears around 286.5 eV that can be attributed to C-CF_x bonds [20]–[23]. Also, starting from -110°C and below, peaks at around 291.8 eV and 293.7 eV can be detected.

In Fig. III. 14. e, F 1s peaks are presented depending on the temperature. No fluorine peak was identified when injecting C_4F_8 at 25°C, meaning no adsorption at this temperature. When decreasing temperature, a first peak is observed at around 688.9 eV that keeps increasing when decreasing the temperature. This peak is related to the carbon peak at 291.8 eV and corresponds to C-F_2 like bonds [21]. Below -110°C, a second peak can be identified around 685.6 eV, that can be attributed to F-OH bonds.

To sum up, in-situ XPS measurements confirmed the observations made by QMS and SE. They enabled to show that the physisorption of fluorine-based species is enhanced with the temperature decrease. The physisorbed molecules are CF_2 like, and do not create any bonds with Si substrate since no new Si peak appears.

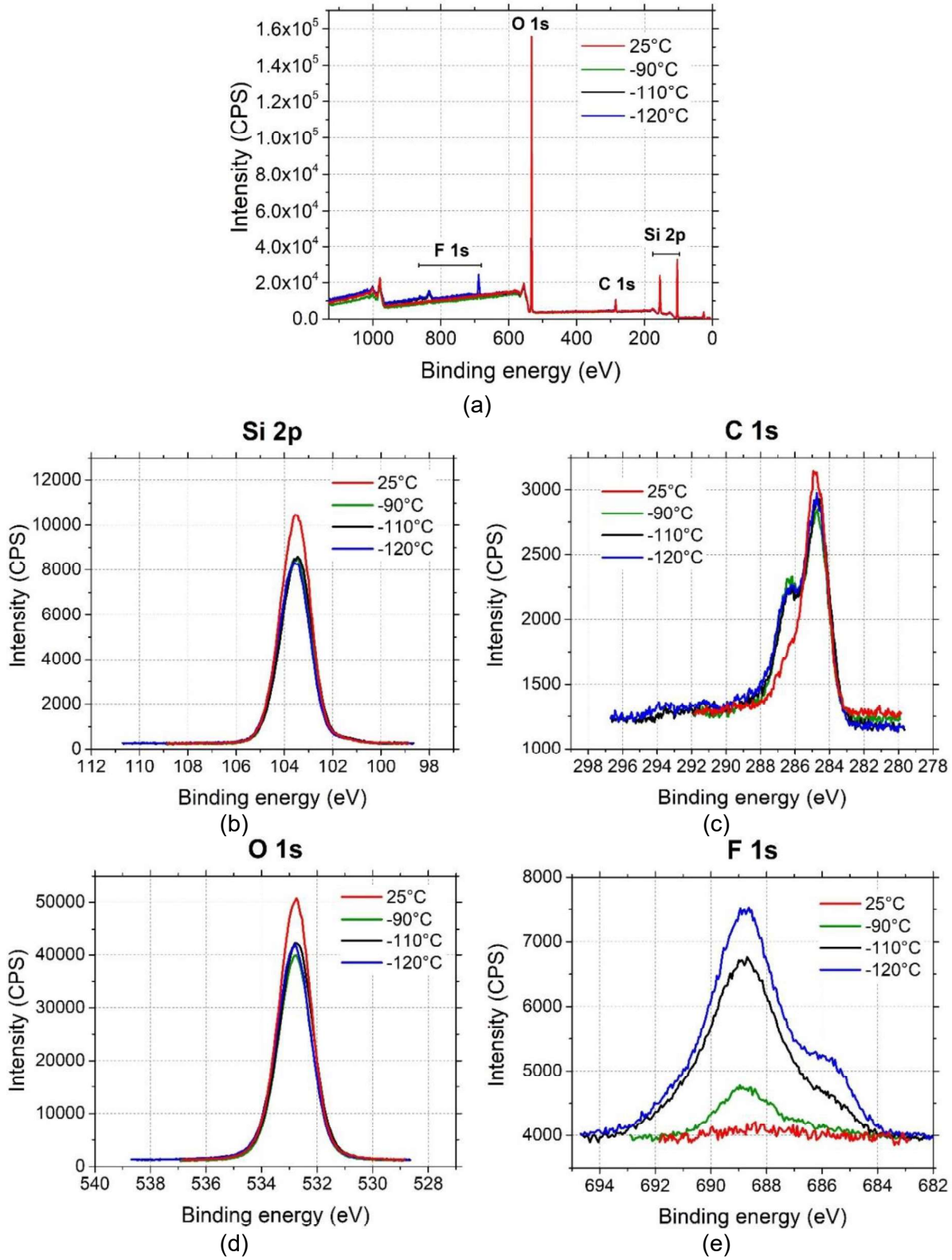

Fig. III. 14. XPS spectra of SiO_2 after exposure to 1 min of C_4F_8 flow at different temperatures, with (a) the wide scan of the sample, (b) the detail for Si 2p, (c) the detail for C 1s, (d) the detail for O 1s and (e) the detail for F 1s

I.7.iii. *Influence of C_4F_8 pressure on its physisorption*

I.7.iii.a. QMS measurements

The influence of the pressure has also been investigated. Same tests have been performed as those presented in section I.7.i.b of this chapter. However, temperature was kept constant at -120°C and pressure was varied from 1.0 Pa to 3.0 Pa. Fig. III. 15 shows behaviors versus pressure similar to those observed versus temperature in Fig. III. 9. The $C_2F_4^+$ signal first increases until reaching the set point pressure. Then, once C_4F_8 is stopped, a first drop appears followed by one to several slopes due to desorption from the cooled surfaces. When the pressure is increased, the amount of physisorbed species measured by SE is also increased. The reason is different from that at low temperature where the residence time was increased inducing a higher adsorbed amount. Indeed, the residence time does not depend on the pressure. Therefore, the increase of the adsorbed amount is rather attributed to the higher quantity of C_4F_8 in the chamber at higher pressure.

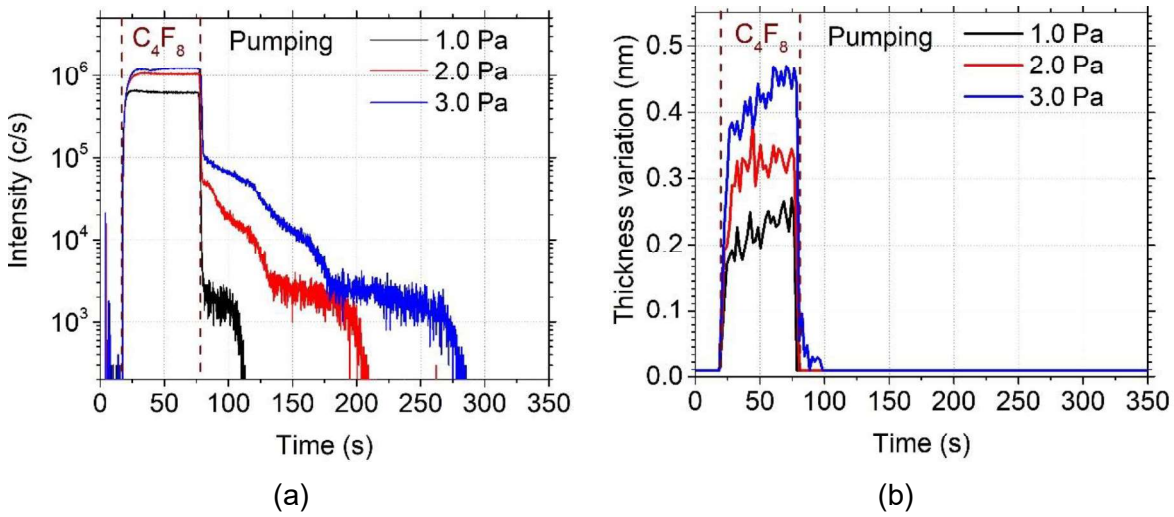

Fig. III. 15. C_4F_8 physisorption on cooled surfaces at different pressures and monitored with (a) (a) $C_2F_4^+$ signal monitored by QMS and (b) the thickness variation on SiO_2 monitored by SE (Experimental conditions: T= -120°C, C_4F_8 flow: 14 sccm, 1 min, followed by pumping) [16]

In Fig. III. 16, the adsorbed amount was evaluated from SE measurements and plotted as a function of the C_4F_8 pressure normalized to the C_4F_8 vapor pressure at each temperature. The same trend is observed at the three temperatures with the increase of the adsorbed amount when the pressure is increased. Relying on the isotherms presented in Fig. III. 4, the obtained isotherms of Fig. III. 16 can be identified as isotherms of type II. Indeed, SiO_2 is a nonporous material and the shapes of the curves obtained are similar to that of isotherms of type II at low relative pressure. As it is hard to identify a knee as B in graph II from Fig. III. 4, it means that the monolayer and multilayer adsorptions overlap. Hence, it will be complicated to identify the

exact pressure for which the monolayer coverage is reached. Consequently, it can be expected that C parameter from BET model will be lower than 50 [10].

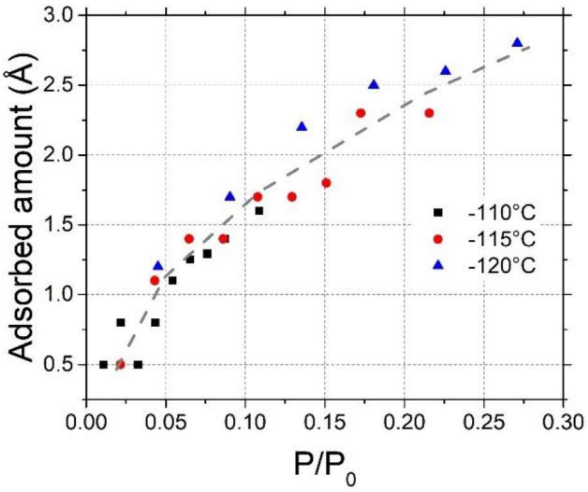

Fig. III. 16. C_4F_8 adsorbed amount as a function of the normalized pressure

I.7.iii.b. BET calculations

Following the data presented in Fig. III. 16, parameters of the BET model were calculated and plotted for -110°C, -115°C and -120°C conditions. BET calculations are valid only if x values are between 0.05 and 0.30. Experiments enable to know x by calculating P / P_0, and v is the thickness increase measured by SE. Thus, *C* and v_m can be calculated using Eq. III. 6 [9]. Indeed, from the plot $\frac{x}{v(1-x)}$ vs x, the intercept corresponds to $\frac{1}{v_m C}$ and the slope to $\frac{C-1}{v_m C}$. The points are plotted in Fig. III. 17, and a linear fit is applied to obtain the intercept and the slope needed to calculate *C* and v_m.

The slope of the curves of the three temperatures tested is almost equal. The difference is only a slight shift of the curve depending on x.

C values are close to 20, and are consistent with the typical values given in literature as there is no clear knee to identify in the data presented in Fig. III. 16. This confirms that there is an overlap between the full monolayer coverage and multilayer physisorption.

$E_{desorb.1} - E_{desorb.i}$, noted as ΔE was calculated, using the Eq. III. 7 and the obtained C values. The results are presented in Fig. III. 17. ΔE is about 0.04 eV for the three studied temperatures, which is in the order of ΔE values in literature [9]. This means that the desorption energy of the first layer is not so high in comparison with the desorption energy of layer i.

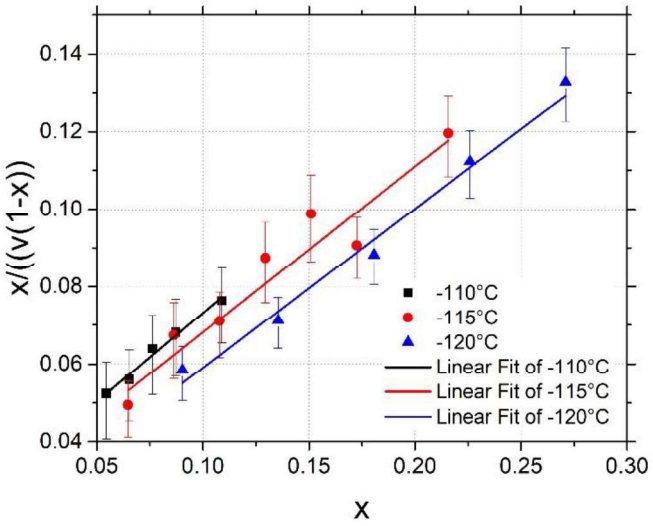

	-110°C	-115°C	-120°C
Intercept	0.027	0.025	0.018
Slope	0.457	0.428	0.411
υ_m **(Å)**	2.06	2.21	2.33
C	17.65	17.85	23.94
***ΔE* (eV)**	0.040	0.039	0.042

Fig. III. 17. BET coefficient calculations for three different temperatures

II. Introduction to cryo-ALE

II.1. Process sequence

The generic process sequence of cryo-ALE, based on the principle depicted at the beginning of the chapter (Fig. III. 1), is presented in Fig. III. 18 below. It is a sequential and cyclic process.

The first step of a cycle is the injection of C_4F_8 gas flow for 5 to 20 s ("Physisorption" in Fig. III. 18). The second step is the pumping of the chamber or the injection of Ar in gas phase to purge the chamber and remove all the C_4F_8 surplus ("purge" in Fig. III. 18). The step duration may vary between 3 to 30 s. The third step is the ignition of the Ar plasma with some bias (between 0 and -20 V) in order to start the etching ("etching" in Fig. III. 18). The fourth and last step of the cycle is a 15 s long pumping step to remove all the etched by-products ("pumping" in Fig. III. 18). Those four steps are then repeated several times and monitored in kinetic mode by SE and by QMS if necessary.

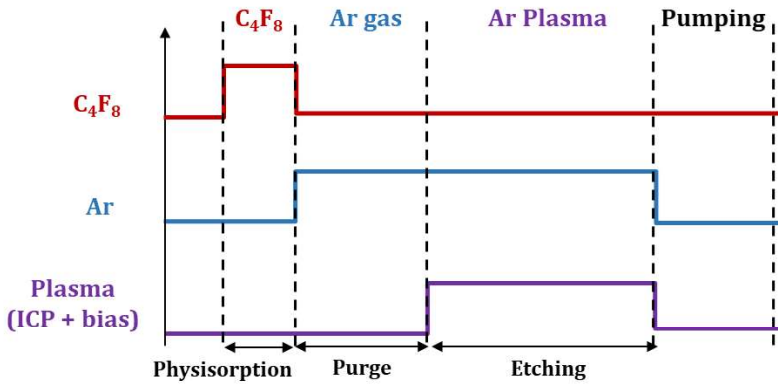

Fig. III. 18. Generic process sequence of a typical cryo-ALE cycle

II.2. Proof of principle

An experiment was performed at two different temperatures to show the feasibility of this new ALE method. The process parameters for each of the steps presented in Fig. III. 18, as well as the obtained SE curves, are presented in Fig. III. 19.

The process under investigation has been performed during 8 cycles on SiO_2 at -110°C and at -120°C, and monitored by in-situ SE.

At -110°C, a very small increase of the thickness is noticed during the injection of C_4F_8. However, it decreases almost immediately, during the purge step and the thickness appears almost constant during the whole process. During the Ar plasma, no etching is observed. This means that:

- first, no more C_4F_8 was present on the surface when the Ar plasma was initiated to enable the etching,
- second, the ion energy during the process is below the sputtering threshold of SiO_2.

When decreasing the temperature to -120°C, around 8.5 nm of SiO_2 was etched after 8 cycles. The SE signal is accurate enough. All the different steps of a cycle are clearly identified. Indeed, when looking at the inset in Fig. III. 19. a, it is possible to distinguish an increase of the thickness during the injection of C_4F_8. Then, the thickness drops a little and is stabilized during the purge step, meaning that only a part of C_4F_8 desorbs, as the thickness is still higher than before C_4F_8 injection. Finally, during the Ar plasma, the thickness keeps decreasing as SiO_2 is etched. However, SLE is not reached.

Fig. III. 19. a highlights the existence of a temperature threshold for sufficient surface residence time and physisorption of C_4F_8 to enable the etching. Indeed, the lack of etching in the curve at -110°C, indicates that, C_4F_8 was removed from the surface and from the reactor chamber during the purge step. This behavior is consistent with QMS measurements presented in Fig. III. 11 and Table. III. 2 of this chapter. The measured t_d for the curve at -

112°C was estimated to about 38 ± 10 s for 1 min of C_4F_8 injection at 3.0 Pa, whereas t_d increased to 193 ± 35 s at -120°C.

Fig. III. 19. b presents the Etch amount Per Cycle (EPC) for the test at -120°C. After the first cycle, 0.6 nm was etched, and the etched amount kept increasing along the cycles until reaching 1.4 nm during the last cycle. This means that, as SLE is not reached from the first cycles, a certain amount of species taking part to the etching is still on the substrate surface at the end of the cycle. This induces a drift in the EPC.

-110 °C / -120 °C	Time (s)	Flow (sccm)	Pressure (Pa)	P_{source} (W)	V_{bias} (V)
1. Physisorption: C_4F_8	20	14	3.0	0	0
2. Purge: Ar	30	100	0.5	0	0
3. Etch Plasma: Ar	120	28	3.4	400	- 20
4. Pumping	15	0	0.5	0	0

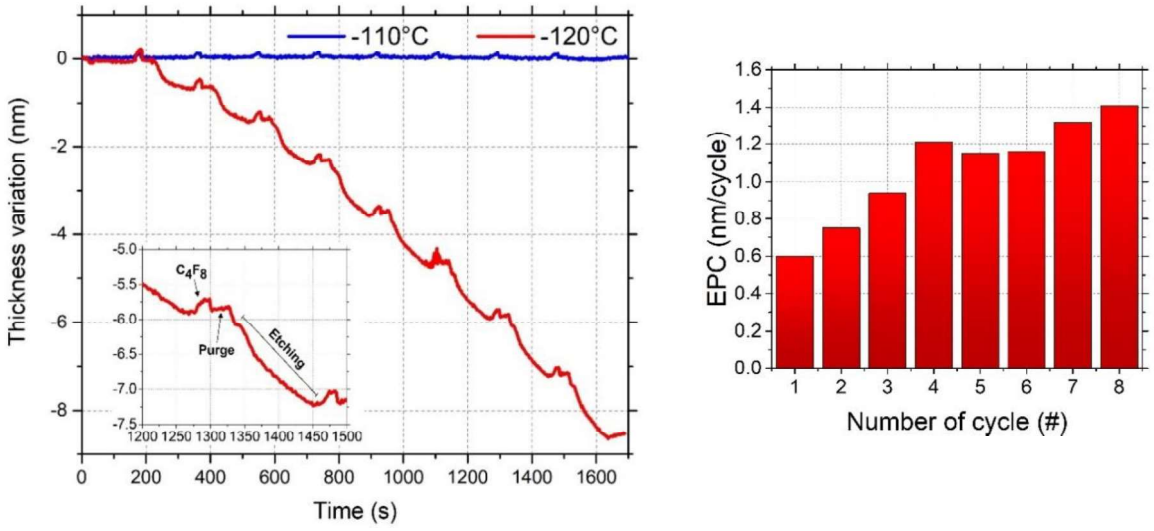

(a) (b)

Fig. III. 19. (a) SiO_2 thickness variation versus time for 8 cryo-ALE cycles performed at -110°C and -120°C with an inset on cycle #7, (b) Etch Per Cycle for the process -120°C

Therefore, this test proves the possibility of removing few monolayers of SiO_2 by cooling the substrate to -120°C in order to enhance the physisorption of C_4F_8. However, the process still needs to be improved to reach SLE and to enlarge the process window.

Along the thesis, tests were performed to understand the influence of each parameter on each step. Tests were all performed on SiO_2 substrates cooled at -120°C, and the thickness variation was followed by in-situ SE.

III. Understanding of process parameters

III.1. Physisorption step

III.1.i. *Effect of step duration*

In plasma ALE of SiO_2, C_4F_8 plasma pulses typically last 1.5 s [24]. Indeed, the step duration has to be very short to control the amount of fluorocarbon in the chamber and enable the possibility of reaching the SLE during the etching step.

The duration of the C_4F_8 gas injection step was investigated. 8 cycles of cryo-ALE were performed on SiO_2 at -120°C, for a C_4F_8 gas injection of 10 s and 20 s. The thickness variation was measured by in-situ SE in kinetic mode. The result is presented in Fig. III. 20.

-120 °C	*Time (s)*	*Flow (sccm)*	*Pressure (Pa)*	P_{source} *(W)*	V_{bias} *(V)*
1. Physisorption: C_4F_8	**10** / **20**	14	1.9	0	0
2. Purge: Ar	30	100	3.4	0	0
3. Etch Plasma: Ar	60	28	3.4	400	- 20
4. Pumping	15	0	0.0	0	0

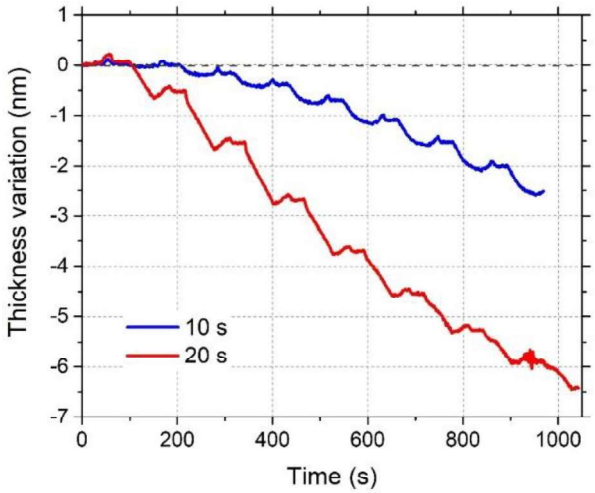

Fig. III. 20. SiO_2 thickness variation versus time for 8 cryo-ALE cycles on SiO_2 performed at -120°C for two different C_4F_8 injection step duration (10 s and 20 s)

In both cases, it is possible to distinguish each step and each cycle, as in the inset of Fig. III. 19. a. In addition, the thickness decreases from one cycle to the other. However, less etching was observed on the curve for 10 s of C_4F_8 gas injection than for 20 s. This means that increasing the step duration of C_4F_8 injection, increases the EPC. Indeed, if C_4F_8 is injected during 10 s only, around 2.5 nm of SiO_2 is etched within 8 cycles, whereas around 6.5 nm of SiO_2 is etched if C_4F_8 is injected for 20 s. This, first, shows that a self-limited state is not reached if the adsorption lasts 10 s, otherwise the EPC would not have changed.

Consequently, increasing the step duration, increased the amount of C_4F_8 brought and physisorbed on the surface. So, once the Ar plasma is ignited, the higher amount of C_4F_8 helps the etch rate to increase.

Looking closer at the curve, corresponding to the 10 s C_4F_8 step, no etching occurs during the first cycle. However, the EPC starts increasing, until reaching a steady state after about 4 cycles, and the SLE is almost achieved. In the case of the 20 s C_4F_8 step, the etching starts from the first cycle. However, the etching seems more difficult to control and the SLE is not achieved. Consequently, if all the physisorbed C_4F_8 is not consumed during a cycle, drifts may appear as in this type of process, which is not desired.

Therefore, for the rest of this section, C_4F_8 step duration was fixed to 10 s.

III.1.ii. *Influence of pressure*

As presented in I.7.iii, the amount of C_4F_8 physisorbed on the surface can be controlled by the pressure during C_4F_8 injection. To better understand the pressure influence and determine the optimal amount to physisorb, 8 cryo-ALE cycles were performed on SiO_2 at four different pressures for C_4F_8 injection (from 0.9 to 2.2 Pa). The thickness variation during each process was monitored by SE, and presented in Fig. III. 21. a as a function of time.

-120 °C	***Time (s)***	***Flow (sccm)***	***Pressure (Pa)***	***P_{source} (W)***	***V_{bias} (V)***
1. Physisorption: C_4F_8	10	14	varied	0	0
2. Purge: Ar	10	100	3.4	0	0
3. Etch Plasma: Ar	60	28	3.4	400	- 20
4. Pumping	15	0	0.0	0	0

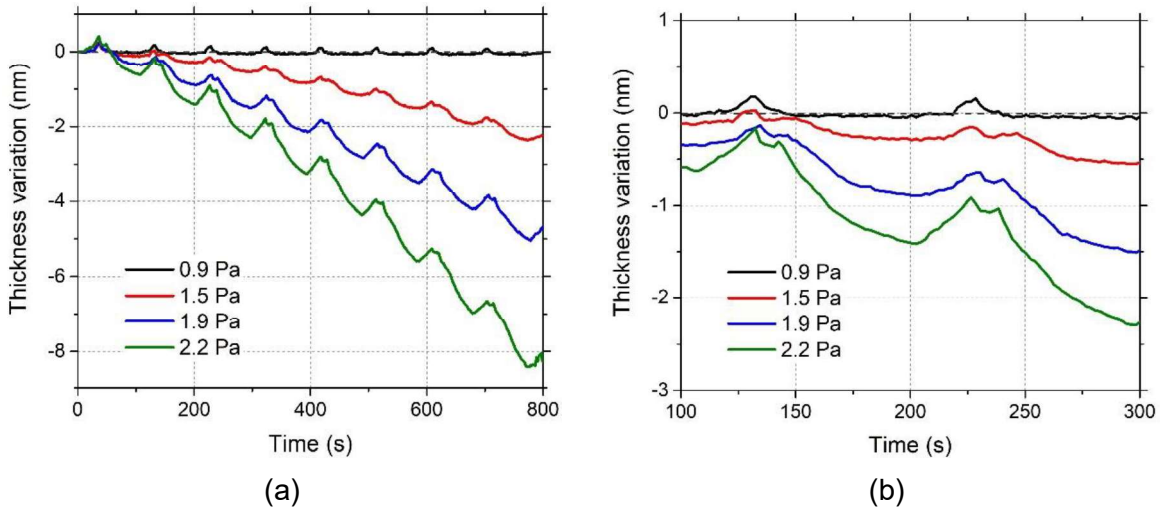

Fig. III. 21. SiO_2 thickness variation versus time for 8 cryo-ALE cycles on SiO_2. (a) Influence of C_4F_8 pressure, (b) an inset on 2nd and 3rd cycles

In the applied conditions, no etching was observed for a C_4F_8 injection at 0.9 Pa. The thickness variation behavior is similar to the one observed at -110°C in Fig. III. 19. a. When looking closer at the inset, even if a thickness increase is first observed, during the 10 s purge, everything desorbs and consequently, no etching is observed at this pressure.
For the three other tested pressures, the adsorbed amount increased with C_4F_8 injection pressure increase as well as the EPC. As presented in the previous section III.1.i, this reveals the absence of saturation behavior for physisorption.

For the rest of the experiments, a pressure of 1.9 Pa was generally applied. At this pressure, it is possible to physisorb a sufficient amount of C_4F_8 on the surface, which will etch SiO_2 and enable to achieve SLE.

III.2. Purge step after physisorption

As described in the principle of cryo-ALE in the beginning of this chapter, the main characteristic and difference between standard plasma ALE and cryo-ALE is the first step, where the reactive gas is physisorbed on a cooled surface instead of being deposited in a plasma phase. Consequently, as presented in the previous section III, the etching amount is directly related to the physisorbed amount of C_4F_8 and its surface residence time. The contribution of the Ar purge step right after, to help the evacuation of C_4F_8 molecules in the chamber, and the importance of controlling it for the process will be investigated in this section.

III.2.i. *Influence of purge step duration*

The step duration is the most critical parameter of the purge step right after the C_4F_8 injection. To check its influence, two purge step durations were tested, 10 s and 30 s during 8 cycles of cryo-ALE on SiO_2. Fig. III. 22 below illustrates its influence by following the thickness variation through cycles by in-situ SE in kinetic mode. When the purge step lasts 30 s, 2.5 nm were etched in 8 cycles, and a plateau can be observed at the end of each Ar plasma meaning that SLE is achieved. Thus, the etching can be considered as controlled and all the physisorbed C_4F_8 is depleted.
However, in the case of the 10 s long purge, the etched thickness is higher, 5 nm in 8 cycles, but no SLE was observed.

-120 °C	Time (s)	Flow (sccm)	Pressure (Pa)	P_{source} (W)	V_{bias} (V)
1. Physisorption: C_4F_8	10	14	1.9	0	0
2. Purge: Ar	**10** / **30**	100	3.4	0	0
3. Etch Plasma: Ar	60	28	3.4	400	- 20
4. Pumping	15	0	0.0	0	0

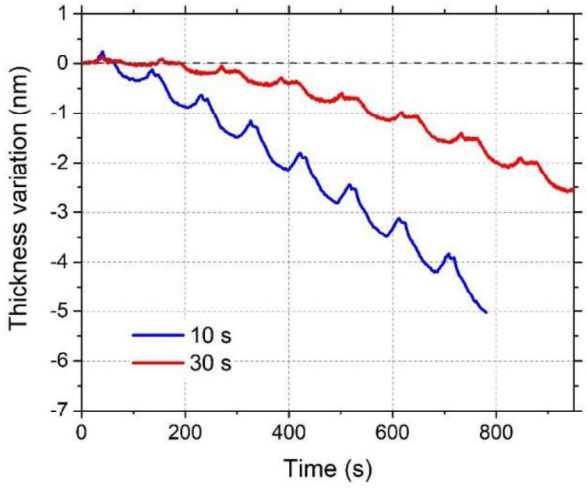

Fig. III. 22. SiO_2 thickness variation versus time for 8 cryo-ALE cycles on SiO_2 - Influence of the purge step duration (10 s and 30 s)

In Fig. III. 23 same test was performed as in Fig. III. 15 but at 27°C. In this test, C_4F_8 was also injected during 1 min but at 27°C. At this temperature and pressures tested, physisorption of C_4F_8 is not possible. Thus, the sharp decrease of $C_2F_4^+$ signal after the C_4F_8 flow was stopped in Fig. III. 23, shows that C_4F_8 molecules are pumped in about 6 s from the reactor chamber. And Fig. III. 11 has showed that physisorbed C_4F_8 desorbs from the surface through time. This means, that when the Ar purge step is increased to 30 s, a higher amount of C_4F_8 will desorb from the cooled surface than after only 10 s of purge. In other words, the difference in the EPC by only changing the purge step time is due to a higher amount of C_4F_8 molecules available after 10 s of purge than 30 s.

To sum up, if the purge step time is too long, meaning longer than the surface residence time of C_4F_8, the latter will desorb from the surface and no etching will be achieved.

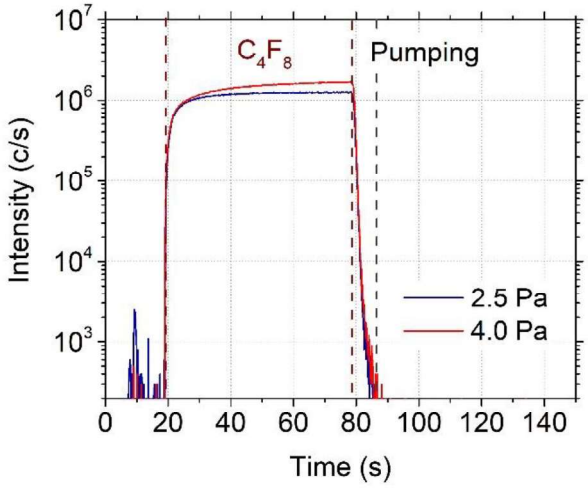

Fig. III. 23. C_4F_8 residence time in the chamber at monitored by QMS by following the $C_2F_4^+$ signal (Experimental conditions: T= 27°C, C_4F_8 flow: 14 sccm, 1 min, followed by pumping)

Conversely, if the purge step duration is not long enough, deposition will occur instead of etching, as presented in Fig. III. 24.

-120 °C	***Time (s)***	***Flow (sccm)***	***Pressure (Pa)***	***P_{source} (W)***	***V_{bias} (V)***
1. Physisorption: *C_4F_8*	15	14	2.6	0	0
2. Purge: *Ar*	**15**	100	3.4	0	0
3. Etch Plasma: *Ar*	60	28	3.4	400	- 20
4. Pumping	15	0	0.0	0	0

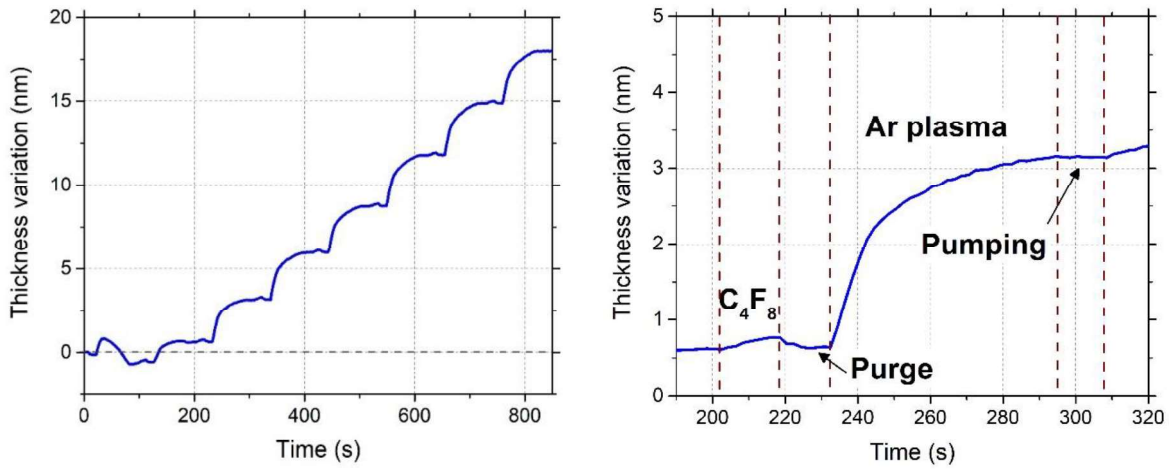

Fig. III. 24. SiO_2 thickness variation versus time - Deposition behavior in the case of a 15 s long purge step, (a) 8 cryo-ALE cycles on SiO_2, (b) zoom on cycle #3

The step duration of C_4F_8 was increased to 15 s instead of 10 s, and the pressure was tested at 2.6 Pa instead of 1.9 Pa as in Fig. III. 22. However, the Ar purge step was decreased to 15 s. During the first cycle in Fig. III. 24. a, some small etching can be observed. However, no etching occurs during the subsequent cycles, but instead of it, deposition takes place. As all

those cycles are similar, a zoom on cycle #3 was added (Fig. III. 24. b) to observe the thickness behavior. During the C_4F_8 injection, a small thickness increase is observed. However, the thickness significantly increases during the Ar plasma. This means that some C_4F_8 remained in the reactor chamber after the Ar purge, and when the Ar plasma was ignited. This created CF_x species, inducing deposition on the substrate and all over the reactor walls.

III.2.ii. *Effect of the Ar purge pressure*

In this paragraph, the influence of pressure during the purge step is investigated. Two different purge pressures were tested, 0.5 Pa and 3.4 Pa, during 8 cycles of cryo-ALE. The thickness variation versus time of those tests is plotted in Fig. III. 25. In both cases, during a cycle, the thickness increased during C_4F_8 injection due to physisorption, and then decreased during the Ar plasma due to the layer etching. At 0.5 Pa, the throttle valve is almost totally open, increasing the efficiency of the pumping. Therefore, as observed in Fig. III. 25, the etched amount goes from 5 nm to 2 nm when decreasing the pressure from 3.4 Pa to 0.5 Pa.

-120 °C	***Time (s)***	***Flow (sccm)***	***Pressure (Pa)***	***P_{source} (W)***	***V_{bias} (V)***
1. Physisorption: *C_4F_8*	10	14	1.9	0	0
2. Purge: *Ar*	10	100	**0.5** / **3.4**	0	0
3. Etch Plasma: *Ar*	60	28	3.4	400	- 20
4. Pumping	15	0	0.0	0	0

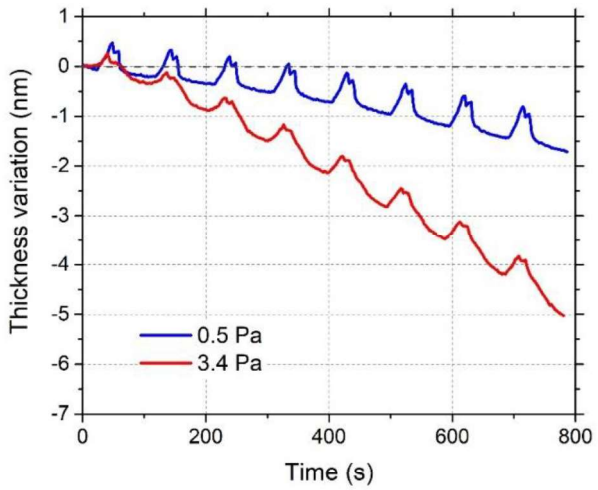

Fig. III. 25. SiO_2 thickness variation versus time for 8 cryo-ALE cycles on SiO_2 - Influence of the pressure during the purge step

III.2.iii. *Influence of Ar purge flow*

The Ar flow during the purge was also investigated. Its influence was tested for two different Ar flows, 28 sccm and 100 sccm during 8 cryo-ALE cycles on SiO_2. The thickness variation during the process versus time is plotted and presented in Fig. III. 26. In both cases, the process is in an etching regime, and steps in each cycle can be identified. The purge is more efficient when increasing the Ar flow. Indeed, the total thickness etched decreased from 6.0 nm to 2.5 nm, when the flow was increased from 28 sccm to 100 sccm. If only 28 sccm is used, more C_4F_8 remains on the SiO_2 surface, contributing to etch about 1 nm per cycle, which is more than 2 SiO_2 monolayer thick. If 100 sccm is used for the purge, the etching takes few cycles to start, and the EPC at the end of the process is about 0.5 nm, which is of the order of one monolayer of SiO_2. In this case, SLE is reached at each cycle, and the process is better controlled.

To perform this test, due to software and hardware issues, the flow of Ar for the plasma step had also to be changed. However, this should not affect the etching.

-120 °C	***Time (s)***	***Flow (sccm)***	***Pressure (Pa)***	***P_{source} (W)***	***V_{bias} (V)***
1. Physisorption: *C_4F_8*	10	14	1.9	0	0
2. Purge: *Ar*	30	**28 / 100**	3.4	0	0
3. Etch Plasma: *Ar*	60	**100 / 28**	3.4	400	- 20
4. Pumping	15	0	0.0	0	0

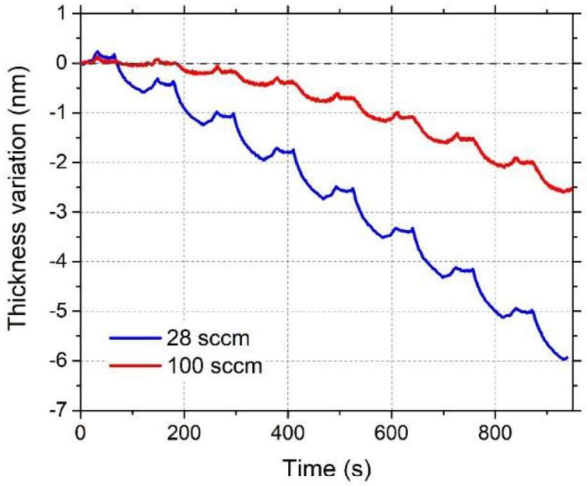

Fig. III. 26. SiO_2 thickness variation versus time for 8 cryo-ALE cycles on SiO_2 - Influence of Ar flow during the purge step on the purge efficiency

III.3. Etching step parameters understanding

III.3.i. *Plasma characterization by Langmuir probe*

For the etching step, an Ar plasma has always been used. Langmuir probe measurements have been performed to characterize it. In Fig. III. 27, the plasma potential (V_p) and the ion density (N_i) were measured at the center of the reactor diffusion chamber during an Ar plasma at 3.0 Pa, and plotted versus the source power.

By increasing the source power, V_p slightly increases, whereas the ion density is tripled between 300 and 600 W. In our processes, the applied source power was always about 400 W. At this power, V_p is about 10 V, which allows staying below the sputtering threshold by ion bombardment of SiO_2 even with an applied bias of -20 V. The ion density at this power is about $4.9x10^{10}$ cm^{-3}.

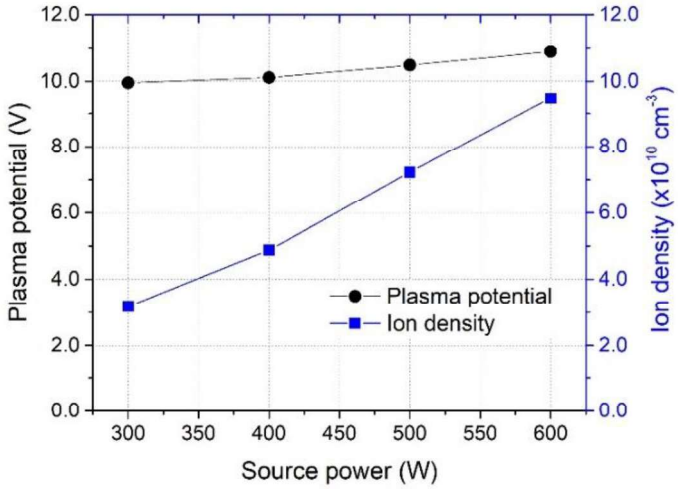

Fig. III. 27. Plasma potential and ion density measurements versus the source power of an Ar plasma at 3 Pa performed by Langmuir probe at the center of the diffusion chamber

III.3.ii. *Effect of the applied source power*

The effect of the applied source power on etching was investigated during cryo-ALE processes and presented below in Fig. III. 28. At 300 W, only 1.0 nm in 8 cycles is etched whereas 2.5 nm are etched at 400 W. As shown in Fig. III. 27, the ion density at 400 W is 1.5 time higher than at 300 W. At the surface, C_4F_8 is consequently better dissociated providing more CF_2 species that are needed for the etching [25]. In the three cases, a plateau can be noticed, which is characteristic of achieving SLE. However, at 600 W, the high ion density ($9.5x10^{10}$ cm^{-3} according to Fig. III. 27) could be responsible of C_4F_8 molecules desorption from the surface, which will inhibit the etching. Hence, in conclusion, 400 W appears to be an optimal source power for etching.

-120 °C	Time (s)	Flow (sccm)	Pressure (Pa)	P_{source} (W)	V_{bias} (V)
1. Physisorption: C_4F_8	10	14	1.9	0	0
2. Purge: Ar	30	100	3.4	0	0
3. Etch Plasma: Ar	60	28	3.4	**300** / **400** / **600**	- 20
4. Pumping	15	0	0.0	0	0

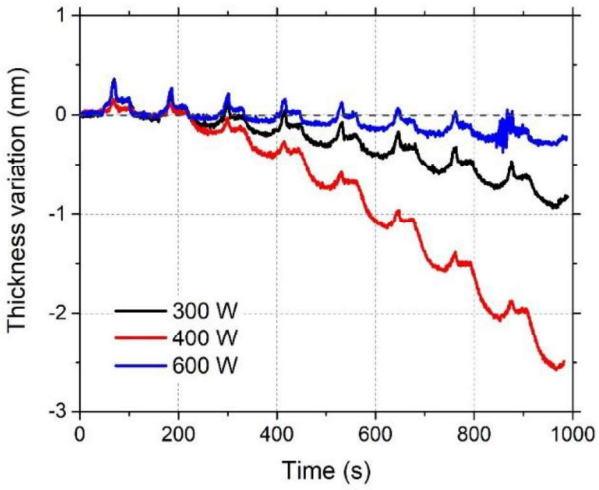

Fig. III. 28. SiO_2 thickness variation versus time for 8 cryo-ALE cycles on SiO_2 - Influence of plasma source power of the etching plasma

III.3.iii. *Effect of the applied bias*

As explained in Chapter I, the bias is a critical parameter in an etching process since it enables anisotropic etching. However, in the case of ALE, it has to be accurately controlled and limited to prevent sputtering. Therefore, three different biases were tested during 8 cycles of cryo-ALE. The thickness variation versus time was plotted for each process and presented in Fig. III. 29. Without any bias, even though an increase of the thickness is observed during C_4F_8 physisorption, no etching occurs at all during the Ar plasma. This means that there is not enough energy provided by the ions to start the etching.

Then at -10 V and -20 V, respectively ~ 0.9 nm and 2.5 nm were etched in 8 cycles. Both of those curves present a plateau at the end of the Ar plasma at each step, showing the etch stop. Two explanations can be given to interpret the difference in the total amount etched in both conditions with -10 V and -20 V of bias. The first one is that, the ion energy is still too low and the etching is not complete at -10 V bias. The second possibility is that some removal by sputtering is occurring when -20 V bias is applied.

-120 °C	Time (s)	Flow (sccm)	Pressure (Pa)	P_{source} (W)	V_{bias} (V)
1. Physisorption: C_4F_8	10	14	1.9	0	0
2. Purge: Ar	30	100	3.4	0	0
3. Etch Plasma: Ar	60	28	3.4	400	**0** / **-10** / **-20**
4. Pumping	15	0	0.0	0	0

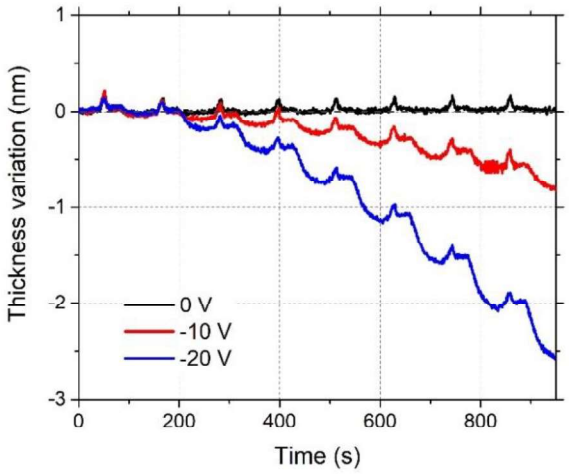

Fig. III. 29. SiO_2 thickness variation versus time for 8 cryo-ALE cycles on SiO_2 - Effect of the bias voltage during the etching plasma

Hence, to check this second possibility, a dedicated cryo-ALE process was suggested where C_4F_8 was replaced by Ar.

-120 °C	Time (s)	Flow (sccm)	Pressure (Pa)	P_{source} (W)	V_{bias} (V)
1. Physisorption: Ar	30	28	3.3	0	0
2. Etch Plasma: Ar	180	100	3.1	400	-20
3. Pumping	15	0	0.0	0	0

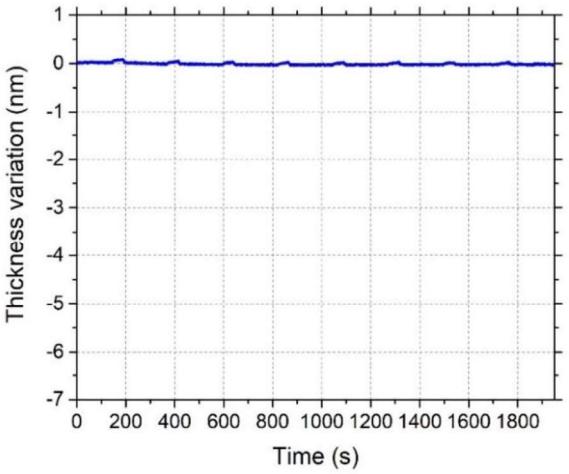

Fig. III. 30. SiO_2 thickness variation versus time for 8 cryo-ALE cycles on SiO_2 with Ar replacing C_4F_8 in the physisorption step

Consequently, as no fluorine was injected, chemical etching was not expected, which means that if any etching was observed, it would have been attributed to sputtering by Ar^+. Fig. III. 30 above presents the result of this test. A small thickness increase is observed during the injection of Ar in gas phase. This is mainly due to some remaining water contamination in the line. However, this physisorbed layer is removed shortly after the plasma is started. No etching is observed after, even after 3 min of Ar plasma.

This result suggests that, at -10 V, the process is in incomplete removal regime, which corresponds to the rising edge of the energy scan presented in Fig. I. 20 of Chapter I. However, at -20 V, the process is in the ALE Window as the etching is in the order of 0.5 nm, so about one monolayer of SiO_2.

III.3.iv. *Step time dependency*

In this paragraph, the Ar plasma step time has been increased from 60 s to 120 s. The results of the thickness variation versus time during 8 cycles of cryo-ALE are presented in Fig. III. 31. a.

-120 °C	***Time (s)***	***Flow (sccm)***	***Pressure (Pa)***	***P_{source} (W)***	***V_{bias} (V)***
1. Physisorption: *C_4F_8*	10	14	1.9	0	0
2. Purge: *Ar*	10	100	3.4	0	0
3. Etch Plasma: *Ar*	**60** / **120**	28	3.4	400	- 20
4. Pumping	15	0	0.0	0	0

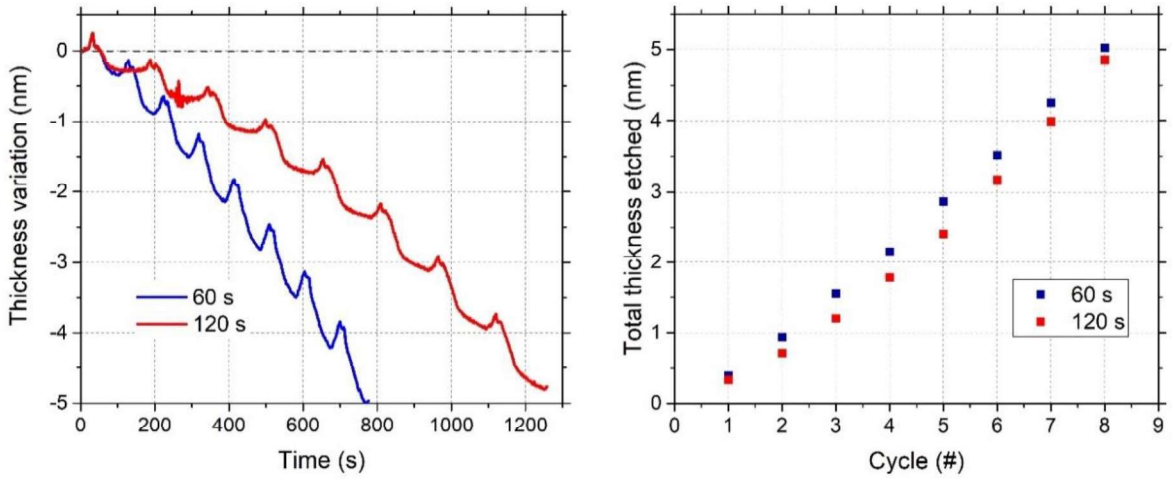

(a) (b)

Fig. III. 31. (a) SiO_2 thickness variation versus time for 8 cryo-ALE cycles on SiO_2 - Influence of Ar plasma step time duration, (b) cumulative etched thickness along cycles

When 60 s of Ar plasma is applied, etching takes place all along the plasma without reaching the SLE. But, if the plasma is extended for up to 120 s, the characteristic plateau of SLE is reached. However, at the end of the 8 cycles, the same amount was etched, which is around 5.0 nm. In Fig. III. 31. b, the etched thickness in each cycle was measured in order to add it to the thickness etched in the previous cycles. Thus, in this figure, the etched thickness accumulated along the cycles is plotted for both conditions: 60 s and 120 s. This graph shows the same etching evolution and same amount etched in both cases. This means that extending the Ar plasma to 120 s enables to check the self-limiting behavior. However, 60 s of Ar plasma is sufficient to deplete all C_4F_8.

III.4. Influence of the pressure in the pumping step after etching

A pumping step after the Ar plasma step can be very important for repeatability and linearity of the process. Indeed, it aims to remove all the etching by-products from the reactor before starting a new cycle. To ensure a repeatable etching from a cycle to another, the substrate surface as well as the chamber walls have to remain the same from a cycle to another. Also, as processes are performed at low temperature, not only C_4F_8 surface residence time is increased, but also the surface residence time of the etching by-products. Therefore, to ensure the desorption and pumping of all the etching products, 15 s of pumping is performed at the end of each ALE cycle.

-120 °C	***Time (s)***	***Flow (sccm)***	***Pressure (Pa)***	***P_{source} (W)***	***V_{bias} (V)***
1. Physisorption: *C_4F_8*	10	14	1.9	0	0
2. Purge: *Ar*	10	100	0.5	0	0
3. Etch Plasma: *Ar*	60	28	3.4	400	- 20
4. Pumping	15	0	**0.0** / **0.5**	0	0

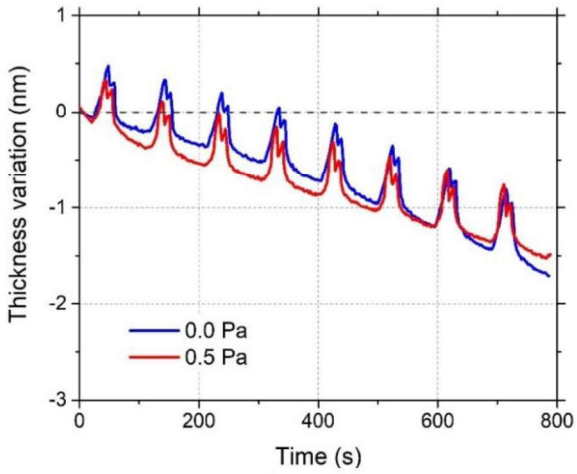

Fig. III. 32. SiO_2 thickness variation versus time for 8 cryo-ALE cycles on SiO_2 - Pumping step influence on the etching cycles

The efficiency of the pumping step has been tested depending on the throttle valve opening. Two opening positions were tested during 8 cryo-ALE cycles on SiO_2. Fig. III. 32 shows the thickness variation obtained versus time for both positions. In the first case, the throttle valve was almost totally opened, greatly reducing the pressure, whereas the red curve is at controlled opening throttle valve, making the pressure decrease in 15 s until reaching 0.5 Pa. The pumping is hence supposed to be more efficient in the first case.
However, when looking at Fig. III. 32 it is possible to conclude that the influence of the different pumping pressures is low. Indeed, as all the other parameters are the same, and so as the EPC is also similar, it is possible to conclude that the opening position of the throttle valve during pumping has no effect on the process.

IV. Self-limiting etching

Once all the process parameters were optimized, very clear self-limiting etching was investigated and obtained, as observed in Fig. III. 33.
The black curve corresponds to the thickness variation of SiO_2 monitored by SE. As usual, an increase of the thickness is observed during C_4F_8 injection (see Fig. III. 33. b). During the purge step, the thickness decreases, but stays higher than before C_4F_8 injection, meaning that some C_4F_8 desorbs from the surface, but one other part remains. Once the Ar plasma is ignited, the thickness starts decreasing and reaches a plateau after few seconds of plasma. This plateau corresponds to the so-called SLE. An Ar plasma time of 2 min was suggested to reach the plateau and prove that no etching occurred during the plasma.
At the same time, the process was monitored by QMS in order to monitor the etched by-products, and in particular, to detect SiF_4 molecules with the SiF_3^+ signal during the etching. Indeed, in our conditions, SiF_3^+ is the main fragmentation ion of SiF_4 [26], that is one of the main etching products of SiO_2. However, this peak at 85 amu, is close to that of $C_4F_2^+$ (86 amu) which is a fragmentation ion of C_4F_8 [19]. Therefore, in Fig. III. 33, $C_4F_2^+$ signal was also plotted. For this ion, and as expected, it is possible to observe a peak during C_4F_8 injection. Once C_4F_8 is stopped, the signal sharply decreases. In the case of SiF_3^+, the signal intensity is lower than for $C_2F_4^+$ and two peaks at 85 amu are observed in a cycle. The first peak perfectly coincides with $C_2F_4^+$ and hence is attributed to the tail of the 86 amu line, indicating that there is a small deviation in the calibration of the QMS, due to the small mass difference between the two ions. The second peak starts with the ignition of the Ar plasma, then the signal decreases along the plasma. This behavior correlates with the SE signal and confirms that SiO_2 is chemically etched and that the etch stops once C_4F_8 is depleted, even if the Ar plasma is maintained.
However, when looking at the trend of SiF_3^+ signal along cycles, and more specifically the first cycles, it can be noticed, that the second peak related to the etching is not observed during

the first cycle, and that the signal intensity increases along cycles. By comparing it with SE signal, we can also notice that almost no etching is achieved in this first cycle, and that the removed thickness increases through cycles. So, again, both QMS and SE are correlated. Hence this test shows that in-situ monitoring of the etching can also be done by QMS, and not only by SE. Also, when looking closer at the first cycles, it may be noticed that etching takes time before reaching a constant EPC. This can be due to a time delay before removing some surface contamination (as carbon) [23]. Or it can also be due to the formation of the mixing layer SiOCF needed for the etching. So during the first cycles, the process is in transient state, where the EPC increases from a cycle to another, before it reaches a steady state and a constant EPC [27], [28].

-120 °C	***Time (s)***	***Flow (sccm)***	***Pressure (Pa)***	***P_{source} (W)***	***V_{bias} (V)***
1. Physisorption: *C_4F_8*	10	14	1.9	0	0
2. Purge: *Ar*	30	28	3.4	0	0
3. Etch Plasma: *Ar*	120	100	3.4	400	- 20
4. Pumping	15	0	0.0	0	0

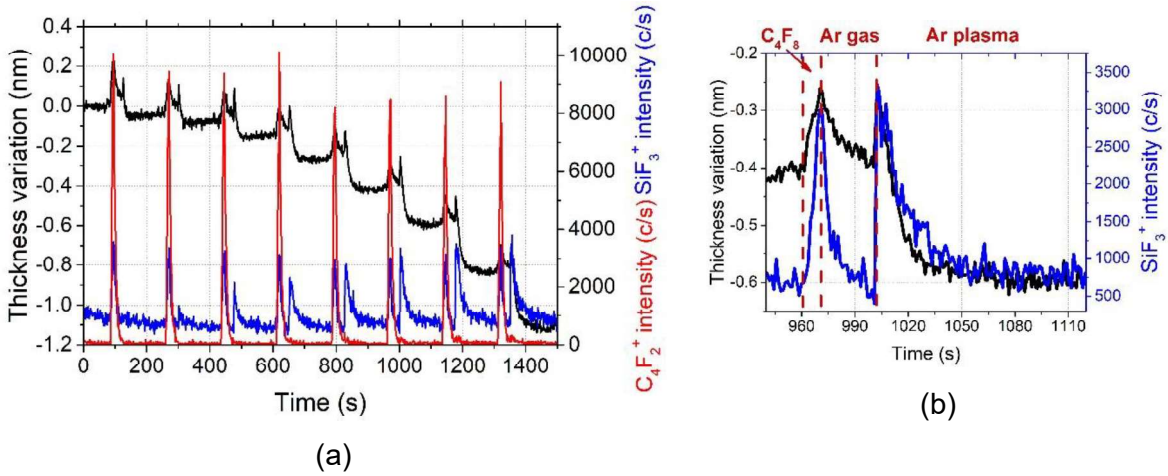

Fig. III. 33. (a) SiO_2 thickness variation, $C_4F_2^+$ ion peak intensity, SiF_3^+ ion peak intensity versus time for 8 cycles of the optimized cryo-ALE process with SLE behavior monitored by SE and QMS, (b) zoom on cycle #6 [16]

V. Long cycle processes and process enhancement

One of the main issues encountered in plasma ALE is process drift that is observed after few cycles due to the reactor wall contamination by fluorine and carbon deposition on the chamber walls from the precursor [29]. Indeed, as the precursor is formed in plasma phase, deposition occurs not only on the wafer, but also on the reactor walls. Hence, after few cycles, fluorine and CF_x will accumulate on reactor walls. Consequently, processes that have presented SLE behavior on the first cycles, lose this trend and the EPC gets higher along the cycles. The main advantage of Cryo-ALE based on C_4F_8 physisorption, is that the amount of precursors is better controlled and placed directly on the surface of interest where it sticks. Therefore, it is expected that using optimized processes, where the physisorption is controlled to reach SLE, should limit the contaminations.
Long processes, with several cycles, were performed and are presented in this section in order to check the repeatability through cycles and the absence of drifts in cryo-ALE.
Also, etching uniformity and selectivity of SiO_2 over Si_3N_4 and a-Si are discussed in this section.

V.1. Long process at -120°C

In this paragraph, 70 cycles of cryo-ALE were performed on SiO_2 at -120°C. In comparison to the parameters presented in the previous section, several data have changed. In this process, the pressure is higher than for the already presented processes. The purge is shorter, but stays efficient as the pressure decreases sharply. One minute of Argon plasma is considered sufficient to deplete all C_4F_8, as for a longer plasma, a plateau will be observed, characteristic of SLE. Even though no sputtering occurs on SiO_2 even when applying -20 V of bias, it was set at -10 V, to prevent sputtering of other materials such as a-Si and Si_3N_4, the samples of which may also be placed on the carrier wafer.
The curve in Fig. III. 34 presents the thickness variation measured by in-situ SE of a SiO_2 coupon glued on the center of a 6" SiO_2 carrier wafer. The etching is very linear along cycles, which shows that the etching has not suffered from any drift. That means that the reactor wall contamination is significantly reduced, and low enough to prevent any increase of the etch rate, by using this type of process. Moreover, it shows that fluorine and CF_x amounts in the reactor were controlled and depleted all along the process.
On the same wafer, an a-Si coupon and a Si_3N_4 coupon were also glued in order to investigate the selectivity of SiO_2 etching. SE ex-situ measurements have shown nearly no selectivity between the three materials. Indeed, the etched amount was between 25 and 28 nm for all materials (~ 0.38 nm per cycle, close to a SiO_2 monolayer).

Firstly, it is reported that, to achieve selectivity of SiO_2 over Si or Si_3N_4 using C_4F_8 plasma, low ion energy is needed as the energy sputtering threshold of Si and Si_3N_4 is close to 20 eV, whereas it is about 50 eV for SiO_2 [30], [31]. Secondly, C_4F_8 plasma may etch more SiO_2 as carbon will consume the oxygen and silicon will react with fluorine.

In cryo-ALE, where C_4F_8 molecules are only physisorbed at the surface, the bonds with the surface are quite weak as compared to the bonds made by chemisorption, and the layer may be thinner. Consequently, it is not possible to build a thick enough layer on Si and Si_3N_4 to prevent their etching and hence, to enhance the etching selectivity of SiO_2 [28], [30]. Thus, the etching is the same for the three materials.

-120 °C	***Time (s)***	***Flow (sccm)***	***Pressure (Pa)***	***P_{source} (W)***	***V_{bias} (V)***
1. Physisorption: *C_4F_8*	10	14	2.7	0	0
2. Purge: *Ar*	10	100	0.5	0	0
3. Etch Plasma: *Ar*	60	28	3.4	400	- 10
4. Pumping	15	0	0.0	0	0

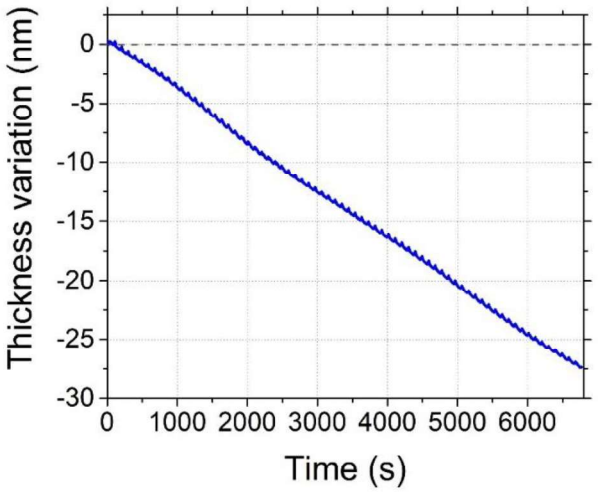

Fig. III. 34. SiO_2 thickness variation versus time for 70 cryo-ALE cycles on SiO_2 - performed at -120°C, adapted from [1]

The surface roughness evolution was also investigated by AFM for the three materials, and results are summarized in Table. III. 3 below. It was reported in [27] that ALE helps keeping the surface smooth and even sometimes makes it smoother. However, in our case, the surfaces, were slightly rougher than before etching for the three materials. Indeed, the arithmetic mean roughness (R_a) increases of about 1.0 nm for a-Si and Si_3N_4 and 0.7 nm on SiO_2. Several explanations are possible. The modified layer may have been not completely removed, creating roughness. As C_4F_8 adsorption depends on its surface residence time, some molecules may have desorbed from the surface and hence may have created non-uniform physisorbed layer at the surface when the etching started. Or also, the weak bonds of C_4F_8

with the surface, may make them be removed quickly during the plasma. Finally, the ion energy may have been still too high for a-Si and Si_3N_4 inducing some undesired sputter etching.

Table. III. 3 AFM measurements before and after 70 cycles of cryo-ALE at -120°C, with image size corresponding to 500 nm (process from Fig. III. 34)

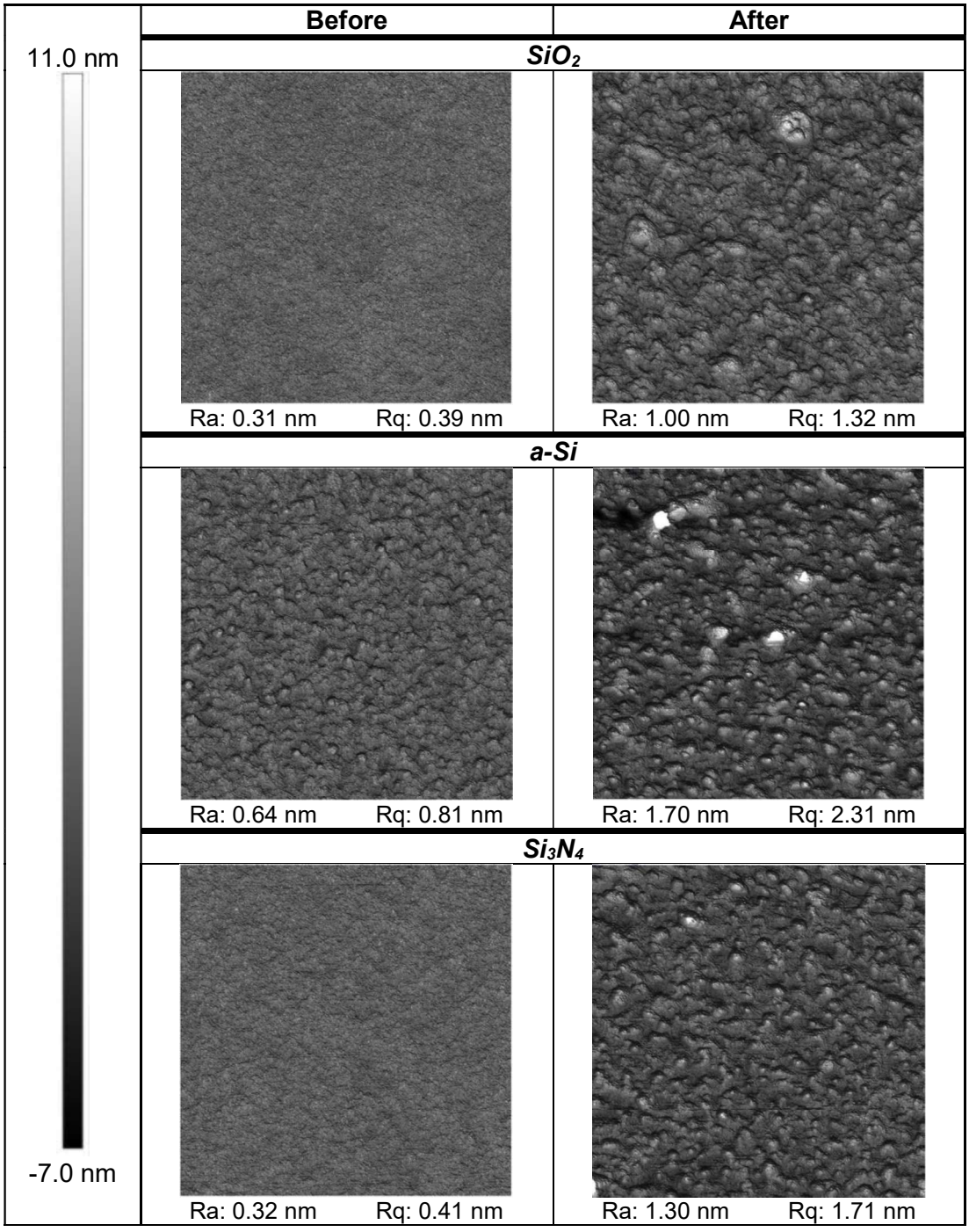

Despite those results, as very linear etching has been performed on SiO_2 with a roughness increase of less than 1 nm, it has been decided to improve the process by increasing the temperature window.

V.2. Long process at -90°C

Experiments presented in section I.6.iv of this chapter have demonstrated that increasing the pressure, even though it did not increase the surface residence time of C_4F_8, enabled to physisorb more molecules and hence keep them longer on the surface.

This is also proved in Fig. III. 35 below. The "C_4F_8 physisorption test" was conducted as in Fig. III. 9, where C_4F_8 was injected for 1 min on a cooled surface and then stopped. At the same time, $C_2F_4^+$ signal was followed by QMS. The test was conducted at -90°C at 3.0 Pa and 6.5 Pa to confirm the effect of the pressure. The curve at -112°C at 3.0 Pa, is the same as in Fig. III. 9 and is added for comparison to check the effect of temperature. The curves show that at -90°C, when C_4F_8 is injected at 3.0 Pa, the C_4F_8 molecules are almost instantly pumped from the reactor. However, if the pressure is increased to 6.5 Pa, same behavior is observed as if the injection was at lower temperature and pressure (-112°C, 3.0 Pa). Few additional seconds are consequently needed before all C_4F_8 is depleted from the cooled substrate surface and from the reactor. This means that, at higher temperature, the pressure needs to be higher as well to keep sufficient amount of C_4F_8 physisorbed at the surface.

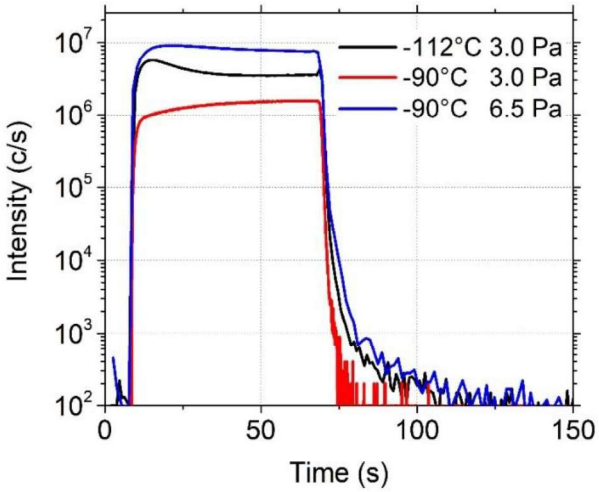

Fig. III. 35. C_4F_8 physisorption on SiO_2 at different pressures and temperatures, monitored by QMS by following the $C_2F_4^+$ signal versus time
(Experimental conditions: T= -90°C / -112°C, C_4F_8 flow: 14 sccm, 1 min, followed by pumping) [16]

Based on these new data, new cryo-ALE tests were performed, but in this case, at -90°C instead of the usual -120°C. The thickness variation versus time, monitored by SE, for those tests are presented in Fig. III. 36. To enable the etching, process parameters were modified. As a pressure about 6.0 Pa had to be reached, and the mass flow controller could not reach a flow higher than 14 sccm, the C_4F_8 injection step time was increased to 20 s. As noticed in Fig. III. 35, the surface residence time of C_4F_8 being short, the Ar purge step has to be shortened, hence the time was first set to for 4 s. The Ar flow during the pumping was increased

to 280 sccm, and the throttle valve was totally opened, in order to evacuate quickly non-physisorbed C_4F_8 from the chamber.

However, as observed in Fig. III. 36, even though an increase of the thickness was observed during C_4F_8 injection, 4 s of purge seemed too long as very little etching was achieved (0.5 nm in 8 cycles).

This is why, a second test was performed, decreasing the purge step to 3 s. In this case, 2.5 nm were etched in 8 cycles without reaching SLE yet. Moreover, the etching was very linear.

So, to check if the etching occurs indeed using C_4F_8 physisorbed on the surface, same test with a purge of 3 s long has been performed at 20°C. In the latter case, almost no etching was observed. This means, that C_4F_8 contributing to the etching at -90°C, is provided by the physisorbed molecules and not from un-pumped and residual molecules in the chamber, and therefore the purge step is efficient.

20°C / -90 °C / -90 °C	***Time (s)***	***Flow (sccm)***	***Pressure (Pa)***	***P_{source} (W)***	***V_{bias} (V)***
1. Physisorption: *C_4F_8*	20	14	6.1	0	0
2. Purge: *Ar*	**3 / 3 / 4**	280	**2.8 / 2.8 / 1.2**	0	0
3. Etch Plasma: *Ar*	60	28	3.4	400	- 15
4. Pumping	15	0	0.0	0	0

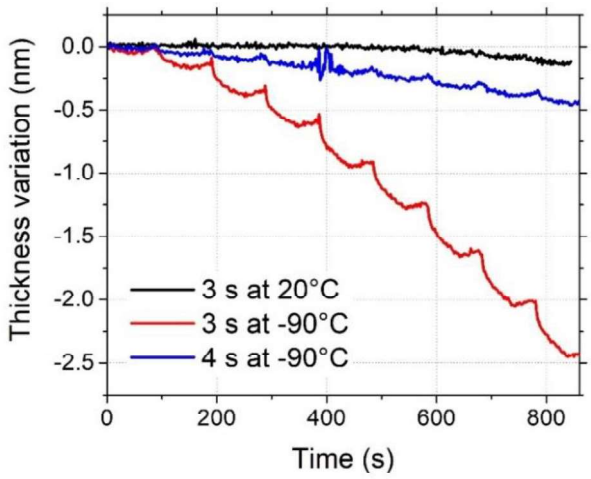

Fig. III. 36. SiO_2 thickness variation versus time for 8 cycles of cryo-ALE on SiO_2 performed at -90°C, and depending on the purge step time and temperature [16]

Again, a long process was performed to check repeatability through cycles. The curve obtained at -90°C with 3 s of purge displayed in Fig. III. 36 has shown that most of the etching occurs during the first few seconds of the Ar plasma. Therefore, the plasma for the test below in Fig. III. 37 lasted only 15 s, and a process with 150 cycles was performed.

The global curve is presented in Fig. III. 37. a, and like Fig. III. 34 at -120°C, shows a very linear etching, meaning no drift due to contamination from the reactor walls. But, when looking

at the first cycles (Fig. III. 37. b), about 16 cycles and so between 0.5 nm and 1 nm etched, are needed before a steady EPC is reached. At the first cycles, the EPC is about 0.05 nm/cycle, and increases up to 0.13 nm/cycle for the subsequent cycles. This means that it takes few cycles before starting with the same surface from a cycle to the next one. It can be due to some carbon contamination at the substrate surface that has first to be removed, before reaching the real SiO_2 surface [23]. But it can also be due to the formation of a mixing layer SiOCF that takes few cycles to reach a steady state, because only a small amount of C_4F_8 is supplied by each cycle [27], [28].

-90 °C	***Time (s)***	***Flow (sccm)***	***Pressure (Pa)***	***P_{source} (W)***	***V_{bias} (V)***
1. Physisorption: *C_4F_8*	20	14	5.7	0	0
2. Purge: *Ar*	3	280	1.2	0	0
3. Etch Plasma: *Ar*	15	28	3.4	400	- 15
4. Pumping	15	0	0.0	0	0

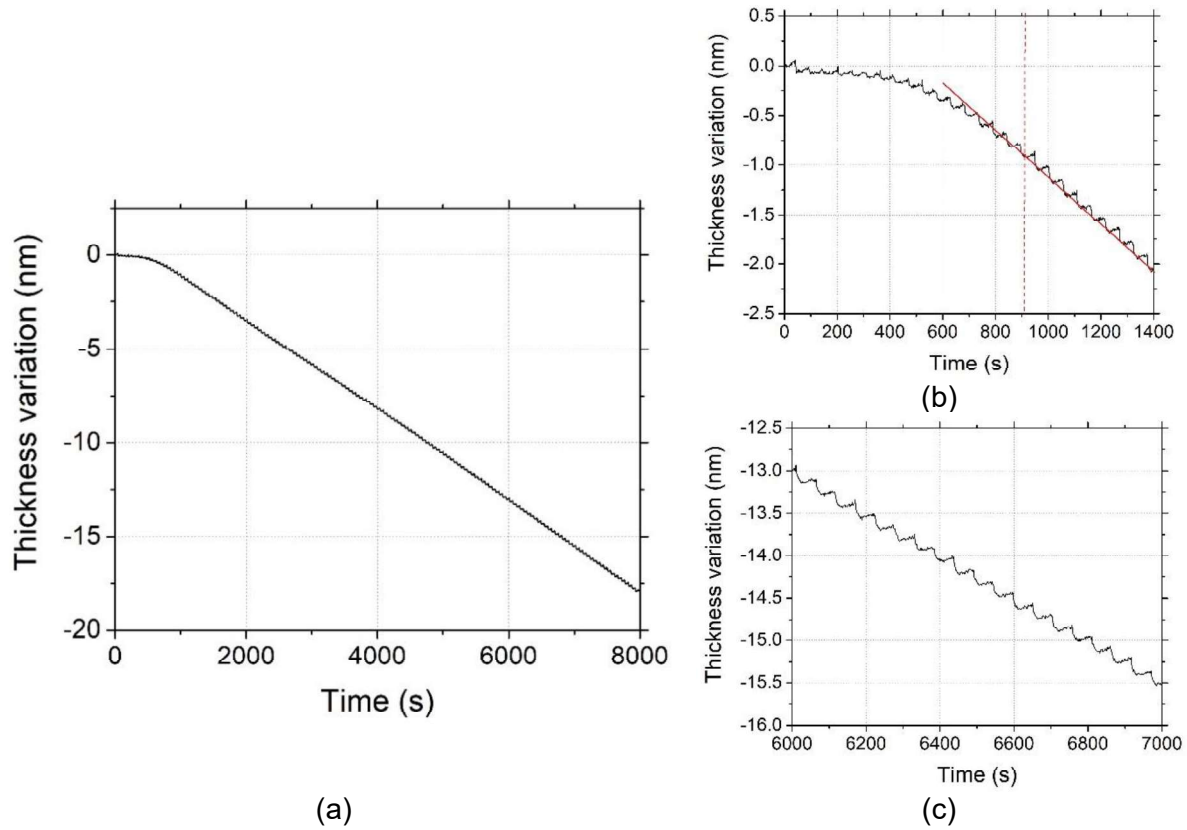

Fig. III. 37. (a) SiO_2 thickness variation versus time for 150 cycles of cryo-ALE performed at -90°C, (b) zoom on the first cycles, (c) zoom on the cycles close to the end of the process [16]

VI. Additional characterizations

VI.1. Uniformity & selectivity

VI.1.i. *Investigation on the etching uniformity*

In addition to the process development and optimization, uniformity and selectivity were of interest especially at the beginning of the project. To evaluate both of them, several samples of SiO_2 and a-Si were glued at the center and lateral sides on a 6" SiO_2 wafer (see Fig. III. 38. a).

-120 °C	***Time (s)***	***Flow (sccm)***	***Pressure (Pa)***	***P_{source} (W)***	***V_{bias} (V)***
1. Physisorption: *C_4F_8*	10	10	1.9	0	0
2. Purge: *Ar*	30	100	3.4	0	0
3. Etch Plasma: *Ar*	180	100	3.4	400	- 20

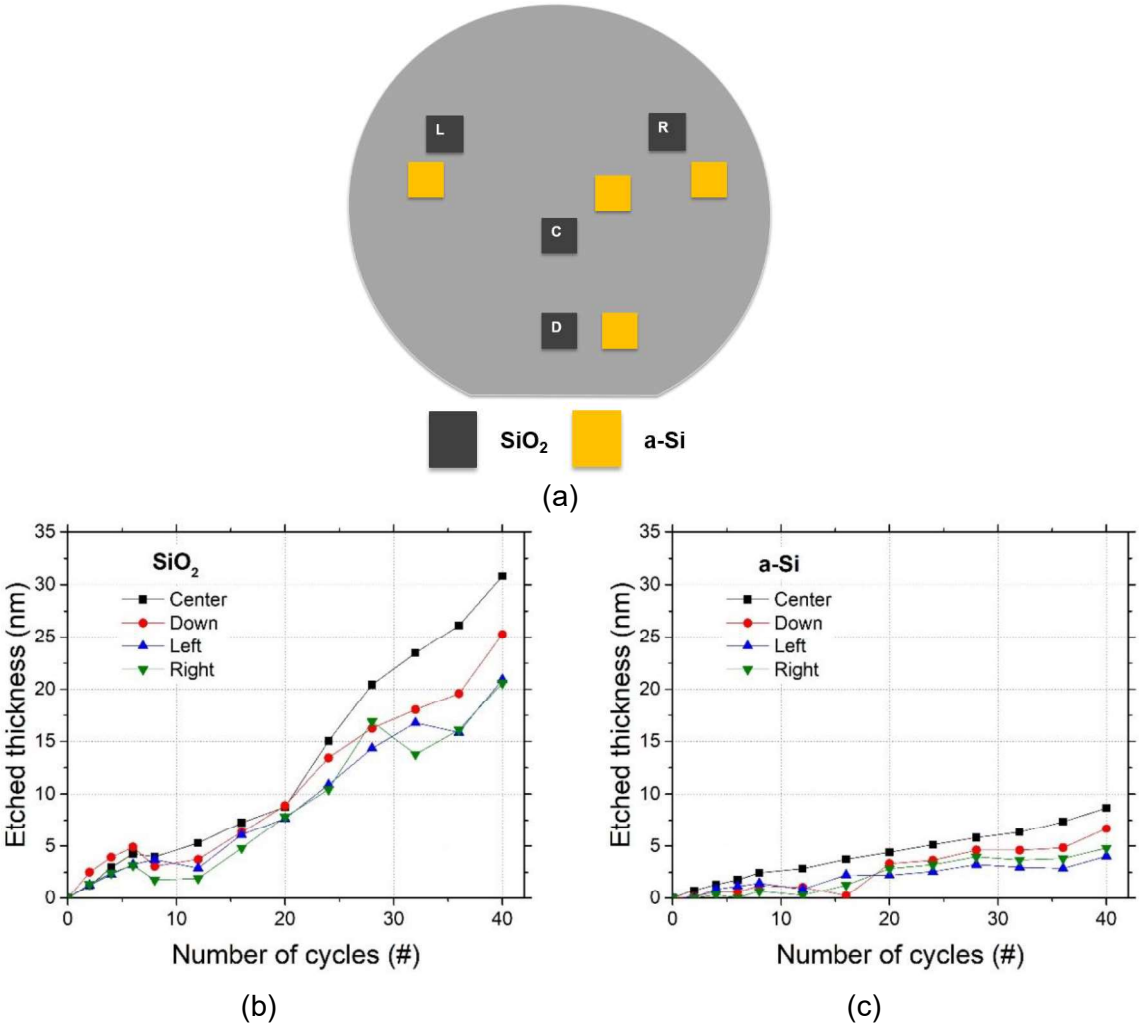

Fig. III. 38. (a) Sketch of the position of the coupons, thickness variation versus time for (b) SiO_2, (c) a-Si.

An ex-situ SE measurement was performed on each coupon after each 2 or 4 cycles. The parameters used in each cycle are presented above in Fig. III. 38. The evolution of the etched thickness versus the etch cycle number is presented in Fig. III. 38. b for SiO_2 and Fig. III. 38. c for a-Si. The lack of uniformity starts to be significant after 10 nm etched material, with, the highest etched rate in the center (C in Fig. III. 38. a). The EPC is quite similar on samples located on the left (L in Fig. III. 38. a) and on the right (R in Fig. III. 38. a) side of the carrier wafer, where the etching was the shallowest. Samples placed near the flat of the wafer (D in Fig. III. 38. a) have an EPC between the one obtained in the center and the lateral positions. This lack of uniformity can be due to a non-uniformity of the plasma and / or in the sample cooling. In all cases, SiO_2 was always more etched than Si with a selectivity of SiO_2 over a-Si higher than 3:1 for the samples in the center.

VI.1.ii. *Selectivity*

The selectivity was investigated by running a cryo-ALE on SiO_2 and a-Si but separately, to be able to measure the thickness variation on each material using in-situ SE in kinetic mode. Fig. III. 39 presents the curves for both materials. After few cycles, the etching trend of both materials seems very similar. However, at the first cycles, a-Si shows a lower etch rate than SiO_2. At the end of the process, about 7 nm was etched for a-Si and about 9 nm for SiO_2. The selectivity remains quite low.

-120 °C	***Time (s)***	***Flow (sccm)***	***Pressure (Pa)***	***P_{source} (W)***	***V_{bias} (V)***
1. Physisorption: *C_4F_8*	10	14	1.9	0	0
2. Purge: *Ar*	30	28	3.4	0	0
3. Etch Plasma: *Ar*	120	100	3.4	400	- 20
4. Pumping	15	0	0.5	0	0

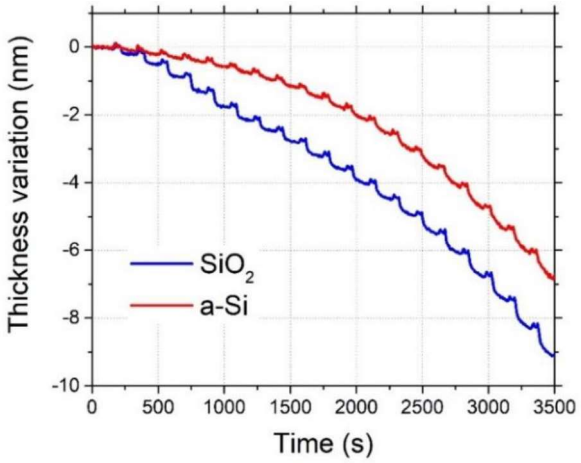

Fig. III. 39. Thickness variation versus time for SiO_2 and a-Si for the cryo-ALE process parameters given above - Evolution of the selectivity through cycles

VI.2. Quasi in-situ XPS measurement after "cryo-ALE" cycles

XPS measurements were presented in section I.6.iv of this chapter to evaluate C_4F_8 physisorption. In this paragraph, the Ar plasma step is investigated as well as the surface characterization after several cycles of cryo-ALE.

VI.2.i. *Surface contamination by carbon*

Before performing any etching cycle, an Ar plasma of 1 min was performed on the SiO_2 coupon at 200 W source power and without bias, in the OPTIMIST reactor. The surface has been analyzed by XPS before the plasma and after.

C 1s component is plotted in Fig. III. 40. a. The black curve corresponds to carbon peak before any treatment on the sample. Two peaks can be identified. The first peak around 284.6 eV corresponds to C-C bonds, and the second peak around 286.6 eV corresponds to C-O bonds. After 1 min of Ar plasma, all carbon was removed from the surface. These peaks could be useful to better detect an increase in the carbon signal when C_4F_8 is injected.

However, at the same time, some fluorine from the reactor walls redeposit on SiO_2 surface during the Ar plasma. Indeed, one main fluorine component can be detected around 687.3 eV and corresponds to F-SiO bonds.

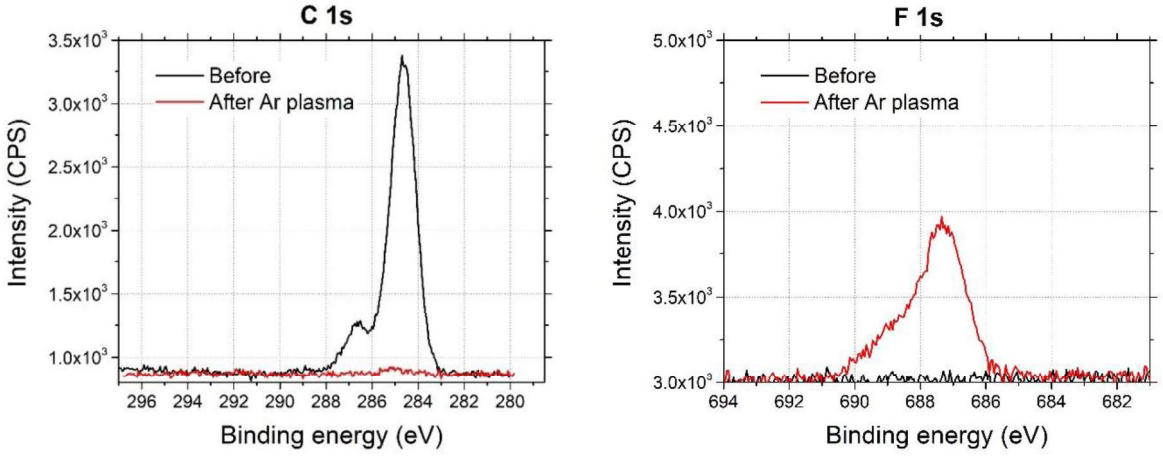

(a) (b)

Fig. III. 40. XPS measurement before and after an Ar plasma performed on SiO_2 of component (a) C 1s , (b) F 1s

VI.2.ii. *6 "Quasi" cryo-ALE cycles*

In order to check the surface state after etching, some "cryo-ALE" tests were performed in the OPTIMIST reactor in order to analyze the surface while keeping the temperature at -120°C. As the commands on OPTIMIST are done manually, 2 cycles of quasi-ALE without bias were first processed. The parameters for each step of the cycle are presented in Fig. III. 41. Then, a bias of -25 V has been added during the Ar plasma to get closer to the conditions used on the Alcatel reactor. Spectra were acquired on SiO_2 before the cycles at room temperature. Then, acquisitions were performed at -120°C after the 6 cycles, and after warming the sample to 20°C. The acquired spectra are presented in Fig. III. 41.

At -120°C, water condensation due to leakage in the equipment has totally covered the surface. Consequently, the intensity of Si 2p and O 1s peaks, that are related to the substrate, have strongly decreased (Fig. III. 41. a, b. and d.). On the other hand, F 1s has strongly increased (Fig. III. 41. e). The peak is situated at around 685.7 eV and corresponds to F-Si bonds. Once the sample is brought back to room temperature, Si 2p and O 1s peaks have almost the same intensity as before the process. The peaks are respectively situated at 103.5 eV and 532.8 eV and both are related to SiO_2 bonds. The peaks having recovered their intensity after heating, confirms that the surface was covered by a physisorbed layer that desorbs at room temperature.

The fluorine peak F 1s at 685.7 eV totally disappears meaning that the physisorbed layer at -120°C has desorbed. The peak at 688.6 eV for CF_x bonds is however slightly higher than before etching. At the same time, peaks at 293.6 eV, 291.3 eV and 285.3 eV are identified for C 1s and respectively correspond to C-F_3, C-F_2 and C-C bonds (Fig. III. 41. c). This confirms that a slight modified layer remains at the substrate surface even after heating back the sample.

To summarize, although it was difficult to interpret the results at -120°C because of the water condensation on the surface; warming to 20°C made it possible to identify a residual CF_x on the surface.

-120 °C, 2 + 4 cycles	Time (s)	Flow (sccm)	Pressure (Pa)	P_{source} (W)	V_{bias} (V)
1. Physisorption: C_4F_8	10	15	3.3	0	0
2. Purge: Ar	60	28	4.0	0	0
3. Etch Plasma: Ar	60	28	4.0	200	0 / ~ -25
4. Pumping	35	0	-	0	0

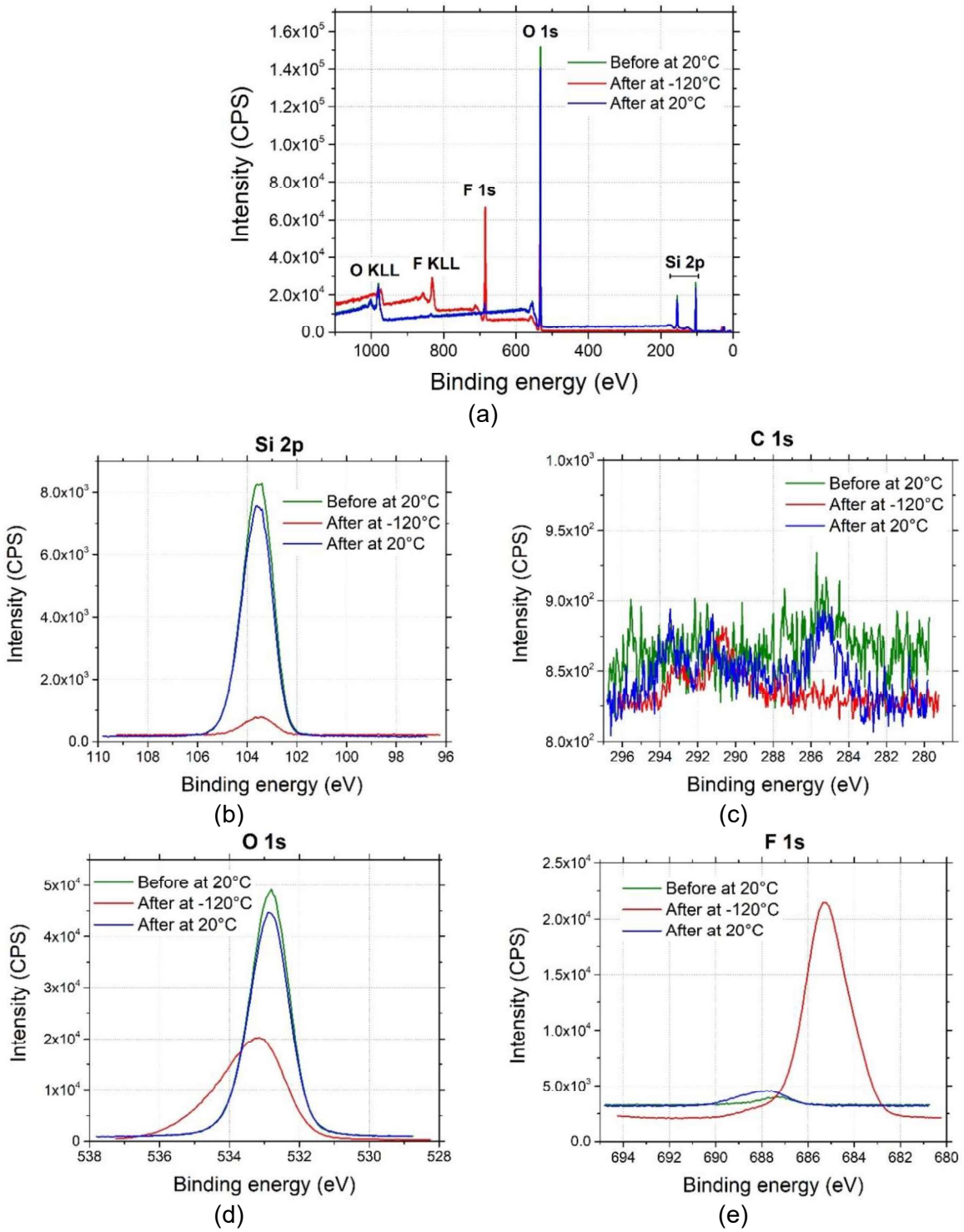

Fig. III. 41. XPS spectra of SiO_2 after 6 cycles of quasi-ALE at -120°C, (a) the wide scan of the sample, (b) the detail for Si 2p, (c) the detail for C 1s, (d) the detail for O 1s and (e) the detail for F 1s

VII. Conclusion

In this chapter, cryo-ALE was demonstrated on SiO_2 by physisorbing C_4F_8 on a cooled SiO_2 surface followed by an Ar plasma. QMS was used to evaluate the C_4F_8 residence time in the chamber and at the SiO_2 surface. The purge step time was optimized after C_4F_8 injection in order to keep enough adsorbed molecules at the surface. Self-Limiting Etching behavior was also demonstrated during a process by recording SiF_3^+ signal, which was correlated to the thickness variation measured by SE.

XPS measurements also enabled to confirm the increase of C_4F_8 surface residence time by decreasing the temperature. Indeed, it showed an increase of fluorine content on the surface with the temperature decrease. The XPS analyses of quasi-cryo-ALE have also demonstrated the sensitivity of the process to leakage inducing water condensation and trapping fluorine. Some CF_x radicals remain at the surface even after bringing back the substrate to room temperature. Moreover, XPS measurements also showed that a carbon contamination layer can be found on the substrate surface, and that a plasma is needed to remove it.

During the first cycles of a process, etch does not occur. Then, after few cycles, ALE reaches a steady EPC. The carbon contamination at the surface may explain the etch start delay. The other reason which can explain this delay relies on the need to form the SiOCF mixing layer necessary to activate the etching mechanism. Depending on the temperature and on the amount of C_4F_8 brought at the surface, the number of cycles needed to reach this steady state may vary.

Long process tests with 70 and 150 cycles were performed. In both cases, a quite constant EPC and a very linear temporal evolution of the etching was observed confirming that there is nearly no contribution of any contamination from the reactor walls.

The sensitivity of the process to the temperature has also been tested. No etching was obtained at -110°C and at 3.0 Pa of C_4F_8, but only at -120°C. However, if the C_4F_8 pressure is increased, the process temperature can also be increased. Etching was hence achieved at -90°C with a C_4F_8 pressure of about 6.0 Pa.

From all the results presented in this chapter, two mechanisms can be proposed for physisorption based cryo-ALE. The first one is that, during the Ar plasma, the physisorbed C_4F_8 molecules dissociate into CF_x on SiO_2 surface and react with it. The second possibility is that during the Ar plasma, all physisorbed C_4F_8 molecules first desorb from the cooled surfaces, then dissociate in plasma phase into CF_x radicals, and finally redeposit and react with SiO_2. Molecular dynamics could be performed in order to determine which mechanism is most likely.

In addition, the etching selectivity remains challenging. According to literature, selectivity to etch SiO_2 over other silicon based materials can be challenging even in continuous etching

[32], [33]. However, to increase selectivity, a sufficiently thick CF_x layer should remain on Si_3N_4 and a-Si to prevent their etching, which is more complicated with physisorbed C_4F_8. On the other hand, to etch Si_3N_4 and a-Si selectively to SiO_2, the bias should be increased [34]. During this project, the bias has never been increased beyond -20 V. Cryo-ALE based on physisorption remains a quite relevant process. Other tests could be performed with other chemistries, maybe more favorable to etch selectively the materials, and that can condensate at higher temperature than C_4F_8 to avoid cooling to a too low temperature. Compared to other more classical processes, this process is quite linear and no process drift was observed even after 150 cycles, which makes this technique quite promising.

VIII. References

[1] G. Antoun *et al.*, "Cryo atomic layer etching of SiO_2 by C_4F_8 physisorption followed by Ar plasma," *Appl. Phys. Lett.*, vol. 115, no. 15, p. 153109, 2019.

[2] G. Antoun *et al.*, "Plasma etching method and plasma etching apparatus," WO2019117130A1, 2019.

[3] A. E. Rodrigues, M. D. LeVan, and D. Tondeur, Eds., *Adsorption: Science and Technology*. Springer Netherlands, 1989.

[4] P. Lefort and S. Valette, "Cinétique des réactions du solide à températures élevées - Notions de base et processus élémentaires," *Techniques de l'ingénieur*, vol. AF3688 V1, p. 21, 2009.

[5] H. J. Kreuzer and Z. W. Gortel, *Physisorption kinetics*, vol. 1. Springer-Verlag Berlin Heidelberg, 1986.

[6] I. Langmuir, "The adsorption of gases on plane surfaces of glass, mica and platinum.," *J. Am. Chem. Soc.*, vol. 40, no. 9, pp. 1361–1403, 1918.

[7] S. Tinck, E. C. Neyts, and A. Bogaerts, "Fluorine–Silicon Surface Reactions during Cryogenic and Near Room Temperature Etching," *J. Phys. Chem. C*, vol. 118, no. 51, pp. 30315–30324, 2014.

[8] L.-M. Sun, F. Meunier, N. Brodu, and M.-H. Manero, "Adsorption - Aspects théoriques," *Techniques de l'ingénieur*, vol. J2730 V2, p. 24, 2016.

[9] S. Brunauer, P. H. Emmett, and E. Teller, "Adsorption of Gases in Multimolecular Layers," *J. Am. Chem. Soc.*, vol. 60, no. 2, pp. 309–319, 1938.

[10] M. Thommes *et al.*, "Physisorption of gases, with special reference to the evaluation of surface area and pore size distribution (IUPAC Technical Report)," *Pure and Applied Chemistry*, vol. 87, no. 9–10, pp. 1051–1069, 2015.

[11] J.-N. Jaubert and L. Schuffenecker, "Pressions de vapeur saturantes des composés organiques," *Techniques de l'ingénieur*, vol. K670 V2, p. 18, 1997.

[12] "NIST webbook." https://webbook.nist.gov/chemistry/name-ser/.

[13] W. D. McCain and W. T. Ziegler, "Critical temperature, critical pressure, and vapor pressure of argon," *J. Chem. Eng. Data*, vol. 12, no. 2, pp. 199–202, 1967.

[14] A. B. Kletskii and L. E. Petric, "Dependence of Vapor Pressure of Perfluorocyclobutane," *Zh. Fiz. Khim.*, vol. 41, pp. 1183–1184, 1967.

[15] D. R. Stull, "Vapor Pressure of Pure Substances. Organic and Inorganic Compounds," *Ind. Eng. Chem.*, vol. 39, no. 4, pp. 517–540, 1947.

[16] G. Antoun, P. Lefaucheux, T. Tillocher, R. Dussart, J. Faguet, and K. Maekawa, "Mechanism understanding in cryo Atomic Layer Etching of SiO_2 based upon C_4F_8 physisorption," *Sci. Rep.*, vol. 11, no. 357, 2021.

[17] R. H. Valentine, G. E. Brodale, and W. F. Giauque, “Trifluoromethane: entropy, low temperature heat capacity, heats of fusion and vaporization, and vapor pressure,” *J. Phys. Chem.*, vol. 66, pp. 392–395, 1962.

[18] X. Li *et al.*, “Properties of C_4F_8 inductively coupled plasmas. I. Studies of Ar/c-C_4F_8 magnetically confined plasmas for etching of SiO_2,” *J. Vac. Sci. Technol. A*, vol. 22, no. 3, p. 11, 2004.

[19] NIST, “Cyclobutane, octafluoro-,” *Chemistry WebBook NIST, SRD 69*. https://webbook.nist.gov/cgi/formula?ID=C115253&Units=CAL&Mask=200#Mass-Spec.

[20] M. Schaepkens, T. E. F. M. Standaert, N. R. Rueger, P. G. M. Sebel, G. S. Oehrlein, and J. M. Cook, “Study of the SiO_2 -to- Si_3N_4 etch selectivity mechanism in inductively coupled fluorocarbon plasmas and a comparison with the SiO_2-to-Si mechanism,” *J. Vac. Sci. Technol. A*, vol. 17, no. 1, pp. 26–37, 1999.

[21] C. Cardinaud, A. Rhounna, G. Turban, and B. Grolleau, “Contamination of Silicon Surfaces Exposedto CHF_3 Plasmas,” *J. Electrochem. Soc.*, vol. 135, no. 6, p. 6, 1988.

[22] Y. Kim, S. Lee, Y. Cho, S. Kim, and H. Chae, “Plasma atomic layer etching of SiO_2 and Si_3N_4 with heptafluoropropyl methyl ether ($C_3F_7OCH_3$),” *J. Vac. Sci. Technol. A*, vol. 38, no. 2, p. 022606, 2020.

[23] S. S. Kaler, Q. Lou, V. M. Donnelly, and D. J. Economou, “Atomic layer etching of silicon dioxide using alternating C_4F_8 and energetic Ar^+ plasma beams,” *J. Phys. D: Appl. Phys.*, vol. 50, no. 23, p. 234001, 2017.

[24] D. Metzler, R. L. Bruce, S. Engelmann, E. A. Joseph, and G. S. Oehrlein, “Fluorocarbon assisted atomic layer etching of SiO_2 using cyclic Ar/C_4F_8 plasma,” *J. Vac. Sci. Technol. A*, vol. 32, no. 2, p. 020603, 2014.

[25] J. W. Butterbaugh, “Plasma–surface interactions in fluorocarbon etching of silicon dioxide,” *J. Vac. Sci. Technol. B*, vol. 9, no. 3, p. 1461, 1991.

[26] NIST, “Silicontetrafluoride.” https://webbook.nist.gov/cgi/cbook.cgi?ID=C7783611&Units=SI&Mask=200#Mass-Spec.

[27] K. J. Kanarik *et al.*, “Predicting synergy in atomic layer etching,” *J. Vac. Sci. Technol. A*, vol. 35, no. 5, p. 05C302, 2017.

[28] D. Metzler, C. Li, S. Engelmann, R. L. Bruce, E. A. Joseph, and G. S. Oehrlein, “Characterizing fluorocarbon assisted atomic layer etching of Si using cyclic Ar/C_4F_8 and Ar/CHF_3 plasma,” *J. Chem. Phys.*, vol. 146, no. 5, p. 052801, 2017.

[29] R. J. Gasvoda, A. W. Van De Steeg, R. Bhowmick, E. A. Hudson, and S. Agarwal, “Surface Phenomena During Plasma-Assisted Atomic Layer Etching of SiO_2,” *ACS Appl. Mater. Interfaces*, vol. 9, no. 36, pp. 31067–31075, 2017.

[30] C. Li, D. Metzler, C. S. Lai, E. A. Hudson, and G. S. Oehrlein, “Fluorocarbon based atomic layer etching of Si_3N_4 and etching selectivity of SiO_2 over Si_3N_4,” *J. Vac. Sci. Technol. A*, vol. 34, no. 4, p. 041307, 2016.

[31] D. Metzler, C. Li, S. Engelmann, R. L. Bruce, E. A. Joseph, and G. S. Oehrlein, "Fluorocarbon assisted atomic layer etching of SiO_2 and Si using cyclic Ar/C_4F_8 and Ar/CHF_3 plasma," *J. Vac. Sci. Technol. A*, vol. 34, no. 1, p. 01B101, 2016.

[32] T. E. F. M. Standaert, C. Hedlund, E. A. Joseph, G. S. Oehrlein, and T. J. Dalton, "Role of fluorocarbon film formation in the etching of silicon, silicon dioxide, silicon nitride, and amorphous hydrogenated silicon carbide," *J. Vac. Sci. Technol. A*, vol. 22, no. 1, pp. 53–60, 2004.

[33] K. J. Kanarik, S. Tan, and R. A. Gottscho, "Atomic Layer Etching: Rethinking the Art of Etch," *J. Phys. Chem. Lett.*, vol. 9, no. 16, pp. 4814–4821, 2018.

[34] D. Nakayama *et al.*, "Highly selective silicon nitride etching to Si and SiO_2 for a gate sidewall spacer using a $CF_3I/O_2/H_2$ neutral beam," *J. Phys. D: Appl. Phys.*, vol. 46, no. 20, p. 205203, 2013.

Chapter IV.

Cryo-atomic scale etching based on chemisorption in SiF_4 / O_2 plasma

In the previous chapter, a proof of principle of cryo-ALE of SiO_2 based on C_4F_8 physisorption followed by argon plasma was provided. However, the developed process did not achieve a sufficient selectivity between the tested silicon-based materials.

Therefore, in this chapter, a different approach of cryo-ALE is suggested to etch at the nanoscale, while achieving some selectivity between a-Si and Si_3N_4.

The study of the SiO_xF_y layer formed at low temperature and involved in the passivation of the trench sidewalls in Si deep etching has inspired this research topic.

The state of the art of standard cryoetching is first presented for a better understanding of the SiO_xF_y passivation layer formation in this kind of process. Then a short study of SiF_4 physisorption justifies the need of a plasma to form SiF_x radicals that physisorb at the surface. In the third section, cryo-ALE process using a thin SiO_xF_y passivation layer as the adsorbate is investigated. More especially, the effect of temperature and the substrate composition on the SiO_xF_y layer growth and its effect on etching are studied.

I. Study of the silicon oxyfluoride passivation layer

In Chapter I, it has been mentioned that a silicon oxyfluoride (SiO_xF_y) passivation layer is formed on the trench sidewalls during Si deep etching by SF_6 / O_2 plasma, especially at low temperature. Due to this SiO_xF_y layer which prevents lateral etching, high aspect ratio etched structures can be obtained using this process. Many studies were conducted in order to have a better understanding on the mechanisms responsible for its formation and its properties.

Studies at ambient temperature conducted by Oehrlein *et al*. [1], [2] have demonstrated that etching Si by pure SF_6 plasma results in isotropic etching, while adding O_2 to the plasma, enables anisotropic etching. The anisotropy increases with the O_2 percentage, until 60% of oxygen. Therefore, the F/O ratio is important to control. In order to limit the undercutting effect, the ratio has to be decreased. However, beyond a certain amount of oxygen, etching stops if the ion bombardment is reduced. From those tests, the authors concluded that fluorine is replaced by oxygen on the sidewalls, which are hence oxidized instead of being etched, since nearly no ion bombardment occurs on the trench sidewalls. The opposite is obtained at the

trench bottom where fluorine can etch Si since the ion bombardment reduces the oxidation by sputtering. A global reaction (Eq. IV. 1) is proposed to summarize the SiO_xF_y layer formation:

$$Si + xF + yO \rightarrow SiO_xF_y \quad \text{IV. 1}$$

In case of pure oxidation without fluorine, the reaction Eq. IV. 2 dominates at the surface:

$$Si + 2O \rightarrow SiO_2 \quad \text{IV. 2}$$

Without oxygen in the plasma, fluorine reacts directly with Si to form the volatile by-product SiF_4 (Eq. IV. 3):

$$Si + 4F \rightarrow SiF_4 \quad \text{IV. 3}$$

XPS measurements were performed on Si sidewalls after reactive ion etching by SF_6 / O_2 50%. The sample was not exposed to air before XPS analysis. The results have shown that the passivation layer at the sidewalls is close to a silicon dioxide with some fluorine, with O / Si ratio 1.7 and F / Si ratio of 1.0.

In 1988, Tachi *et al*. demonstrated the possibility of etching Si anisotropically with only an SF_6 plasma. According to the authors, sidewalls etching was reduced due to the low temperature that inhibits the reactions probability [3], [4]. In addition, Tsujimoto *et al*. show in [5] that lateral etching is strongly reduced at temperatures below -130°C, while maintaining a high vertical etch rate. They presented a high selectivity to the photoresist, higher than 40 at -90°C while reducing the undercut. They again claimed, as in [4], that the reduction of lateral etching at low temperatures was probably due to the decrease of reaction probabilities rather than to products condensation, as the latter was not possible in the process conditions used. However, some years after, Bartha *et al* [6] demonstrated that a source of oxygen is necessary to enable the formation of an efficient passivation layer on Si trenches sidewalls. They indeed showed that only isotropic Si etching was obtained when performing a plasma of pure SF_6. Hence, they were able to conclude that the anisotropic etching performed by Tachi *et al.* [3]–[5] was in fact due to the erosion of the quartz by the plasma, providing a source of oxygen.

Since the end of the 1990's, the etching team at GREMI has been working on cryogenic etching, and on the understanding of the passivation mechanisms. They also developed new cryogenic processes for trenches and TSV etching. [7]–[21]. Moreover, bowing and undercut formation in cryoetching processes were studied and significantly reduced [9], [10], [13]. More precisely, they showed the importance of finding an optimal O_2 / SF_6 ratio to keep a good compromise between etching and passivation. Indeed, with an optimal ratio, both the sidewalls and the bottom of the trenches are passivated. Then, using directional ion bombardment, the passivation layer is weakened and removed at the etch front, leaving a silicon surface that can be etched. However, if the O_2 / SF_6 ratio is not high enough, the passivation layer will stay weak and depassivation may occur, inducing damages to the trench profile. At the contrary, if the ratio is too high, the passivation layer can become too strong and thick, which can slow or even stop the etching [9]. Also, they showed in [10] that applying a too low RF source power

prevents the etching of the bottom trenches, that becomes narrower. However, a too high RF source power may induce profile destruction due to high ion density. It is therefore necessary to find an optimal power.

From their study, Blauw *et al* [22] suggested that the SiO_xF_y passivation layer formed at cryogenic temperatures may change once warmed back to ambient temperature. This was confirmed by Dussart *et al* [11], where they observed, using Scanning Electron Microscopy (SEM) and X-Ray Photoelectron Spectroscopy (XPS) characterization methods, that the passivation layer created at low temperature desorbs when heated to ambient temperature.

They also demonstrated that not only O_2 but also SF_6 is needed to build the SiO_xF_y layer. However, the sulfur does not play any role in the formation of the passivation layer, but just fluorine is needed.

In addition to SEM and XPS, QMS and ellipsometry measurements were performed to complete the study. After depositing the passivation layer at cryogenic temperature using SiF_4 / O_2 plasma, the substrate was gradually heated and SiF_3^+ signal (main ion from the fragmentation of SiF_4) was recorded by Quadrupole Mass Spectrometry (QMS), as well as the thickness by spectroscopic ellipsometry (SE) [12]. The increase of SiF_3^+ signal, mainly at temperatures between -80°C and -30°C, showed that desorption of SiF_4 molecules was occurring. At the same time, it was shown by in-situ SE, that part of the SiO_xF_y layer had desorbed, as the deposited thickness decreased from 19.3 nm down to 15.7 nm. Therefore, it was concluded that SiF_4 was involved in the passivation mechanism [12].

In the same article, it was also confirmed that ion bombardment could enhance removal of the passivation layer. The following mechanism was suggested in the case of SiF_4 / O_2 plasma: SiF_4 is dissociated in the plasma into SiF_x that subsequently deposits at low temperature to the substrate surface and then react with oxygen radicals from the plasma to create the SiO_xF_y passivation layer. In the case of SF_6 / O_2 plasma, two mechanisms were proposed to explain the formation of the passivation at cryogenic temperature. On the one hand, SiF_x is provided by the main etching product (SiF_4) desorbed from the etched Si surface. It is then dissociated in the plasma into SiF_x that deposit at low temperature to the substrate surface and then react with oxygen radicals from the plasma to create the SiO_xF_y passivation layer. On the other hand, unsaturated SiF_x sites, resulting from adsorption and diffusion of fluorine from the SF_6 / O_2 plasma in few atomic layers of silicon, react preferably with oxygen radicals. According to the authors, oxygen radicals have a higher sticking coefficient at low temperature, which enhances the formation of SiO_xF_y layer [12].

In [15], an oxidation threshold necessary to build SiO_xF_y layer is observed. It corresponds to an O_2 percentage sufficiently large in the SF_6 / O_2 plasma to grow an efficient passivation layer. However, Si will no longer be etched efficiently if the threshold is exceeded. This threshold can be affected by temperature, bias and / or oxygen concentration. Indeed, this threshold is

observed for lower O_2 content when low temperatures are used and at higher O_2 content when the plasma source or the bias are increased.

In an effort to learn more about the mechanisms involved in the growth of the passivation layer at the sidewalls, a system of three grids was mounted above the substrate, in order to repel charged particles. Thus, a representative study of the reality on the trench sidewalls, ideally free of ion bombardment, could be carried out on a Si flat surface. The deposited amount was then monitored by in-situ SE. While previous studies enabled to measure a growth of 19 nm of SiO_xF_y in 10 min of SiF_4 / O_2 plasma, a 90 nm thick layer was deposited with the grid in the same conditions. After heating and hence desorption, the remaining layer was 18 nm thick. Again, this test confirmed the sensitivity of the layer towards ion bombardment. It also showed that along the SiF_4 / O_2 plasma, the layer grows linearly versus time, without observing any saturation behavior [16]. Also, in this article, it was shown that the passivation can grow using separated SiF_4 and O_2 plasmas. This demonstrates that the SiO_xF_y film grows at the surface from SiF_x and O radicals formed in plasma phase. Therefore, it is unlikely that SiO_xF_y species are created in the plasma and subsequently deposit on the substrate. Finally, from additional XPS measurements, it was assumed that the stoichiometry at the SiO_xF_y top surface was close to $SiOF_3$ at -100°C. When the sample is brought back to room temperature, the SiO_xF_y is rearranged. The surface diffusion of the different species is increased, which leads to the formation of SiF_4 that desorbs from the surface [18].

In conclusion, the studies made until now have shown that the passivation efficiency in the cryogenic process was strongly dependent on the temperature, the oxygen content in the plasma and the bias. However, we shall see in the following sections that the passivation mechanisms is more complex and needs in-situ measurements to make the right interpretation. In the following section, the SiO_xF_y passivation layer is further investigated as a function of the substrate temperature and the SiF_4 / O_2 gas mixture.

II. Preliminary tests for the characterization of SiO_xF_y layer

At the beginning of the thesis, part of the work was dedicated to the characterization of the SiO_xF_y passivation layer on Si formed in SiF_4 / O_2 plasma.

II.1. Investigation on the effect of temperature

II.1.i. *Thickness variation as a function of temperature*

Firstly, the growth of a passivation layer by SiF_4 / O_2 plasma as function of temperature has been investigated. A SiF_4 / O_2 plasma was used to deposit a SiO_xF_y layer on a-Si sample

(with a 50 nm thick a-Si layer, as presented in Chapter II). The thickness of this layer was first measured in-situ by SE at the deposition temperature. Then, the sample was unloaded and kept in the loadlock under N_2 atmosphere until it reached room temperature (with no specific heating). Finally, the sample was transferred back to the chamber to perform SE measurement in order to measure the desorbed thickness. At the end, the remaining layer was etched by SF_6 plasma and its etch rate was measured.

II.1.i.a. Presentation of the ellipsometry model and fit

The growth of the passivation layer by SiF_4 / O_2 plasma has been monitored by in-situ SE before, during and after the deposition. As the deposited layer was a SiO_xF_y material on a-Si of 50 nm thick, a specific model has been designed to fit the measurements. The following model that is presented here has been used to fit all the measurements reported in this chapter. In Chapter II, the model used to fit a-Si has been presented in Table. II. 2 and is reminded below in Table. IV. 1. A new amorphous dispersion formula is used to model the thin layer of a-Si and a mix of a-Si and void layer is used to represent the roughness of the surface. When a new sample is used, a fit is performed on the material parameters and on the thickness and then they are saved.

Table. IV. 1. Fit model for a-Si

Layer N°	***Fit***	***Thickness (nm)***	***Fit***	***Material***
Layer 3	F	3.00	F	a-Si_nam.dsp + Void.ref
Layer 2	F	50.00	F	a-Si_nam.dsp
Layer 1		100.00		SiO_2.dsp
Substrate				c-Si_HJY.ref

A new model is created to fit the thickness after deposition of the SiO_xF_y layer. It is presented in Table. IV. 2 below. Instead of modeling *Layer 3* as the roughness of the a-Si layer, it is replaced by a mix of SiO_2 and void, to model the deposited layer that can be porous. However, as the deposited layer is not exactly a SiO_2 but a SiO_xF_y material, the parameters from the classical dispersion formula of the material SiO_2 are recalculated during the fit and saved as SiO_xF_y new material. Nevertheless, the void percentage in the layer has usually not fitted, but was kept at 50% a-Si and 50% void.

Table. IV. 2. Fit model for a-Si with a SiO_xF_y deposited layer

Layer N°	Fit	Thickness (nm)	Fit	Material
Layer 3	F	10.00	F	SiO_xF_y.dsp + Void.ref
Layer 2	F	50.00		a-Si_nam.dsp
Layer 1		100.00		SiO_2.dsp
Substrate				c-Si_HJY.ref

A fit using this model presented in the Table. IV. 2 has been tested after deposition of a SiO_xF_y layer by SiF_4 / O_2 plasma on a-Si and at -100°C. The parameters used for the deposition are presented in Table. IV. 3.

Table. IV. 3. Parameters of SiF_4 / O_2 deposition plasma

	Time (s)	Flow (sccm)	Pressure (Pa)	P_{source} (W)	V_{bias} (V)
SiF_4 / O_2	30	50 / 50	3.0	1000	0

The resulting fit is presented in Fig. IV. 1. The ellipsometric parameters Is and Ic of the measure and the fit are plotted as a function of the photon energy. The *Measure* corresponds to the curve obtained from the acquisition and the *Fit* corresponds to the curve obtained by calculation. Fig. IV. 1 shows that the curves *Measure* and *Fit* match very well. χ^2, that gives the uncertainty of the fit, is lower than 5 and hence is considered as acceptable. The refractive index has also been calculated and is about 1.33 ± 0.02.

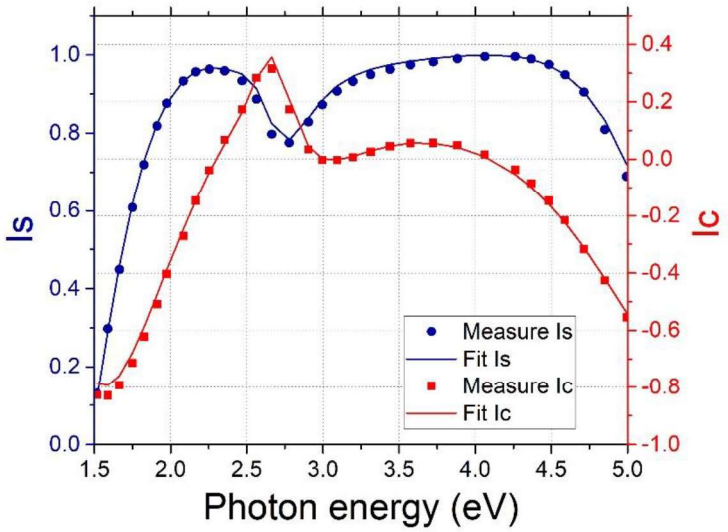

χ^2	2.99
Layer 3	46.52 ± 0.15 nm
Layer 2	47.13 ± 0.21 nm

Fig. IV. 1. Ellipsometric parameters Is and Ic measured and fitted as a function of the photon energy for a deposition of SiO_xF_y layer at -100°C, with the thickness values obtained

Thus, the model with the created SiO_xF_y material in Table. IV. 2 is considered as accurate and valid to be used to calculate the thickness of the deposited layer. This same model, based on a stack of three layers, is then used to accurately fit the acquisitions in kinetic mode during the deposition. Fig. IV. 2 shows the obtained curve displaying for the thickness evolution in real

time of the deposited *Layer 3*, as calculated in Fig. IV. 1. The thickness increases linearly versus time during the 30 s of SiF_4 / O_2 plasma, with a deposition rate about 1.6 $nm.s^{-1}$. The deposited thickness measured in the kinetic mode in Fig. IV. 2 is about 47 nm which is close to the one calculated in Fig. IV. 1 (about 46.5 nm for *Layer 3*).

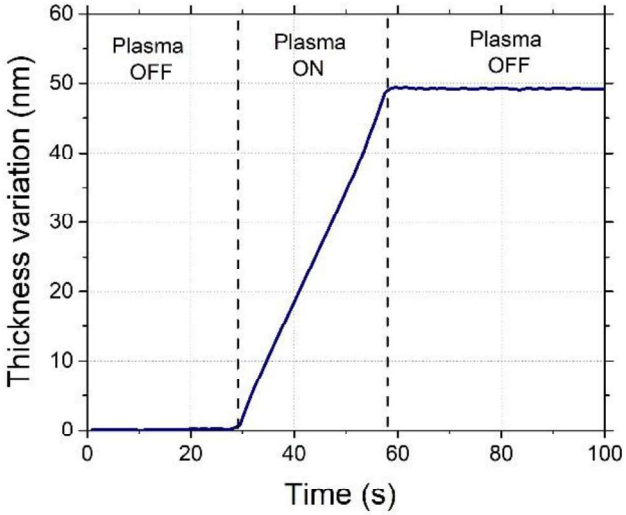

Fig. IV. 2. Thickness evolution of the deposited passivation layer versus time measured by in-situ SE, during SiF_4 / O_2 deposition plasma at -100°C (process from Table. IV. 3)

II.1.i.b. Thickness evolution after SiO_xF_y deposition layer

Fig. IV. 3 displays the thickness of the deposited passivation layer SiO_xF_y as function of the temperature in two cases: before venting (thickness measured immediately after the process) and after venting (thickness measured after that the wafer has been unloaded, hence warmed to room temperature). The SiF_4 / O_2 plasma parameters for the deposition are the same as in Table. IV. 3. In both cases, the deposited layers at 25°C and -50°C are the same, and are close to 30 nm (Fig. IV. 3. a). However, if the temperature is decreased to -100°C, the deposited layer thickness increases up to 49 nm and then, it decreases. Below -130°C, the process tends into an opposite regime: instead of obtaining some SiO_xF_y layer deposition, the Si starts to be slightly etched (1 nm in 30 s) (not represented on the graph).

From [12], it is known that SiF_4 / O_2 plasma creates SiF_x that deposit on cooled surfaces, and that O radicals then react to deposit a SiO_xF_y layer. Fig. IV. 3 shows that the deposited amount increases with the temperature decrease (until -100°C), which means that there is an increase of SiF_x concentration at the surface at low temperatures. This can be due to a higher surface residence time of SiF_x at low temperatures. However, when the temperature is below -100 °C, a decrease is observed in the thickness of the deposited layer. This means that there is a temperature threshold below which there is a change that prevents the build-up of the layer. As below -130°C, a-Si is etched by the SiF_4 / O_2 plasma, it is possible that fluorine residence time is also increased at low temperatures which will favor Si etch.

Fig. IV. 3. a also shows that the thickness of the passivation layer is slightly lower after venting for all the temperatures. However, below -100°C, the difference before and after venting gets higher, with a great decrease of the thickness after venting at -125°C. As explained in [12], SiF_x concentration is increased at low temperature. In addition, in [12], it is shown that SiF_4 desorbs from the deposited SiO_xF_y when warming the sample to 20°C. So, it is possible to conclude that, after venting, SiF_4 would desorb from the SiO_xF_y layer, which explains the decrease of the thickness.

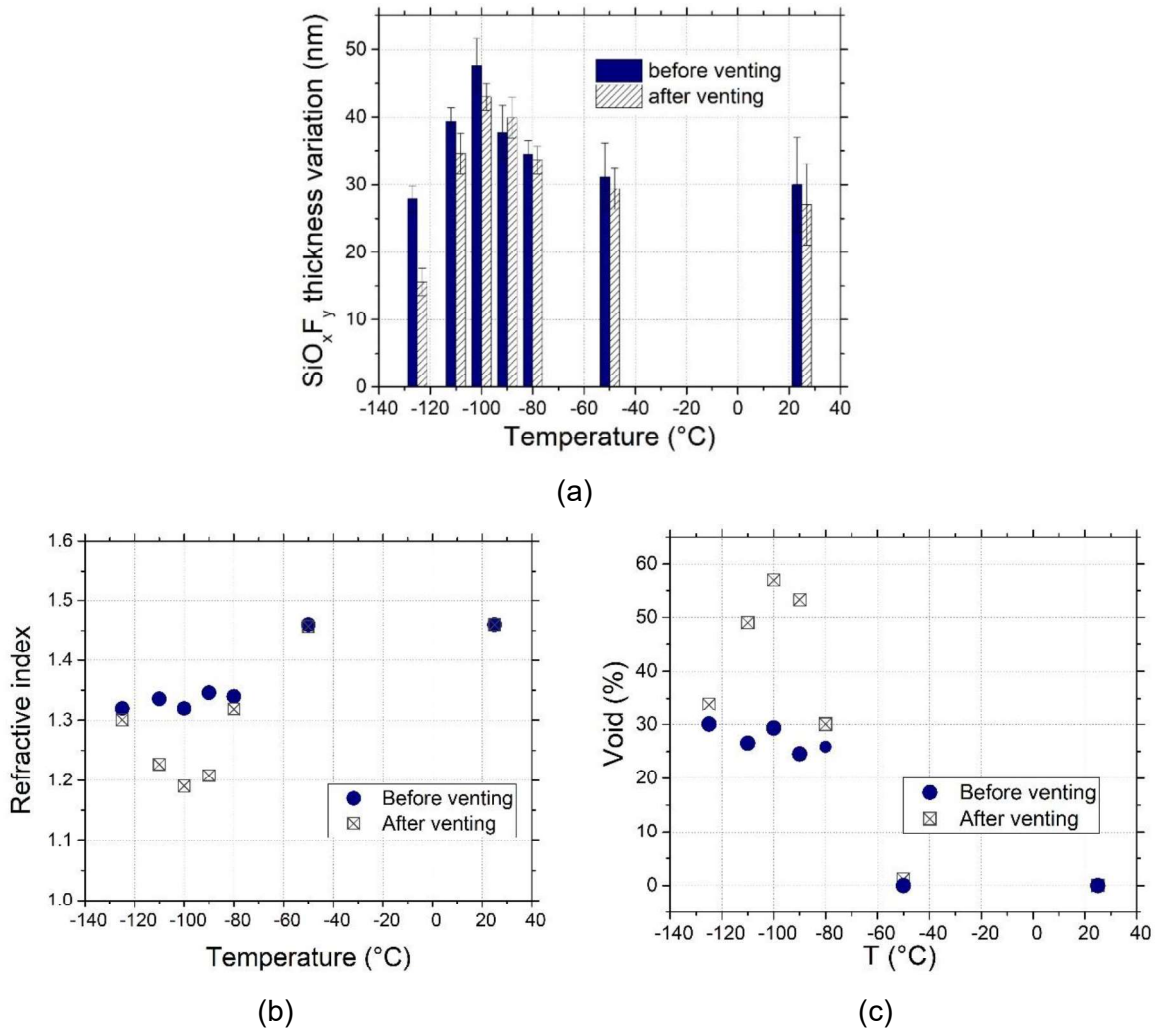

Fig. IV. 3. SE measurement for (a) the thickness of the deposited SiO_xF_y layer, (b) its optical index, (c) the percentage of void in the layer, adapted from [21] (process from Table. IV. 3)

The refractive index and the void proportion of the layer are plotted versus temperature respectively in Fig. IV. 3. b and Fig. IV. 3. c. Both of them are constant before and after venting the sample at 25°C and -50°C. This can be expected when comparing with the thickness that remains also almost constant at those temperatures. At those temperatures, the refractive index of the deposited layer is about 1.46, which is similar to SiO_2 [23].

However, at lower temperatures, the refractive index decreases after venting, while the void percentage increases. These behaviors are consistent, as porosity in a layer (modelled by void

in SE) decreases the refractive index of a layer. Therefore, it can be understood from these results that the part of the SiO_xF_y layer that desorbs after venting, induces some porosity, which results in a decrease of the refractive index.

II.1.ii. Etching of the deposited layer by SF_6 plasma

In the STiGer process presented in Chapter I, Si deep etching is achieved by alternating a SiF_4 / O_2 plasma for passivation and SF_6 plasma for etching. It is hence important to know the robustness of the deposited SiO_xF_y layer to the etching SF_6 plasma. Therefore, the deposited layers presented in Fig. IV. 3 have been etched by an SF_6 plasma at ambient temperature in order to determine their etch rate (ER). The parameters used for the SF_6 plasma are presented in Fig. IV. 4. This figure also shows the ER of each SiO_xF_y layer as a function of its deposition temperature. When the deposition temperature decreases, the ER increases, which is consistent with a more porous SiO_xF_y layer at lower deposition temperature, as it has been shown from Fig. IV. 3. c. As the porosity is increased, fluorine radicals can diffuse more easily in the material and the etch rate is enhanced.

At -125°C, the ER drastically increases as a-Si layer of the sample is quickly reached and etched by SF_6 plasma with an ER of 2.25 $nm.s^{-1}$.

25°C	***Flow (sccm)***	***Pressure (Pa)***	***P_{source} (W)***	***V_{bias} (V)***
SF_6	200	3.0	1000	Floating

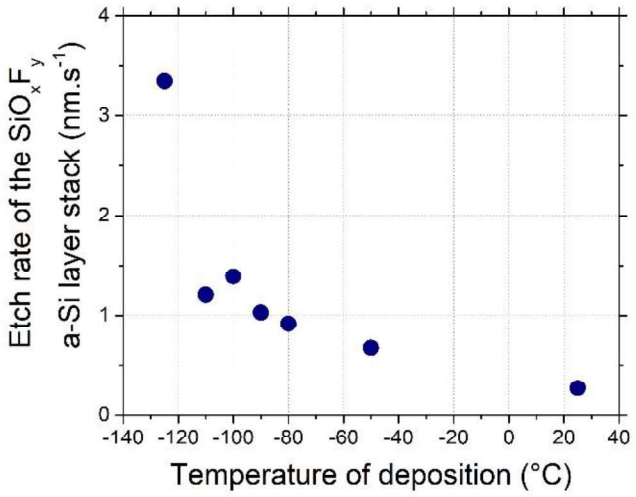

Fig. IV. 4. Etch rate of SiO_xF_y layer versus the deposition temperature, etched by SF_6 plasma

II.2. Surface analysis by XPS measurement

Ex-situ XPS measurement at IMN laboratory was performed on a SiO_xF_y layer deposited on Si substrate at -110°C by SiF_4 / O_2 plasma (with the parameters displayed in Table. IV. 5). The sample was analyzed once it was heated back to room temperature. The XPS scans can be found in [21] and the layer composition is presented in Fig. IV. 5. It has a composition close to that of SiO_2 with 33.6% of silicon, 60.0% of oxygen, 2.2% of fluorine and 4.2% of carbon. This confirms that the layer is poor in fluorine when the sample is brought back to ambient temperature [21]. According to [24], this is due to hydrolysis reaction between water from the air and the SiO_xF_y layer, desorbing fluorine as HF.

-110°C	*Time (s)*	*Flow (sccm)*	*Pressure (Pa)*	P_{source} *(W)*	V_{bias} *(V)*
SiF_4 / O_2	60	50 / 50	2.8	1000	Floating

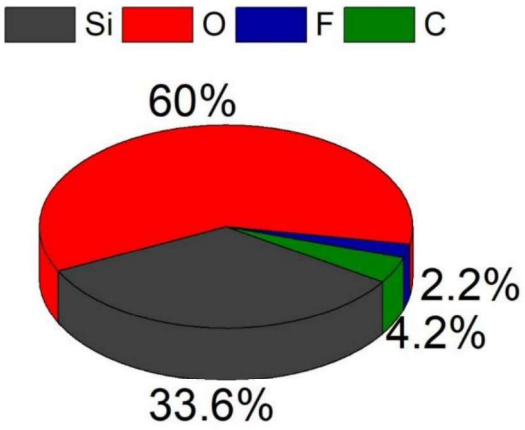

Fig. IV. 5. Composition of the SiO_xF_y layer deposited on Si and determined by ex-situ XPS

II.3. Investigation on SiF_4 influence

II.3.i. *Description of the cavity test*

The “cavity test” is an experiment where etched profiles are studied in order to evaluate the robustness of the passivation layer. The principle is to first etch isotropically by SF_6 plasma a Si patterned sample in order to create an isotropic cavity. This initial step is called *INI* (“initial step”). Then, the substrate is exposed to a plasma or a flow of SiF_4 / O_2 to passivate the sidewalls of the cavity formed if it is efficient,.

Finally, a second plasma of SF_6 is performed (called *FIN*, for final step) to evaluate the robustness of the passivating layer.

INI and *FIN* steps are always the same. Their process parameters are presented below in Table. IV. 4.

Table. IV. 4. Parameters of SF_6 plasmas for the initial and final steps of cavity tests

	Time (min)	Flow (sccm)	Pressure (Pa)	P_{source} (W)	V_{bias} (V)
1. Initial INI: SF_6	10	200	2.8	1000	0
2. Final FIN: SF_6	3	200	2.8	1000	- 37

Fig. IV. 6 clarifies the purpose of the test. The first isotropic profile (INI) is drawn in yellow. If after the *FIN step,* the reference cavity is extended and if there is one cavity only, as in Fig. IV. 6. a, this means that no passivation layer was deposited with SiF_4 / O_2 treatment or at least that the deposited layer was cleared quickly. If a second cavity appears, as in Fig. IV. 6. b, this means that the SiF_4 / O_2 treatment is efficient enough to build a passivation layer on the first cavity sidewalls. The appearance of a second cavity is due to ion bombardment that removes the passivation layer at the bottom of the cavity, and enables isotropic etching by the SF_6 plasma.

The cavity shapes were always analyzed by Scanning Electron Microscopy (SEM) on patterns with an initial opening width of 5 µm.

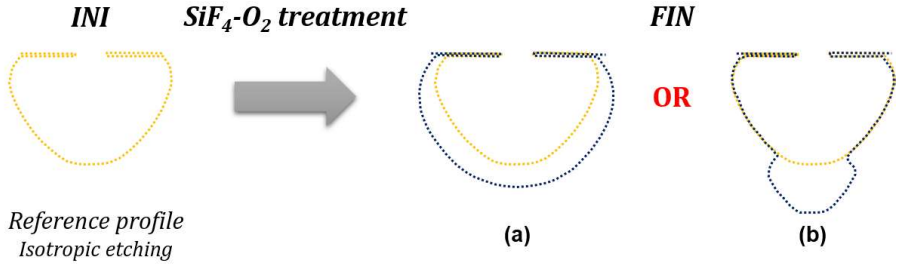

Fig. IV. 6. Principle of the cavity test, with (a) one cavity etched isotropically, (b) two cavities

II.3.ii. *Experimental parameters used*

In [25], the authors show by molecular dynamics simulations that it is possible to physisorb several layers of SiF_4 on a-Si at -100°C. Therefore, to verify this information and understand the role of SiF_4 in the formation of the passivation layer, cavity tests have been performed. Same *INI* and *FIN* steps as those described in Table. IV. 4 are used at the beginning and at the end of the process for isotropic etch. The passivation step is composed itself of a sequence of 3 sub steps cycled 10 times:

Step 1: An O_2 plasma of 30 s

Step 2: 3 different configurations have been compared to investigate the role of SiF_4: a 30 s SiF_4 plasma, SiF_4 gas flow, and an Ar gas flow

Step 3: An Ar flow of 10 s to purge the chamber

The three tests were performed at -100°C and all parameter details are given in Table. IV. 5.

So, the parameters change is in the step 2. The condition ***a.*** with SiF_4 plasma, enables to check the possibility to passivate the sidewalls by alternating O_2 plasma and SiF_4 plasma. And hence to know if SiF_x radicals play a role in the passivation. The condition ***b.*** with SiF_4 gas, helps checking if physisorbed SiF_4 molecules are directly involved in the passivation mechanisms. Finally, the condition ***c.*** with Ar flow, aims to confirm the role of SiF_4 species in the passivation mechanism. Indeed, as Ar cannot passivate the surface, it is expected to observe mainly the first cavity profile extended as in Fig. IV. 6. a. However, if any passivation is observed, leading to the same profile as that obtained with conditions ***a.*** and / or ***b.***, it would mean that the passivation in conditions ***a.*** and / or ***b.*** is not due to the investigated species (SiF_x or SiF_4).

Table. IV. 5. Parameters used in SiF_4 role investigation

-100°C 10 cycles	***Time (s)***	***Flow (sccm)***	***Pressure (Pa)***	***P_{source} (W)***	***V_{bias} (V)***
a. ***Step 1:*** O_2	30	50	2.8	1000	Floating
Step 2: SiF_4	30	50	2.8	1000	Floating
Step 3: *Ar*	10	100	2.8	0	0
b. ***Step 1:*** O_2	30	50	2.8	1000	Floating
Step 2: SiF_4	30	50	2.8	0	0
Step 3: *Ar*	10	100	2.8	0	0
c. ***Step 1:*** O_2	30	50	2.8	1000	Floating
Step 2: *Ar*	30	50	2.8	0	0
Step 3: *Ar*	10	100	2.8	0	0

II.3.iii. *Role of SiF_4*

Fig. IV. 7 shows the profiles obtained after the processes presented in Table. IV. 5 and observed by SEM.

Fig. IV. 7. a, corresponds to process ***a.*** in Table. IV. 5. The first cavity perfectly fits with the sketch of the reference cavity. A second cavity is formed at the bottom with a narrow opening, slightly bigger than the pattern in the mask opening.

In Fig. IV. 7. b, SiF_4 was only injected in gas phase. It corresponds to the conditions ***b.*** in Table. IV. 5. The top of the first cavity has been protected by a passivation layer but, unlike in Fig. IV. 7. a, the etching at the bottom occurs on a larger area, showing that passivation is less efficient here. Almost the same profile is observed in Fig. IV. 7. c, where the SiF_4 flow is replaced by an Ar flow ***c.*** in Fig. IV. 6. The isotropic profile shows that SiF_4 does not play a role

in the weak passivation. The protection of the sidewalls with this process is rather due to an oxidation of silicon with the O_2 plasma.

Only conditions ***a***. (O_2 plasma followed by SiF_4 plasma) enabled to create an efficient passivation layer. This explains why the first cavity was so well protected. Indeed, only the passivation layer at the bottom of the cavity was broken through by ion bombardment, allowing the Si etch.

This experiment proves that SiF_4 physisorption does not occur at this temperature and is not responsible for the formation of the passivation layer SiO_xF_y whereas SiF_x radicals (produced when SiF_4 is in plasma phase) do play an important role as observed in Fig. IV. 7. a.

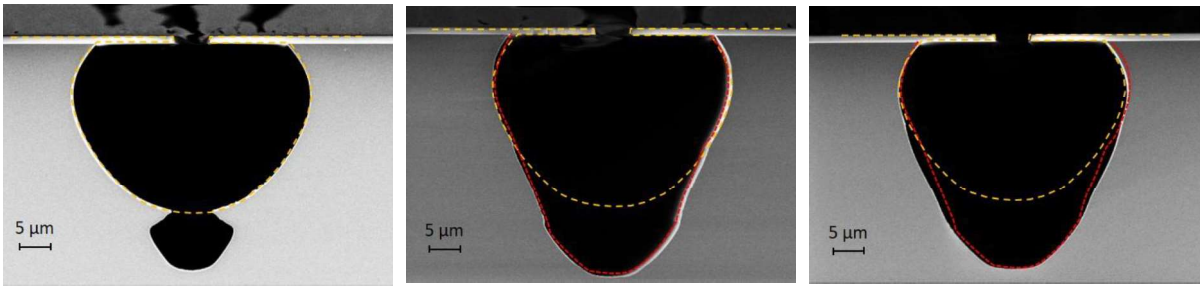

(a) (b) (c)

Fig. IV. 7. SEM images of Si etched cavities of 5 µm opening width, observed in InLens mode using a magnification of 5.0 k, with cavity etched in conditions a, b and c

Fig. IV. 8 presents the growth of the passivation layer when alternating SiF_4 and O_2 plasmas without bias. It shows, once again, the effect of temperature on the layer growth. The layer grows only during SiF_4 plasma and the rate is doubled at -100°C compared to 20°C. Indeed, about 5 nm are deposited in a cycle at -100°C, whereas only 2.5 nm are deposited per cycle at 20°C. This shows that SiO_xF_y deposition is increased at low temperature. According to [25], this can be due to the residence time of SiF_x species that increases at low temperature.

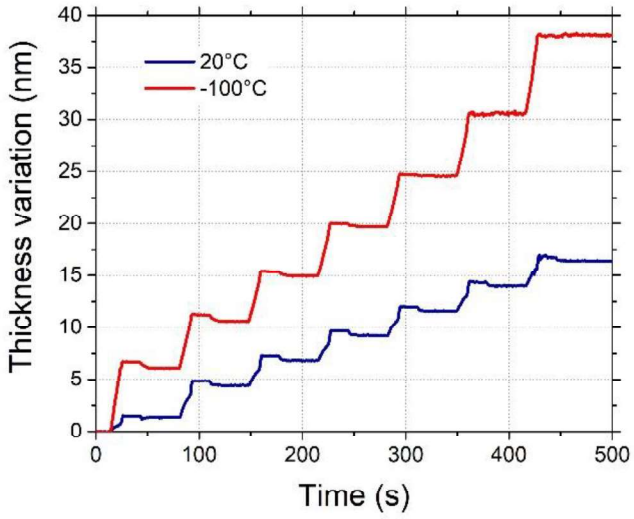

Fig. IV. 8. SiO_xF_y layer growth at -100°C and 20°C by alternating 13 s SiF_4 plasma and 14 s O_2 plasma separated with a purge step

II.4. Investigation of O_2 proportion in SiF_4 / O_2 plasma

It was shown in literature that the oxygen percentage also plays a role in the passivation efficiency [15]. In Fig. IV. 9, the deposited layer thickness was studied as a function of O_2 content in SiF_4 / O_2 mix. The highest thickness is deposited in pure SiF_4 plasma with more than 110 nm. This is consistent with Fig. IV. 8 where the thickness increase was observed during SiF_4 step. At 80% of O_2, a very small amount, of less than 10 nm, thick is deposited. Between those two percentages, the thickness decreases with oxygen increase.

After venting, the SiO_xF_y thickness always decreases. The optical path nL in Fig. IV. 9. b shows even a larger gap between before and after venting, and more specifically for low oxygen content. This tends to confirm that some SiF_x species desorb after venting.

-100 °C	*Time (s)*	*Total flow (sccm)*	*Pressure (Pa)*	*P_{source} (W)*	*V_{bias} (V)*
SiF_4 / O_2	30	40	3.0	1000	Floating

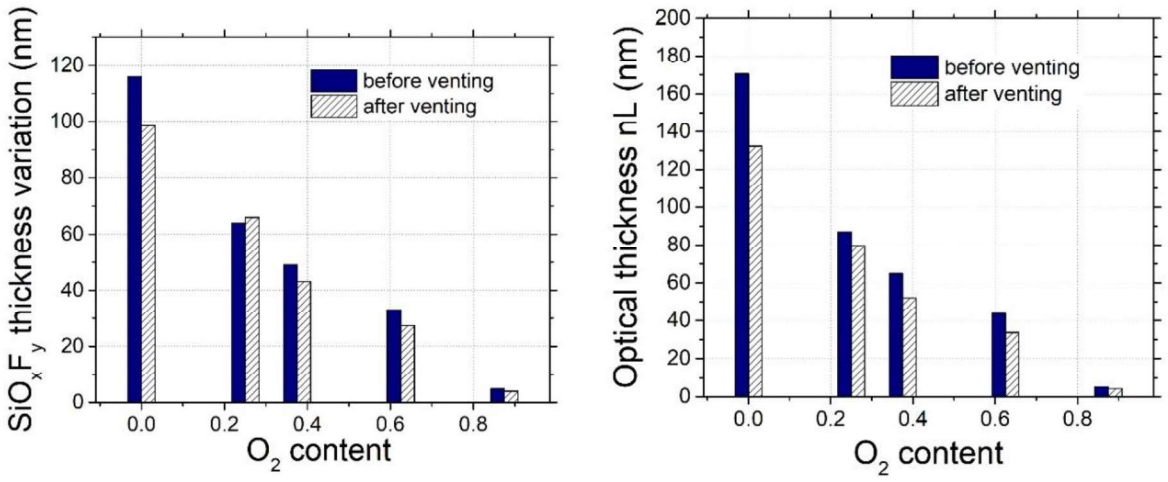

(a) (b)

Fig. IV. 9. SE measurement of (a) the thickness of the deposited SiO_xF_y layer, (b) its optical path, both versus the oxygen proportion, adapted from [21]

III. Physisorption of SiF_4

III.1. SiF_4 vapor pressure curve

In Chapter III, cryo-ALE based on the physisorption of C_4F_8 gas on a cooled surface was demonstrated. The pressure and temperature parameters must be accurately chosen to get close to the condensation conditions, with an increased surface residence time of the species, but without really reaching the condensation regime, where species accumulate continuously on the surface.

In the previous section, it was suggested that SiF_4 does not physisorb in the investigated experimental conditions, which is a point that needs to be clarified. Fig. IV. 10, that displays the SiF_4 vapor pressure curve plotted as a function of temperature using Antoine parameters taken from [26], gives a first insight into the conditions of condensation. As the data cover a temperature range between -144°C to -95°C, an extrapolation was performed to extend the curve down to -180°C. Extrapolation of the vapor pressure curve of C_4F_8 curve was added for comparison [27].

It appears from the curve in Fig. IV. 10 that, for a same pressure, SiF_4 molecules condense at much lower temperatures than C_4F_8 molecules. Indeed, for a pressure of 1.0 Pa for example, C_4F_8 gas would condense from -130°C, whereas, temperature needs to be decreased below -160°C in the case of SiF_4 gas to enable some condensation.

However, operating at temperatures close to -160°C would favor water condensation at the same time. Moreover, special equipment that can endure such low temperatures is necessary, as well as a large consumption of liquid nitrogen. So, from this curve, processing in conditions of SiF_4 physisorption appeared challenging and not of great interest.

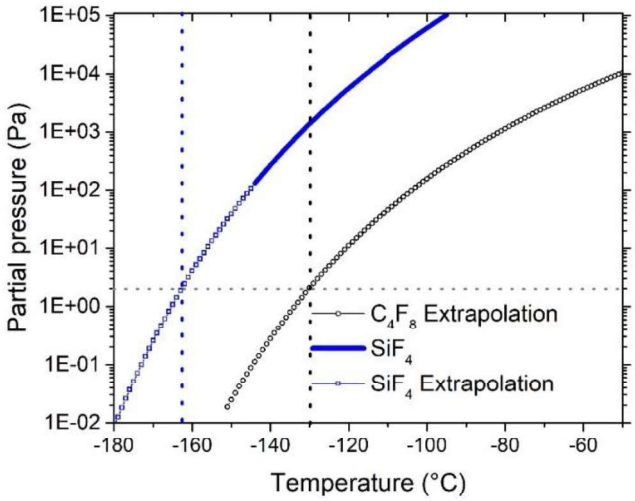

Fig. IV. 10. SiF_4 and C_4F_8 vapor pressure curves as a function of temperature

III.2. Investigation of SiF_4 physisorption by Quadrupole Mass Spectrometry

Even if Fig. IV. 10 showed that SiF_4 should not condense in the experimental conditions reported so far, "physisorption" test was performed and is presented in Fig. IV. 11, in order to confirm its behavior. Same test approach as for C_4F_8 was performed (see section I.7.i.b of Chapter III). SiF_4 was injected for 1 min at 1.0 Pa, then stopped, while at the same time, the SiF_3^+ ion peak intensity, was monitored by QMS. This experiment has been performed at two different temperatures, 20°C and -130°C. Fig. IV. 11 shows that there is no significant difference between the SiF_3^+ signal evolution at -20°C and at -130°C. According to Fig. IV. 10 at 20°C and 1.0 Pa, the process conditions are very far from the condensation conditions of SiF_4. Moreover, there is no desorption slopes observed as for C_4F_8 (see section I.7.i.b of Chapter III). Consequently, it can be assumed that there is no physisorption at 20°C. Thus, as the curve at -130°C is very similar, it confirms again, that there is no SiF_4 physisorption in the conditions used.

It should be noted that, once the SiF_4 flow is stopped, the SiF_3^+ signal decreases first sharply and then more slowly without reaching the minimum observed in the previous experiments. In order to check if this is due to any leakage in the line, SiF_4 was replaced by N_2 using the same gas line and the test was repeated at 20°C with 1 min of N_2 injected at 1.0 Pa. In this case, the signal is decreased very quickly to the background level, which means that N_2 is evacuated rapidly from the reactor chamber. Therefore, this shows that there is a background desorption of SiF_4 inducing a longer time detection. However, this is not related to low temperature physisorption.

20°C / 20°C / -130°C	***Time (s)***	***Flow (sccm)***	***Pressure (Pa)***	***P_{source} (W)***	***V_{bias} (V)***
N_2 or SiF_4	60	50	1.0	0	0

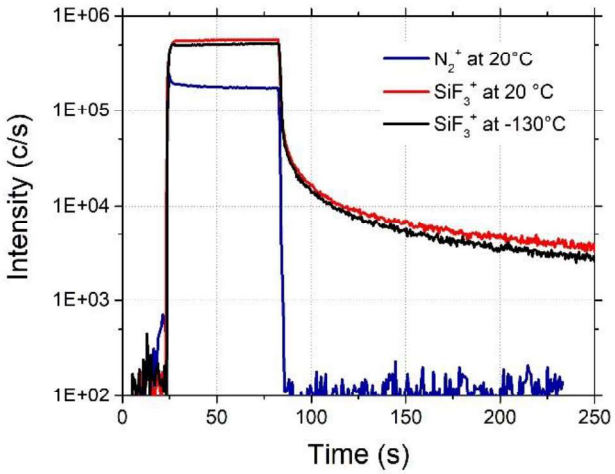

Fig. IV. 11. QMS signal for SiF_3^+ and N_2^+ after 1 min of gas injection

Since there is no clear evidence of SiF_4 physisorption in our experimental conditions, it was decided to not perform tests for atomic scale etching using SiF_4 gas physisorption. Instead of that, and based on the results presented in section III, it is clear that a SiF_4 / O_2 plasma has to be performed at low temperature to increase the surface residence time of SiF_x species and to build an efficient SiO_xF_y layer. Therefore, it was decided to use SiF_4 / O_2 mixture in plasma phase as the modification step of the ALE sequence, and to work at low temperature.

IV. Application to nanoscale etching

It has been reported in [9] and [28] that the formation of a passivation layer in particular, in SF_6 / O_2 plasma, made it possible to obtain a selectivity of approximately 400:1 between Si and SiO_2. For this promising selectivity and based on previous results, it has been decided to use SiF_4 / O_2 plasma to develop cryo-ALE on a-Si. However, as it will be shown in the next section, our experiments could not achieve any self-limiting behavior. Therefore, this process is rather referenced here to as cryogenic nanoscale etching.

IV.1. Presentation

The approach of the nanoscale etching process is quite similar to that of cryo-ALE using C_4F_8. The generic process sequence for one cycle is presented in Fig. IV. 12. First, the substrate cooled at cryogenic temperature is exposed to a short SiF_4 / O_2 plasma without bias in order to modify the substrate surface by depositing a thin SiO_xF_y layer. Then, a step of about 30 s of pumping is inserted to remove all the remaining species from the gas in the reactor chamber. Afterwards, an Ar plasma is ignited to initiate the etching. Depending on the process conditions, a low bias could be applied. After the Ar plasma, a second pumping step is inserted to evacuate all the etch products from the reactor before starting a new cycle.

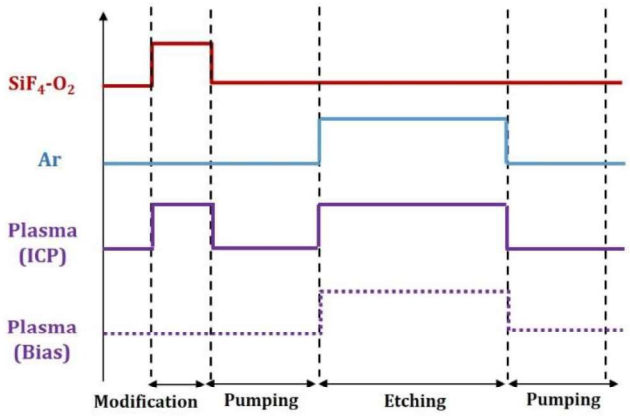

Fig. IV. 12. Time diagram of a cycle using the SiF_4 / O_2 plasma process

IV.2. Effect of substrate temperature

Following the process sequence presented previously in Fig. IV. 12, the first step was consisting in investigating the effect of temperature on the process. Tests were performed on three different materials in order to check the selectivity between them. a-Si coupon was glued in the center of a 6" SiO_2 wafer. At the lateral sides, Si_3N_4 and SiO_2 coupons were also glued. A sketch of this setup is presented in Fig. IV. 13. a.

Fig. IV. 13. b shows the thickness variation during 8 cycles of the process described in Fig. IV. 13 on a-Si, monitored by in-situ SE in kinetic mode, at different temperatures. At 20°C, the process is in deposition regime. The SiO_xF_y thickness increases during each SiF_4 / O_2 plasma. Then, for the two first cycles, the thickness of the deposited layer does not vary during Ar plasma. From the third cycle, a slight decrease of the thickness starts to be observed during the Ar plasma steps. However, even after 8 cycles, the SiO_xF_y layer still accumulates on the surface and the substrate is not etched at all.

The first two cycles of the processes performed between -40°C and -65°C behave in the same way. However, from the third cycle, the effect of temperature begins to appear as the cycles progress. Indeed, from the third cycle, the thickness decreases during the Ar plasma steps. However, the thickness etched per cycle during the Ar plasma step is higher when the temperature is lower. Therefore, after the 8 cycles, at -40°C, the remaining deposited thickness is only 0.54 nm thick, whereas at -65°C, about 0.45 nm of a-Si is etched.

When decreasing the process temperature to -70°C, a deposition is observed during SiF_4 / O_2 plasma steps and a-Si is etched from the first cycle during the Ar plasma step. Same behavior is observed at -80°C, however a higher amount (about 0.2 nm more) is etched per cycle in comparison to -70°C.

Finally, at -100°C, the process is always in etching regime. At this temperature, the SiF_4 / O_2 plasma already etches a-Si as the thickness decreases during this step. And during the Ar plasma steps, the etching continues, without observing any self-limiting behavior. At the end of the 8 cycles, about 6.5 nm of a-Si were etched.

In summary, these tests have shown the existence of a threshold temperature. At a temperature higher than this threshold, the process is in a deposition regime, while at a lower temperature, it goes into an etching regime.

This threshold between deposition to etching is observed at a temperature around -60°C.

In Fig. IV. 13. d, a zoom is performed on the fourth cycle achieved on a-Si at -65°C to highlight the thickness evolution during a cycle. During the SiF_4 / O_2 plasma, the thickness increases linearly as the SiO_xF_y layer is deposited on the sample surface. Then, during the 30 s long pumping step, residual species that did not adsorb to the surface are evacuated, and the thickness remains constant. During this step, no desorption is observed and the deposited

layer thickness is stable. Then, during the Ar plasma, the thickness decreases continuously due to constant etching. The SLE is not reached, which means that the thickness of the deposited layer must be thinner to control more accurately the EPC. Finally, during the last step, a second pumping step is performed, where the thickness does not vary.

	Time (s)	***Flow (sccm)***	***Pressure (Pa)***	***P_{source} (W)***	***V_{bias} (V)***
1. Modification: *SiF_4 / O_2*	3	5 / 35	0.7	1500	Floating
2. Pumping:	30	0	0.1	0	0
3. Etch plasma: *Ar*	180	100	3.1	400	Floating
4. Pumping:	15	0	0.1	0	0

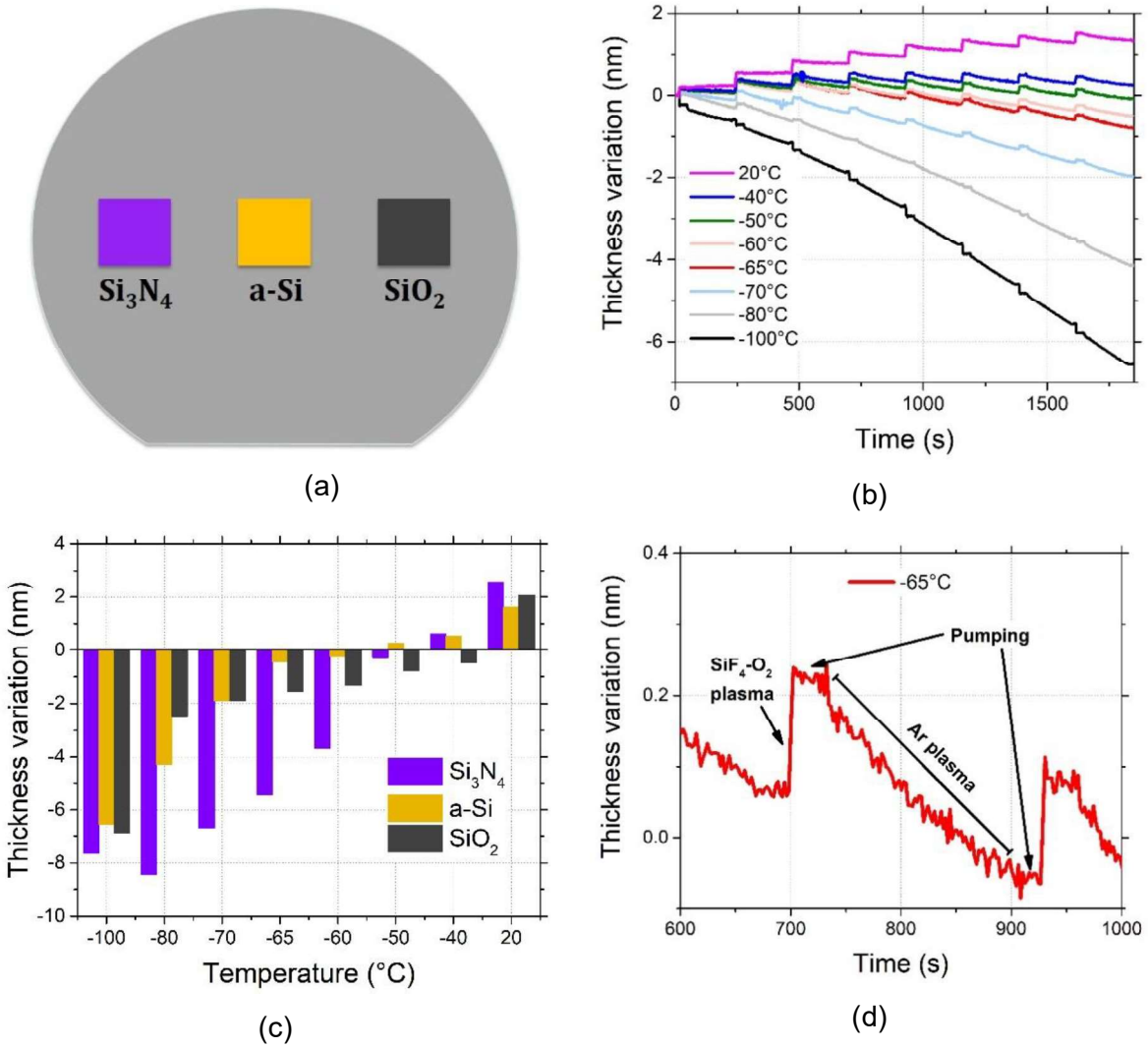

Fig. IV. 13. Effect of substrate temperature on the etching in a SiF_4 / O_2 process performed during 8 cycles, (a) coupons glued on a 6'' SiO_2 carrier wafer (b) a-Si thickness variation versus time monitored in kinetic mode by in-situ SE, (c) Thickness variation of Si_3N_4, SiO_2 and a-Si versus temperature measured ex-situ, (d) zoom on one cycle from the curve -65°C in (b) on a-Si

Fig. IV. 13. c shows the thickness variation measured by ex-situ SE on the three different materials after 8 cycles versus temperature.

In the case of SiO_2, at the end of the 8 cycles, there was no etching of the material at 20°C but a deposition of about 2.1 nm. However, when the temperature was decreased to -40°C and below, SiO_2 was always etched at the end of the process. And the total etched amount increases with the temperature decrease. Indeed, about 0.5 nm was etched at -40°C and 6.9 nm at -100°C.

In the case of Si_3N_4, the process was in a deposition regime at 20°C and -40°C, as respectively 2.6 nm and 0.6 nm were deposited at the end of the 8 cycles. Thus, the total deposited amount decreased with temperature decrease. And when the process temperature was at -50°C and below, Si_3N_4 was always etched. As for SiO_2 and Si_3N_4, the total etched amount increased with temperature decrease. Indeed, about 0.3 nm were etched at -50°C, and 7.6 nm at -100°C.

In summary, there was always a deposition on the three materials for the processes at 20°C. In [2], the authors reported that O atoms are in competition with F atoms to create the SiO_xF_y layer on Si. At high O concentration, a higher ion bombardment energy is needed for etching. So, as in Fig. IV. 13 there is no etching during the Ar plasma which is run without bias, it may mean that an oxide layer was deposited on Si surface at 20°C.

Then, there is a threshold temperature below which these materials are etched. And the more the temperature is decreased, the more the total etched thickness increases.

Nevertheless, the threshold temperature is not the same for the three materials. Indeed, the etching regime is reached at -40°C for SiO_2, close to -50°C for Si_3N_4 and about -60°C for a-Si. Thus, the temperature seems to be an important factor to reach high selectivity over the materials. Indeed, for example, for temperatures between -60°C and -70°C, a selectivity as high as 14:1 is obtained between Si_3N_4 and a-Si.

On the other hand, selectivity between a-Si and SiO_2 drops by decreasing the temperature. The mechanisms involved in this selectivity will be discussed in section V.2.iv of this chapter.

IV.3. Influence of SiF_4 / O_2 mixture

In Fig. IV. 14, the influence of the relative concentration of SiF_4 in the SiF_4 / O_2 deposition plasma has been studied during 8 cycles of the atomic scale etching process at -65°C. The thickness of a-Si was followed as a function of time by SE in kinetic mode on the sample glued at the center of the wafer (Fig. IV. 14. a), whereas the thickness of SiO_2 and Si_3N_4 was measured by ex-situ SE after the process (Fig. IV. 14. b). The configuration of the coupons glued on the carrier wafer was the same as in Fig. IV. 13. a.

The curves displayed in Fig. IV. 14. a. show that, when the SiF_4 content is increased, the thickness of the deposited layer is increased at the end of the process.

If looking closer at one cycle, it is observed that the amount deposited on a-Si increases with the SiF_4 content during the SiF_4 / O_2 plasma. Then, if looking at the curve corresponding to

20 sccm SiF_4 / 20 sccm O_2, it can be noticed that the deposited layer is half removed during the Ar plasma at the first cycles. Then, the etched amount tends to decrease along the cycles, and consequently, the SiO_xF_y layer grows cycle after cycle. The same behavior is observed for the 15 sccm SiF_4 / 25 sccm O_2. However, the decrease of the SiF_4 flow by 5 sccm induces a significant decrease of the deposited amount during a SiF_4 / O_2 plasma. Indeed, about 4 nm were deposited in average during a single modification step with 20 sccm SiF_4 / 20 sccm O_2, and it drops to 0.85 nm deposited with 15 sccm SiF_4 / 25 sccm O_2.

For the 10 sccm SiF_4 / 30 sccm O_2, and 5 sccm SiF_4 / 35 sccm O_2, about 0.3 nm and 0.12 nm are deposited respectively during SiF_4 / O_2 plasma. However, the thickness variation follows a different evolution for these two mixtures. During the four first cycles for the 10 sccm SiF_4 / 30 sccm O_2, the total thickness increases, and then starts to decrease. Nevertheless, a-Si is not etched even after 8 cycles.

For the 5 sccm SiF_4 / 35 sccm O_2 condition, during the three first cycles, only the deposited layer is etched. And from the fourth cycle, a-Si is also etched.

Hence, only the 5 / 35 sccm flow ratio has enabled to etch a-Si at the end of the 8 cycles.

-65°C	***Time (s)***	***Flow (sccm)***	***Pressure (Pa)***	***P_{source} (W)***	***V_{bias} (V)***
1. Modification: *SiF_4 / O_2*	3	varied	0.7	1500	Floating
2. Pumping:	30	0	0.1	0	0
3. Etch plasma: *Ar*	180	100	3.1	400	Floating
4. Pumping:	15	0	0.1	0	0

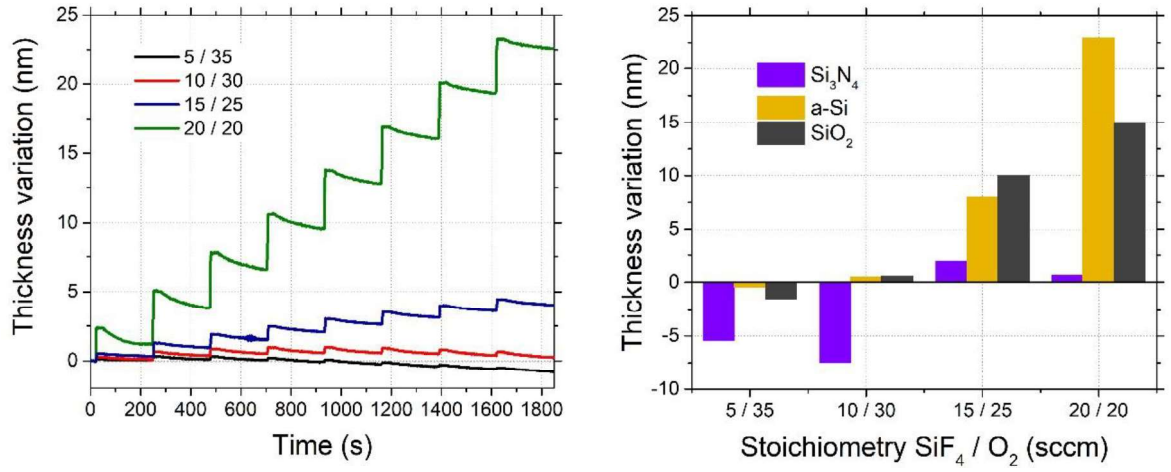

Fig. IV. 14. 8 cycles of etching performed at -65°C depending on SiF_4 / O_2 mixture and monitored by SE, (a) on a-Si in kinetic mode, (b) in Mono mode on a-Si, Si_3N_4 and SiO_2

For SiO_2 and Si_3N_4, the thickness variation was evaluated only at the end of the cycles, and results are presented in Fig. IV. 14. b. The 8 cycles processes with 15 sccm SiF_4 / 25 sccm O_2, and 20 sccm SiF_4 / 20 sccm O_2 always led to an increase of the thickness (resulting in a deposition regime). With 5 sccm SiF_4 / 35 sccm O_2, the process was in etching regime for all

materials. The most promising and interesting selectivity was obtained for the process with 10 sccm SiF_4 / 30 sccm O_2, for which about 7 nm of Si_3N_4 were etched, while a thin deposited layer remains on a-Si and SiO_2 samples.

V. Study on one long cycle for the understanding of the modification step

V.1. Process sequence

To better understand the involved mechanisms giving such a good selectivity, it has been chosen to perform one cycle only with longer time steps. The process and the parameters used are presented in Fig. IV. 15. Each material was studied separately. a-Si coupon was glued on a Si 6" wafer, Si_3N_4 coupon on a 6" SiN wafer and SiO_2 on a SiO_2 6" wafer to avoid any contamination of the plasma. The coupons were always glued in the middle of the carrier wafer in order to acquire in-situ SE measurements.

Instead of applying SiF_4 / O_2 plasma for only 3 s as in a process sequence of several cycles, the plasma time was extended to 30 s to deposit a sufficient amount for analysis. An accurate in-situ ellipsometric spectrum was acquired before and after this deposition step. This accurate spectrum acquisition requires about 4 min. Therefore, the pumping step time after the SiF_4 / O_2 plasma was increased to 4.5 min to perform the acquisition. Then, the Ar plasma etching step was set to 15 minutes. Another final accurate SE acquisition was performed after the Ar plasma. Tests were performed at -40°C, -65°C and -100°C for the three materials.

-40°C / -65°C / -100°C	***Time (min)***	***Flow (sccm)***	***Pressure (Pa)***	***P_{source} (W)***	***V_{bias} (V)***
1. Modification: *SiF_4 / O_2*	0.5	10 / 30	1.2	1500	Floating
2. Pumping:	≈ 4.5	0	0.1	0	0
3. Etch plasma: *Ar*	15	100	3.1	400	-10

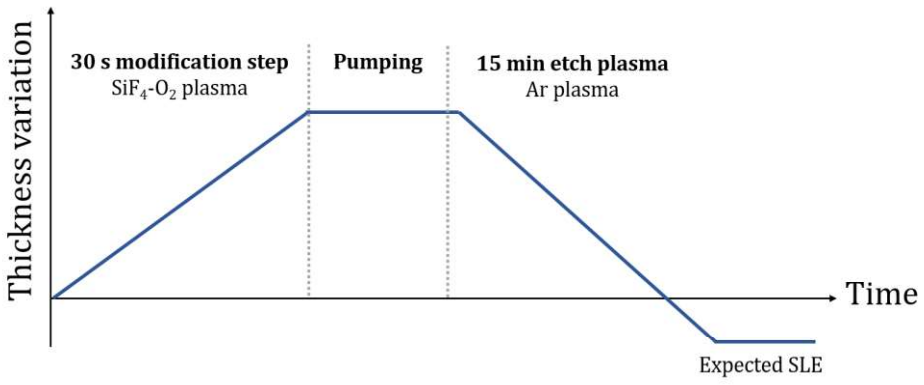

Fig. IV. 15. Expected behavior for the thickness in a one cycle process

XPS measurements were also performed at IMN Nantes in the Optimist reactor on a-Si and Si_3N_4 samples after a process similar to that described in Fig. IV. 15. As the reactors are different, some parameters were adjusted. The power was decreased to 200 W and the pressure increased to 3.0 Pa in order to be able to start the plasma. Since the O_2 mass flow controller (MFC) was limited to 20 sccm, the SiF_4 and O_2 flow were respectively decreased to 6.6 sccm and 20 sccm to keep the same SiF_4 / O_2 ratio. Parameters are summarized in Table. IV. 6.

The surface was analyzed by XPS immediately after SiF_4 / O_2 plasma at the same three different temperatures (-40°C, -65°C and -100°C) and a second analysis was performed once the sample was brought back to room temperature.

Table. IV. 6. Process parameters used in OPTIMIST to build-up SiO_xF_y layer for XPS analysis

-40°C / -65°C / -100°C	***Time (s)***	***Flow (sccm)***	***Pressure (Pa)***	***P_{source} (W)***	***V_{bias} (V)***
SiF_4 / O_2	30	6.6 / 20	3.0	200	Floating

V.2. Characterization of the SiO_xF_y layer as a function of the substrate material

V.2.i. *a-Si*

V.2.i.a. Thickness variation as a function of temperature

The process presented in Fig. IV. 15 was first run on a-Si and the thickness variation was monitored by SE. Fig. IV. 16. a shows the growth of SiO_xF_y layer versus time at three different temperatures. At -40°C and -65°C, the SiO_xF_y layer grows linearly during SiF_4 / O_2 plasma with a deposition rate of respectively 0.48 $nm.s^{-1}$ and 0.45 $nm.s^{-1}$. There is no saturation of the deposition, as the thickness keeps growing. Once the Ar plasma is started, no significant thickness variation is observed, which means that the layer could not be etched.

However, at -100°C, the deposited layer is less than 0.5 nm thick, much thinner than at -40°C and at -65°C, as shown in Fig. IV. 16. a. Once the Ar plasma is started at -100°C, the deposited layer is removed and then, about 10 nm of a-Si is etched in about 15 min.

Chemical etching is achieved during this Ar plasma step. However, when having a closer look at the -100°C curve in Fig. IV. 16. b we can notice a slope break (represented with dotted lines) at around 500 s (8 min of Ar plasma). This can be due to fluorine amount on the surface being reduced or depleted. However, the etching continues due to fluorine deposited on the reactor sidewalls.

The other explanation would be that some undesired sputtering is occuring. Indeed, the Langmuir probe measurements presented in Fig. III. 27 of Chapter III showed that the plasma potential of the Ar plasma at 400 W is about 10 V. Therefore, with the -10 V applied bias, the ion energy is estimated at ≈ 20 eV. And according to [29], the physical sputtering threshold of Si is close to 20 eV. If the etching occurring after the break is considered to be only due to sputtering, the related ER can be estimated to ≈ 0.08 Å.s^{-1} by considering 3 nm etched in 375 s. Fig. IV. 16. c summarizes the thickness variation versus the temperature: in full color, the SiO_xF_y deposited layer on a-Si after the SiF_4 / O_2 plasma, and in hatched color, the thickness after Ar plasma. They were measured by SE in monochromator acquisition mode. Those measurements provide a higher accuracy than the measurements taken in kinetic regime, with the multi wavelengths acquisition mode. The measured thickness may vary by few nm between the 2 modes. The graph highlights that etching is only achieved after Ar plasma at -100°C, whereas at higher temperatures, there is deposition.

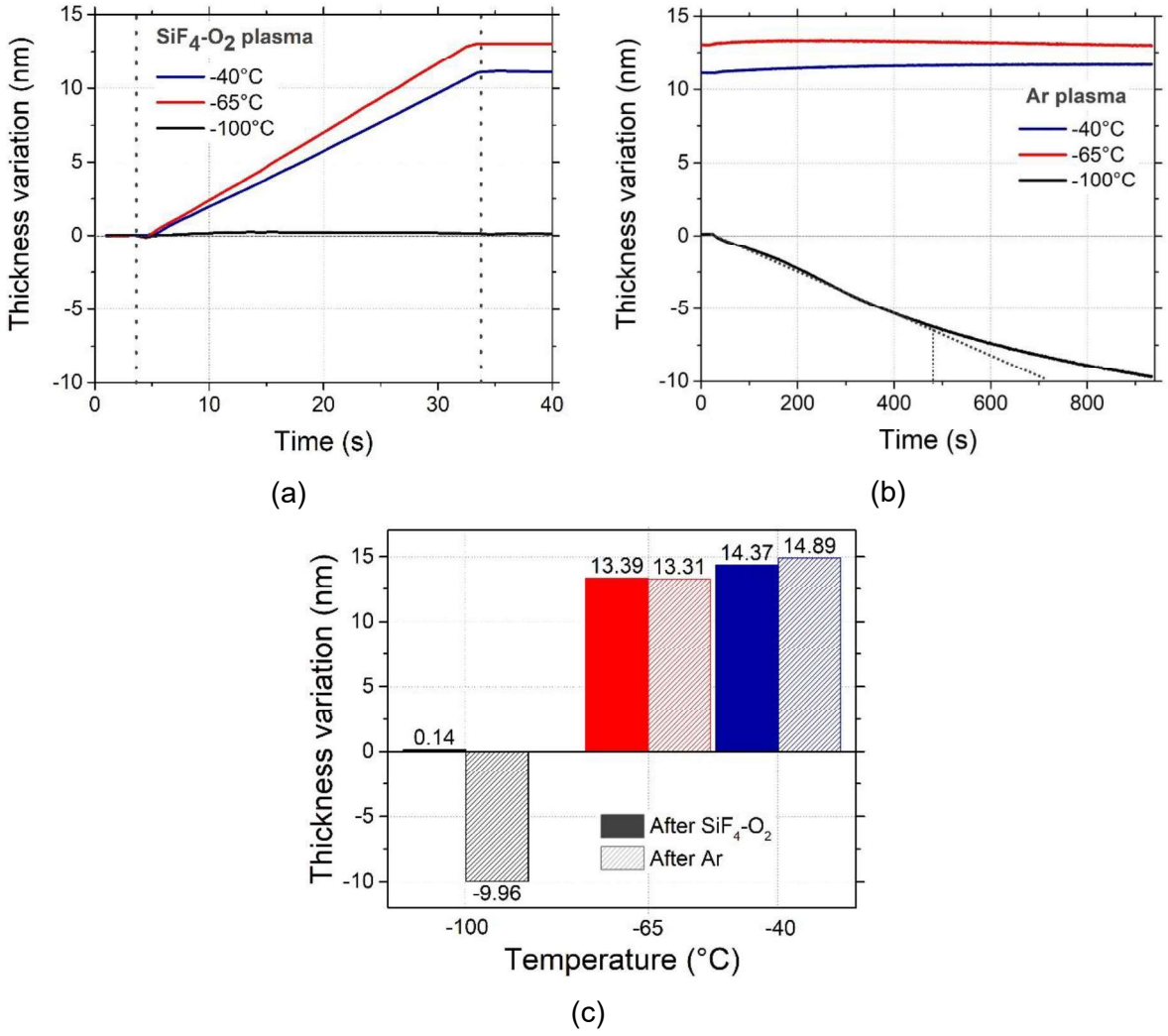

Fig. IV. 16. Thickness variation of a-Si measured by SE depending on temperature during (a) Measurements in kinetic mode during SiF_4 / O_2 plasma, (b) measurements in kinetic mode during Ar plasma, (c) measurements in Mono mode after each plasma

V.2.i.b. Surface analysis by X-ray Photoelectron Spectroscopy

As explained above, XPS measurements were performed to investigate the a-Si surface evolution during deposition and etching at the three different temperatures. The F 1s, O 1s, C 1s and Si 2p components are plotted before deposition, after deposition and after the a-Si sample is heated to room temperature for each deposition temperature from Fig. IV. 17 to Fig. IV. 20. Then, both the large spectrum and the percentage quantification are presented in Fig. IV. 21 and in Fig. IV. 22 respectively, under the same experimental conditions as in Table. IV. 6. Peak identification was carried out using different sources from literature [1], [11], [18], [24], [30].

Fig. IV. 17 presents the fluorine F 1s core level for each temperature: the spectrum of the raw sample, after deposition and then after warming up to room temperature (without Ar plasma exposure). Firstly, it shows that the raw sample did not have any fluorine on its surface. At -40°C and -65°C (Fig. IV. 17. a and Fig. IV. 17. b), a peak appears at 687.2 eV. It corresponds to F-Si(O) bonds. This peak is very similar for the two temperatures and does not vary after warming the sample back to 20°C. However, a small tail can be observed after deposition at -65°C at 685.5 eV. It can also be attributed to F-Si bonds. At -100°C (Fig. IV. 17. c) and according to [12] the sticking coefficient of SiF_x is higher, which may explain the intensity increase of the peak at around 685.5 eV for that temperature. And when the substrate is heated to room temperature, a significant part of fluorine desorbs. This confirms that, at the opposite to -40°C and -65°C, the bonds at -100°C are weak and are probably related to physisorption, but not chemisorbed species.

Fig. IV. 18 shows O 1s core level variation for the three temperatures. One peak is observed at all temperatures for the reference sample and remains even after deposition at -40°C and -65°C (Fig. IV. 18. a and Fig. IV. 18. b). This peak is located at 532.7 eV and corresponds to O-Si bonds of native oxide at the surface of Si. Indeed, this can be expected as there is always few nanometers of native oxide at the surface of Si. This peak remains almost identical after deposition and after warming at -40°C and -65°C. At those temperatures, the oxygen brought by the plasma would simply bond to Si and oxidizes the Si surface.

However at -100°C (Fig. IV. 18. c), the peak intensity decreases and the peak is slightly shifted to 534 eV. The decrease of the peak at 532.7 eV shows that the surface is covered by a deposited layer. The shifted peak at 534 eV corresponds to O-H bonds and confirms that some water is physisorbed at that temperature. Two other peaks that were not present at higher temperatures appear at -100°C at 541 eV and 545.5 eV. They are attributed to some contamination. Those peaks as well as that at 534 eV disappear when the sample is brought back to room temperature. This suggests here as well that the bonds are weak at low temperature and can be attributed to physisorbed species.

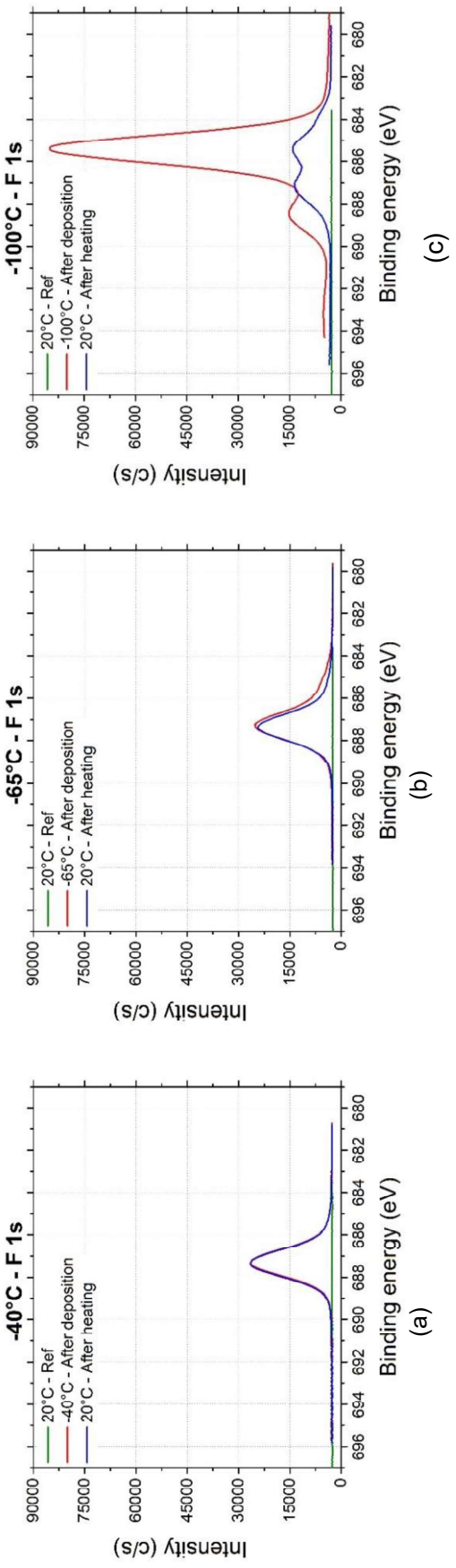

Fig. IV. 17. XPS scan of F 1s component on a-Si coupon: before, after deposition, and after heating. For deposition at (a) -40°C, (b) -65°C and (c) -100°C, using plasma parameters of Table. IV. 6

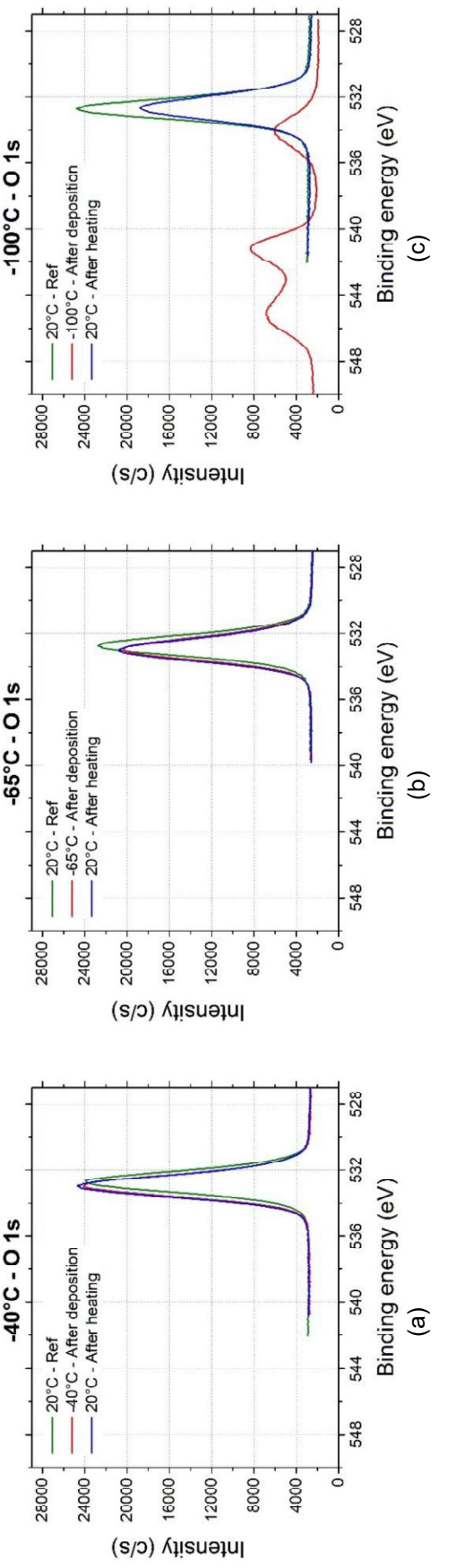

Fig. IV. 18. XPS scan of O 1s component on a-Si coupon: before, after deposition, and after heating. For deposition at (a) -40°C, (b) -65°C and (c) -100°C, using plasma parameters of Table. IV. 6

Fig. IV. 19 shows the evolution of the core level C 1s. The reference samples always presented a small peak at 285 eV. It corresponds to some surface contamination by carbon. After deposition, this peak is not detected anymore, even after warming. Therefore, the acquisitions were not performed on C 1s after heating, as no more carbon can be detected on the wide spectra in Fig. IV. 21. Two peaks appear at 291 eV and 293 eV after deposition at -100°C and disappear after warming. Again, this could be related to physisorbed species, trapped by water that condenses and then desorb after heating up to room temperature.

Fig. IV. 20 presents the evolution of the Si 2p core level. Two Si typical peaks of reference samples are detected. The first, observed at 99.2 eV, corresponds to Si-Si bonds and the second, located at 103.5 eV, is related to Si-O bonds. The latter is due to the native oxide present at the silicon surface, and confirms the peak at 532.7 eV of the O 1s peak.

When deposition is performed on the Si sample at -40°C and -65°C, the Si-O peak at 103.5 eV shifts to 104.5 eV (Fig. IV. 20. a and Fig. IV. 20. b). This shifted peak also corresponds to Si-O bonds, but comes from a silicon oxyfluoride layer. The peak is still present after heating, like what was reported for the F 1s. This confirms the modification of the surface into a $Si_xO_yF_z$ chemisorbed layer that does not desorb at room temperature. At -100°C, the peak at 99.2 eV totally disappears. At this temperature, silicon is covered by fluorine based species (Fig. IV. 20. c). Hence, it can be concluded that Si detected at 104.5 eV is related to the deposited layer from SiF_4 / O_2 plasma, but not from the substrate.

When the sample is brought back to room temperature, desorption occurs from the surface. The Si-O peak at 104.5 eV shifts back to 103.5 eV and the peak Si-Si at 99.2 eV is detected again. This shows that, at -100°C, and contrary to the two other temperatures, the deposited layer desorbs.

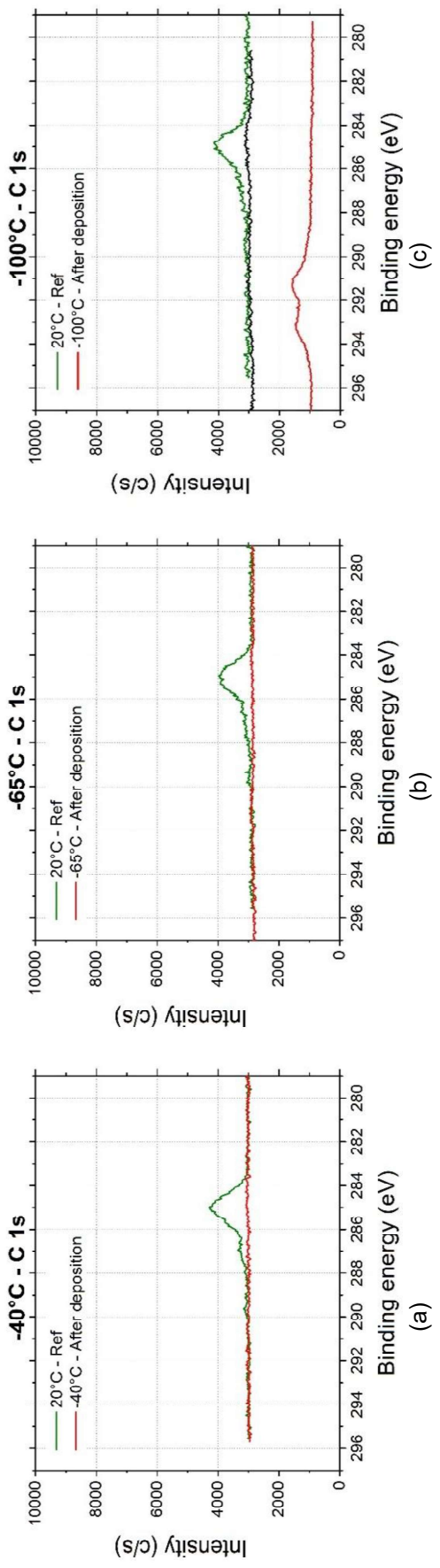

Fig. IV. 19. XPS scan of C 1s component on a-Si coupon: before, after deposition, and after heating. For deposition at (a) -40°C, (b) -65°C and (c) -100°C, using plasma parameters of Table. IV. 6

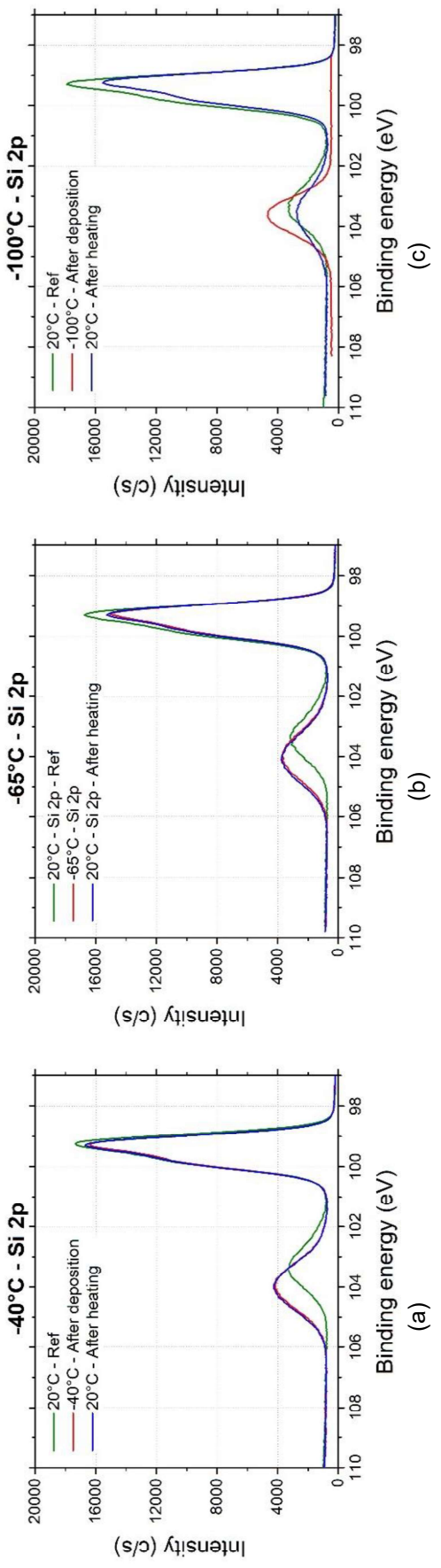

Fig. IV. 20. XPS scan of Si 2p component on a-Si coupon: before, after deposition, and after heating. For deposition at (a) -40°C, (b) -65°C and (c) -100°C, using plasma parameters of Table. IV. 6

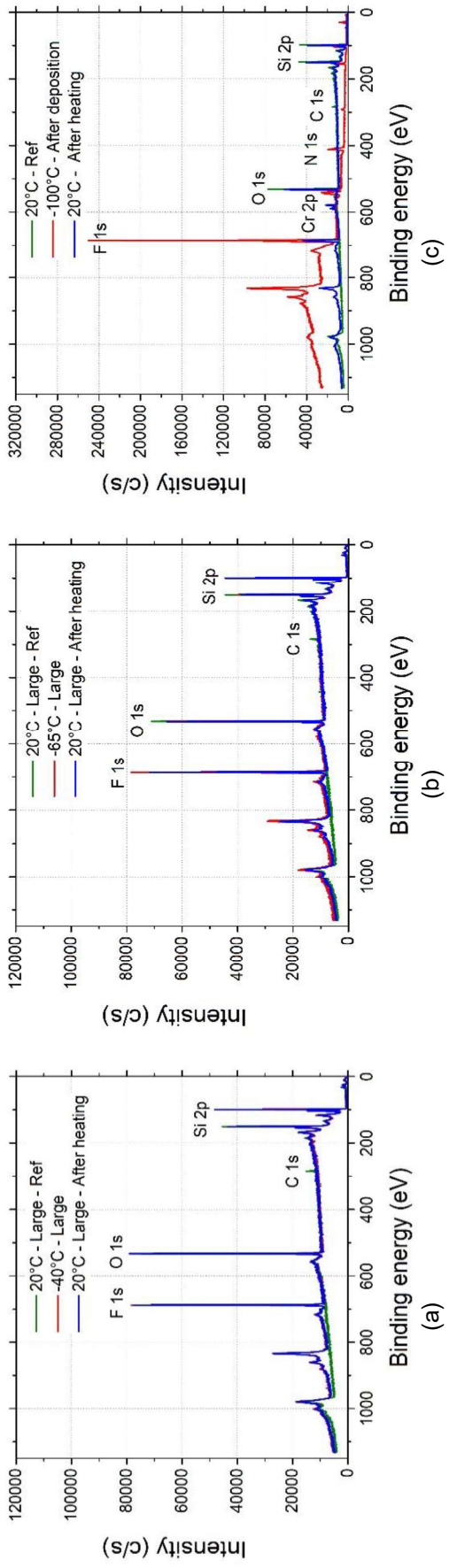

Fig. IV. 21. XPS wide scan of a-Si coupon: before, after deposition and after heating. For deposition at (a) -40°C, (b) -65°C and (c) -100°C, using plasma parameters of Table. IV. 6

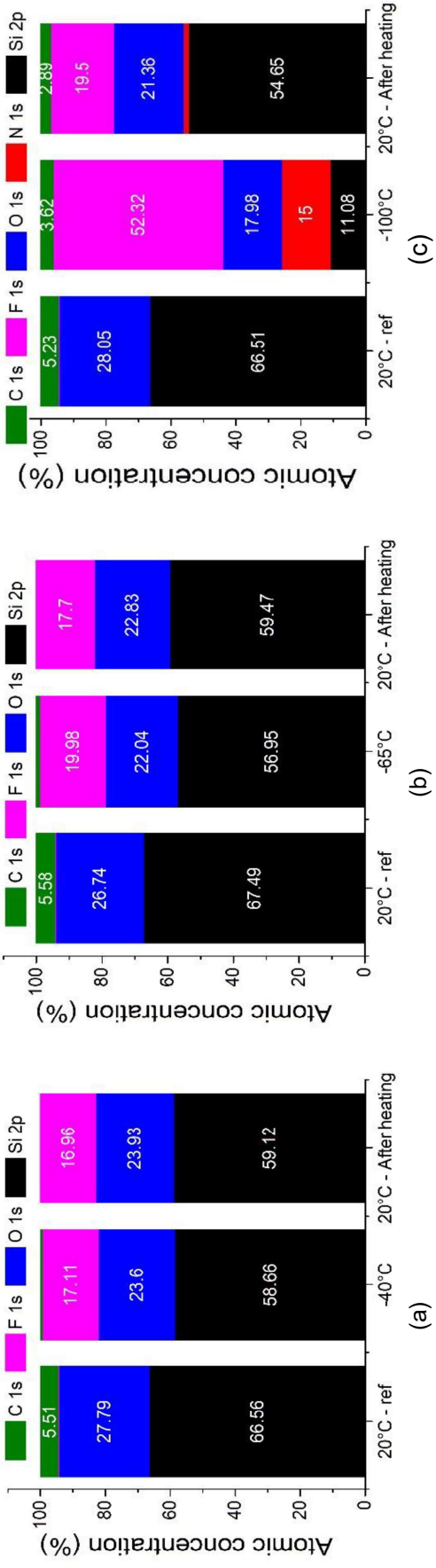

Fig. IV. 22. Quantification of surface composition determined by XPS before, after deposition and after heating. For deposition at (a) -40°C, (b) -65°C and (c) -100°C, using plasma parameters of Table. IV. 6

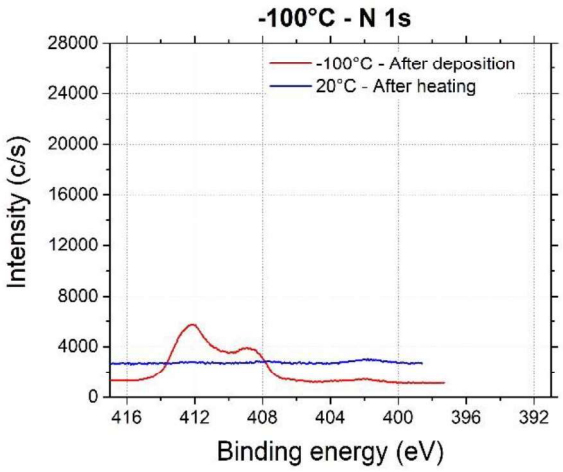

Fig. IV. 23. XPS scan of N 1s component on a-Si coupon: before, after deposition, and after heating.
For deposition at (a) -40°C, (b) -65°C and (c) -100°C, using plasma parameters of Table. IV. 6

Fig. IV. 21, which displays wide spectra, sums up the modification for each temperature. It is clear that the surface is quite similar after deposition and heating at -40°C and -65°C because, as shown in more details previously, the F 1s, O 1s and Si 2p peaks do not evolve significantly from one temperature to the other (Fig. IV. 21. a and Fig. IV. 21. b). A very different behavior is obtained at -100°C, where significant changes can be observed (Fig. IV. 21. c). Note that the peak observed at 579.6 eV is related to Cr 2p core level, coming from some contamination from the Ni / NiCr thermocouple welded at the rear of the sample holder.

Fig. IV. 22 provides the relative composition of the surface. From Fig. IV. 22. a and Fig. IV. 22. b, it is confirmed that the deposited layer has a similar composition at -40°C and -65°C. It confirms that there is no significant desorption involved when the deposition is performed at these two temperatures. At these two deposition temperatures, the layers are composed of about 59 % of Si, 23 % of O and 18 % of F. But, when the temperature is decreased to -100°C, the surface is covered by a much higher amount of fluorine (about 52%) (Fig. IV. 22. c). It covers the substrate surface which explains that Si amount corresponds to about 11 % of the composition and O amount to 18 %. As observed in Fig. IV. 22 and Fig. IV. 23, nitrogen is also detected at -100°C with a content of 15 %, which shows that some contamination occurs, due to residual species on the reactor wall or due to some leak of the reactor. However, it is not involved in the deposition mechanism. After heating, a large part of fluorine containing species desorbs, and the final surface composition is close to those obtained at -40°C and -65°C.

In conclusion, lowering the temperature below -65 °C changes the stoichiometry of the SiO_xF_y layer which becomes richer in fluorine. The residence time of species (probably SiF_x) increases at low temperature, allowing a greater probability of surface reaction.

The XPS scans at -100°C confirmed that there is a reorganization of the layer when warming up the substrate to room temperature. This may lead to the formation of SiF_4 as observed by QMS in [12].
Finally, those results also confirm the measurements carried out by SE showing the decrease of the thickness when the sample is brought back to room temperature, and presented previously in section II of this chapter.

V.2.ii. Si_3N_4

V.2.ii.a. Thickness variation as a function of temperature

The same experiment as for a-Si was performed on Si_3N_4: the same process parameters were applied, as presented in Fig. IV. 15.
Fig. IV. 24. a shows the evolution of the thickness measured by SE in kinetic mode on Si_3N_4 during 30 s of SiF_4 / O_2 plasma, versus time for three temperatures, -40°C, -65°C and -100°C. At -40°C and -65°C, as for a-Si, the thickness increases. This indicates that a thin layer of SiO_xF_y is deposited on the substrate. At -40°C, the layer deposition increases linearly, whereas deposition at -65°C is slower and seems to saturate before the end of the deposition step.
Fig. IV. 24. c presents in full color, the thickness measured after SiF_4 / O_2 plasma, in monochromator acquisition mode. It shows that, the deposited layer at -40°C is much thicker (≈ 13 nm) than at -65°C (≈ 4.7 nm).
Interestingly, at -100°C, the thickness decreases directly. There is no deposition like in the case of a-Si, and Si_3N_4 is etched on about 3.7 nm during the SiF_4 / O_2 plasma step (Fig. IV. 24. c).
Then once the Ar plasma is started (Fig. IV. 24. b), the thickness of the deposited layer at -40°C increases, due probably to some small redeposition from the reactor sidewalls. However, at -65°C, the layer is consumed and Si_3N_4 is eventually etched. At -100°C, a small etching is observed, although there was no deposited layer. Once again, no self-limiting behavior is observed. As with a-Si, the slope break observed at -65°C can be due to fluorine on the surface being close to be depleted or to Si_3N_4 sputtering. Indeed, the physical sputtering threshold for this material is about 20 eV ([31]), so a slight sputtering may occur during the Ar plasma. Fig. IV. 24. c sums up in hatched color, the thickness measured after Ar plasma on Si_3N_4. It shows that Si_3N_4 is etched after Ar plasma at both -65°C and -100°C, whereas at -40°C there is a deposited layer that is not etched.

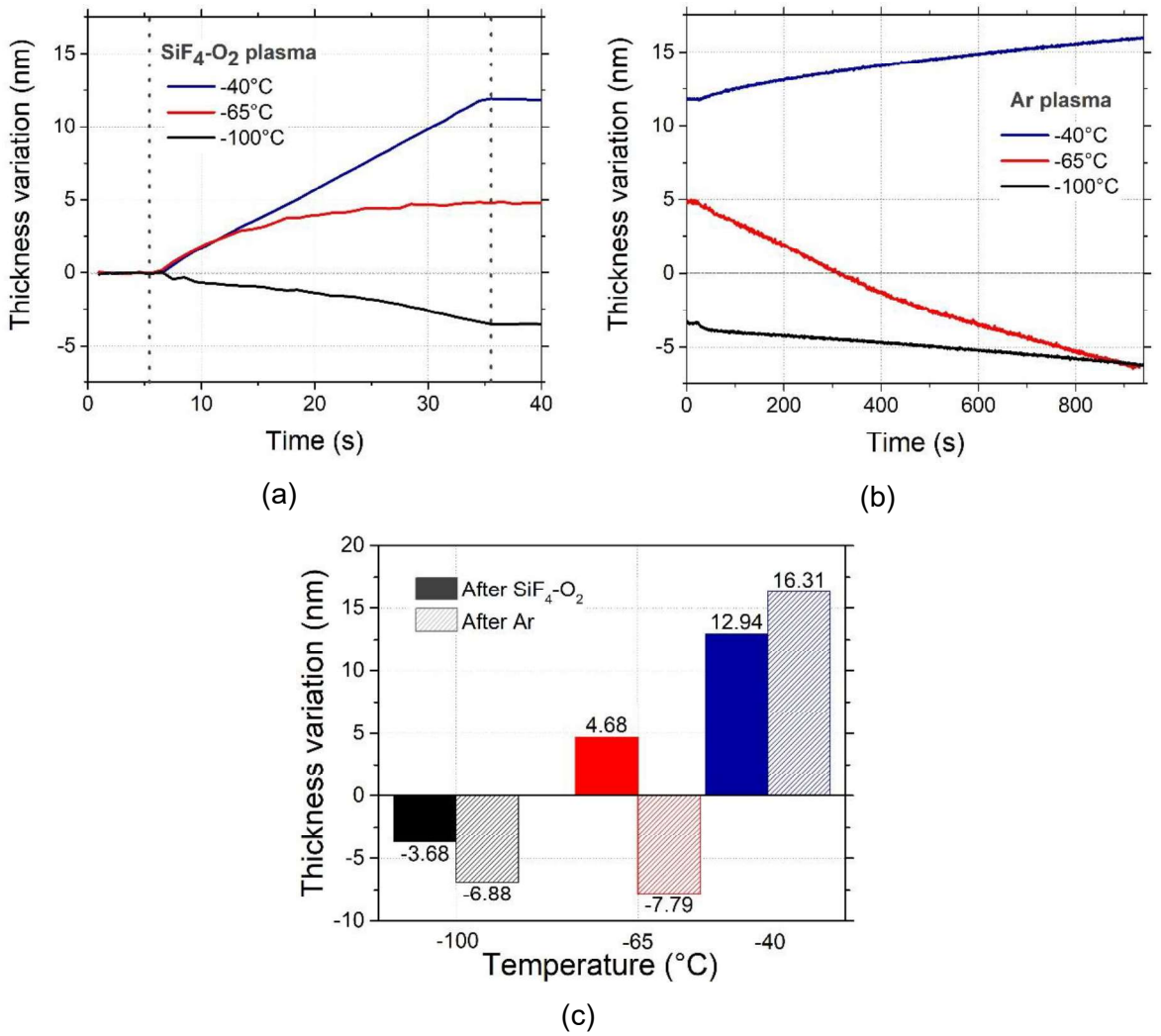

Fig. IV. 24. Thickness variation of Si_3N_4 measured by SE depending on temperature (a) measurements in kinetic mode during SiF_4 / O_2 plasma, (b) measurements in kinetic mode during Ar plasma, (c) measurements in Mono mode after each plasma

V.2.ii.b. Repeatability

As the etching of Si_3N_4 presents a real interest, thanks to its promising selectivity with a-Si, repeatability of the deposition step has been checked on Si_3N_4 for the three temperatures, -40°C, -65°C and -100°C. For each repetition at each temperature, the thickness, measured by in-situ SE versus time, is plotted in Fig. IV. 25. Tests were repeated each time on a new Si_3N_4 coupon, and the delay between each test was from one week to one month.

As it can be noticed in Fig. IV. 25. a and Fig. IV. 25. c, tests at -40°C and -100°C are quite repeatable, with a difference of the order of 1 nm on the final thickness variation after the SiF_4 / O_2 plasma step. Since the process regime moves from deposition at -40°C to etching at -100°C, it means that there is a threshold temperature in between. Tests are less repeatable at -65°C, with a maximum thickness variation of 6 nm between the tests. Hence, it can be

expected that the threshold temperature to switch the process from deposition to etch is close to -65°C and is quite sensitive. However, for all the temperatures, it can be noticed that the deposition rate is quite repeatable during the first 3 seconds of the SiF_4 / O_2 plasma. This is a good point for the nanoscale process which involves a SiF_4 / O_2 plasma step of 3 s.

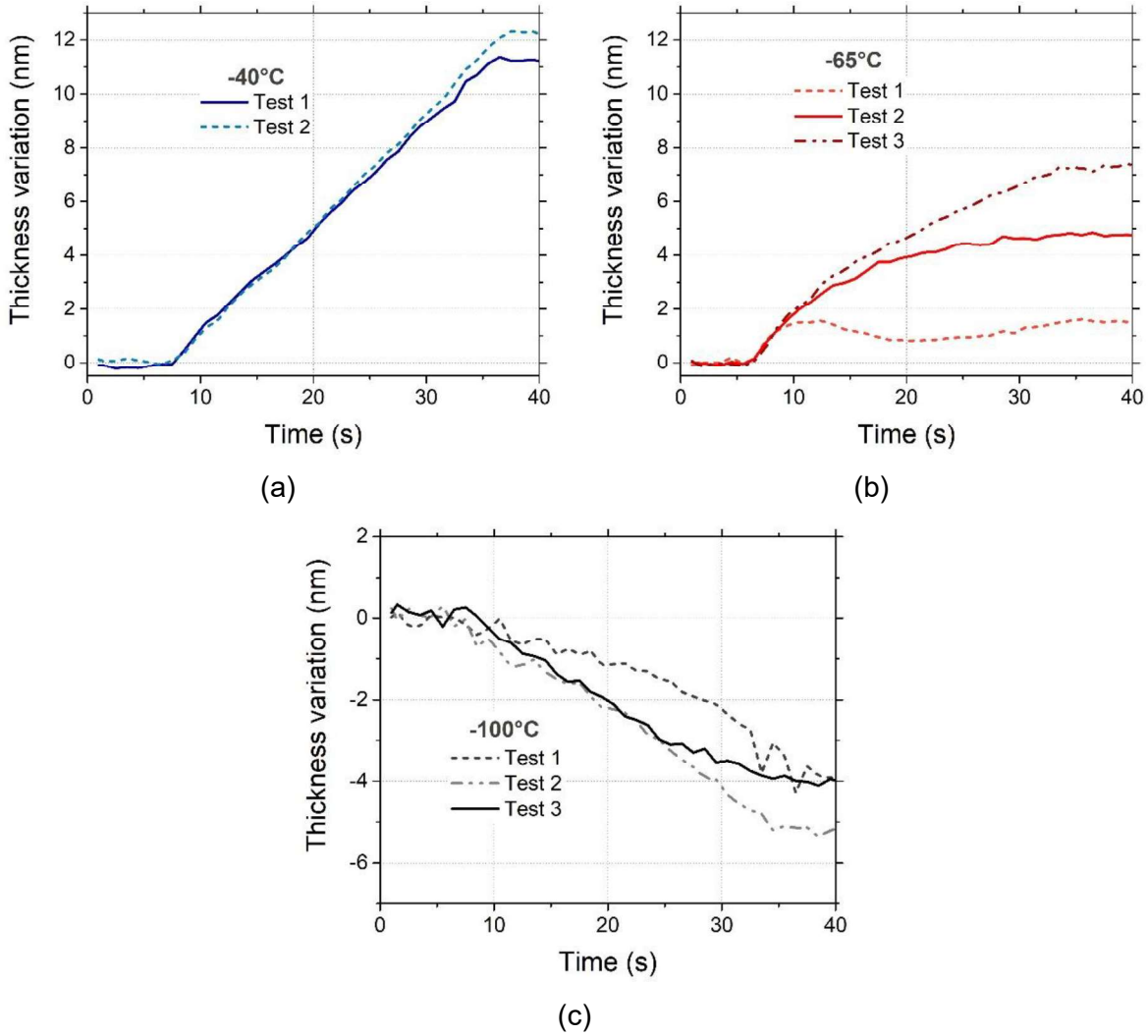

Fig. IV. 25. SiF_4 / O_2 plasma of 30 s performed on Si_3N_4 repeated several times with the thickness monitored by SE at (a) -40°C, (b) -65°C, (c) -100°C

V.2.ii.c. Surface analysis by X-ray Photoelectron Spectroscopy

XPS analysis has also been performed on Si_3N_4 coupons for the three temperatures of interest: -40°C, -65°C and -100°C treated by the process presented in Table. IV. 6 and with the same methodology as for a-Si. Fig. IV. 26 to Fig. IV. 32 present the wide and detailed XPS scans. Peak identification was performed using different articles [1], [11], [18], [30], [32].

Fig. IV. 26 presents the fluorine peaks before and after the SiF_4 / O_2 plasma for three different process temperatures and when the sample is brought back to room temperature after treatment. As for a-Si, there is no fluorine on the samples before the processes. At -40°C (Fig. IV. 26. a) a peak appears at 687.6 eV and stays even after heating, with only a low decrease of its intensity. It corresponds to F-Si bonds. When the temperature is decreased to -65°C (Fig. IV. 26. b), an intense peak appears at 685.5 eV. It also corresponds to F-Si bonds. When the sample is brought back to room temperature, this peak at 685.5 eV disappears almost totally, and only the peak at 687.6 eV remains. The same behavior is observed at -100°C in Fig. IV. 26. c, even though the peak at 687.6 eV (F-Si bonds) is easier to distinguish. Unlike the results at -65°C, a small peak remains at 685.5 eV even after heating.

Fig. IV. 27 shows the O 1s component before and after deposition, after heating and versus temperature. A peak at 532.7 eV corresponding to O-Si bonds is detected on the reference samples. It comes from the native oxide layer. This peak slightly shifts to 534 eV when deposition is achieved at lower temperature related to SiO_xF_y.

At -40°C, in Fig. IV. 27. a, this O 1s peak intensity increases, and slightly shifts, after deposition and keeps increasing after heating the sample up to the room temperature. Oxygen atoms are provided by the SiF_4 / O_2 plasma and react with the deposited species at the surface.

At -65°C and -100°C (Fig. IV. 27. b and Fig. IV. 27. c), the O peak intensity decreases after deposition, which can be explained by a coverage of the substrate surface by SiF_x species. This is confirmed by the fact that the peak increases back after heating, due to the desorption of part of the deposited layer.

Two other peaks appear at 541 eV and 545.5 eV for -65°C and -100°C only after deposition and then disappear during heating. They can be related to physisorbed contamination.

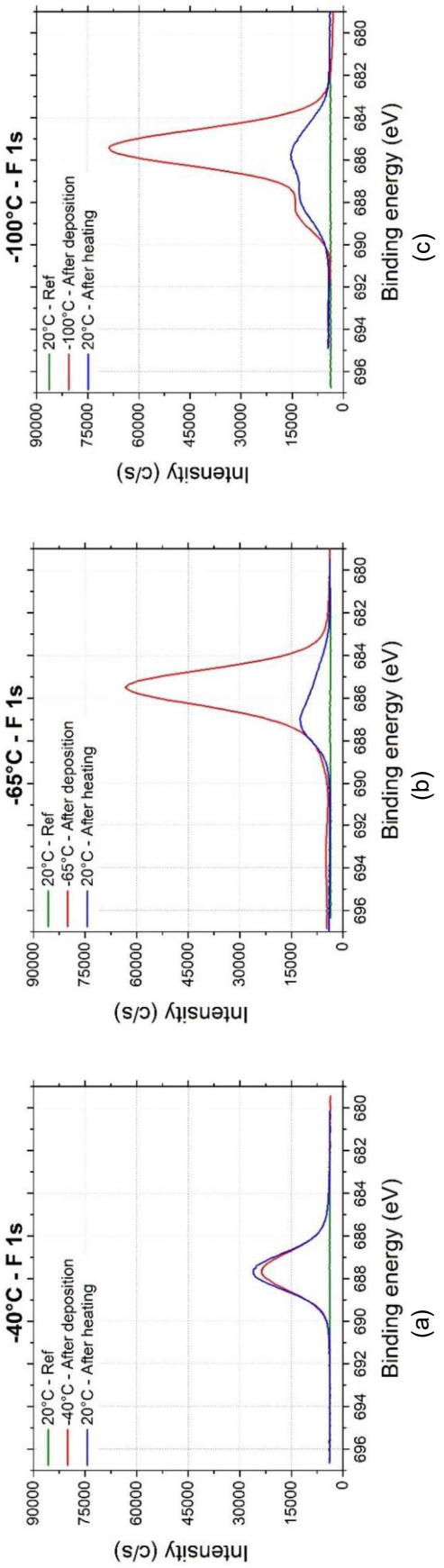

Fig. IV. 26. XPS scan of F 1s component on Si_3N_4 coupon: before, after deposition, and after heating. For deposition at (a) -40°C, (b) -65°C and (c) -100°C, using plasma parameters of Table. IV. 6

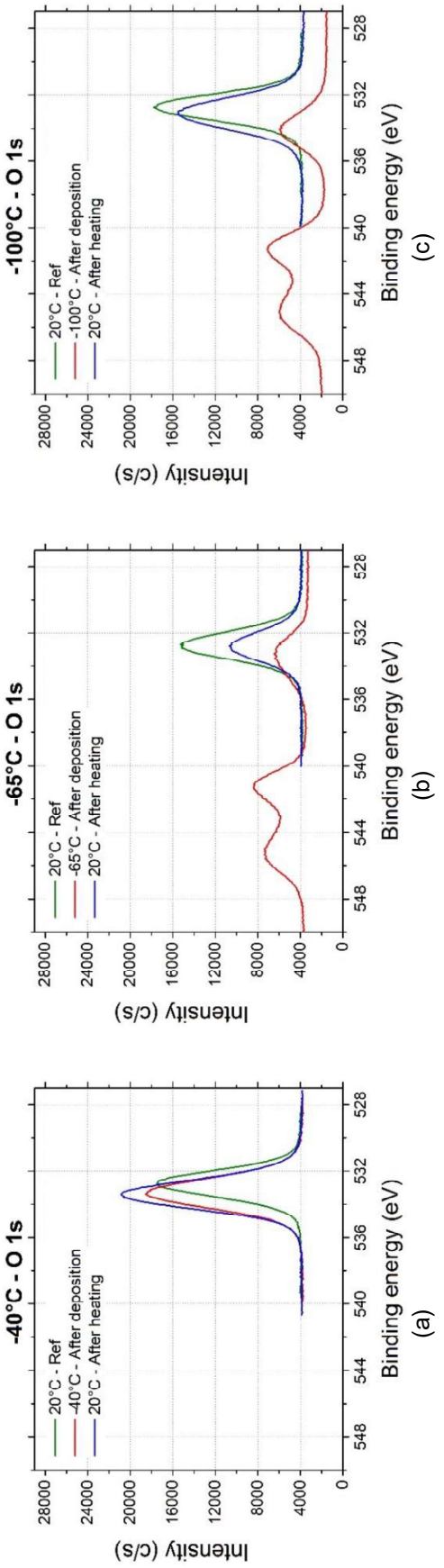

Fig. IV. 27. XPS scan of O 1s component on Si_3N_4 coupon: before, after deposition, and after heating. For deposition at (a) -40°C, (b) -65°C and (c) -100°C, using plasma parameters of Table. IV. 6

Fig. IV. 28 shows the results for N 1s peak as a function of temperature. In the reference sample, a peak is observed at 397.9 eV which corresponds to the N-Si bonds. In Fig. IV. 28. a, at -40°C, the nitrogen peak does not change after the plasma and after the heating to the room temperature. This mean that there is no new type of bonds created between N and other species.

When the surface temperature is -65°C during the deposition step (Fig. IV. 28. b), the intensity of the peak at 397.9 eV decreases significantly. At -100°C (Fig. IV. 28. c), this peak does not appear anymore. Again, this is due to the surface coverage by the SiO_xF_y layer deposited on the surface. When heating the sample to room temperature, the peak appears again, which shows that most of the SiO_xF_y layer desorb from the surface if we increase again the temperature.

Moreover, at those two temperatures, new peaks appear at 409 eV and 413 eV during deposition, probably also due to some physisorbed contamination, as they disappear after heating.

The evolution of C 1s component has also been investigated. Fig. IV. 29 shows that, as on a-Si, there is a small peak at 285 eV due to carbon contamination on the substrate surface. After deposition and heating, there is no more carbon detected on the surface at -65°C (Fig. IV. 29. a). The C 1s peak variation was not monitored with accuracy at -40°C, since it is similar to that at -65°C. However, it is possible to observe in the wide scan (Fig. IV. 31. a and Fig. IV. 31. b) that there is no more carbon detected after deposition neither after heating.

Fig. IV. 29. b shows the carbon variation after deposition at -100°C and after heating. The peak at 285 eV totally disappears because of the deposited layer and two peaks probably related to physisorbed species appear at 293 eV and 291 eV. When the sample is brought back to room temperature, those peaks are not detected anymore and the peak at 285 eV appears again but with a lower intensity.

In Fig. IV. 30, silicon peaks from the core level Si 2p are detected. The reference sample shows one peak only at 102.2 eV, which is attributed to Si-N bonds. At -40°C (Fig. IV. 30. a.), the Si peak shows a shoulder at about 104.5 eV in addition to the first main peak. This peak could correspond to Si-O bonds and / or Si-F bonds. After heating, the spectrum remains similar, meaning that there is no desorption observed and that the deposited layer remains at the surface.

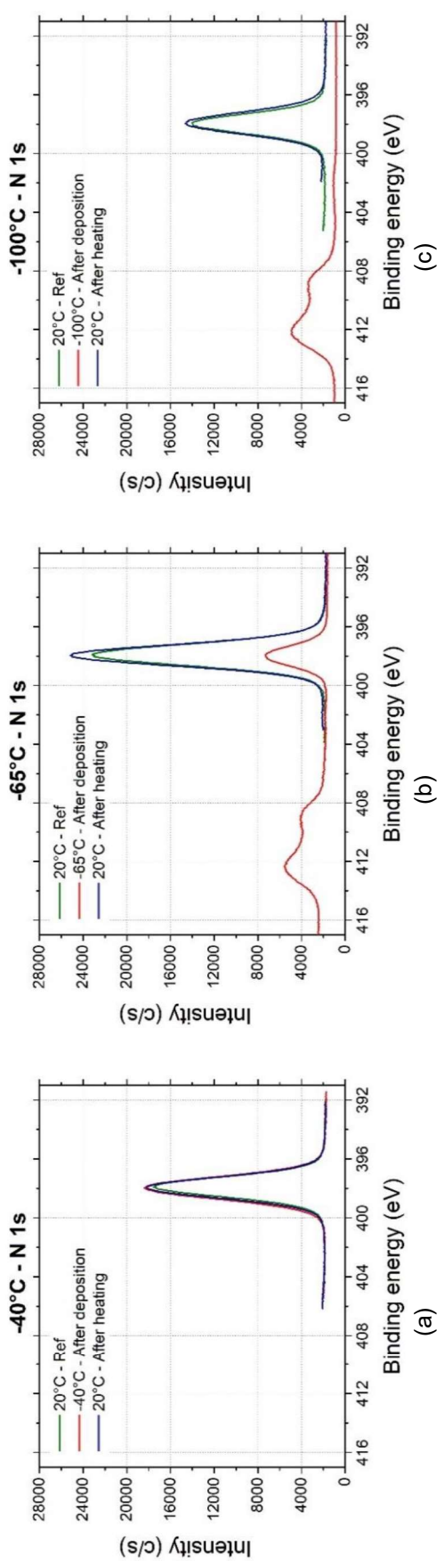

Fig. IV. 28. XPS scan of N 1s component on Si_3N_4 coupon: before, after deposition, and after heating. For deposition at (a) -40°C, (b) -65°C and (c) -100°C, using plasma parameters of Table. IV. 6

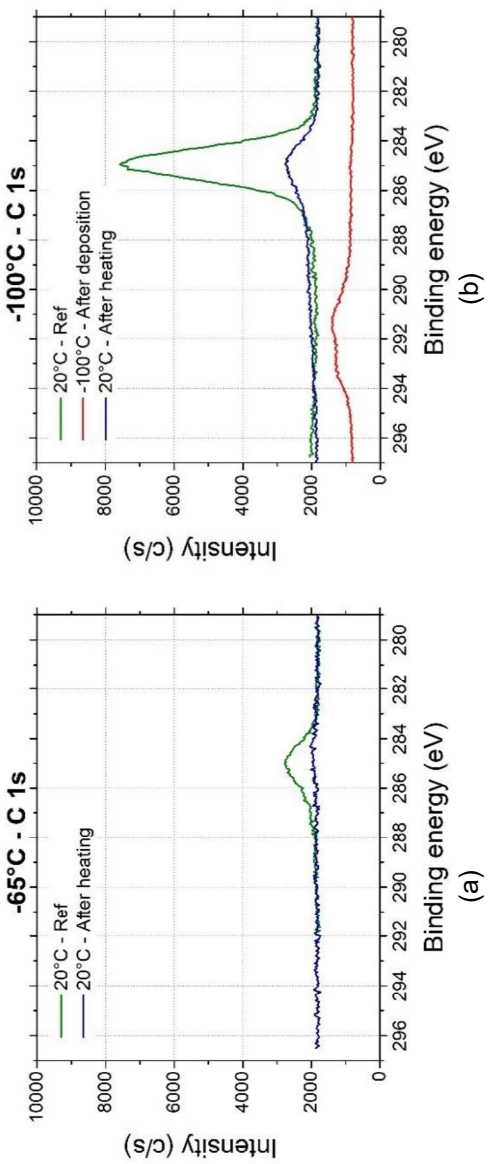

Fig. IV. 29. XPS scan of C 1s component on Si_3N_4 coupon: before, after deposition, and after heating. For deposition at (a) -65°C and (b) -100°C, using plasma parameters of Table. IV. 6

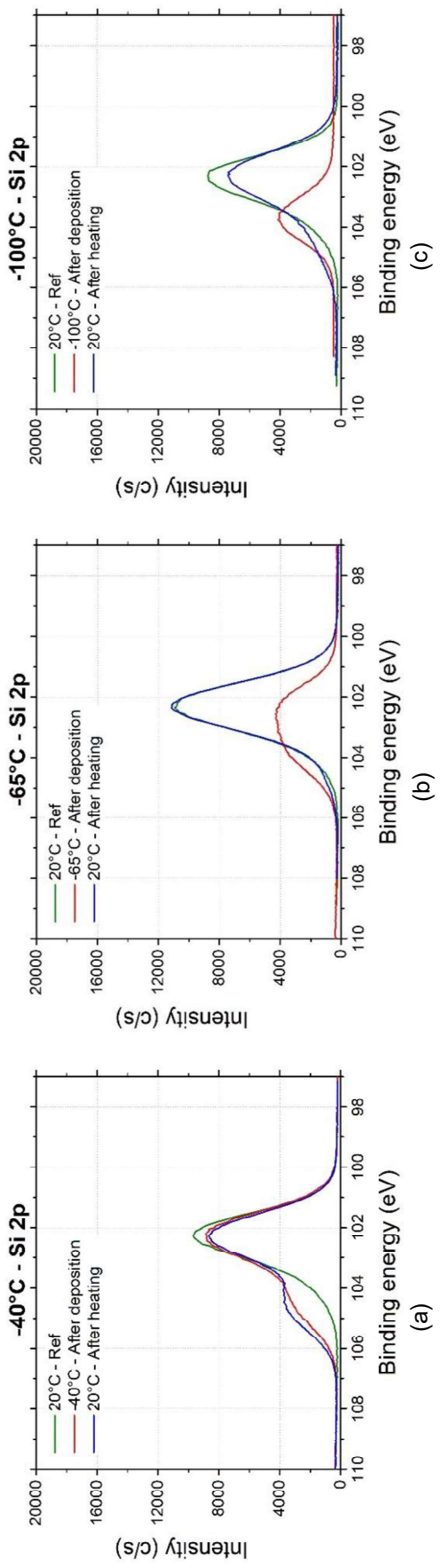

Fig. IV. 30. XPS scan of Si 2p component on Si_3N_4 coupon: before, after deposition, and after heating. For deposition at (a) -40°C, (b) -65°C and (c) -100°C, using plasma parameters of Table. IV. 6

In Fig. IV. 30. b, a wide peak is observed after deposition at -65°C. This peak can be decomposed into two peaks, one at 102.2 eV due to Si-N bonds of the sample material and a second one at 104.5 eV assigned to Si-O and / or Si-F bonds. Therefore, it is believed that a SiO_xF_y layer has grown on the Si_3N_4 surface. After heating, the spectrum of this Si 2p component has the same shape as before deposition. This means that the main part of the SiO_xF_y layer has desorbed.

At -100°C (Fig. IV. 30. c), almost same behavior is observed as at -65°C. Nevertheless, the peak related to Si-N bonds at 102.2 eV is not detected and hence only the peak of Si-O / Si-F is visible at 104.5 eV. This shows that the surface is covered by a thick fluorinated layer after deposition. After heating, the shape of the spectrum is similar to the reference sample, with one peak at 102.2 eV just like the case at -65°C.

Fig. IV. 31 shows the wide scans at different temperatures. As for a-Si, Cr 2p peak is also detected at 579.6 eV due to some contamination from the Ni / NiCr thermocouple at the sample holder after deposition and heating at -65°C and -100°C.

Finally, the composition percentage of the sample surface is presented in Fig. IV. 32 versus the different temperatures. At -40°C, there is nearly no change in the composition between “after deposition” and “after heating”. This confirms that there is almost no desorption and / or surface modification during heating at this temperature. Significant adsorption of fluorine is observed in Fig. IV. 32. b at -65°C, with a slight increase of oxygen content. This deposited SiO_xF_y layer covers the substrate surface, which explains the decrease of Si and N amount of the analyzed thin layer. A more pronounced effect is observed in Fig. IV. 32. c at -100°C and after deposition, where a higher increase of fluorine amount is observed while Si and N percentages are clearly reduced. After heating, the composition of the surface at -100°C is close to that observed after heating at -40°C. It confirms the increase of fluorine based species amount at the surface after the deposition at low temperature. It also shows that a large part desorbs during the heating. The remaining surface composition is the same independently of the deposition temperature (-100°C or -40°C). A residual fluorine based layer stays at the surface. However, this is different at -65°C, where there is less fluorine and oxygen after heating, which shows that at this temperature, there is a rearrangement with some species desorption.

Those XPS scans showed that the deposited layer gets richer in fluorine with temperature decrease. However, a different behavior after heating the substrate is observed as a function of the deposition temperature, which is different from a-Si behavior.

Mechanisms will be discussed in more details later in this chapter.

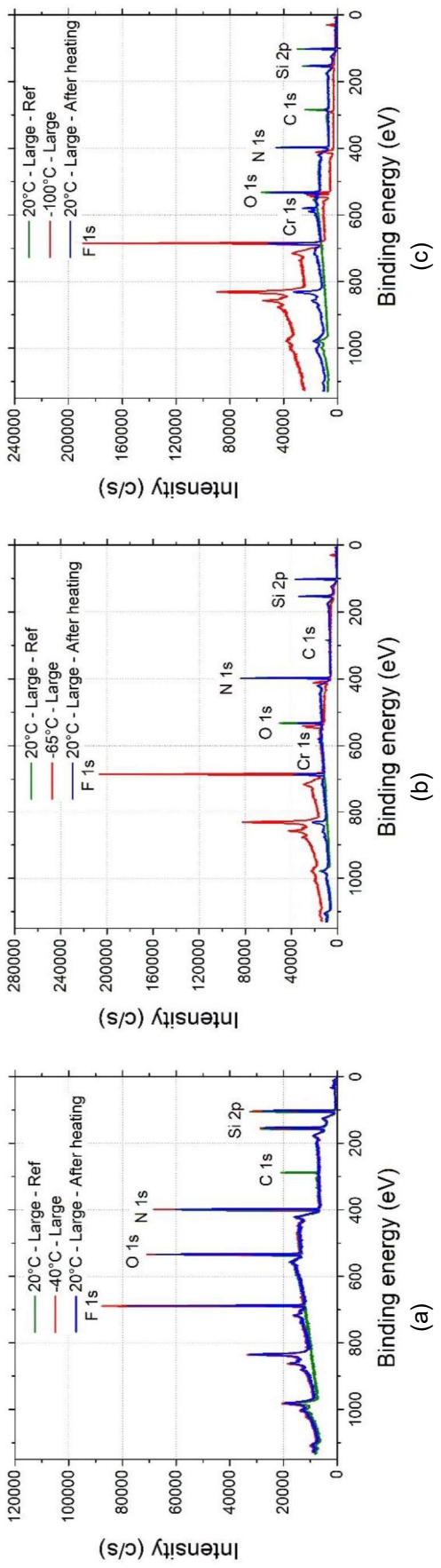

Fig. IV. 31. XPS wide scan of Si_3N_4 coupon before, after deposition and after heating. For deposition at (a) -40°C, (b) -65°C and (c) -100°C, using plasma parameters of Table. IV. 6

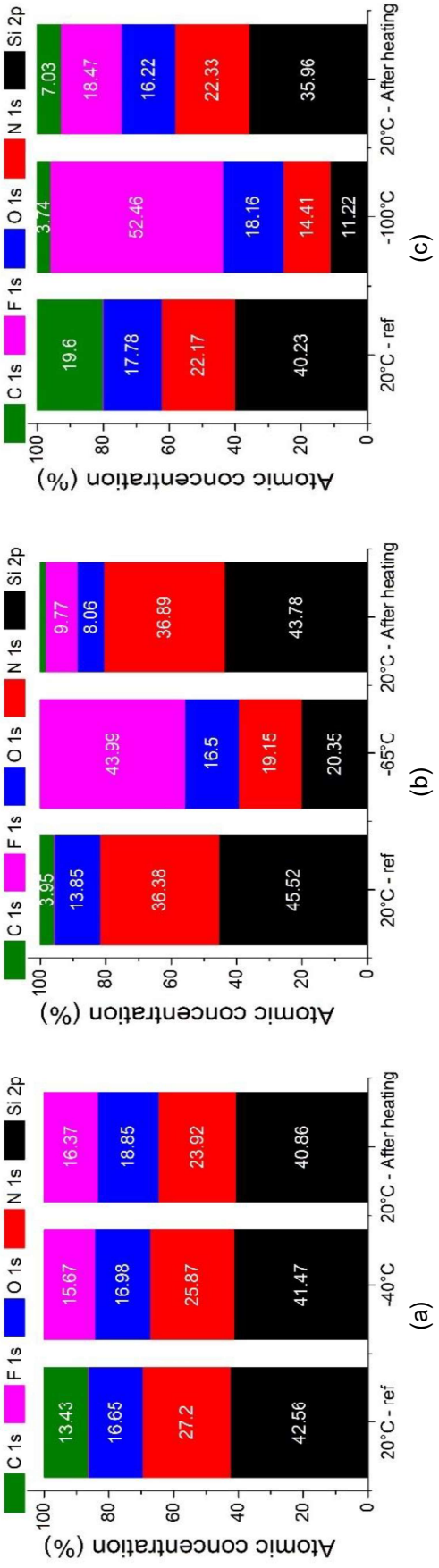

Fig. IV. 32. Quantification of surface composition determined by XPS before, after deposition and after heating on Si_3N_4. For deposition at (a) -40°C, (b) -65°C and (c) -100°C, using plasma parameters of Table. IV. 6

V.2.iii. Thickness variation as a function of temperature on SiO_2

The same study as that of the two previous sections was also conducted on SiO_2. Same process parameters were used as presented in Fig. IV. 15. Fig. IV. 33. a, shows that the thickness of the SiO_xF_y layer deposited during the SiF_4 / O_2 plasma increases linearly and continuously without any saturation behavior. Unlike the materials investigated previously, the passivation layer is deposited at the same rate at -40°C and -65°C. An SiO_xF_y layer of about 14 nm is deposited at both temperatures (Fig. IV. 33. c). However, at -100°C, there is almost no deposition during SiF_4 / O_2 plasma. During the Ar plasma (Fig. IV. 33. b), at -40°C and -65°C the thickness of the deposited layer remains almost constant. At -100°C, about 6 nm of SiO_2 are etched with an etch rate as low as 0.4 $nm.s^{-1}$.

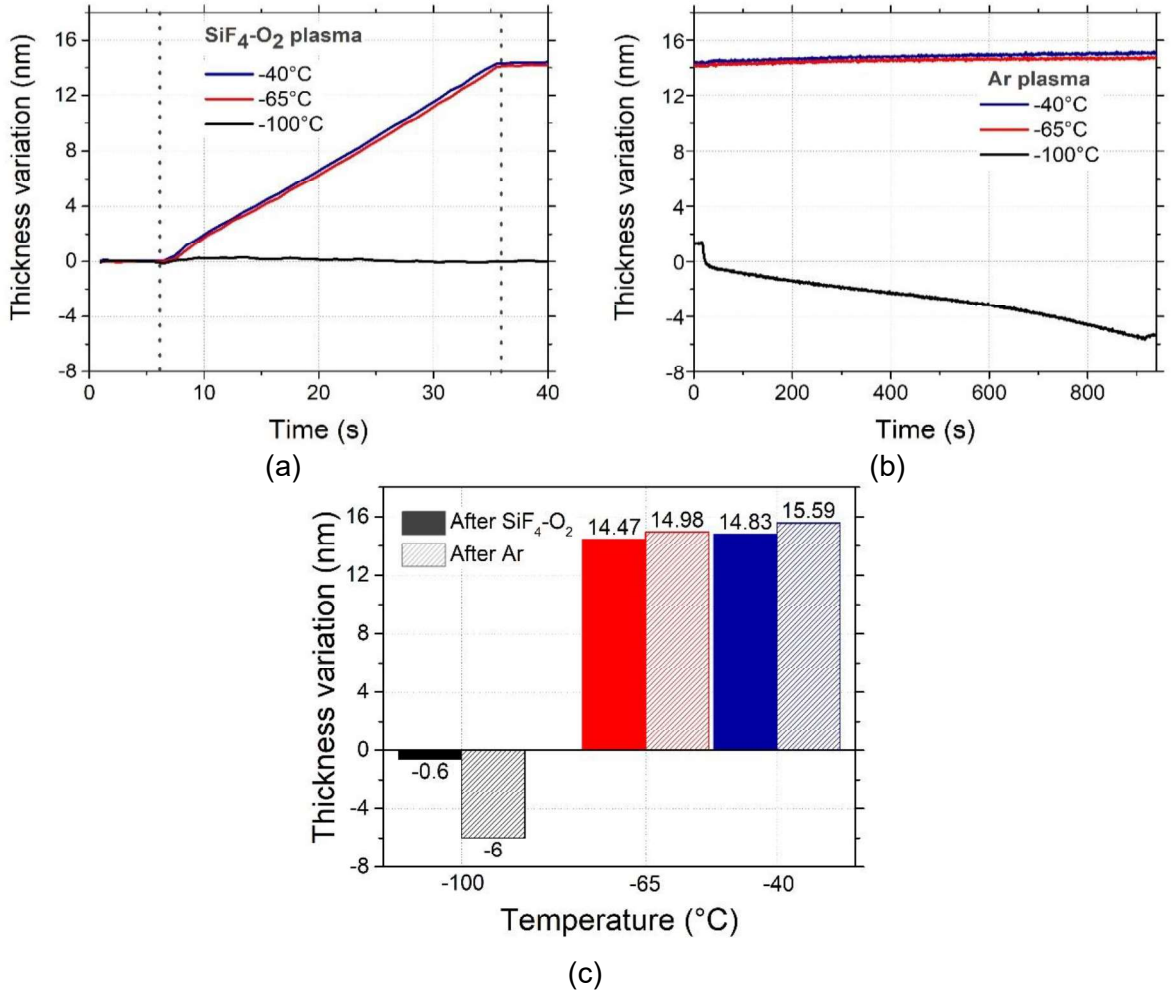

Fig. IV. 33. Thickness variation of SiO_2 measured by SE depending on temperature during (a) measurements in kinetic mode during SiF_4 / O_2 plasma, (b) measurements in kinetic mode during Ar plasma, (c) measurements in Mono mode after each plasma

V.2.iv. *Comparison of the three materials and discussion of mechanisms*

In conclusion, for a-Si, Si_3N_4 and SiO_2, a thin layer of about 13 to 14 nm is deposited at -40°C. This layer is expected to be dense, rich in oxygen and poor in fluorine as it was not possible to etch the substrate with the Ar plasma [2]. At -65°C, about 7.8 nm of Si_3N_4 was etched after Ar plasma, whereas no etching was observed on a-Si or SiO_2, but a SiO_xF_y layer of about 14 nm thick remained on their surface. Finally, at -100°C, the three materials were etched. Consequently, an etching selectivity between Si_3N_4 over a-Si and SiO_2 could be achieved at -65°C.

XPS measurements performed on a-Si and Si_3N_4 have shown that for deposition at -40°C and -100°C, the surface composition is similar for both materials. At -40°C, the surface does not vary after deposition and after heating, with about 17%-23% of oxygen and 17% of fluorine. At -100°C, the surface is richer in fluorine after deposition (about 52%) with 18% of oxygen. And for both materials, after heating, part of fluorine species desorb, leaving a surface with about 19% of fluorine and 16-20% of oxygen.

However, at -65°C, whereas the deposited layer on a-Si has the same behavior with same composition as at -40°C, there is a higher adsorption amount of fluorine species on Si_3N_4 at -65°C (44% instead of 15-20% at -40°C). And after heating, a significant part of the fluorine desorbs, as the surface contains only 10% of F after heating.

To sum up, the composition of the deposited layer changes depending on the temperature and the material of the substrate. In general, the layer gets richer in fluorine when deposition is carried out at low temperature (below -65°C). However, when the sample was warmed up to room temperature, part of the layer, and more specifically fluorine desorbed. These results are consistent with the analysis carried out during SiF_4 / O_2 plasma on Si by QMS in [12] and by SE in section II.1.i and V.2.i.a of this chapter, where it was shown that the deposited layer desorbs by releasing SiF_4. Then, when Ar plasma is performed after the deposition, etching is achieved if the deposition is performed at -65°C and below for Si_3N_4 and close to -100°C for a-Si. Lowering the temperature during the deposition changes the composition of the SiO_xF_y layer which can therefore be adjusted in terms of fluorine content. The deposited layer then partially desorbs when the substrate is brought back to 20°C. This higher concentration of fluorine at low temperature is attributed to the much longer residence time of SiF_x at the surface when the sample is cooled. The oxygen can then oxidize the SiF_x type species making the layer more resistant to ion bombardment [2]. However, if the oxygen concentration is low compared to the concentration of fluorine, the layer will remain fragile. When the fluorine content is sufficiently high in the deposited layer, the substrate can be etched under ion bombardment.

Moreover, by contrast to a-Si, oxygen does not help to oxidize Si_3N_4 surface or limit its etching, but it can bond with nitrogen from the sample, creating NO species [33]–[35]. Therefore, at low temperatures, the SiO_xF_y layer growth is reduced on Si_3N_4 and SiF_x as well as O species from the SiO_xF_y deposited layer will contribute to the etching afterwards.

So a real promising selectivity has been noted between Si_3N_4 and a-Si. Fig. IV. 34 below sums up the main information gathered on a-Si and Si_3N_4 for increasing selectivity.

a-Si	Si_3N_4
From 20°C to -40°C	
SiO_xF_y layer rich in oxygen Deposition during SiF_4 / O_2 plasma Hard to etch by Ar plasma	
Same behavior => Poor selectivity	
At -65°C	
SiO_xF_y layer rich in oxygen Deposition during SiF_4 / O_2 plasma Hard to etch by Ar plasma	Reaction between SiF_x, O and the substrate Small deposition during SiF_4 / O_2 plasma Can be etched by Ar plasma
Different behavior => Promising selectivity	
Close to -100°C	
SiO_xF_y layer rich in fluorine Can be etched by SiF_4 / O_2 plasma Can be etched by Ar plasma	
Same behavior => Poor selectivity	

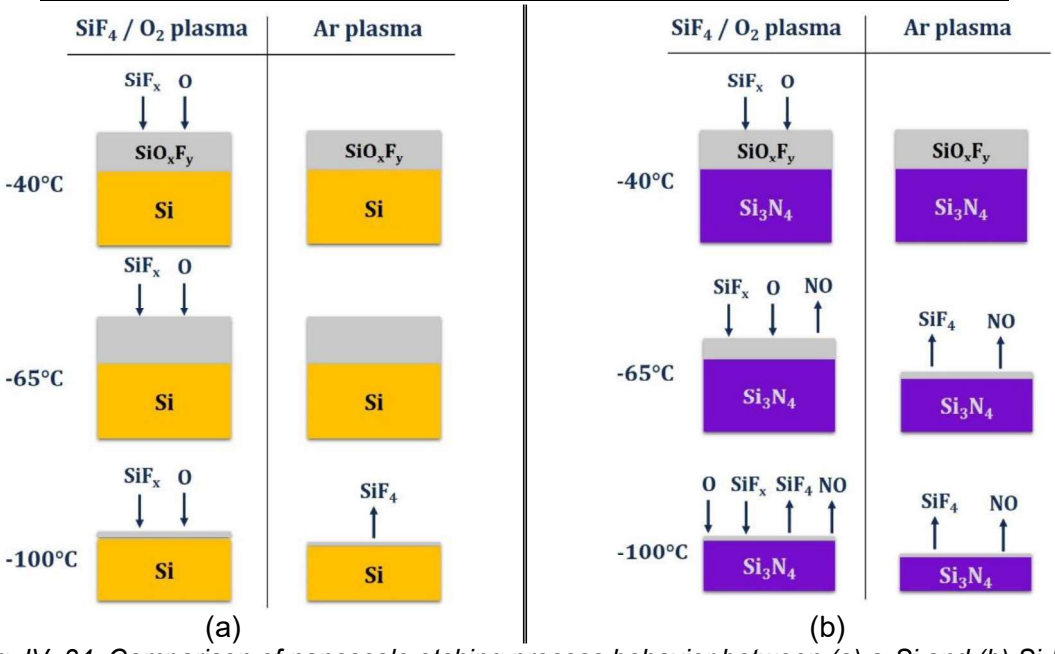

Fig. IV. 34. Comparison of nanoscale etching process behavior between (a) a-Si and (b) Si_3N_4

VI. Influence of parameters during a process

VI.1. Influence of source power during the modification step

In addition to the previous tests, the influence of the source power was investigated during a process at -65°C. Tests were conducted with the same sample configuration as in Fig. IV. 13. a. a-Si coupon was glued on the center of the wafer and its thickness variation was followed by in-situ SE versus time for three source powers, 500 W, 1000 W an 1500 W. The results are presented in Fig. IV. 35. a. For the three powers, the thickness after a cycle was increased during the first three cycles. And then, only at 1500 W, the trend starts to reverse, with the thickness decreasing from one cycle to the other.

Fig. IV. 35. b shows a zoom on the sixth cycle of the curve at 1500 W in Fig. IV. 35. a. It illustrates the evaluated thickness increase during SiF_4 / O_2 plasma for each cycle (D in Fig. IV. 35. b) and the measured thickness decrease during the Ar plasma (E in Fig. IV. 35. b). The thickness E was then subtracted to the measured thickness D for each cycle and each condition of Fig. IV. 35. a. The resulting graphs are plotted in Fig. IV. 35. c for each source power. For all powers, at the first cycle, a small amount is deposited but a-Si is not etched. Then, at the second cycle, the deposited amount increases without being completely etched after by Ar. However, starting from the third cycle, the difference between the deposited and the etched amount reduces. The values for an applied power of 500 W and 1000 W are always positives, even after 8 cycles, which means that the deposited amount was always higher than the etched amount all along the process. However, this thickness difference decreases along cycles. And at 1500 W, there is a higher amount etched with Ar plasma than deposited with SiF_4 / O_2 plasma from the fifth cycle. Therefore, relying on the last 4 cycles, when the power is decreased, it takes more cycles to reach a regular etch regime.

The thickness variation was also measured on SiO_2 and Si_3N_4 before and after the process by ex-situ SE. For comparison, this thickness variation has been plotted for the three materials in Fig. IV. 35. d. For the three source powers tested, Si_3N_4 was etched whereas a deposition occurred on SiO_2 and a-Si. However, as explained previously, the deposited amount on a-Si, as well on SiO_2, was lower when the power was higher. Moreover, the etched amount was higher at the highest source power for Si_3N_4.

Therefore, the 1500 W source power was chosen for processes because the selectivity of Si_3N_4 to the two other materials was higher. Indeed, at this power, it is possible to etch about 6.5 nm of Si_3N_4, while depositing about 0.5 nm on a-Si. At 1500 W, SiF_4 is more dissociated than at 500 W and SiF_x seems to react more favorably with Si_3N_4 as it is more etched than a-Si.

-65°C	Time (s)	Flow (sccm)	Pressure (Pa)	P_{source} (W)	V_{bias} (V)
1. Modification: SiF_4 / O_2	3	10 / 30	0.7	varied	Floating
2. Pumping:	30	0	0.1	0	0
3. Etch plasma: Ar	180	100	3.1	400	Floating
4. Pumping:	15	0	0.1	0	0

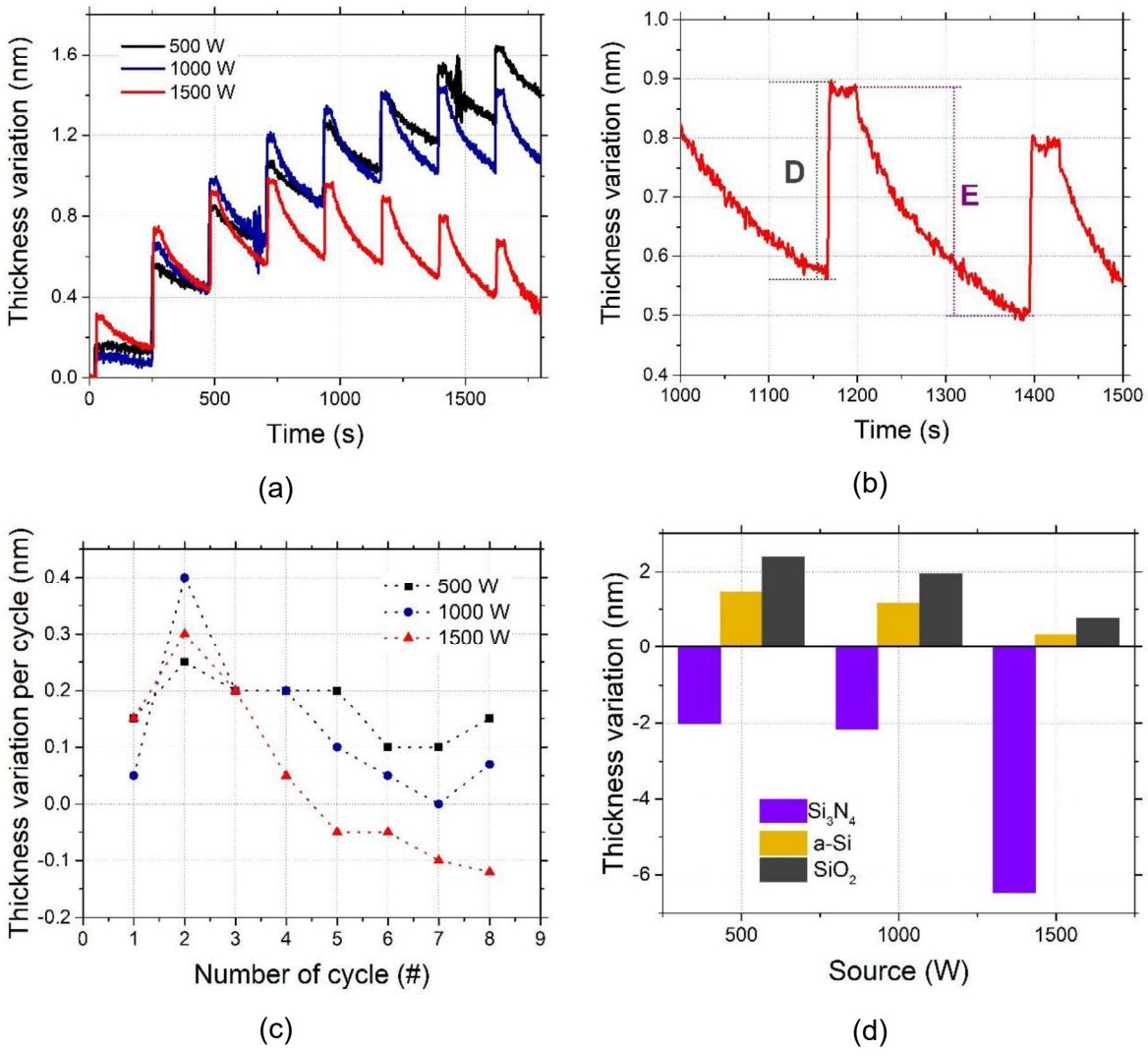

Fig. IV. 35. (a) Thickness evolution of a-Si measured by in-situ SE in kinetic mode versus time for 8 cycles etching process performed at -65°C depending on the source power, (b) zoom on cycle 6 of the curve at 1500 W to explain the measured deposited and etched thickness (c) Plot of the thickness variation deduced from (a) and (b), (d) Thickness variation of a-Si, Si_3N_4 and SiO_2 after the 8 cycles, measured by ex-situ SE in Mono mode

VI.2. Study of the etching step

VI.2.i. *Influence of the source power*

In this paragraph, the influence of the source power during Ar plasma has been investigated during 8 cycles of the process. Curves presented in Fig. IV. 36. a were obtained by in-situ SE in kinetic mode on a-Si. They show the thickness evolution during 8 cycles when the Ar plasma power is changed. Two powers were tested: 400 W and 700 W. As observed in Chapter III with the process involving C_4F_8, there is less etching when the power is increased and even, in this case, more deposited amount during SiF_4 / O_2 plasma. The plasma characteristics were measured by Langmuir probe in the diffusion chamber in an Ar plasma at 3.0 Pa. Results are reported in Table. IV. 7. The plasma potential (V_p) slightly increases at 700 W than at 400 W, whereas the ion density (N_i) is significantly higher. This may induce a more efficient dissociation of SiF_x. Consequently, even though a higher amount is etched during Ar plasma, the ion bombardment creates SiF_x sites at the surface that would react with oxygen or would bond to other SiF_x during a subsequent SiF_4 / O_2 plasma. Consequently, a higher amount is deposited during SiF_4 / O_2 plasma.

Table. IV. 7. Plasma characteristics of an Ar plasma, measured in the center of the diffusion chamber of the reactor by Langmuir probe

3 Pa	***Floating potential (V)***	***Electron temperature (eV)***	***Plasma potential (V)***	***Ion density ($x10^{10}$ cm^{-3})***
400 W	0.7	1.8	10.1	4.9
700 W	1.8	1.7	11.1	11.8

Fig. IV. 36. b shows the total thickness variation after the 8 cycles for the three studied materials, Si_3N_4, a-Si and SiO_2. Note that a reproducibility problem has been encountered as the deposited amount during the first SiF_4 / O_2 plasma is not the same in both conditions (see the green short dot circle in Fig. IV. 36. a). This one is not supposed to vary as no Ar plasma has been performed yet. However, deposition occurred on the three materials at 700 W, with less deposition on Si_3N_4 and more on SiO_2 as on a-Si, like at 400 W. However, only Si_3N_4 is etched at 400 W, whereas a-Si and SiO_2 are not.

-65°C	Time (s)	Flow (sccm)	Pressure (Pa)	P_{source} (W)	V_{bias} (V)
1. Modification: SiF_4 / O_2	3	10 / 30	0.7	1500	Floating
2. Pumping:	30	0	0.1	0	0
3. Etch plasma: Ar	180	100	3.1	**400 / 700**	Floating
4. Pumping:	15	0	0.1	0	0

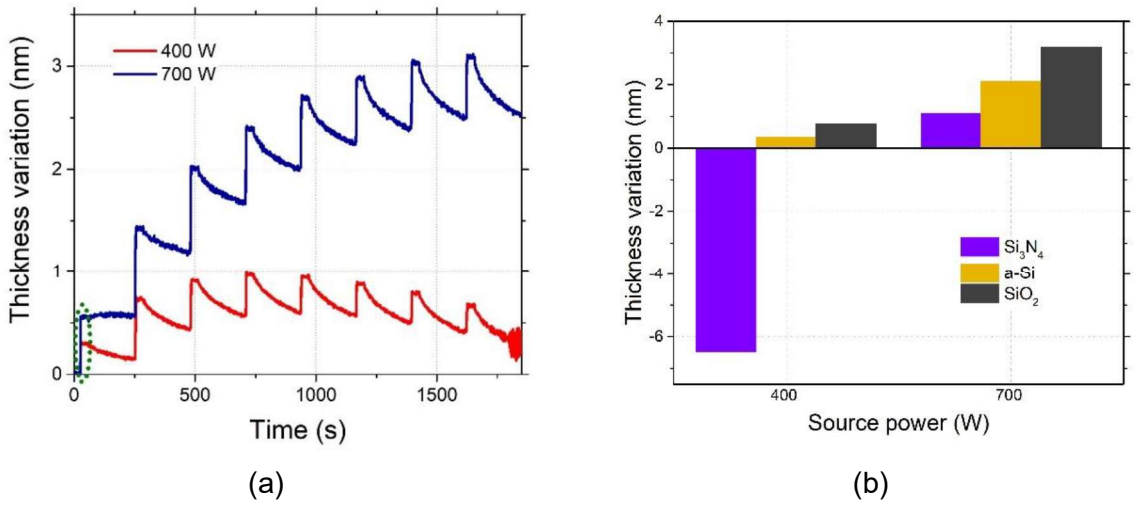

(a) (b)

Fig. IV. 36. (a) Thickness variation of a-Si measured by in-situ SE in kinetic mode versus time for an 8 cycles etching process depending on Ar plasma source power at -65°C (b) Thickness variation after the same 8 cycles process on a-Si, Si_3N_4 and SiO_2

VI.2.ii. *Influence of the bias in the Ar plasma step*

The bias effect was also investigated for its critical role in the etching mechanism and in anticipation of future experiments for the study of patterned samples. The sample configuration is the same as in Fig. IV. 13. a with a-Si in the center for the in-situ SE measurements in kinetic mode (Fig. IV. 37. a). Ex-situ SE measurements were performed to evaluate the selectivity between Si_3N_4, SiO_2 and a-Si (Fig. IV. 37. b).

Fig. IV. 37. a shows the thickness evolution versus time during 8 cycles depending on the bias for the Ar plasma: without bias or with -10 V. Applying a low bias (-10 V) increases the etched amount during Ar plasma, although this also slightly increases the deposited amount. Therefore, the increase of the total thickness at the end of a cycle, during the first cycles is reduced and it becomes possible to etch a-Si instead of depositing on it. As explained in section V.2.i.a., some sputtering of a-Si may occur when a bias of -10 V is applied, since the ion energy may exceed its sputtering threshold. It also enables to break through the SiO_xF_y deposited layer easier. Fig. IV. 37. b shows the thickness variation for each material measured accurately by ex-situ SE before and after 8 cycles. For all of them, the material was etched at the end of the 8 cycles performed at -10 V, which is not the case for the process without bias where a remaining deposited layer is obtained on a-Si and SiO_2. By applying a bias of -10 V,

the total etched thickness of Si_3N_4 is 7.4 nm against 6.5 nm without bias, which gives a variation of 0.9 nm. For a-Si, no deposition is obtained with a bias of -10 V, and the variation of the thickness after 8 cycles is almost non-existent, of the order of 0.1 nm. For SiO_2, from no bias to -10 V bias, the process switches from deposition regime to etching, with an etched depth of the order of 1.5 nm.

-65°C	*Time (s)*	*Flow (sccm)*	*Pressure (Pa)*	*P_{source} (W)*	*V_{bias} (V)*
1. Modification: *SiF_4 / O_2*	3	10 / 30	0.7	1500	Floating
2. Pumping:	30	0	0.1	0	0
3. Etch plasma: *Ar*	180	100	3.1	400	**0 / -10**
4. Pumping:	15	0	0.1	0	0

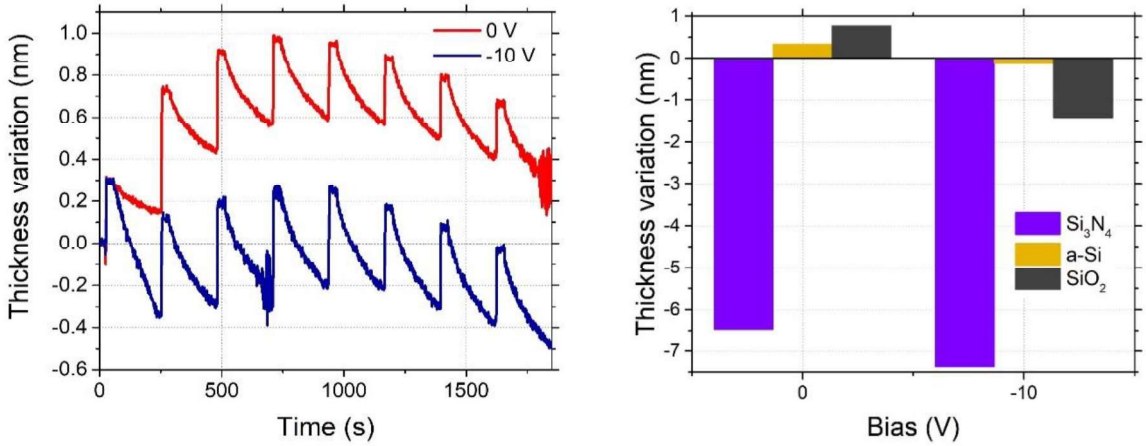

(a) (b)

Fig. IV. 37. (a) Thickness variation of a-Si measured by in-situ SE in kinetic mode versus time for 8 cycles etching process at -65°C depending on the applied bias, (b) Thickness variation after the same 8 cycles process, measured by ex-situ SE on a-Si, Si_3N_4 and SiO_2

VII. Study and improvement of selectivity between Si_3N_4 and a-Si

VII.1. Investigation on Si_3N_4 etching over a-Si

The thickness variation is measured, for the first time in the manuscript, on Si_3N_4, by in-situ SE in kinetic mode during a process in order to monitor its behavior during SiF_4 / O_2 plasma. Same test was performed separately on a-Si and on Si_3N_4 coupons glued in the center of the carrier wafer. The results are given in Fig. IV. 38. A zoom on the second cycle in Fig. IV. 38. b shows that a small thickness increase can be observed on a-Si during SiF_4 / O_2 plasma, whereas none is observed on Si_3N_4. As presented above, during a cycle performed on a-Si, the etched thickness is very thin and the Ar plasma step mainly removes the SiO_xF_y deposited

layer. On the contrary, on Si_3N_4, there is no SiO_xF_y deposited layer and the sample is etched during Ar plasma as early as the first cycle. At the end of the process, the a-Si thickness variation was close to zero, while about 14 nm of Si_3N_4 was etched with an EPC of 2.3 nm. So the selectivity is quasi-infinite between the two tested materials.

-65°C	*Time (s)*	*Flow (sccm)*	*Pressure (Pa)*	*P_{source} (W)*	*V_{bias} (V)*
1. Modification: *SiF_4 / O_2*	3	10 / 30	0.7	1500	Floating
2. Pumping:	30	0	0.1	0	0
3. Etch plasma: *Ar*	180	100	3.1	400	-10
4. Pumping:	15	0	0.1	0	0

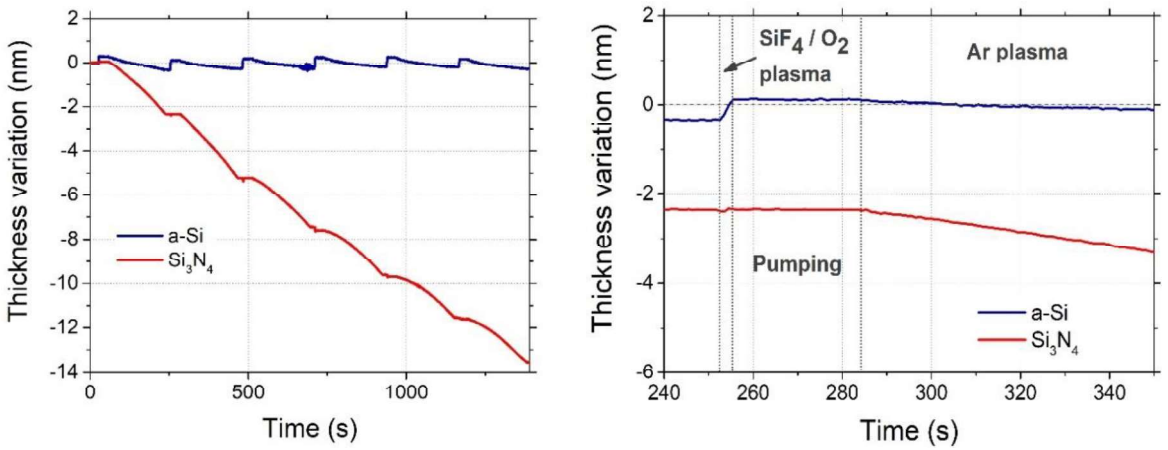

Fig. IV. 38. (a) Thickness evolution of a-Si and Si_3N_4 during 6 cycles monitored by in-situ SE in kinetic mode, (b) zoom on cycle #2

VII.2. Evolution of selectivity during long processes

As observed in Fig. IV. 35. a and Fig. IV. 37. a, for a process of 8 cycles, the two to three first cycles are in deposition regime before it switches to etching regime. Therefore, long processes with more cycles have been run in order to check process stability as well as the selectivity evolution with increasing number of cycles.

25 cycles were performed in order to make a comparison for selectivity with a process of 8 cycles. The thickness evolution through cycles for both processes is presented in Fig. IV. 39. The position of the samples is the same as in the case presented in Fig. IV. 13. a, with the a-Si coupon at the center in order to monitor its thickness by SE in kinetic mode. Fig. IV. 39. a shows that tests are repeatable over the 8 first cycles at least, since the two curves almost overlap. Again, the thickness increases during the first cycles before etching starts. Once the etching has started, the substrate is etched at almost the same rate from one cycle to another. Therefore, the etching per cycle seems also quite repeatable, which enables to achieve

constant etch rate in time. Fig. IV. 39. b shows the total thickness variation at the end of the 8 and the 25 cycles long processes for the three materials: Si_3N_4, a-Si and SiO_2. After 8 cycles, a Si_3N_4 thickness of 6.5 nm is etched, whereas a small deposition (less than 1 nm) occurs on a-Si and SiO_2 leading to a promising selectivity, which is expected to be infinite. Moreover, if the cycles are continued up to 25 cycles, Si_3N_4 keeps being etched. It can be noticed that the average etch rate tends to decrease along cycles. Indeed, the Etching amount Per Cycle (EPC) for Si_3N_4, was about 0.8 nm for the 8 first cycles, and decreases to a value of 0.6 nm for 25 cycles. At the same time, a total a-Si thickness of about 1.5 nm is etched. The selectivity of Si_3N_4 over a-Si is hence no longer infinite, and is equal to (10:1). The etching of SiO_2 using the same process gives intermediate results, with a thickness of 4 nm etched during the 25 cycles long process.

-65°C	***Time (s)***	***Flow (sccm)***	***Pressure (Pa)***	***P_{source} (W)***	***V_{bias} (V)***
1. Modification: *SiF_4 / O_2*	3	10 / 30	0.7	1500	Floating
2. Pumping:	30	0	0.1	0	0
3. Etch plasma: *Ar*	180	100	3.1	400	Floating
4. Pumping:	15	0	0.1	0	0

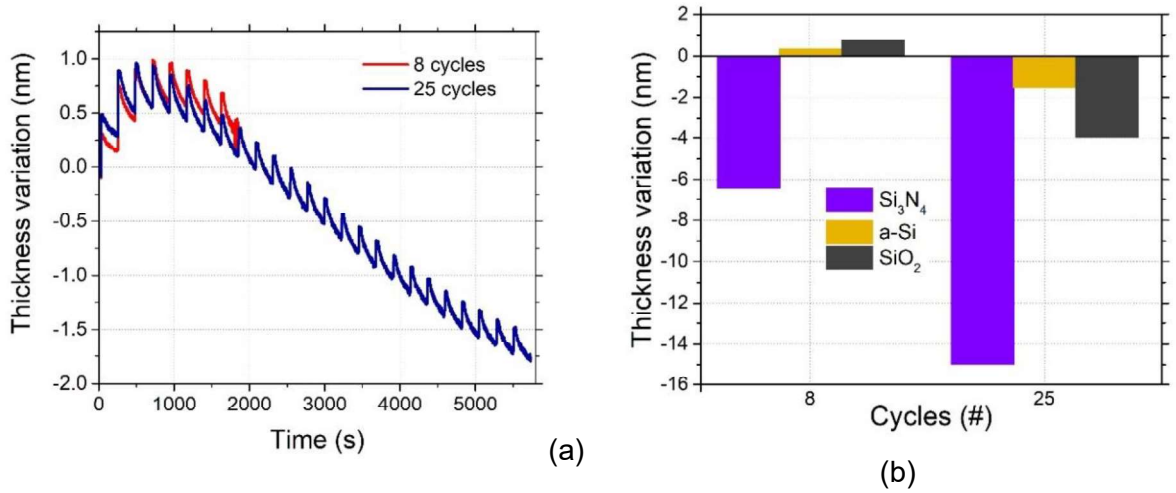

Fig. IV. 39. (a) Thickness variation of a-Si measured by in-situ SE in kinetic mode versus time, for 8 and 25 etching cycles at -65°C, (b) Thickness variation after the same 8 and 25 cycles processes, measured by ex-situ SE on a-Si, Si_3N_4 and SiO_2

VII.3. New process proposal to maintain a high selectivity

Fig. IV. 39 showed that the selectivity of Si_3N_4 over a-Si decreases through cycles. To avoid this loss of selectivity, it is proposed to perform few additional seconds of SiF_4 / O_2 plasma before the repetition of cycles. Indeed, as shown in Fig. IV. 16, no etching was observed on a-Si when a SiO_xF_y layer was deposited on it at -65°C, while Si_3N_4 was etched (Fig. IV. 24). The resulting time evolution of the Si_3N_4 thickness variation, performed at -65°C with the

modified process, is presented below in Fig. IV. 40. In this case, a significant amount of SiO_xF_y was deposited during the initial deposition step: a 4 nm thick layer was deposited after 10 s and 12 nm after 30 s. These 2 values suggest that the deposition rate may be linear with time. However, this significant deposited amount prevents from etching Si_3N_4 even after 10 cycles.

	-65°C	Time (s)	Flow (sccm)	Pressure (Pa)	P_{source} (W)	V_{bias} (V)
1 time	0. Deposition : SiF_4 / O_2	0 / 10 / 30	10 / 30	1.2	1500	Floating
10 cycles	1. Modification : SiF_4 / O_2	3	10 / 30	0.7	1500	Floating
	2. Pumping:	30	0	0.1	0	0
	3. Etch plasma: Ar	180	100	3.1	400	-10
	4. Pumping:	15	0	0.1	0	0

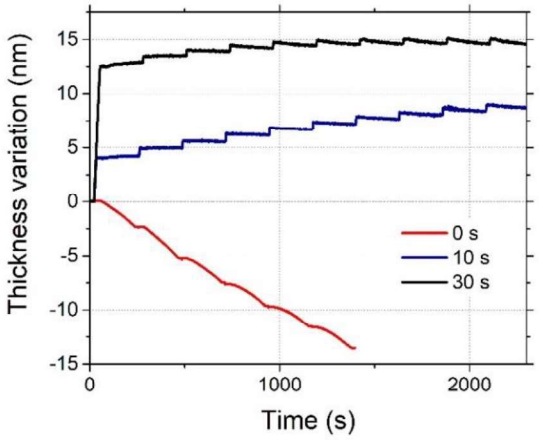

Fig. IV. 40. Thickness variation of Si_3N_4 measured by in-situ SE in kinetic mode versus time for a 10 cycles etching process with or without a SiF_4 / O_2 plasma additional step as long as 10 s or 30 s at the very beginning of the process

Consequently, to switch from deposition to etching regime only for Si_3N_4, a new process was imagined based on observations performed in previous tests. In the new process, first, 4 cycles from the process in Fig. IV. 40 were performed to start the etching on Si_3N_4. Then, a 10 s SiF_4 / O_2 plasma is run before performing 40 other cycles, in order to deposit a thin layer of SiO_xF_y to passivate a-Si. Indeed, when looking at the behavior during the first cycles on a-Si (for example in Fig. IV. 38) no etching is observed, while some should occur on Si_3N_4.

An Ar plasma followed the 10 s deposition step, instead of starting the cycle as usual by the 3 s SiF_4 / O_2 plasma step. And the process was stopped after an Ar plasma step. The process parameters are presented below. The test was performed with Si_3N_4 coupon glued in the center on a carrier wafer with also a-Si and SiO_2 on both sides (Fig. IV. 41. a).

The process curve presented in Fig. IV. 41. b corresponds to the thickness variation of Si_3N_4 measured by in-situ SE in kinetic mode for 44 cycles. As on a-Si, in this case, during the first

3 cycles, the process was in deposition regime, then switched to etching regime starting from the fourth cycle. There is no significant difference and thickness increase during the 10 s of SiF_4 / O_2 plasma. However, during the Ar plasma right after, about 2 nm were etched. Then, it took two additional cycles before the EPC get constant, close to 0.7 nm / cycle.

The total etched amount for Si_3N_4 and SiO_2 were respectively about 27.6 nm and 5.0 nm. At the end of the process, there was neither deposition neither etch of a-Si as the thickness was almost the same as before process. So, as there was no thickness increase from any deposited layer, this could mean that increasing the number of cycles would have etched the material. Hence a second step of 10 s of SiF_4 / O_2 may be required each 30 or 40 cycles to ensure the non-etch of a-Si, and obtain infinite selectivity of Si_3N_4 over a-Si.

-65°C		***Time (s)***	***Flow (sccm)***	***Pressure (Pa)***	***P_{source} (W)***	***V_{bias} (V)***
4 cycles	***1. Modification:*** *SiF_4 / O_2*	3	10 / 30	0.7	1500	Floating
	2. Pumping:	30	0	0.1	0	0
	3. Etch plasma: *Ar*	180	100	3.1	400	-10
	4. Pumping:	15	0	0.1	0	0
1 time	***1. Deposition :*** *SiF_4 / O_2*	10	10 / 30	1.2	1500	Floating
40 cycles	***1. Etch plasma:*** *Ar*	180	100	3.1	400	Floating
	2. Pumping:	15	0	0.1	0	0
	3. Modification: *SiF_4 / O_2*	3	10 / 30	0.7	1500	-10
	4. Pumping:	30	0	0.1	0	0

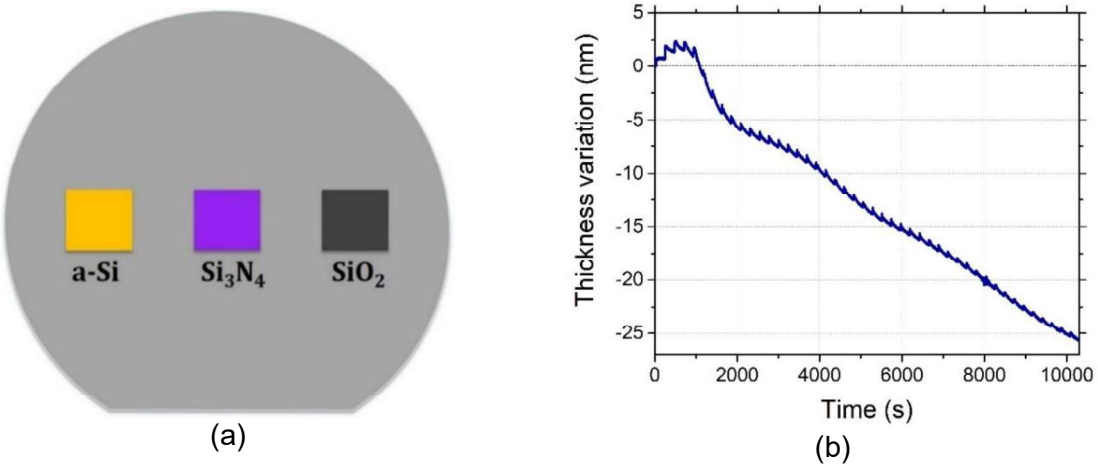

(a) (b)

Fig. IV. 41. (a) Coupons configuration on SiO_2 carrier wafer, (b) Thickness variation of Si_3N_4 measured in kinetic mode by in-situ SE at -65°C

VIII. Conclusion

In this Chapter, a new cryogenic process was proposed based on the knowledge on the passivation layer SiO_xF_y to etch silicon based materials at nanoscale. The process was configured as for ALE, which means cyclic four steps: modification, pumping, etching and pumping. The modification step was performed using SiF_4 / O_2 plasma. A promising selectivity (14:1) was found between Si_3N_4 and Si when SiF_4 / O_2 ratio is 1 / 3 and when the deposition was achieved closed to -65°C. Deposition at high temperatures (above -40°C) provides a layer rich in oxygen. However, deposition at lower temperatures (below -80°C) provides a layer rich in SiF_x species and in fluorine. Consequently, at high temperatures (above -40°C), the oxidized "thick" layers will be hard to etch by Ar plasma, whereas the fluorinated "thin" deposited layers at low temperatures (below -65°C) will contribute to the etching of the sample. Also, if the temperature is too low, etching will be achieved even during the SiF_4 / O_2 plasma. This is valid for all the materials. Nevertheless the temperature threshold is not the same for all of them, which provides an etching selectivity. Indeed, when decreasing the temperature, at 10 sccm of SiF_4 and 30 sccm of O_2, first Si_3N_4 will be etched (around -60°C), then SiO_2 (between -60°C and -100°C), and finally a-Si (close to -100°C).

The influence of the source power in the deposition and etching plasmas was also investigated in order to determine the optimal parameters for the process. It was shown that a source power set at 1500 W during the deposition step, enabled a better dissociation of SiF_4 and a higher ER of Si_3N_4 in comparison to lower powers. In the case of the etching plasma, it was shown that a source power of 400 W and without bias enabled to etch Si_3N_4 but not a-Si. However, applying -10 V bias increased the ER of Si_3N_4, and the selectivity between Si_3N_4 and a-Si was 74:1.

From those information, a new process has been proposed where a step of SiF_4 / O_2 plasma is added after 4 cycles in order to ensure the passivation of a-Si surface, while etching Si_3N_4, providing an infinite selectivity. Only SE and XPS measurements have been performed and presented in this chapter. To further improve our understanding of the mechanisms involved in this cryogenic etching, additional tests could be performed. For example Optical Emission Spectroscopy (OES) to learn more about species in plasma phase, or Quadrupole Mass Spectrometry (QMS) to follow the desorption when the layer is warmed up to room temperature. Also additional XPS measurements could be performed.

IX. References

[1] G. S. Oehrlein, K. K. Chan, M. A. Jaso, and G. W. Rubloff, "Surface analysis of realistic semiconductor microstructures," *J. Vac. Sci. Technol. A*, vol. 7, no. 3, pp. 1030–1034, 1989.

[2] G. S. Oehrlein and Y. Kurogi, "Sidewall surface chemistry in directional etching processes," *Mater. Sci. Eng., R*, vol. 24, no. 4, pp. 153–183, 1998.

[3] S. Tachi, K. Tsujimoto, and S. Okudaira, "Low-temperature reactive ion etching and microwave plasma etching of silicon," *Appl. Phys. Lett.*, vol. 52, no. 8, pp. 616–618, 1988.

[4] S. Tachi, K. Tsujimoto, S. Arai, and T. Kure, "Low-temperature dry etching," *J. Vac. Sci. Technol. A*, vol. 9, no. 3, pp. 796–803, 1991.

[5] K. Tsujimoto, S. Okudaira, and S. Tachi, "Low-Temperature Microwave Plasma Etching of Crystalline Silicon," *Jpn. J. Appl. Phys.*, vol. 30, no. 12A, pp. 3319–3326, 1991.

[6] J. W. Bartha, J. Greschner, M. Puech, and P. Maquin, "Low temperature etching of Si in high density plasma using SF_6/O_2," *Microelectron. Eng.*, vol. 27, no. 1–4, pp. 453–456, 1995.

[7] S. Aachboun and P. Ranson, "Deep anisotropic etching of silicon," *J. Vac. Sci. Technol. A*, vol. 17, no. 4, pp. 2270–2273, 1999.

[8] S. Aachboun, P. Ranson, C. Hilbert, and M. Boufnichel, "Cryogenic etching of deep narrow trenches in silicon," *J. Vac. Sci. Technol. A*, vol. 18, no. 4, pp. 1848–1852, 2000.

[9] M. Boufnichel, S. Aachboun, F. Grangeon, P. Lefaucheux, and P. Ranson, "Profile control of high aspect ratio trenches of silicon. I. Effect of process parameters on local bowing," *J. Vac. Sci. Technol. B*, vol. 20, no. 4, p. 1508, 2002.

[10] M. Boufnichel, S. Aachboun, P. Lefaucheux, and P. Ranson, "Profile control of high aspect ratio trenches of silicon. II. Study of the mechanisms responsible for local bowing formation and elimination of this effect*," *J. Vac. Sci. Technol. B*, vol. 21, no. 1, p. 267, 2003.

[11] R. Dussart *et al.*, "Passivation mechanisms in cryogenic SF_6/O_2 etching process," *J. Micromech. Microeng.*, vol. 14, no. 2, p. 190, 2003.

[12] X. Mellhaoui *et al.*, "SiO_xF_y passivation layer in silicon cryoetching," *J. Appl. Phys*, vol. 98, no. 10, p. 104901, 2005.

[13] M. Boufnichel, P. Lefaucheux, S. Aachboun, R. Dussart, and P. Ranson, "Origin, control and elimination of undercut in silicon deep plasma etching in the cryogenic process," *Microelectron. Eng.*, vol. 77, no. 3–4, pp. 327–336, 2005.

[14] R. Dussart *et al.*, "Silicon columnar microstructures induced by an SF_6/O_2 plasma," *J. Phys. D: Appl. Phys.*, vol. 38, pp. 3395–3402, 2005.

[15] T. Tillocher *et al.*, "Oxidation threshold in silicon etching at cryogenic temperatures," *J. Vac. Sci. Technol. A*, vol. 24, no. 4, pp. 1073–1082, 2006.

[16] R. Dussart, X. Mellhaoui, T. Tillocher, P. Lefaucheux, M. Boufnichel, and P. Ranson, “The passivation layer formation in the cryo-etching plasma process,” *Microelectron. Eng.*, vol. 84, no. 5–8, pp. 1128–1131, 2007.

[17] T. Tillocher *et al.*, “Two Cryogenic Processes Involving SF_6/O_2, and SiF_4 for Silicon Deep Etching,” *J. Electrochem. Soc.*, vol. 155, no. 3, p. D187, 2008.

[18] J. Pereira *et al.*, “In situ x-ray photoelectron spectroscopy analysis of SiO_xF_y passivation layer obtained in a SF_6/O_2 cryoetching process,” *Appl. Phys. Lett.*, vol. 94, no. 7, p. 071501, 2009.

[19] T. Tillocher *et al.*, “Optimization of submicron deep trench profiles with the STiGer cryoetching process: reduction of defects,” *J. Micromech. Microeng.*, vol. 21, no. 8, p. 085005, 2011.

[20] M. Kulsreshath *et al.*, “High aspect ratio etched sub-micron structures in silicon obtained by cryogenic plasma deep-etching through perforated polymer thin films,” *Micro and Nano Engineering*, vol. 1, pp. 42–48, 2018.

[21] G. Antoun *et al.*, “The role of physisorption in the cryogenic etching process of silicon,” *Jpn. J. Appl. Phys.*, vol. 58, no. SE, p. SEEB03, 2019.

[22] M. A. Blauw, T. Zijlstra, R. A. Bakker, and E. Van der Drift, “Kinetics and crystal orientation dependence in high aspect ratio silicon dry etching,” *J. Vac. Sci. Technol. B*, vol. 18, no. 6, p. 3453, 2000.

[23] W. A. Pliskin and R. P. Esch, “Refractive Index of SiO_2 Films Grown on Silicon,” *J. Appl. Phys*, vol. 36, no. 6, pp. 2011–2013, 1965.

[24] M. Gaudig *et al.*, “Elemental evolution of the $SiO_{xF}y$ self-masking layer of plasma textured silicon and its modification during air exposure,” *J. Appl. Phys*, vol. 121, no. 6, p. 063301, 2017.

[25] S. Tinck, E. C. Neyts, and A. Bogaerts, “Fluorine–Silicon Surface Reactions during Cryogenic and Near Room Temperature Etching,” *J. Phys. Chem. C*, vol. 118, no. 51, pp. 30315–30324, 2014.

[26] D. R. Stull, “Vapor Pressure of Pure Substances. Organic and Inorganic Compounds,” *Ind. Eng. Chem.*, vol. 39, no. 4, pp. 517–540, 1947.

[27] A. B. Kletskii and L. E. Petric, “Dependence of Vapor Pressure of Perfluorocyclobutane,” *Zh. Fiz. Khim.*, vol. 41, pp. 1183–1184, 1967.

[28] R. Dussart, T. Tillocher, P. Lefaucheux, and M. Boufnichel, “Plasma cryogenic etching of silicon: from the early days to today’s advanced technologies,” *J. Phys. D: Appl. Phys.*, vol. 47, no. 12, p. 123001, 2014.

[29] D. Metzler, C. Li, S. Engelmann, R. L. Bruce, E. A. Joseph, and G. S. Oehrlein, “Fluorocarbon assisted atomic layer etching of SiO_2 and Si using cyclic Ar/C_4F_8 and Ar/CHF_3 plasma,” *J. Vac. Sci. Technol. A*, vol. 34, no. 1, p. 01B101, 2016.

[30] C. Powell, “X-ray Photoelectron Spectroscopy Database XPS,Version 4.1, NIST Standard Reference Database 20.” National Institute of Standards and Technology, 1989.

[31] C. Li, D. Metzler, C. S. Lai, E. A. Hudson, and G. S. Oehrlein, “Fluorocarbon based atomic layer etching of Si_3N_4 and etching selectivity of SiO_2 over Si_3N_4,” *J. Vac. Sci. Technol. A*, vol. 34, no. 4, p. 041307, 2016.

[32] N. Posseme, V. Ah-Leung, O. Pollet, C. Arvet, and M. Garcia-Barros, “Thin layer etching of silicon nitride: A comprehensive study of selective removal using NH_3/NF_3 remote plasma,” *J. Vac. Sci. Technol. A*, vol. 34, no. 6, p. 061301, 2016.

[33] B. E. E. Kastenmeier, P. J. Matsuo, J. J. Beulens, and G. S. Oehrlein, “Chemical dry etching of silicon nitride and silicon dioxide using CF_4/O_2/N_2 gas mixtures,” *J. Vac. Sci. Technol. A*, vol. 14, no. 5, pp. 2802–2813, 1996.

[34] B. E. E. Kastenmeier, P. J. Matsuo, G. S. Oehrlein, and J. G. Langan, “Remote plasma etching of silicon nitride and silicon dioxide using NF_3/O_2 gas mixtures,” *J. Vac. Sci. Technol. A*, vol. 16, no. 4, pp. 2047–2056, 1998.

[35] B. E. E. Kastenmeier, P. J. Matsuo, and G. S. Oehrlein, “Highly selective etching of silicon nitride over silicon and silicon dioxide,” *J. Vac. Sci. Technol. A*, vol. 17, no. 6, pp. 3179–3184, 1999.

General conclusion

The project on Cryogenic Atomic Layer Etching was carried out in collaboration with Tokyo Electron Ltd. The purpose of this project is to create a new ALE process to etch silicon-based materials at the nanoscale by taking advantage of the low temperature of the substrate (below -100°C). In a first type of process, the gas is injected in gas phase instead of plasma phase unlike usual plasma-ALE processes. The low temperature increases the residence time of molecules at the surface. The gas injection is followed by a purge or a pumping step to evacuate all non-physisorbed species from the reactor chamber. Then, an Ar plasma is started to dissociate the physisorbed species and create radicals to react with the material. This step is finally followed by a pumping step in order to ensure the removal of all the etching products from the reactor chamber. Those four steps (adsorption, purge, etching and pumping) form one cycle that is repeated as many times as needed to reach the desired etch depth. The purpose of this process is to etch, in the most controlled way, the substrate monolayer by monolayer. So basically, it is expected to etch about 0.5 nm per cycle for SiO_2.

The main advantage of this technique relies on the fact that precursors physisorb only on cooled surfaces, while the reactor walls are kept clean. This makes a significant difference with more standard ALE, where a plasma is created during the first step and deposition is achieved on both the substrate and the chamber walls. This technique does not enable to deposit selectively on the surface of interest. Consequently, during the etching plasma step, the reactor walls can be sputtered and the deposited reactive species can redeposit on the substrate and contribute to its etching. This would induce undesired etching and drifts in the process. To prevent it, it is necessary to clean the process chamber frequently, which can be very time consuming in industrial manufacturing.

In the proposed cryogenic process, the precursor physisorbs only on the cooled surfaces. So, as the reactor walls are at room temperature, there will not be any physisorbing layer on it. Hence, there will not be any reactor walls contamination, neither drifts. And a chamber cleaning will be less needed.

It has been chosen to conduct the study for proof of principle on SiO_2, using C_4F_8 gas. C_4F_8 is a good candidate as it can physisorb at temperatures close to -120°C at a pressure of the order of 1 Pa. This low temperature can be reached with the equipment at GREMI by using liquid nitrogen. It is also a good candidate for SiO_2 etching.

First, a study on C_4F_8 physisorption has been conducted using in-situ SE and QMS. This study is necessary to better control the physisorption during process development. It showed that multilayer physisorption occurs following adsorption isotherm of type II. The parameters from the BET model were hence calculated. Those tests highlighted the presence

of a process temperature window above which there will be no physisorption and below which there is undesired water condensation.

The first process tests demonstrated the feasibility of the process at -120°C and 3.0 Pa. Self-limiting etching was achieved with an EPC of 0.5 nm / cycle. However, it also highlighted the sensitivity of the process to temperature. Indeed, the same process performed at -110°C did not enable any etching at this pressure. Further characterizations with the use of QMS, enabled to estimate the residence time of C_4F_8 at the surface which is increased with the temperature decrease. The influence of the pressure was also studied. It showed that increasing the pressure enabled to deposit a higher amount of C_4F_8, and makes it possible to operate at higher temperatures. Consequently, cryo-ALE at higher temperature (-90°C) was performed at a C_4F_8 pressure of 6.0 Pa in order to increase the amount of physisorbed C_4F_8 molecules. Since the surface residence time of C_4F_8 is lower at -90°C than at -120°C, the purge step time was also decreased in order to prevent all physisorbed species desorption before the Ar etch plasma. The advantage of working at higher temperatures (around -90°C) is, first of all, to prevent water condensation on the substrate.

With this process at -90°C, it was possible to etch SiO_2 at 0.13 nm / cycle and have a constant EPC from one cycle to the other. The linear shape of the etch curve obtained by SE confirms that there were no drifts during the process and so no reactor wall contamination.

However, the drawbacks observed in this technique so far is the lack of selectivity, in addition to the sensitivity of temperature variation. Indeed, no test allowed a selectivity of more than 2 or 3 of SiO_2 etching over a-Si or Si_3N_4.

Another process has been investigated, based on a SiF_4 / O_2 plasma for the modification step. Some studies on the SiO_xF_y layer formed by SiF_4 / O_2 plasma were already conducted some years ago. They showed an interesting behavior of this layer at low temperatures. This chemistry has been proposed for nanoscale etching by controlling the SiO_xF_y layer thickness, as to limit Si etching on trench sidewalls in deep etching processes. SiF_4 condenses at temperatures much lower than C_4F_8 (close to -160°C at about 1 Pa) and a process such as the one described above cannot be used with SiF_4: such a low temperature is out of the working range recommended for our cryogenic chuck, and water condensation would become a real issue. Therefore, it has been decided to use SiF_4 / O_2 plasma instead of C_4F_8 gas in the deposition step of a plasma ALE process. The use of a plasma instead of a gas, enables to form SiF_x and O atoms necessary to build the passivation layer, but also to increase the temperature of the process. Thus, most of the processes were finally conducted at about -65°C, as the selectivity was the highest at this temperature. Indeed, whereas this process was first designed for Si etching, it was shown that at temperatures close to -65°C, and if SiF_4 / O_2 has a ratio close to 1 / 3, it is possible, in a cycle, to etch Si_3N_4 while growing a passivation layer on a-Si. It was also demonstrated that, for the three materials, deposition

occurs at higher temperatures (above -40°C) due to oxygen rich layers, whereas etching occurs at lower temperatures (below -80°C) due to fluorine rich layers. Indeed, decreasing the temperature enhances the adsorption and increases the residence time of fluorine-based species instead of oxygen. Between those temperatures, a SiO_xF_y layer grows on the substrate, and the Ar plasma step is necessary to etch the material. However, the threshold temperature between deposition and etching was not the same for the three materials. Indeed, the first material to be etched in a pure SiF_4 / O_2 plasma was Si_3N_4 for temperatures between -80°C and -100°C whereas, for the same plasma parameters, spontaneous etching of a-Si occurs for temperatures below -100°C. Therefore, the selectivity can be controlled by carefully adjusting the temperature so that the process is in deposition regime for one material and in etching regime for the other.

To understand the mechanisms involved in this nanoscale process, in-situ XPS measurements were performed on the OPTIMIST platform at IMN laboratory. Those studies confirmed the observations made by SE. Indeed, XPS scans showed that at -40°C, a SiO_xF_y layer is deposited on both materials with less than 20% of fluorine content in it, and does not desorb after warming to 20°C. At -65°C, same observation is performed on a-Si. However, for Si_3N_4 the deposited layer gets richer in fluorine (up to 44%) and then part of the fluorine desorbs once the sample is brought back to room temperature. Finally, at -100°C, the deposited layer is rich in fluorine (up to 53% of the layer content) on both materials. Once again, a significant part of fluorine desorbs after warming to 20°C. This experiment confirmed that fluorine based species have their residence time increased at enough low temperature. It also explains the selectivity between a-Si and Si_3N_4 observed when varying the process temperature.

Based on this information, a pulsed process similar to an ALE process was performed. However, an additional step consisting on a longer deposition step of SiF_4 / O_2 was performed after 4 cycles to ensure the passivation of a-Si. Thus, it was possible to achieve an infinite selectivity where, Si_3N_4 was etched on about 27.6 nm and not a-Si after about 40 cycles.

In this PhD, only fluorine-based gases have been tested. It can however be intended to try chlorine based gases for Si etching. Also, -90°C was the highest temperature where Cryo-ALE tests based on C_4F_8 physisorption were achieved. Therefore, it can be interesting to try gases with higher condensation properties, in order to increase the temperature of processes based on physisorption to -50°C. This will enable to use only a chiller to cool the substrate instead of using liquid nitrogen. Finally, changing the gas chemistry used in physisorption processes would also be helpful to achieve greater selectivity between the different materials.

This PhD also aimed to show the feasibility of cryogenic nanoscale etching on blank materials. For the continuation of the project, it will be interesting to perform those tests on patterned samples in order to check the anisotropy of those processes.

Finally, additional characterization tests can be planned, such as Optical Emission Spectroscopy for plasma characterization, as well as other QMS and XPS tests. Those tests could help identify the species involved in the deposition step and / or etching step. Once those species have been identified, it will be possible to monitor their evolution through time and along the process. Processes could then be optimized by reducing the time needed to achieve a controlled etching. Finally, the additional data provided would make it possible to carry out molecular dynamics which would also improve the knowledge on the mechanisms involved in Cryo-ALE processes

Publications

Japanese Journal of Applied Physics **58**, SEEB03 (2019) **REGULAR PAPER**
https://doi.org/**10.7567/1347-4065/ab1639**

The role of physisorption in the cryogenic etching process of silicon

G. Antoun[1*], R. Dussart[1*], T. Tillocher[1], P. Lefaucheux[1], C. Cardinaud[2], A. Girard[2], S. Tahara[3], K. Yamazaki[4], K. Yatsuda[4], J. Faguet[5], and K. Maekawa[5]

[1]*GREMI, Orléans University-CNRS, 14 Rue d'Issoudun BP 6744, 45067 Orléans, France*
[2]*IMN, Institut des Matériaux Jean Rouxel, Université de Nantes, CNRS, BP32229, 44322 Nantes Cedex 3, France*
[3]*Tokyo Electron Miyagi Limited, 1 Techno Hills, Taiwa-cho, Kurokawa-gun, Miyagi, Japan*
[4]*Tokyo Electron Limited, Akasaka Biz Tower, 3-1 Akasaka 5-chome, Minato-ku, Tokyo, Japan*
[5]*TEL Technology Center, America, LLC, NanoFab 300 South 255 Fuller Rd., Suite 214, Albany, NY, United States of America*

[*]E-mail: gaelle.antoun@univ-orleans.fr; remi.dussart@univ-orleans.fr

Received January 22, 2019; revised March 22, 2019; accepted March 25, 2019; published online May 17, 2019

The growth mechanism of the passivation layer in the cryogenic process used for silicon deep etching is explored experimentally in an inductively coupled plasma reactor. In particular, the role of SiF_4 etching by-products on the SiO_xF_y layer deposition is investigated. The deposition of a SiO_xF_y layer using SiF_4 and O_2 gases is studied by in situ ellipsometric spectroscopy in different experimental configurations to devise the deposition mechanism: SiF_4/O_2 plasma mixture, alternation of SiF_4 plasma and O_2 plasma steps and alternation of SiF_4 flow without plasma and O_2 plasma steps. The refractive index and the thickness of the deposited layer are measured for different substrate temperatures, from −125 °C to 20 °C. Although some of the passivation layer is removed during the wafer warm up, a residual amount remains at the surface. The deposited SiO_xF_y layer forms more efficiently at low temperature with an optimal temperature of −100 °C in our experimental conditions. The passivation layer was etched by a SF_6 plasma without bias versus the deposition temperature, to evaluate its resistance to plasma etching steps. The passivation layer was analyzed by ex situ EDX and XPS. We investigated the role of SiF_4 low temperature physisorption in the formation of the passivation layer on the sidewalls of the features that are being etched, which are not submitted to ion bombardment. It is shown that physisorption of SiF_x species play an important role because their residence time at the surface is longer, thus increasing the probability of reaction with oxygen.

1. Introduction

Cryo-etching of silicon was first introduced by a Japanese team at the end of the 1980s.[1)] High aspect ratio Si structures can be obtained using this particular process at low substrate temperature as reported in Refs. 2–14. The standard cryo-etching process consists in using an SF_6/O_2 plasma mixture interacting with a low temperature silicon wafer (typically −100 °C). The passivation mechanisms were studied extensively.[15–20)] The SiO_xF_y passivation layer, which only forms at low temperature is mostly removed when the wafer is warmed to room temperature.[15,18)] By analyzing the desorbed species from the substrate surface at low temperature by in situ ellipsometry and in situ XPS, it was shown that the surface was reorganized during the warming forming SiF_4 molecules which desorb, leaving the surfaces quite clean compared to those obtained in other processes such as the so-called Bosch process.[16,19)] In order to reinforce the sidewall passivation, the alternation of SiF_4/O_2 plasma deposition steps with SF_6 plasma etching steps was proposed: this is the STiGer process.[21,22)] This process achieves quite similar performance as the Bosch process but, in the conditions of our experiments, the passivation layer growth is favored on low temperature surfaces so as to minimize deposition on the reactor wall. Using the STiGer process rather than the Bosch process avoids CF_x contamination of the reactor wall, process drifts and the necessity of cleaning steps between wafer etchings. Besides, cryogenic processes are also useful when the surface diffusion of the species has to be limited to avoid material damage. This benefit was successfully demonstrated when etching porous SiOCH low-k structures.[22–26)]

The passivation layer obtained in SF_6/O_2 plasma at room temperature in over-passivating regime (high oxygen content) was recently studied by Ref. 27 who characterized the deposited layer in SF_6/O_2 plasma when forming some self-textured silicon (equivalent to black silicon). They found that the fluorine concentration of the SiO_xF_y layer was twice larger than the oxygen concentration. In another hand, they showed that fluorine was desorbing when the sample was exposed to air, leaving a surface of SiO_2 having a thickness corresponding to that of a native oxide layer. In the standard cryo-etching process, the O_2 content in the plasma mixture is typically below 10%, so that nearly no remaining oxidation layer can be evidenced by ex situ XPS measurements.[15)]

When using the STiGer process,[21)] the SiO_xF_y passivation layer is reinforced by SiF_4/O_2 plasma steps. Mechanisms of SiOF film deposition by SiF_4/O_2 plasma have already been studied and reported by Ref. 28, but the SiOF layer was deposited at rather high temperature (between 347 and 567 K). At low temperature, the growth mechanism can be quite different. Reference 29 showed by molecular dynamics that probabilities for immediate sticking upon impact of various impinging SiF_x or F_x species on different surfaces do not vary with temperature between −100 °C and 20 °C. They also mentioned that the residence time of physisorbed species at the surface, and in particular SiF_4, is significantly increased at low temperature. One of the objectives of this paper is to evaluate the role of physisorbed SiF_4 in the SiO_xF_y passivation layer formation. The deposition mechanism is investigated by cavity test experiments, which can be used to confirm the formation of a passivation layer and evaluate its robustness.[16)] The layer growth on a planar area was characterized by in situ spectroscopic ellipsometry using three different ways to create the SiO_xF_y layer: SiF_4/O_2 plasma mixture, alternation of SiF_4 plasma and O_2 plasma, alternation of SiF_4 gas flow and O_2 plasma.

2. Experimental method

The experiments were carried out using an inductively coupled plasma reactor with a diffusion chamber. A diagram of the reactor can be found in.[20)] O_2, SiF_4 and SF_6 gases are injected from the top of the plasma source. The source power

was varied between 1000 and 1500 W. 150 mm diameter silicon wafers were used for the experiments. For cavity test experiments and ellipsometry, coupons were uniformly glued on a carrier wafer with a paste having a very good thermal conductivity. For patterned wafers, an SiO_2 mask with a thickness of 300 or 1000 nm was used. For ellipsometry analysis, we used silicon coupons coated with SiO_2 (100 nm) and a-Si (50 nm). Note that no specific surface preparation has been carried out on the coupons. The mask used for deep etching experiments contains a high density of 0.8 μm wide trenches. Contrary to what is mentioned in,[30] where the authors claim the difficulty and slowness of working at low temperatures, the cooling step to reach the low temperature is performed only once for the first wafer. Since a load-lock is attached to the process chamber, the next wafers are loaded/unloaded without heating and cooling the chuck each time. The substrate holder is equipped with a cooling circuit using liquid nitrogen and the temperature is regulated by a proportional-integral-derivative controller and electrical resistance. The temperature is measured by a Pt100 probe inside the chuck, 2 cm below its surface. As soon as the substrate holder is cooled, wafers can be treated one after the other rapidly, just like in processes at room temperature. Typically, a delay of 2 min is set to reach the right helium backside pressure and thermalize the wafer.

A UVISEL spectroscopic ellipsometer from Horiba Jobin–Yvon was installed on the reactor at 70° angle of incidence. It is equipped with 32 photomultipliers to acquire simultaneously the multiwavelength signal in the UV—visible spectrum and perform kinetic measurements. The acquisition time was set to 400 ms.

Profiles were analyzed using a SUPRA-40 Zeiss SEM (scanning electron microscope) equipped with a Bruker energy dispersive X-ray spectroscopy (EDS) diagnostic.

XPS analyzes were realized ex situ using an Axis Ultra photoelectron spectrometer from Kratos Analytical. This system is equipped with a monochromatized Al Kα X-ray source operating at 15 kV and 20 mA. Survey spectra were acquired between 1200 and 5 eV (binding energies) at a pass energy of 80 eV with an energy step of 1 eV. High resolution spectra were further acquired at a pass energy of 20 eV with an energy step of 0.1 eV on all spectral regions of interest. In both cases, the spectrometer is operated in the "hybrid" mode, using the "slot" aperture; in this combination, the analyzed surface area is approximately $700 \times 300\ \mu m^2$. Charge compensation was obtained by means of the in-built charge neutralizer. Such system is very efficient to stabilize the surface charge but the energy reference is typically lost and the spectra need to be calibrated using an internal reference. The O1s core level has been chosen at 532.6 eV, as in SiO_2.

3. Results

3.1. Growth of the SiO_xF_y in SiF_4/O_2 plasma versus temperature

SiO_xF_y growth on silicon by a SiF_4/O_2 plasma mixture was studied at different substrate temperatures. For this experiment, a (100) silicon wafer covered by a 100 nm thick SiO_2 layer and by a 50 nm thick a-Si layer was used. Delta and psi ellipsometric angles were measured in real time every second at 32 wavelengths. The acquisition duration for each point was 500 ms. The ellipsometric spectrum was simulated using a classical model (Drude and Lorentz models).

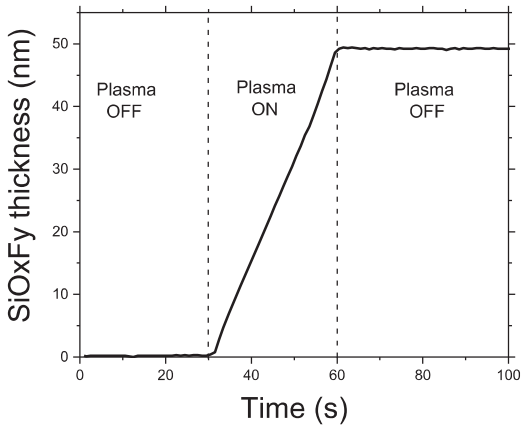

Fig. 1. Growth time evolution of the SiO_xF_y layer on a-Si obtained with a SiF_4/O_2 plasma. (Experimental conditions: O_2 flow = SiF_4 flow = 50 sccm, P_{source} = 1000 W, P_{bias} = 0 W, Pressure = 3 Pa, substrate temperature = −100 °C, process duration: 30 s).

In Fig. 1, the time evolution of the SiO_xF_y layer thickness is shown for a source power of 1000 W. The gas flow of SiF_4 and O_2 was each set to 50 sccm and the total pressure was 3 Pa. No bias power was applied to the substrate. The growth is linear with a deposition rate of 1.6 nm s^{-1}. The refractive index of the deposited layer after deposition was estimated by in situ ellipsometry to be 1.33 ± 0.02 at 1.96 eV before venting.

The same experiment was repeated at different temperatures between −130 °C and +25 °C. The SiO_xF_y layer thickness was evaluated before and after venting. The results are shown in Figs. 2(a) and 2(b) where the SiO_xF_y layer thickness and the optical index are plotted versus the temperature of deposition. Note that "Before venting" corresponds to characterization done at the deposition temperature, directly after the deposition step and before translating the carrier wafer and the sample to the load-lock. Then the sample is kept in the load-lock under N_2 atmosphere at atmospheric pressure until its temperature is back to room temperature. The "after venting" measurement is taken after bringing back the sample to the reactor chamber for additional characterization by ellipsometry. The deposited layer thickness increases by cooling the substrate. It reaches 32 nm at 25 °C and 49 nm at −100 °C. Below −100 °C, the deposited layer thickness decreases. At −130 °C, no deposition was obtained, but a slight etching of about 1 nm was observed instead (not represented on the graph). At 25 °C and at −50 °C, the deposited layer thickness and its optical refractive index remain quite close for both temperatures and are of the order of 30–35 nm and 1.4 respectively). At lower temperature the refractive index drops to a typical value of about 1.3. After venting, a variation of the total thickness of the SiO_xF_y layer was systematically observed accompanied by a decrease of the index. This observation is in good agreement with the observations reported in[16,18,19] of the partial desorption of the layer when the sample is warmed to room temperature. However, in these experimental conditions of SiF_4/O_2 plasma, a significant amount of the deposited layer remains after venting. The same model was applied with a very good fit for thickness

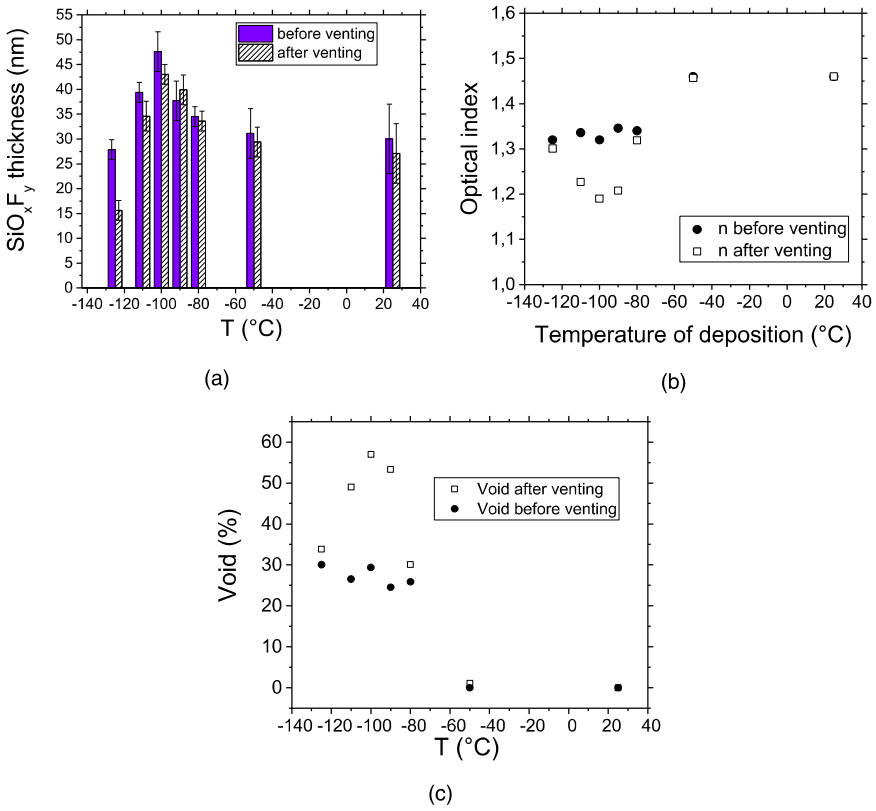

Fig. 2. (Color online) SiO_xF_y layer thickness (a), optical index (b), and void percentage (c) versus the deposition temperature.

characterization before and after venting. The model simulates a mixture of SiO_2 material and void in the Delta Psi 2 software. The drop of the optical index indicates that the layer is less dense after venting, suggesting that the remaining SiO_xF_y layer is quite porous. In Fig. 2(c), ellipsometric modeling of the layer tends to show that the void percentage in the layer increases when deposited at lower temperature. This void percentage reaches about 55% after venting when the layer is deposited at −100 °C whereas the layer can be well fitted by a 100% SiO_2 material when deposited at 25 °C. That higher porosity after venting is due to fluorine species desorption when bringing back the sample to room temperature.

Finally, to evaluate its robustness, the SiO_xF_y layer obtained at different deposition temperatures was submitted to a plasma of pure SF_6 (200 sccm, 1000 W, 3 Pa) without bias and at room temperature. We could evaluate by ellipsometry the time to etch both the SiO_xF_y layer and the 50 nm thick a-Si film. The estimated etch rate is reported on Fig. 3 as a function of the deposition temperature. It is clear that the layer is etched faster when the deposition is performed at low temperature. This is consistent with the fact that the layer is more porous at low temperature, favoring the etching of the material by fluorine atoms. At −125 °C, the deposited SiO_xF_y layer being quite thin, is rapidly etched, exposing the a-Si layer which has an etch rate of 2.25 nm s^{-1} in the SF_6 plasma. Consequently, the overall etch rate obtained at this deposition temperature corresponds mainly to a-Si etching.

3.2. Growth of the SiO_xF_y in SiF_4/O_2 plasma versus O_2 content

A study of the SiO_xF_y growth at low temperature (−100 °C) in SiF_4/O_2 plasma was carried out by varying the O_2 content

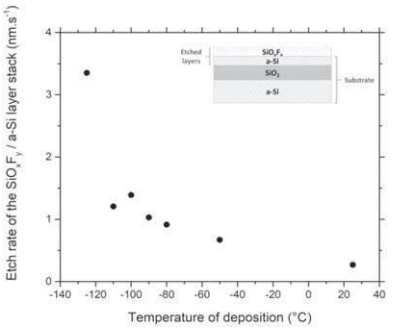

Fig. 3 Etch rate of the film composed of the deposited SiO_xF_y layer and the 50 nm thick a-Si layer as a function of the deposition temperature. The etching parameters are: pure SF_6, 200 sccm, 1000 W, 3 Pa, $T = 25$ °C Inset: sketch of the layer stack submitted to the SF_6 plasma.

from 0% to 87.5%. The experiments were performed on 50 nm thick a-Si film, with a total power of 1000 W, without bias, a total pressure of 3 Pa and a total gas flow of 40 sccm. The thickness was evaluated by in situ ellipsometry directly after the deposition step and after venting in the load-lock (few minutes in air). The results are presented in Figs. 4(a) and 4(b). The maximum thickness is obtained for pure SiF_4 plasma (116 nm). By increasing the O_2 content in the plasma, Si concentration is thus weaker and therefore the total deposited SiO_xF_y layer thickness decreases as well. After venting, the total thickness decreases except for the case of 25% of oxygen where it seems to remain more or less constant. However, if we plot the optical thickness nL [Fig. 4(b)] instead of the thickness L [Fig. 4(a)], we observe a systematic decrease after venting. The optical path (product n times L) is sometimes a more relevant parameter especially with porous material to evaluate the quantity of remaining material instead of the remaining thickness.

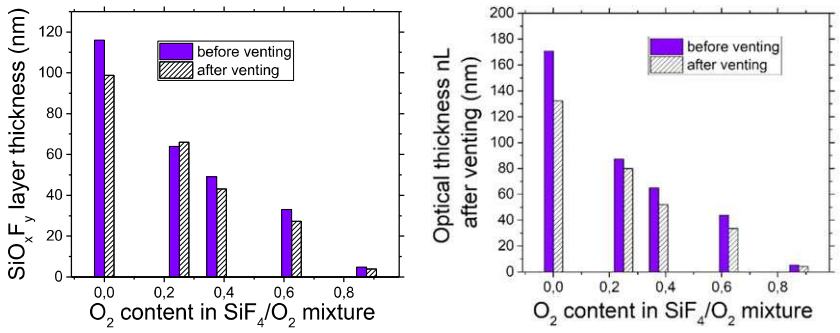

Fig. 4. (Color online) SiO_xF_y layer thickness (a) and optical thickness nL (b) versus O_2 content after a plasma of SiF_4/O_2 of 30 s, total flux = 40 sccm, Pressure = 3 Pa, P_{source} = 1000 W, P_{bias} = 0 W, Pressure = 3 Pa, substrate temperature = −100 °C, process duration: 30 s.

3.3. Chemical analysis of the SiO_xF_y obtained by SiF_4/O_2 plasma at low temperature of the substrate

The SiO_xF_y layer obtained on silicon and on the SiO_2 mask was analyzed by EDX and XPS. A typical EDX spectrum is given in Fig. 5(a). The layer is mainly composed of silicon, oxygen and fluorine. Some carbon contamination is observed. The small peak of Al comes from the sample holder used for the SEM analysis. A very small amount of sulfur could also be detected. A SEM picture of the SiO_xF_y deposited on both silicon and SiO_2 (mask) is shown in Fig. 5(b). The same region was analyzed by EDX in 2D to determine the repartition of chemical elements on the sample surface [Fig. 5(c)]. One can clearly distinguish the different regions of silicon, SiO_2 and the passivation layer, which is composed of silicon, fluorine and oxygen as expected.

In order to have a finer characterization of the surface, ex situ XPS analysis of the passivation layer was carried out. Note that the analysis was carried out several days after the process and in an external lab. A 1 min long SiF_4/O_2 plasma without bias was used to deposit a 160 nm thick layer. The deposition temperature was −110 °C. Typical spectra (wide scan and individual lines) are provided in Fig. 6 and the composition of the layer at the surface is given in Table I.

According to XPS analysis, the layer is composed of 33.6% Si, 60.0% O, 4.2% C and 2.2% F. From the survey scan and the F1s and C1s core background levels, it is clear that carbon and fluorine species are localized at the surface and not in the depth of the film. The chemical composition of the latter is close to that of SiO_2, but probably quite porous as already mentioned in the previous part. This interpretation is supported by the experimental energy gap between the O1s and Si2p3/2 core levels, which is 429.4 eV as in SiO_2 material and by the single chemical contribution in the O1s and Si2p spectra. The C1s spectrum shows four contributions, which are typical for carbonaceous atmospheric contamination: 284.5 eV (C–C/C–H), 286.3 eV (C–O), 287.8 eV (C=O) and 289.2 eV (O–C=O). The F1s (687.0 eV) is characteristic of fluorine bound to SiO_x environment.[31]

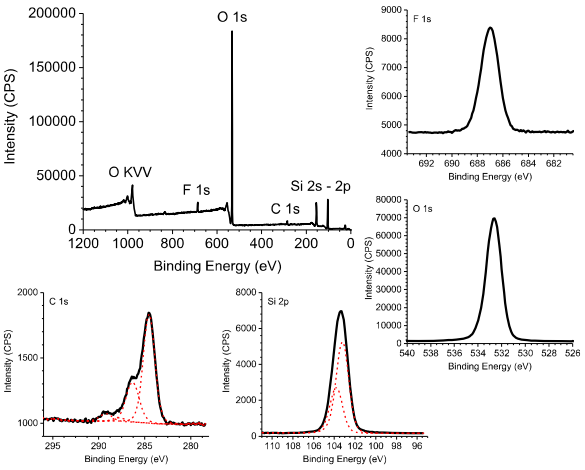

Fig. 6. (Color online) (top-left) Wide scan of an XPS spectrum of the SiO_xF_y layer obtained after 1 min of SiF_4/O_2 plasma at −110 °C. (bottom and right) Spectrum decomposition of F1s, O1s, C1s and Si2p lines. The dashed lines (in red) correspond to the components.

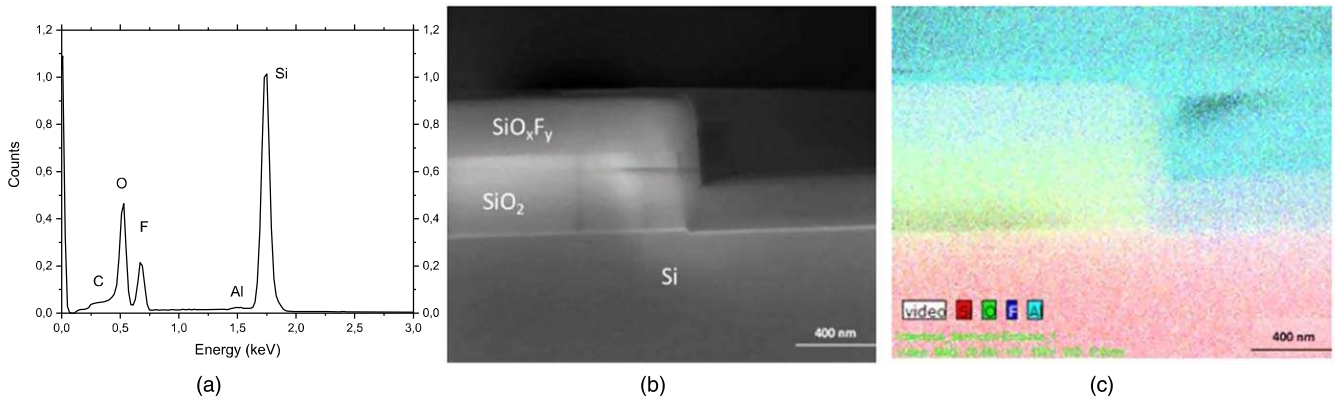

Fig. 5. (Color online) (a) EDX analysis of the SiO_xF_y layer. (b) SEM picture of the deposited layer on silicon and on the SiO_2 mask. (c) 2D EDX analysis of the SEM picture showing the chemical composition of the different regions of the sample surface.

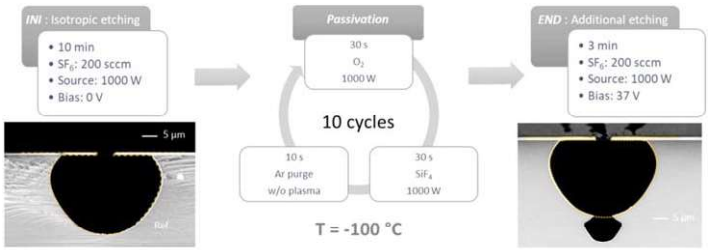

Fig. 7. (Color online) Passivation test experiment. Left: SEM picture of the reference profile after 10 min of pure SF_6 plasma (200 sccm, 1000 W, no bias) Center: diagram of the process steps to form the passivation layer at −100 °C Right: SEM picture of the final profile after the alternated SiF_4 and O_2 plasmas and after 3 min of final etching of pure SF_6 (200 sccm, 1000 W, 40 V bias).

Table I. Composition of the SiO_xF_y layer obtained after 1 min of SiF_4/O_2 plasma at −110 °C. An energy correction of +1.5 eV was applied.

Plasma	Peak name	Position (eV)	FWHM (eV)	% conc.
SiF_4/O_2 1 min	Si 2p3/2	103.78	1.34	22.4
	Si 2p1/2	103.18	1.34	11.2
	F 1 s	686.97	1.58	2.2
	O 1 s	532.60	1.44	60.1
	C 1 s	284.53	1.45	2.8
	C 1 s	286.32	1.59	1.2
	C 1 s	287.80	1.56	0.1
	C 1 s	289.20	1.59	0.2

3.4. Growth of the SiO_xF_y layer by alternating SiF_4 plasma and O_2 plasma

Passivation test experiments have been performed to better understand the passivation layer formation mechanism at the surface of a cavity. All the described processes were carried out at −100 °C. A cavity was first formed by an isotropic etching step of pure SF_6 plasma (200 sccm) with a source power of 1000 W without bias, during 10 min. The resulting profile is shown in the left SEM picture of Fig. 7 for a 5 μm wide trench. This step is called INI. The obtained isotropic profile is very reproducible and is used as a reference for comparison with the final profile. Then, 30 s long steps of SiF_4 plasma and O_2 plasma (50 sccm, 1000 W, no bias) were alternated 10 times as indicated in the diagram in the middle of Fig. 7. Note that a 10 s long Ar purge (100 sccm) was also inserted between SiF_4 plasma and O_2 plasma to make sure that no residual SiF_4 gas was present in the reactor during the O_2 plasma. Finally, an additional 3 min long etching step was added in the same conditions as in the initial process. However, a self-bias of 40 V has been applied by an independent RF power supply of 13.56 MHz, to remove the passivation layer at the bottom in front of the mask aperture. Note that 40 V is the set point but the real value measured on the matching box is only 37 V. The profile is shown on the right SEM picture of Fig. 7. The reference profile is also represented in dashed line for comparison.

The resulting profile consists of two cavities: the large one corresponds exactly to the reference cavity and the small one corresponds to the cavity etched during the 3 additional minutes of etching plasma. Without inserting the passivation step, the profile would have been isotropic with a larger cavity than the reference one (not represented here, but shown in[16]). Here, it can be deduced that the first cavity was efficiently protected by a passivation layer formed during the plasma alternation. It confirms the following mechanism: SiF_x species deposit on the cavity and are oxidized by O atoms.

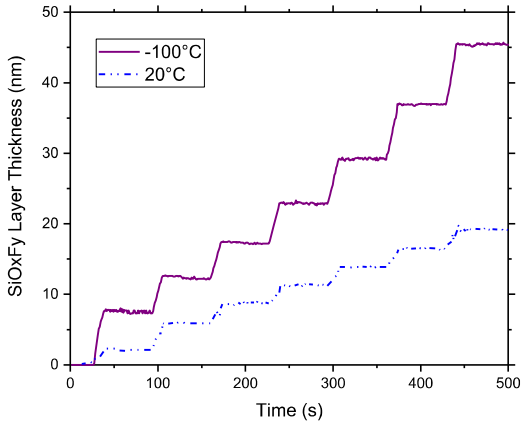

Fig. 8. (Color online) Growth kinetics of the SiO_xF_y layer during the alternated SiF_4 plasma and O_2 plasma without bias measured by in situ ellipsometry for −100 °C and 20 °C.

To better analyze the growth kinetics of the SiO_xF_y, the alternation of SiF_4 plasma and O_2 plasma was performed in the same conditions as in the passivation test experiment on a-Si and the SiO_xF_y layer deposition was monitored by in situ ellipsometry. Figure 8 shows the SiO_xF_y layer thickness plotted as a function of time for two substrate temperatures: −100 °C and 20 °C. For −100 °C, a total thickness of about 45 nm was obtained after 7 cycles. The steep increase of the SiO_xF_y layer is obtained uniquely during the SiF_4 plasma. During the O_2 plasma, the layer thickness remains constant or decreases slightly. For 20 °C, deposition is less efficient: the total deposited layer is only 17 nm thick.

At low temperature, SiF_x species deposit more efficiently. However, it was shown by Ref. 29 that the probability for immediate sticking on silicon surface for species as SiF_x or F_x did not depend on the substrate temperature and was actually the same at −100 °C as at 20 °C. They also reported that the residence time of SiF_x species and in particular, SiF_4 molecules at the surface was increasing significantly at low temperature. The role of physisorbed SiF_4 molecules in the passivation layer formation is studied in the next part.

3.5. Evaluation of the role of the SiF_4 physisorption

Reference 29 showed by molecular dynamic simulation that the desorption rate of SiF_4 species at low temperature is many orders of magnitude lower than that obtained at room temperature. Consequently, physisorbed species accumulate at the surface even if SiF_4 is supposed to be in gas phase at this pressure and temperature according to the vapor pressure curve. To really evaluate the role of SiF_4 physisorption in cryo-etching processes, the same experiment as the one

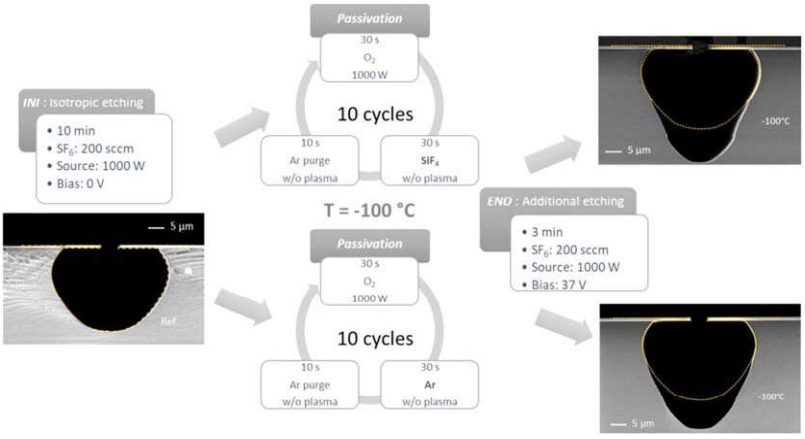

Fig. 9. (Color online) Passivation test experiment by a mechanism of SiF_4 physisorption. Left: SEM picture of the reference profile after 10 min of pure SF_6 plasma (200 sccm, 1000 W, no bias). Center: diagrams of the process steps to test the passivation layer formation. Right: SEM picture of the final profile after the alternated **SiF_4 flow** and O_2 plasma (top) and after the alternated **Ar flow** and O_2 plasma (bottom) followed by the 3 min final etching of pure SF_6 (200 sccm, 1000 W, 40 V bias).

described in the previous paragraph was carried out, but instead of operating a 30 s long SiF_4 plasma, SiF_4 gas flow was injected without plasma during 30 s. An argon purge was performed between SiF_4 flow and O_2 plasma in order to avoid the presence of SiF_4 molecules during the O_2 plasma steps. The etch profile after 10 alternations and the final step of etching is shown on the right-top SEM picture in Fig. 9. The reference profile is also represented in dashed line for comparison. The second cavity is not as well defined as the one shown in Fig. 7, but the upper part of the cavity was protected since it fits very well with the reference profile. This means that this part was protected by a passivation layer which survived after the 3 min final etch step. However, the passivation layer is not as strong as the one obtained in the experiment of Fig. 7, since the first cavity was partly destroyed and a much larger second cavity was formed. To evaluate the role of SiF_4 physisorption in the protection of the upper part of the first cavity, we replaced the SiF_4 flow step of the previous experiment by an Ar flow step in the same conditions without plasma. The SEM cross-section of the final profile is shown at the bottom-right picture of Fig. 9. The final profile is quite similar to that obtained with SiF_4 flow although a slight difference can be observed between the two final profiles. The top of the first cavity was also sufficiently protected even if no SiF_4 was injected during the passivation step. These results suggest that SiF_4 physisorption is not responsible for the formation of the passivation layer. The protection of the upper part of the first cavity is attributed to the O_2 plasma that oxidizes all areas that are not submitted to ion bombardment. Consequently, the contribution of SiF_4 molecule physisorption seems to be quite low at this temperature.

This is confirmed by in situ ellipsometry characterization. The same experiment as the one described above was carried out on a flat surface area of a-Si analyzed by in situ ellipsometry. At 25 °C, the a-Si thickness remains very stable and no SiO_xF_y layer grows. This is expected since SiF_4 is very volatile and does not stick on surfaces at room temperature. Moreover, Ar flow purges are inserted between SiF_4 flow and O_2 plasma steps, so that no SiF_4 remains at the surface during the O_2 plasma step. At −100 °C, no SiO_xF_y layer grows either, confirming the results obtained with the passivation test experiments performed at −100 °C.

By comparison with the results shown in Fig. 7 where SiF_4 plasma and O_2 plasma were alternated, it can be infered that passivation by SiF_x deposition reacting with O atoms is much more efficient to grow a robust passivation layer. By the passivation test experiments, it can be concluded that a SiO_xF_y passivation layer cannot be formed by SiF_4 molecule adsorption followed by reaction with O atoms. Nevertheless, SiF_x species with $x < 4$ also have a much longer residence time at the surface and a much lower desorption rate at low temperature. This would make the reactions of SiF_x species with O atoms more likely at low temperature and would explain why the SiO_xF_y growth is significantly enhanced by decreasing the substrate temperature. As calculated by Ref. 29, the probability for immediate sticking upon impact of impinging SiF molecules on Si and SiF surfaces is higher than the one of SiF_2 molecules, which is itself higher than the one of SiF_3 molecules. The combined probability and the longer residence time at low temperature could explain the necessity of SiF_x species to grow a robust passivation layer at cryogenic conditions.

When created, the remaining layer is probably composed of a mixture of chemisorbed and physisorbed species. By warming up the substrate, diffusion of physisorbed species becomes more important and the passivation layer is rearranged, creating volatile species such as SiF_4. By venting the sample, remaining fluorine atoms desorb from the surface in contact with humid air by hydrolysis reactions with ambient water vapor, forming HF that desorbs as already explained by Ref. 27.

4. Conclusion

We investigated the role of physisorbed species in the passivation layer obtained in the cryogenic etching process of silicon. SiF_4/O_2 plasma chemistry was used to create a SiO_xF_y passivation layer. The SiO_xF_y layer growth obtained in different conditions was characterized by in situ ellipsometry, ex situ XPS and EDS. Its thickness increases by decreasing the temperature down to −100 °C, then decreases beyond −100 °C. The optical index is also reduced at low temperature. A significant change of both layer thickness and index is obtained by warming and venting the samples. The layer after venting is mainly composed of silicon and oxygen.

A small amount of fluorine was detected at the surface. The SiO_xF_y layer can be etched by SF_6 plasma. The etch rate is higher when it is deposited at low temperature.

SiO_xF_y layer formations were carried out by passivation test experiments by separating O_2 plasma and SiF_4 plasma. After 10 cycles, an effective protection of the initial cavity is obtained. To study the role SiF_4 physisorbed species, SiF_4 plasma was replaced by SiF_4 flow. In this case, the initial cavity was only partially protected and mainly by oxidation of the silicon surface. Finally, a better understanding of the cryogenic etching mechanism is suggested: SiF_x $(x < 4)$ physisorbed species have a much longer residence time at $-100\,^{\circ}C$ than at room temperature; they can react with O more efficiently. However, the remaining layer is not as dense as the one that is obtained at room temperature. By warming the sample, a reorganization of the species at the surface is happening as species that are not well bonded desorb from the material, making the material more porous, as shown experimentally by in situ ellipsometry.

Acknowledgments

This work was supported by the CERTeM 2020 platform, which provides most of the equipment.

ORCID iDs

G. Antoun https://orcid.org/0000-0002-3562-541X
R. Dussart https://orcid.org/0000-0003-2001-5034
C. Cardinaud https://orcid.org/0000-0002-9753-8848

1) S. Tachi, K. Tsujimoto, and S. Okudaira, Appl. Phys. Lett. **52**, 616 (1988).
2) H. Jansen, H. Gardeniers, M. de Boer, M. Elwenspoek, and J. K. Fluitman, J. Micromech. Microeng. **6** (1996).
3) S. Aachboun, P. Ranson, C. Hilbert, and M. Boufnichel, J. Vac. Sci. Technol. Vac. Surf. Films **18**, 1848 (2000).
4) G. Craciun, M. A. Blauw, E. Van der Drift, P. M. Sarro, and P. J. French, J. Micromech. Microeng. **12**, 390 (2002).
5) M. D. Henry, C. Welch, and A. Scherer, J. Vac. Sci. Technol. Vac. Surf. Films **27**, 1211 (2009).
6) Ü. Sökmen, A. Stranz, S. Fündling, S. Merzsch, R. Neumann, H.-H. Wehmann, E. Peiner, and A. Waag, Microsyst. Technol. **16**, 863 (2010).
7) A. Kamto, R. Divan, A. V. Sumant, and S. L. Burkett, J. Vac. Sci. Technol. Vac. Surf. Films **28**, 719 (2010).
8) F. Jiang, A. Keating, M. Martyniuk, K. Prasad, L. Faraone, and J. M. Dell, J. Micromech. Microeng. **22** (2012).
9) M. J. de Boer, R. W. Tjerkstra, J. W. Berenschot, H. V. Jansen, G. J. Burger, J. G. E. Gardeniers, M. Elwenspoek, and A. van den Berg, J. Microelectromech. Syst. **9**, 94 (2000).
10) M. W. Pruessner, W. S. Rabinovich, T. H. Stievater, D. Park, and J. W. Baldwin, J. Vac. Sci. Technol. B **25**, 21 (2007).
11) H. V. Jansen, M. J. de Boer, S. Unnikrishnan, M. C. Louwerse, and M. C. Elwenspoek, J. Micromech. Microeng. **19**, 033001 (2009).
12) Z. Liu, Y. Wu, B. Harteneck, and D. Olynick, Nanotechnology **24**, 015305 (2013).
13) M. Kulsreshath, A. Vital, P. Lefaucheux, C. Sinturel, T. Tillocher, M. Vayer, M. Boufnichel, and R. Dussart, Micro Nano Eng. **1**, 42 (2018).
14) H. Miao, L. Chen, M. Mirzaeimoghri, R. Kasica, and H. Wen, J. Microelectromech. Syst. **25**, 963 (2016).
15) R. Dussart, M. Boufnichel, G. Marcos, P. Lefaucheux, A. Basillais, R. Benoit, T. Tillocher, X. Mellhaoui, H. Estrade-Szwarckopf, and P. Ranson, J. Micromech. Microeng. **14**, 190 (2003).
16) X. Mellhaoui, R. Dussart, T. Tillocher, P. Lefaucheux, P. Ranson, M. Boufnichel, and L. J. Overzet, J. Appl. Phys. **98**, 104901 (2005).
17) T. Tillocher, R. Dussart, X. Mellhaoui, P. Lefaucheux, N. M. Maaza, P. Ranson, M. Boufnichel, and L. J. Overzet, J. Vac. Sci. Technol. Vac. Surf. Films **24**, 1073 (2006).
18) R. Dussart, X. Mellhaoui, T. Tillocher, P. Lefaucheux, M. Boufnichel, and P. Ranson, Microelectron. Eng. **84**, 1128 (2007).
19) J. Pereira, L. E. Pichon, R. Dussart, C. Cardinaud, C. Y. Duluard, E. H. Oubensaid, P. Lefaucheux, M. Boufnichel, and P. Ranson, Appl. Phys. Lett. **94**, 071501 (2009).
20) R. Dussart, T. Tillocher, P. Lefaucheux, and M. Boufnichel, J. Phys. Appl. Phys. **47**, 123001 (2014).
21) T. Tillocher, R. Dussart, L. J. Overzet, X. Mellhaoui, P. Lefaucheux, M. Boufnichel, and P. Ranson, J. Electrochem. Soc. **155**, D187 (2008).
22) L. Zhang, R. Ljazouli, P. Lefaucheux, T. Tillocher, R. Dussart, Y. A. Mankelevich, J.-F. De Marneffe, S. De Gendt, and M. R. Baklanov, ECS J. Solid State Sci. Technol. **2**, N131 (2013).
23) F. Leroy, L. Zhang, T. Tillocher, K. Yatsuda, K. Maekawa, E. Nishimura, P. Lefaucheux, J.-F. de Marneffe, M. R. Baklanov, and R. Dussart, J. Phys. Appl. Phys. **48**, 435202 (2015).
24) R. Chanson, L. Zhang, S. Naumov, Y. A. Mankelevich, T. Tillocher, P. Lefaucheux, R. Dussart, S. D. Gendt, and J.-F. de Marneffe, Sci. Rep. **8** (2018).
25) L. Zhang, R. Ljazouli, P. Lefaucheux, T. Tillocher, R. Dussart, Y. A. Mankelevich, J.-F. de Marneffe, S. de Gendt, and M. R. Baklanov, ECS Solid State Lett. **2**, N5 (2012).
26) F. Iacopi, J. H. Choi, K. Terashima, P. M. Rice, and G. Dubois, Phys. Chem. Chem. Phys. **13**, 3634 (2011).
27) M. Gaudig, J. Hirsch, V. Naumann, M. Werner, S. Großer, C. Hagendorf, N. Bernhard, and D. Lausch, J. Appl. Phys. **121**, 063301 (2017).
28) J. Zhang and E. R. Fisher, J. Appl. Phys. **96**, 1094 (2004).
29) S. Tinck, E. C. Neyts, and A. Bogaerts, J. Phys. Chem. C **118**, 30315 (2014).
30) B. Wu, A. Kumar, and S. Pamarthy, J. Appl. Phys. **108**, 051101 (2010).
31) C. Cardinaud and G. Turban, Appl. Surf. Sci. **45**, 109 (1990).

Applied Physics Letters ARTICLE scitation.org/journal/apl

Cryo atomic layer etching of SiO_2 by C_4F_8 physisorption followed by Ar plasma

Cite as: Appl. Phys. Lett. **115**, 153109 (2019); doi: 10.1063/1.5119033
Submitted: 8 July 2019 · Accepted: 30 September 2019 ·
Published Online: 10 October 2019

G. Antoun,[1,a)] P. Lefaucheux,[1] T. Tillocher,[1] R. Dussart,[1] K. Yamazaki,[2] K. Yatsuda,[2] J. Faguet,[3] and K. Maekawa[3]

AFFILIATIONS

[1]GREMI, Orléans University-CNRS, 14 Rue d'Issoudun BP 6744, 45067 Orléans, France
[2]Tokyo Electron Limited, Akasaka Biz Tower, 3-1 Akasaka 5-chome, Minato-ku, Tokyo 107-6325, Japan
[3]TEL Technology Center, America, LLC, NanoFab 300 South 255 Fuller Rd., Suite 214, Albany, New York 12203, USA

[a)]gaelle.antoun@univ-orleans.fr

ABSTRACT

Atomic Layer Etching is performed on SiO_2 samples cooled down to a very low temperature (below −100 °C). C_4F_8 gas flow is injected and molecules physisorb on the cooled surfaces. Etching is then carried out using argon plasma with a low ion energy. Atomic layer etching of SiO_2 has been proved for a temperature of −120 °C, whereas no etching was obtained at −110 °C. The etched amount per cycle is 0.4 nm. Self-limiting etching was achieved and evidenced by *in situ* ellipsometry. It is also shown that working at low sample temperature with this type of process prevents reactor wall contamination. This enables us to process many etching cycles without drift in etched amount per cycle. In order to characterize the surface roughness after etching, Atomic Force Microscopy has been performed, showing a slight increase of about 0.8 nm for a 27 nm SiO_2 etched depth.

Moore's law introduced in 1965 has started to be pushed to its limits as we have entered the atomic-scale era. To keep evolving, the semiconductor industry needs to find or improve techniques in order to get smaller and more precise etched patterns.[1–3]

Atomic Layer Etching (ALE) was first studied by Yoder in 1988, and a real gain of interest has started since 2005.[4] Many works have been reported on SiO_2 (ALE) etching at room temperature using C_4F_8 plasma as the fluorination step before etching.[4–13] However, fluorocarbon plasmas induce reactor wall contamination and a drift in etching through cycles.[6,14]

Cryogenic etching was first studied for anisotropic etching to limit defects.[15] It was then developed for silicon deep etching.[16–18] It was shown that working at low temperature was limiting reactor wall contamination[19] and was providing some clean trench sidewalls after etching.[20,21] Consequently, cryo-ALE appears as an elegant process to limit this reactor wall contamination and to have a better control on etching.

The purpose of this study was to show the feasibility of cryo-ALE on SiO_2 using a C_4F_8 gas flow instead of C_4F_8 plasma in the process. C_4F_8 molecules are physisorbed on the cooled wafer before initiating an Argon plasma. The sequence of C_4F_8 gas exposure, Ar purge and then Ar only plasma instead of the C_4F_8 plasma required for higher temperature etching, enables selective etching on the cooled surfaces only, while no deposition at all is obtained over the reactor walls.

In order to achieve this research, an Alcatel 601E, which is an inductively coupled plasma reactor, has been used. Its characteristics can be found in Ref. 19. Fast atomic layer deposition (ALD) diaphragm valves for C_4F_8 gas injection have been added to the reactor to avoid residual gas when the Ar plasma step is operated. It enables us to proceed with high precision as their response time for opening and closure is better than 15 ms. All presented results have been realized on (100) silicon samples covered by a 100 nm thick silicon oxide layer. For practical reasons, the samples are coupons glued to a carrier wafer using a special glue having a very good thermal conductivity. However, tests could have also been performed on full sheet wafers, preventing the use of any glue.

Ellipsometric angles Ψ and Δ have been monitored at 32 wavelengths in kinetic mode using an UVISEL spectroscopic ellipsometer from Horiba Jobin-Yvon in order to determine the thickness variation in real time. It is installed on the reactor at a 70° angle of incidence. The classical model (Lorentz and Drude models) has been used to simulate ellipsometric spectra. An Atomic Force Microscope [AFM, Bruker Scanning Probe Microscope (SPM) Dimension Icon] was used to compare sample roughness before and after etching. Analyses were performed with PeakForce tapping mode on a 500 nm × 500 nm scanning area.

Figure 1 shows the time chart of one ALE cycle. It starts by an injection of C_4F_8 gas for few seconds in order to physisorb C_4F_8 molecules on the top of the cooled SiO_2 surface. Then, a purge is performed by Argon flow to evacuate all C_4F_8 residual gas from the reactor chamber. Ar plasma is then initiated, with a source power of 400 W for 1–3 min in order to use low energy ion bombardment until reaching the so-called self-limiting etching (SLE) regime.[4,5,7,13,22,23] Finally, a pumping step of 15 s is performed, decreasing the pressure to a value below 7.5×10^{-3} mTorr, in order to evacuate all the etch by-products and to reset the cycle. To ensure that there is no contamination, a 4 min long Argon plasma (in the conditions of the plasma step used in each cycle) is performed before the start of each process. Thus, it is verified that there is no etching by Ar plasma and hence no contamination or sputtering effect.

By exposing the substrate to a C_4F_8 gas flow instead of a C_4F_8 plasma, no deposition at all is obtained over the reactor walls. According to Antoine's curve,[24] at room temperature, a pressure higher than 750 Torr would be needed to get the same condensation of C_4F_8. In order to enable the physisorption at lower pressure, it is necessary to decrease the temperature to a very low value. In the proposed process, only the chuck and the substrate are cooled. Consequently, C_4F_8 molecules will physisorb only on the cooled surfaces (wafer and chuck) without contaminating the reactor walls that are kept at room temperature.

The same process with 8 ALE cycles has been carried out at two different temperatures: −110 °C and at −120 °C.

Figure 2(a) shows the thickness evolution of SiO_2 during the process. One cycle contains four steps as presented in Fig. 1. In this experiment, the first step was consisting of a C_4F_8 gas injection for 20 s with a pressure of 23 mTorr. Then, the second step was a purge using Ar gas flow for 30 s with a pressure as low as 3.8 mTorr. The third step consisted of the ignition of Ar plasma during 2 min at 26 mTorr with a source power of 400 W and a self-bias voltage of −20 V. Finally, the reactor was pumped during 15 s before starting the next cycle.

At −120 °C, the different etching steps and cycles are clearly identified in Fig. 2(a). Figure 2(b) shows a zoom on cycle 7 where the C_4F_8 injection step can be identified by the layer thickness increase. Then, a fast decrease in thickness followed by a plateau is observed, corresponding to the purge step. Continuous etching is finally observed corresponding to the Ar plasma step. The etched amount per cycle (EPC) is plotted vs the cycle number in Fig. 2(c). As in Ref. 25, the EPC is higher through cycles. It increases from 0.6 nm for the first cycle to a value of 1.4 nm for the last cycle, which is more than a monolayer of SiO_2 (~0.4 nm[25]) [Fig. 2(c)]. In contrast, at −110 °C, no etching occurs at all. The small variation observed is related to C_4F_8 injection, but the thickness remains constant from one cycle to the other. At this temperature (−110 °C), physisorption is reduced as compared to −120 °C and the desorption rate is higher so that nearly no C_4F_8 molecules remain at the surface when Ar plasma is initiated.

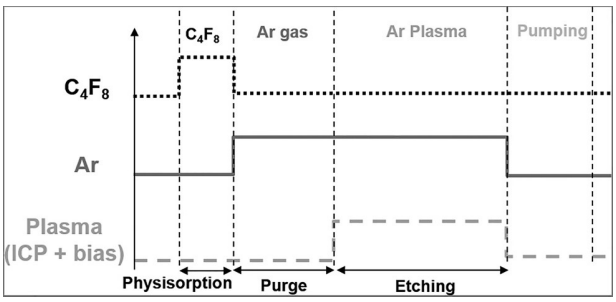

FIG. 1. Time chart of an ALE process cycle.

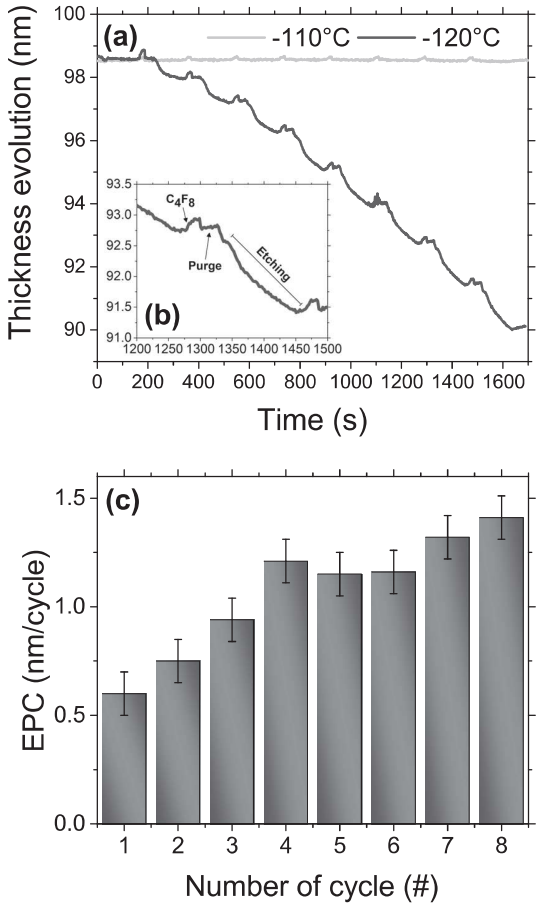

FIG. 2. (a) 8 ALE cycles for −110 °C and −120 °C, (b) zoom of the cycle #7, and (c) evolution of the etching amount per cycle along the process (experimental conditions: C_4F_8 flow: 20 s, 23 mTorr, Ar purge: 30 s, 3.8 mTorr, Ar plasma: 2 min, 23 mTorr, $P_{source} = 400$ W, and $V_{bias} = -20$ V).

This also shows that, at this pressure, the threshold for etching is between −110 °C and −120 °C. Indeed, at this pressure, the residence time of the adsorbed C_4F_8 molecules seems to be too short at −110 °C. Consequently, nearly no C_4F_8 is left at the end of the long purge step. At −120 °C, the residence time of the molecules at the surface is significantly increased and some C_4F_8 molecules are left at the surface when the Ar plasma is switched on. Therefore, both temperature and pressure are essential parameters to allow etching using this process.

In those conditions, self-limiting etching, which is a critical point in an ALE process, has not been reached, since the etching keeps going on during the whole plasma step, especially for the last cycles, Fig. 2(b). A longer Argon plasma would be needed in this case to reach SLE since the slope of the thickness variation tends to decrease in time.

Indeed, at −120 °C, a high amount of C_4F_8 is physisorbed. Consequently, a long enough time of Ar sputtering is needed to consume the deposited species and reach SLE. Nevertheless, in this case, as all the deposited species on the cooled surfaces are not consumed, they accumulate and therefore redeposit on the substrate surface, increasing the etching amount through cycles. Moreover, according to Ref. 26, Ar^+ ion bombardment could create additional active sites for C_4F_8 adsorption and hence affects the EPC. Inversely, at −110 °C, the amount of physisorbed C_4F_8 is too low when argon plasma starts to observe any etching.

The second part of this study was to adapt process parameters in order to achieve the self-limiting etching regime. In Fig. 3(a), the etched thickness is plotted vs time for a process where C_4F_8 injection time and pressure were reduced, but Ar sputter step parameters are the same as in the experiment of Fig. 2. The experiment was performed at −120 °C. Each step is clearly identified by *in situ* ellipsometry in Fig. 3(b): an increase in the thickness is observed when injecting C_4F_8. During the Ar purge, C_4F_8 is evacuated from the reactor, but the physisorbed molecules remain at the surface. Otherwise, the thickness would have become the same as before C_4F_8 injection. After less than 30 s Ar plasma, a plateau is observed, which is the sign that SLE was reached.[3,5] The etched amount per cycle in those conditions was quite constant on the last 6 cycles and was around 0.37 nm etched amount per cycle (EPC) [Fig. 3(c)], which is of the order of one monolayer per cycle. As the C_4F_8 adsorption does not saturate, the C_4F_8 flow and

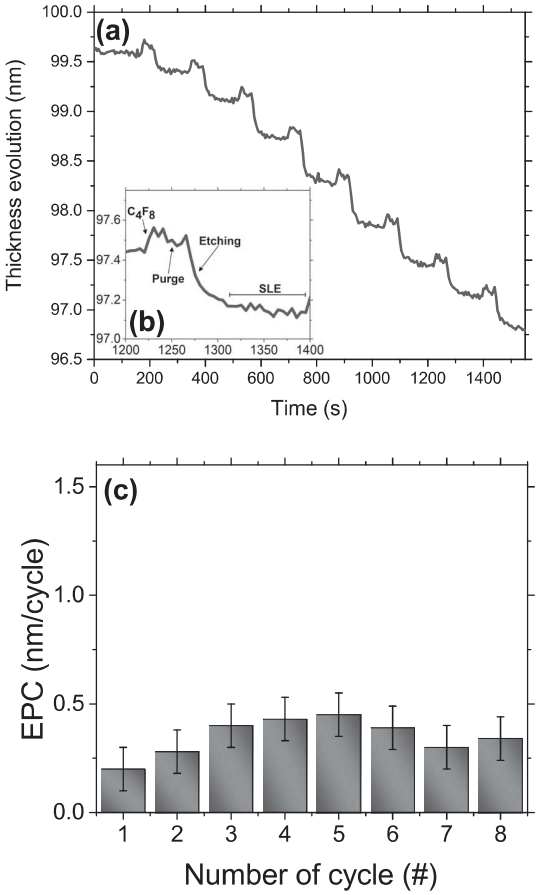

FIG. 3. (a) 8 ALE cycles exhibiting self-limiting etching performed on SiO_2, (b) zoom of the cycle #7, (c) evolution of the etching amount per cycle along the process (experimental conditions: T = −120 °C, C_4F_8 flow: 10 s, 17 mTorr, Ar purge: 30 s, 25 mTorr, Ar plasma: 2 min, 23 mTorr, P_{source} = 400 W, and V_{bias} = −20 V).

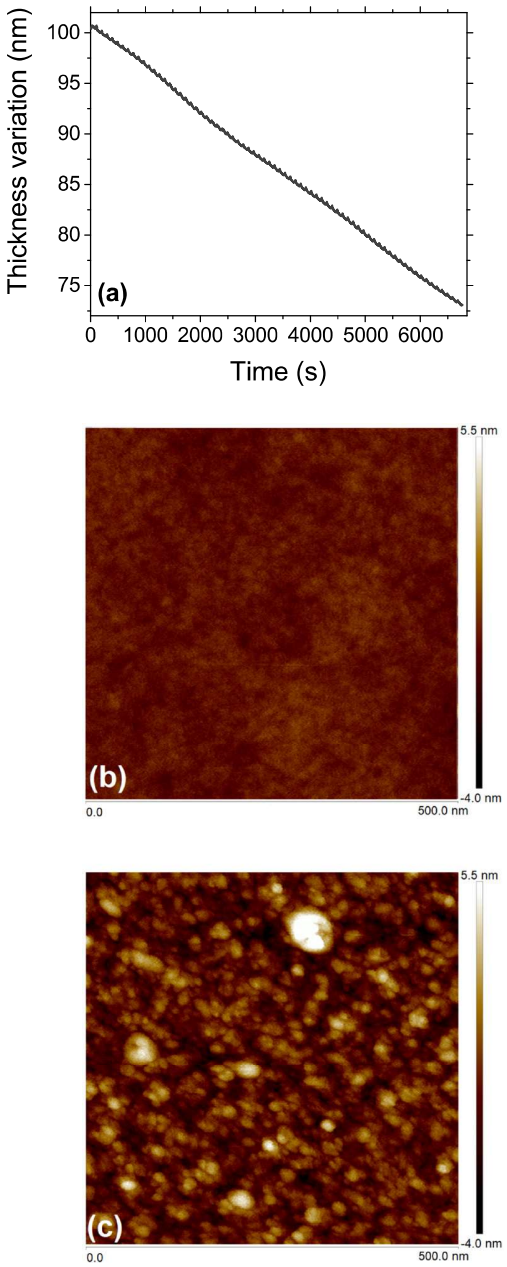

FIG. 4. (a) 70 cycles of ALE performed on SiO_2. (b) Surface roughness before and (c) after etching measured by AFM (experimental conditions: T = −120 °C, C_4F_8 flow: 10 s, 20 mTorr, Ar purge: 10 s, 3.8 mTorr, Ar plasma: 1 min, 25 mTorr, P_{source} = 400 W, and V_{bias} = −10 V).

injection time need to be well controlled in order to keep a constant EPC of the order of one monolayer.

Figure 4(a) shows a very regular etching through 70 cycles with 27 nm etched. The linearity of the curve indicates that there was no drift during the process. The absence of drift confirms that reactor wall contamination is significantly reduced compared to C_4F_8 plasma steps used in ALE at room temperature, which affect the process as in Ref. 6. This also shows that the influence of species adsorbed on the carrier wafer and on the chuck is not too significant and does not induce any ALE process drift.

Surface roughness was evaluated by the AFM measurement. The results are shown before [Fig. 4(b)] and after [Fig. 4(c)] the 70 cryo-ALE steps. The RMS roughness increases slightly from 0.4 nm to 1.2 nm for 27 nm of SiO_2 etched, whereas it is expected in ALE to obtain a smoother surface after processing.[27] Langmuir probe measurements showed that the energy of ions reaching the substrate surface is about 20 eV. However, the SiO_2 physical sputtering energy threshold is about 50 eV,[7,23] and so the surface roughness increase is not due to SiO_2 physical sputtering. However, ion bombardment on C_4F_8 physisorbed molecules can still induce non homogeneous etching and consequently an increase in the surface roughness. The increase in surface roughness could induce the creation of new inhomogeneous specific surfaces for C_4F_8 physisorption, leading to amplification of the roughness.

Cryogenic ALE of SiO_2 was obtained by alternating C_4F_8 molecule physisorption and Argon plasma with low energy ion bombardment. In our pressure conditions, a temperature as low as −120 °C was necessary to make physisorbed C_4F_8 molecules react with the SiO_2 surface during the argon plasma. The etched amount per cycle was of the order of 0.4 nm. The self-limiting etching was reached and evidenced. A total thickness of 27 nm was etched in 70 cycles. The roughness was estimated by AFM and increased slightly during the etching process, probably due to the low energy ion bombardment. The etch rate is quite constant from one cycle to the other, which shows that no major reactor wall contamination occurred during the process. Consequently, plasma cleaning steps are not necessary.

Of course, for industrial applications, it would be much more convenient to work at a higher temperature. This could be done by working at higher pressure or by using a gas which has a higher boiling point and could adsorb at a temperature of typically −50 °C. This type of process development method was applied to porous low-K cryoetching.[28,29]

The authors gratefully thank Shigeru Tahara for all the helpful discussions and support. This work was supported by the CERTeM 2020 platform, which provides most of the equipment.

REFERENCES

[1]G. S. Oehrlein, D. Metzler, and C. Li, ECS J. Solid State Sci. Technol. **4**, N5041 (2015).
[2]C. G. N. Lee, K. J. Kanarik, and R. A. Gottscho, J. Phys. D: Appl. Phys. **47**, 273001 (2014).
[3]K. Ishikawa, K. Karahashi, T. Ichiki, J. P. Chang, S. M. George, W. M. M. Kessels, H. J. Lee, S. Tinck, J. H. Um, and K. Kinoshita, Jpn. J. Appl. Phys., Part 1 **56**, 06HA02 (2017).
[4]K. J. Kanarik, T. Lill, E. A. Hudson, S. Sriraman, S. Tan, J. Marks, V. Vahedi, and R. A. Gottscho, J. Vac. Sci. Technol., A **33**, 020802 (2015).
[5]D. Metzler, R. L. Bruce, S. Engelmann, E. A. Joseph, and G. S. Oehrlein, J. Vac. Sci. Technol., A **32**, 020603 (2014).
[6]M. Kawakami, D. Metzler, C. Li, and G. S. Oehrlein, J. Vac. Sci. Technol., A **34**, 040603 (2016).
[7]C. Li, D. Metzler, C. S. Lai, E. A. Hudson, and G. S. Oehrlein, J. Vac. Sci. Technol., A **34**, 041307 (2016).
[8]T. Tsutsumi, H. Kondo, M. Hori, M. Zaitsu, A. Kobayashi, T. Nozawa, and N. Kobayashi, J. Vac. Sci. Technol., A **35**, 01A103 (2017).
[9]M. Wang, P. L. G. Ventzek, and A. Ranjan, J. Vac. Sci. Technol., A **35**, 031301 (2017).
[10]D. Humbird and D. B. Graves, J. Appl. Phys. **96**, 65 (2004).
[11]D. Metzler, C. Li, S. Engelmann, R. L. Bruce, E. A. Joseph, and G. S. Oehrlein, J. Chem. Phys. **146**, 052801 (2017).
[12]D. Metzler, K. Uppireddi, R. L. Bruce, H. Miyazoe, Y. Zhu, W. Price, E. S. Sikorski, C. Li, S. U. Engelmann, and E. A. Joseph, J. Vac. Sci. Technol., A **34**, 01B102 (2016).
[13]S. S. Kaler, Q. Lou, V. M. Donnelly, and D. J. Economou, J. Phys. D: Appl. Phys. **50**, 234001 (2017).
[14]M. Matsui, T. Usui, and T. Ono, Jpn. J. Appl. Phys., Part 1 **56**, 06HB03 (2017).
[15]S. Tachi, K. Tsujimoto, and S. Okudaira, Appl. Phys. Lett. **52**, 616 (1988).
[16]G. Craciun, M. A. Blauw, E. Van der Drift, P. M. Sarro, and P. J. French, J. Micromech. Microeng. **12**, 390 (2002).
[17]S. Aachboun, P. Ranson, C. Hilbert, and M. Boufnichel, J. Vac. Sci. Technol.,A **18**, 1848 (2000).
[18]M. Boufnichel, P. Lefaucheux, S. Aachboun, R. Dussart, and P. Ranson, Microelectron. Eng. **77**, 327 (2005).
[19]R. Dussart, T. Tillocher, P. Lefaucheux, and M. Boufnichel, J. Phys. D: Appl. Phys. **47**, 123001 (2014).
[20]R. Dussart, M. Boufnichel, G. Marcos, P. Lefaucheux, A. Basillais, R. Benoit, T. Tillocher, X. Mellhaoui, H. Estrade-Szwarckopf, and P. Ranson, J. Micromech. Microeng. **14**, 190 (2004).
[21]X. Mellhaoui, R. Dussart, T. Tillocher, P. Lefaucheux, P. Ranson, M. Boufnichel, and L. J. Overzet, J. Appl. Phys. **98**, 104901 (2005).
[22]C. M. Huard, Y. Zhang, S. Sriraman, A. Paterson, K. J. Kanarik, and M. J. Kushner, J. Vac. Sci. Technol., A **35**, 031306 (2017).
[23]S. Rauf, T. Sparks, P. L. G. Ventzek, V. V. Smirnov, A. V. Stengach, K. G. Gaynullin, and V. A. Pavlovsky, J. Appl. Phys. **101**, 033308 (2007).
[24]A. B. Kletskii and L. E. Petric, Zh. Fiz. Khim. **41**, 1183 (1967).
[25]R. J. Gasvoda, A. W. van de Steeg, R. Bhowmick, E. A. Hudson, and S. Agarwal, ACS Appl. Mater. Interfaces **9**, 31067 (2017).
[26]S. D. Sherpa, P. L. G. Ventzek, M. Lee, G. S. Hwang, and A. Ranjan, J. Vac. Sci. Technol., A **36**, 031303 (2018).
[27]K. J. Kanarik, S. Tan, and R. A. Gottscho, J. Phys. Chem. Lett. **9**, 4814 (2018).
[28]F. Leroy, L. Zhang, T. Tillocher, K. Yatsuda, K. Maekawa, E. Nishimura, P. Lefaucheux, J.-F. de Marneffe, M. R. Baklanov, and R. Dussart, J. Phys. D: Appl. Phys. **48**, 435202 (2015).
[29]R. Chanson, L. Zhang, S. Naumov, Y. A. Mankelevich, T. Tillocher, P. Lefaucheux, R. Dussart, S. D. Gendt, and J.-F. de Marneffe, Sci. Rep. **8**, 1886 (2018).

scientific reports

Check for updates

OPEN

Mechanism understanding in cryo atomic layer etching of SiO_2 based upon C_4F_8 physisorption

G. Antoun[1]✉, T. Tillocher[1], P. Lefaucheux[1], J. Faguet[2], K. Maekawa[2] & R. Dussart[1]✉

Cryogenic Atomic Layer Etching (cryo-ALE) of SiO_2 based on alternating a C_4F_8 molecule physisorption step and an argon plasma step, has been enhanced thanks to a better understanding of the mechanism. First, we used Quadrupole Mass spectrometry (QMS) and spectroscopic ellipsometry analyses to evaluate the residence time of physisorbed C_4F_8 molecules versus temperature and pressure on SiO_2 surface. QMS monitoring of the SiF_4 etching by-product also enabled to follow the self-limiting etching behavior. Finally, a SiO_2 cryo-ALE process was proposed at a temperature of – 90 °C resulting in a very linear etch over 150 cycles and an Etch amount Per Cycle as low as 0.13 nm/cycle.

In the area of nanotechnology and sub-10 nm devices, Atomic Layer Etching (ALE) has become one of the most promising processes to overcome the latest and greatest challenges. More specifically, selective etching of silicon dioxide over other materials such as silicon or silicon nitride have attracted interest from many researchers[1–5]. One of the main solutions to perform anisotropic ALE of SiO_2 is to use fluorocarbon-based plasmas to deposit a very thin FC modified layer on the surface. This layer can then be etched using Ar or O_2 plasma at low ion energy bombardment[2,3,6–11]. However, some drifts were reported in the processes, with an increase of the etch amount per cycle (EPC) due to the fluorine contamination of the reactor walls[8–10,12]. Yet, *Dallorto* et al. have shown that the effect of fluorine from the reactor wall contamination is reduced by decreasing the substrate temperature to – 10 °C and below[12]. More generally, cryogenic processes demonstrated to be clean processes with limited chamber wall contamination[13].

Therefore, cryo-Atomic Layer Etching (Cryo-ALE) is proposed as an alternative to etch SiO_2 in fluorocarbon-based chemistry but without plasma during the deposition step. In this process, the substrate is cooled to a temperature below – 80 °C. A C_4F_8 gas is injected and molecules adsorb on the cooled substrate surface. After purging the gas, an Ar plasma is initiated to activate the etching by low energy ion bombardment. A proof of principle has been previously published[14], showing that cryo-ALE based on C_4F_8 physisorption was working at – 120 °C in our experimental conditions. However, etching was suppressed at – 110 °C, owing to the desorption of C_4F_8 from the substrate surface being too fast if the temperature is not low enough. Thus, at temperatures below – 110 °C, a self-limiting regime was achieved and an etch per cycle as low as 0.4 nm was obtained. With this process, fluorocarbon polymer is no longer deposited on the reactor walls significantly reducing chamber contamination and limiting process drift. As a result, it is easier to control the etching through many etch cycles.

In this article, we report on the residence time of C_4F_8 versus temperature and pressure. Both ellipsometry and mass spectrometry measurements are used to characterize the adsorption and desorption of C_4F_8 from the SiO_2 surface. The improved understanding of the C_4F_8 residence time enabled for a significant extension of the SiO_2 cryo-ALE process temperature range towards higher and more practical temperature.

Experimental methods

In order to understand the adsorption of C_4F_8, 150 mm SiO_2 carrier wafers are used, on which SiO_2 coupons are glued. The SiO_2 coupons are composed of (100) silicon samples with 100 nm thick thermal silicon dioxide layer. A special glue material is spread uniformly on the backside of the sample and is stable at very low temperature. It has a very good thermal conductivity and is easily removed after use.

As the coupons consist of thin films of SiO_2 on silicon, they enable a very accurate fit by ellipsometry at the nanoscale.

[1]GREMI, Orléans University-CNRS, 14 Rue d'Issoudun, BP 6744, 45067 Orléans, France. [2]TEL Technology Center, America, LLC, NanoFab 300 South 255 Fuller Rd., Suite 214, Albany, NY, USA. ✉email: gaelle.antoun@univ-orleans.fr; remi.dussart@univ-orleans.fr

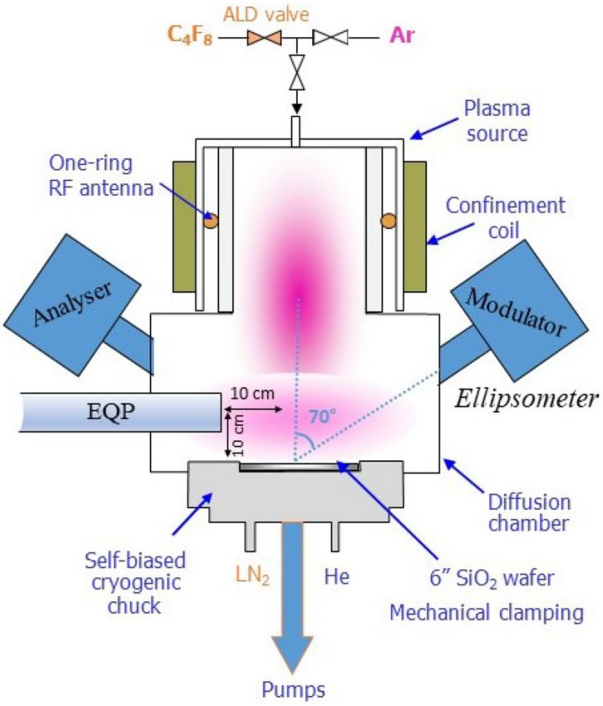

Figure 1. Sketch of the cryogenic ICP reactor equipped with QMS and SE.

The prepared samples are then introduced into an inductively coupled plasma reactor that is equipped with a diffusion chamber and a cryogenic substrate holder. The chuck can be cooled down by liquid nitrogen and temperature is controlled and stabilized using a Proportional Integral Derivative (PID) system. Wafers are mechanically clamped and a backside helium pressure provides for an optimal thermal contact with the chuck. A sketch of the reactor can be seen in Fig. 1.

A Horiba Jobin Yvon UVISEL spectroscopic ellipsometer is coupled to the reactor at an incidence angle of 70° to characterize the substrate surface in-situ. It monitors the thickness variation in kinetic mode at the sample surface during the cycles. The sampling interval is set at 2 s, with an integration time of 0.5 s. For each point of acquisition, spectra are acquired using 32 wavelengths from UV to visible. Lorentz and Drude models were then used to model and fit the ellipsometric spectra.

An Electrostatic Quadrupole Mass Spectrometer (QMS) from Hiden Analytical is used in Residual Gas Analysis (RGA) mode to analyze and monitor the species produced or injected in the reactor during the different steps of the ALE cycles. The mass spectrometer can be used in spectrum mode or in Multiple Ion Detection (MID) mode. The electron energy in the ionization chamber is 70 eV. The QMS entrance slit was positioned at 100 mm above the sample and at 100 mm from the center of the reactor. $C_2F_4^+$ mass (100 amu) corresponds to one of the main peaks from the fragmentation spectrum of C_4F_8[15]. Therefore, its signal was acquired to characterize the kinetics of C_4F_8 molecules in the chamber. The SiF_3^+ line intensity at 85 amu was also recorded, during an ALE process, in order to follow the evolution of SiF_4 molecules in the reactor, especially during the etch step. SiF_3^+ is reported to be the main fragment ion from SiF_4[16]. The intensity of the detected ions is expressed in counts per second (c/s).

Results

Atomic layer etching process at low substrate temperature. In order to characterize and understand the mechanisms involved in Atomic Layer Etching at low substrate temperature, a cryo-ALE process was performed. The generic time chart of cryo-ALE used in[14] is shown as a reminder in Fig. 2.

Figure 3 presents 8 cycles of cryo-ALE monitored by in-situ ellipsometry for the thickness variation and by QMS to follow 85 amu corresponding to SiF_3^+ signal, which represents SiF_4, the main etching by-product. During this process, a C_4F_8 gas flow is first injected for 10 s in order to allow for the molecules to physisorb on the cooled substrate surface (− 120 °C). Then, an Ar purge of 30 s is performed in order to remove C_4F_8 molecules from the chamber. After that, the Ar plasma is ignited to activate the etch and sustained for 2 min to ensure self-limiting etching is achieved. Finally, a pumping step is performed before starting the next cycle, in order to evacuate all the etching by-products from the chamber. The physisorption step is clearly identified by ellipsometry measurements, as well as by the QMS signal. The SiF_3^+ mass of 85 amu is close to the mass of $C_4F_2^+$ (86 amu) which is an ion from the fragmentation of C_4F_8. Hence, as shown in Fig. 3, the first peak of a cycle, observed on QMS signal during the C_4F_8 injection is related to $C_4F_2^+$. When the Ar plasma is initiated, etching is observed by ellipsometry as well as by QMS. During the first three cycles, an increase in SiF_3^+ signal and the EPC is observed, before it reaches a steady amount. This shows that the first cycles are in transient state.

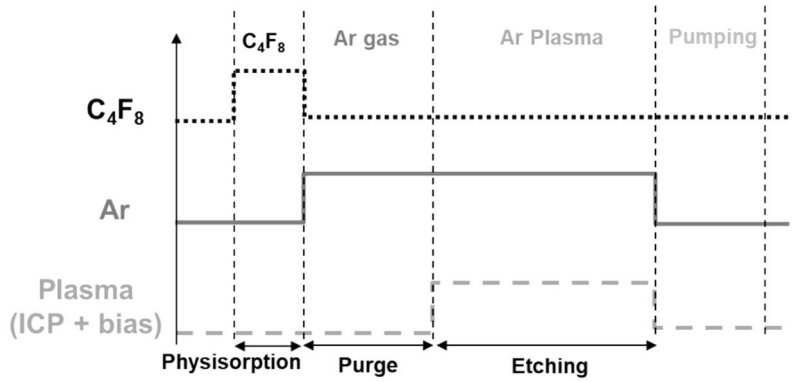

Figure 2. Generic time chart of one cryo-ALE cycle.

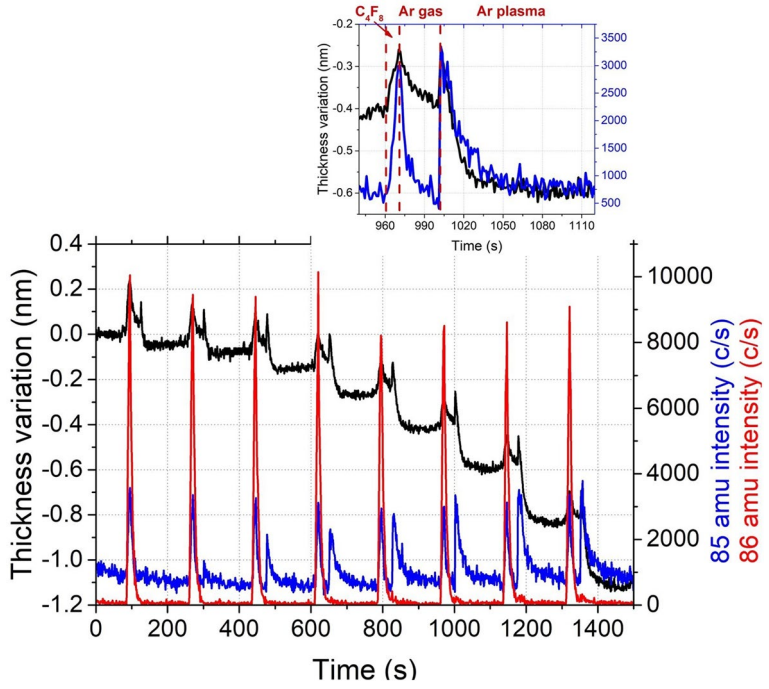

Figure 3. Thickness variation measured by ellipsometry and 85 and 86 amu signals by QMS for 8 ALE cycles performed on SiO_2, (inset) zoom on the second cycle. (Experimental conditions: T = − 120 °C, C_4F_8 flow: 10 s, 1.9 Pa, Ar purge: 30 s, 3.3 Pa, Ar plasma: 2 min, 3.3 Pa, Psource = 400 W, Vbias = − 20 V, pumping: 15 s, 0 Pa).

Surface contamination may limit the etching during these cycles, as well as the formation of a mixing layer such as SiOCF on the surface instead of completion of etching[4,7,17]. Once this layer is formed, the etch amount per cycle becomes constant and self-limiting etching is reached. Then, during the following cycles, the SiF_3^+ signal steeply increases the first few seconds, and then starts to decrease (see the inset of Fig. 3). This behavior shows that self-limiting etching is almost reached, inducing less etching and less SiF_4 by-products. The presence of SiF_3^+ signal clearly indicates that the substrate is etched chemically. Indeed, the presence of the self-limiting etching (SLE) is evidenced from the observation of both the film thickness and the SiF_3^+ signal simultaneous transition to a plateau, confirming that Ar sputtering does not participate to the etching mechanism. Moreover, the same test, performed at − 110 °C, shows no etching, as reported in[14], as all C_4F_8 molecules desorb from the surface before the ignition of the argon plasma.

Characterization of the physisorption. *Temperature dependency.* In order to optimize the duration of the argon purge step before plasma initiation, the residence time of the C_4F_8 molecules was studied as a function of the setpoint temperature. The C_4F_8 gas was injected in the reactor chamber for 1 min at constant pressure (3 Pa) and different temperatures of the SiO_2 substrate. Then the gas was evacuated during several tens of minutes.

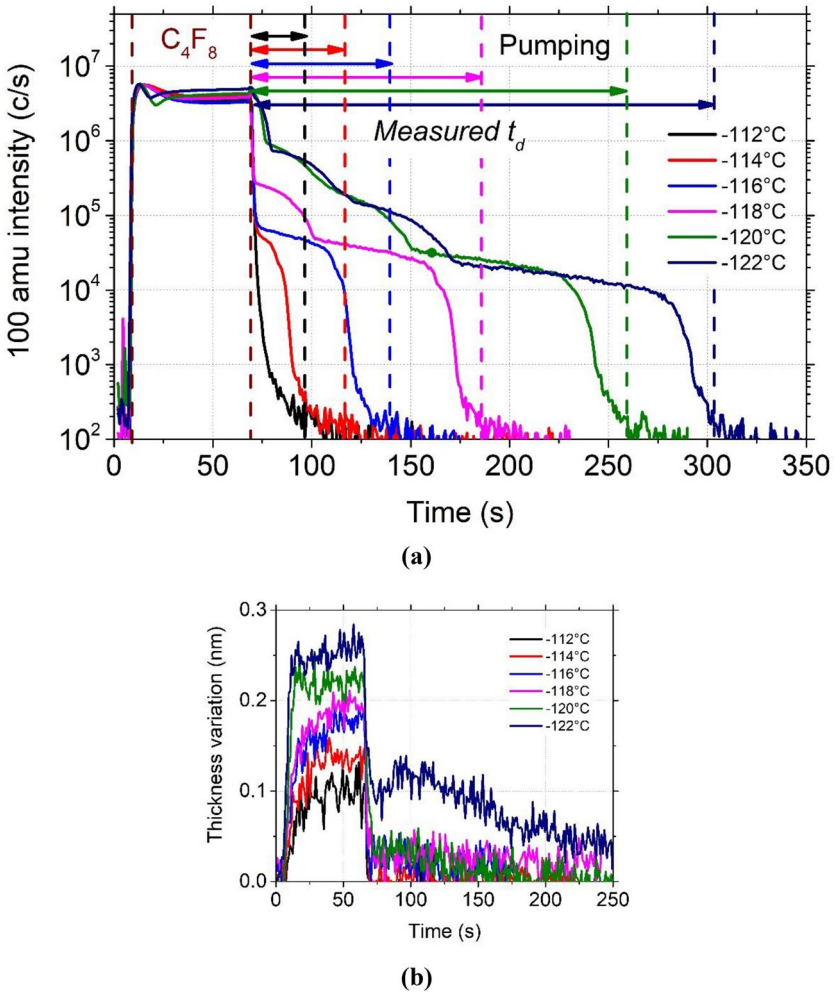

Figure 4. C_4F_8 physisorption on SiO_2 depending on setpoint temperature and monitored (**a**) by QMS by following $C_2F_4^+$ ion peak intensity evolution and (**b**) by ellipsometry following the thickness variation , both versus time. (Experimental conditions: 1 min C_4F_8 flow, 3 Pa followed by a pumping step).

Figure 4a shows the $C_2F_4^+$ line intensity measured by mass spectrometry for various setpoint temperatures between – 112 and – 122 °C. As soon as C_4F_8 gas is injected, the $C_2F_4^+$ signal increases rapidly and stabilizes for a few seconds after injection as the flow is continuously maintained. When the C_4F_8 flow is stopped after 1 min of injection, a sharp drop is first observed for all temperatures. Then, different trends are observed depending on the setpoint temperature. At – 112 °C, the intensity of $C_2F_4^+$ drops quickly down to a value below 10^3 c/s. At – 114 °C, the signal drops down to 8×10^4 c/s, decreases slowly and drops again after about 20 s. At – 120 °C, two different kinetics are observed with two shoulders on the curve: after the $C_2F_4^+$ first drop, a first plateau is reached at 2×10^4 c/s, followed by a second decrease and a second plateau. These different drops and plateaus observed in the $C_2F_4^+$ line intensity correspond to different desorption steps of C_4F_8.

To confirm the origin of the first desorption stage, C_4F_8 was first physisorbed at – 120 °C and then, its desorption was monitored by QMS and ellipsometry. The test was run with and without helium injection between the chuck and the wafer. Without helium, the wafer is not efficiently cooled and nearly no adsorption should occur on it. The results, illustrated in Fig. 5a. show a clear difference between the two cases: the first desorption stage, between 75 and 100 s (indicated in dashed line in Fig. 5a) does not appear when backside helium flow is not used. In Fig. 5b, ellipsometry data confirms that C_4F_8 is not adsorbed without helium. With helium, the thickness grows during the adsorption of C_4F_8, then drops when the flow is stopped. However, a small shoulder can be noticed, between 75 and 100 s (indicated in dash line in Fig. 5b), representative of C_4F_8 desorption. The difference observed with and without helium shows that the first plateau after the main drop corresponds to the desorption of C_4F_8 from the wafer. The other plateaus correspond to desorption of C_4F_8 from other parts of the chuck, which are cooled as well but have a slightly lower temperature.

Adsorption kinetics differ from the first adsorption layer to the following ones. Kinetics for the first adsorbed layer and coverage are described by Langmuir theory. Then, each particle in the first layer may be an adsorption center for further adsorbates for the next layers. This multimolecular adsorption kinetic is covered by the BET (Brunauer, Emmett and Teller) theory [17].

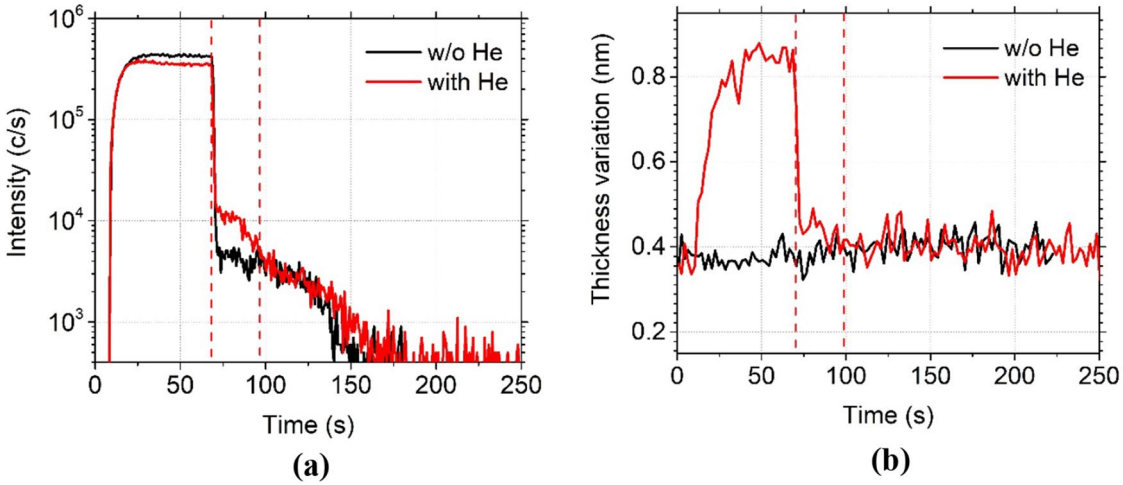

Figure 5. C_4F_8 physisorption on SiO_2 depending on the presence of He backside cooling during the clamping and monitored (**a**) by QMS by following $C_2F_4^+$ ion peak intensity evolution and (**b**) by ellipsometry following the thickness variation , both versus time. (Experimental conditions: T = − 120 °C, 1 min C_4F_8 flow, 3 Pa followed by a pumping).

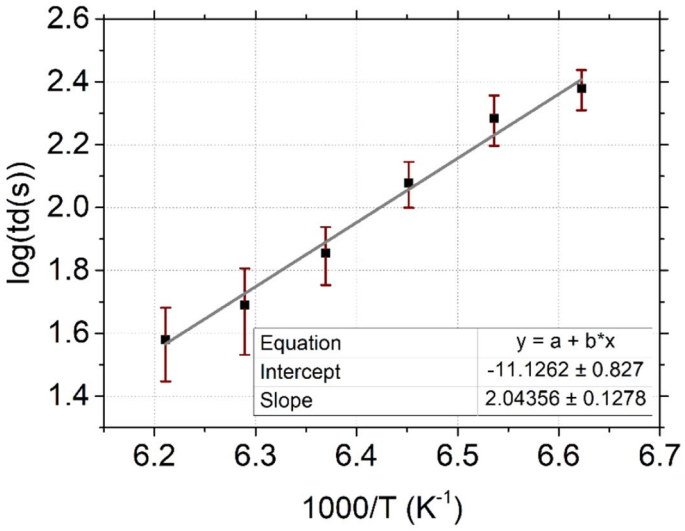

Figure 6. C_4F_8 desorption rate depending on temperature, for a C_4F_8 injection at 3 Pa.

Several layers can adsorb on the wafer surface, and each layer has its specific residence time. The desorption rate decreases with decreasing temperature as the residence time at the surface increases[18]. In the case of those experiments (Fig. 4), according to spectroscopic ellipsometry measurements, the surface coverage is of the order of one or two monolayers at − 120 °C and higher temperatures. Consequently, Langmuir model can be applied. For lower temperatures, several layers can adsorb to the surface. However, the desorption rate of top layers is usually much higher than the one of the adsorbed layer on SiO_2.

Consequently, from those hypotheses and based on the results obtained by QMS, presented in Fig. 4a, we can consider that the C_4F_8 molecules residence time t_d is the delay between the C_4F_8 injection stop and the end of the first slope (Fig. 4a). t_d was plotted as a function of temperature in Fig. 6. As those measures are extracted from the QMS curves, an error of a few seconds is considered per data point. Then, log (t_d) was plotted versus 1000/T and fitted using a linear function. It gave a consistent result with the equation of Frenkel-Arrhenius that enables the determination of surface residence time. The equation being:

$$t_d = t_d^0 exp^{E_d/k_B T} \quad (1)$$

with t_d the residence time (s), t_d^0 is the attempt time of the particle for desorption (s), E_d is the energy to enable the desorption (kJ mol^{-1}), k_B is the Boltzmann constant (kJ K^{-1}) and T the substrate temperature (K)[18–20]. From Eq. (1) and the values obtained with the curve fit, the values of t_d^0 and E_d were determined to be respectively,

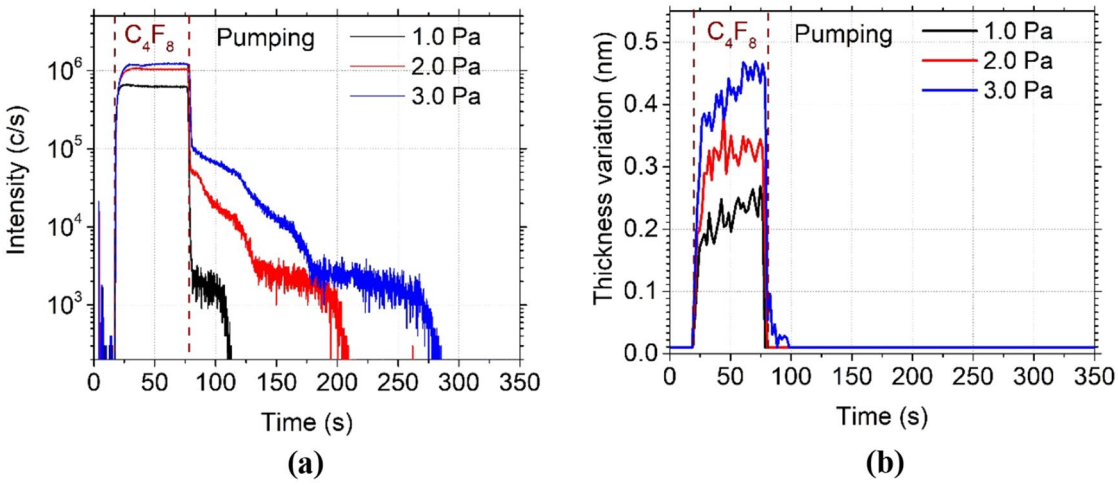

Figure 7. C_4F_8 physisorption on SiO_2 depending on pressure and monitored (**a**) by QMS by following $C_2F_4^+$ ion peak intensity evolution and (**b**) by ellipsometry following the thickness variation , both versus time. (Experimental conditions: T = − 120 °C, C_4F_8 flow: 1 min followed by a pumping).

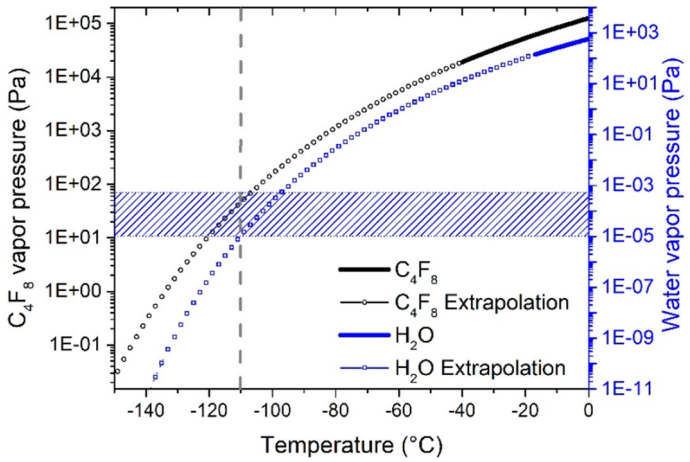

Figure 8. Vapor pressure curves for H_2O and C_4F_8.

1×10^{-11} s and 17 kJ mol^{-1} (0.18 eV). The desorption energy is very low and is of the order of magnitude of typical binding energy for physisorption.

This graph is of interest to design a cryo-ALE process at different temperatures, especially to define the maximum purge duration between C_4F_8 gas injection and the plasma initiation.

Pressure dependency. The influence of C_4F_8 gas pressure was derived from similar tests obtained by injecting C_4F_8 gas for 1 min at different pressures at a temperature set to − 120 °C. The results are shown in Fig. 7. Different desorption rates are observed when increasing the pressure. In fact, by increasing the pressure, the density of C_4F_8 molecules in the reactor is higher and the quantity of physisorbed molecules is increased. This is also observed by ellipsometry measurements, (Fig. 7b) which show that the thickness of the physisorbed layer increases with pressure. Therefore, it takes a longer time to remove the C_4F_8 molecules at a constant desorption rate. Indeed, according to the expression (1) reported in the previous part, the desorption rate does not depend on the gas pressure, but on temperature only.

Water influence. For a better understanding of the role of residual water molecules, the vapor pressures curves of C_4F_8 and water were plotted together in Fig. 8. In order to cover the temperature range of interest, an extrapolation was performed using Antoine equation parameters from NIST database[21,22]. Hence, in Fig. 8, the part of the curves in bold are from the database and the dotted part lines are extrapolated. The air leakage of the reactor chamber was evaluated at around 0.1 sccm from which it was possible to estimate the water partial pressure during the C_4F_8 gas injection. At 3 Pa, the water partial pressure is about 4.3×10^{-4} Pa, decreasing to 1.0×10^{-5} Pa during the pumping. The striped section in Fig. 8 represents the range of water partial pressure in the process

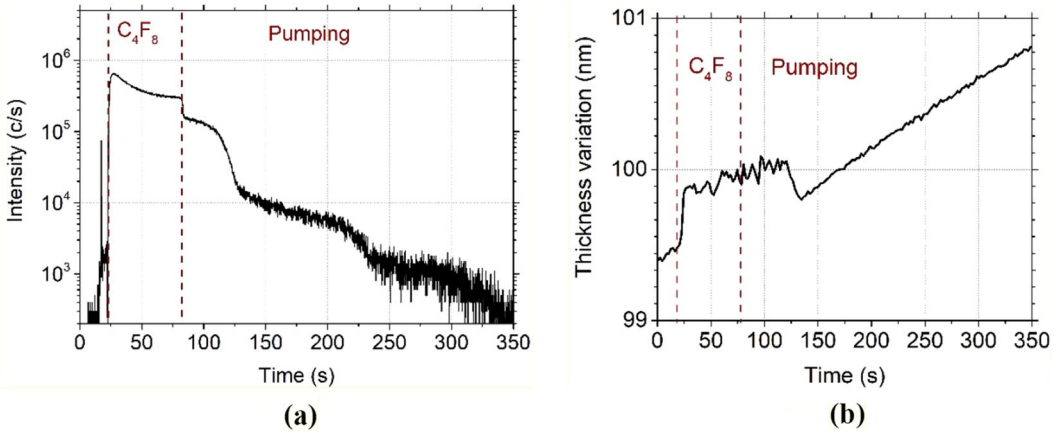

Figure 9. C_4F_8 physisorption on SiO_2 at − 130 °C monitored (**a**) by QMS by following $C_2F_4^+$ ion peak intensity evolution and (**b**) by ellipsometry following the thickness variation , both versus time. (Experimental conditions: T = − 130 °C, 1 min C_4F_8 flow, 3 Pa followed by a pumping step).

conditions. At temperatures higher than − 110 °C, the effect of water is not significant for C_4F_8 physisorption, as in these conditions, water does not condensate (on the right of the water curve).

However, for lower temperatures, the parameters are such that water condenses (on the left side of the water curve).

This behavior is observed in Fig. 9 below where physisorption test was performed at − 130 °C. During the C_4F_8 injection in Fig. 9a the $C_2F_4^+$ signal does not stabilize, but rather decreases although the C_4F_8 flow is maintained constant inside the chamber. At this temperature, the cooled substrate acts like a cryogenic pump, and the amount of C_4F_8 molecules in the chamber is reduced as they start to condense on the cooled surface of the substrate. This is confirmed by ellipsometry measurements in Fig. 9b: the adsorbed film thickness increases during the C_4F_8 injection step instead of reaching a plateau as at higher temperatures (Fig. 4b). This result is consistent with the Antoine's curve giving the vapor pressure of C_4F_8 as a function of temperature. By decreasing the temperature, conditions are closer to condensation. Moreover, the point located at T = − 130 °C and P = 3 Pa is clearly in the condensation part of the water curve. At − 130 °C, water molecules, that are present in the chamber, as evidenced by the continuous signal increase after C_4F_8 is pumped out, start to condense on the substrate surface. Consequently, it prevents from observing the signal saturation as expected from the C_4F_8 physisorption tests in Fig. 4.

Optimization of the process. In the letter dedicated to Cryo-ALE[14], we demonstrated the importance of working at low enough temperature (close to − 120 °C) to reach an etching regime. However, this temperature operating range is often unwanted because it requires the use of liquid nitrogen.

QMS results presented above gave us a better understanding of the mechanisms, enabling the enhancement of the process. The purpose of the following part is to increase the process working temperature.

Influence of purge step. According to the physisorption tests results in Fig. 7, when the pressure during the injection of C_4F_8 is increased, the amount of C_4F_8 molecules that physisorb also increases. Again, this is confirmed in Fig. 10 below, where physisorption tests have been repeated at − 90 °C at two different pressures and $C_2F_4^+$ peak was followed by QMS. It shows that at 3.0 Pa, $C_2F_4^+$ signal decreases sharply when C_4F_8 is stopped. Whereas, few additional seconds are needed at 6.5 Pa to remove all C_4F_8. By comparing this latter with the test at − 112 °C at 3.0 Pa, it is possible to observe that the residence time of C_4F_8 at − 90 °C 6.5 Pa is almost equal to the residence time at − 112 °C at 3.0 Pa. This confirms that increasing the pressure will help processing at higher temperatures.

In Figs. 8, 11 cryo-ALE cycles were performed at − 90 °C. The pressure of C_4F_8 needed to be raised to 6 Pa, which is higher than the usual pressure processing that was used in previous experiments (~ 2–3 Pa), to enable the physisorption of few monolayers of C_4F_8 molecules. However, the subsequent purge step time is also very critical. If the purge step time is too long, all C_4F_8 molecules desorb before starting the argon plasma for the etching step. If it is too short, C_4F_8 gas is not totally evacuated from the reactor chamber and CF_x are created in the chamber during the Ar plasma. The process may thus no longer be controlled. As observed in Fig. 11, a clear difference is obtained by varying the purge step time by only 1 s. Very low etching is observed at 4 s purge time because most of C_4F_8 molecules have desorbed from the surface. Whereas, if the time is decreased to 3 s, a sufficient quantity of molecules is still present at the surface to allow for the etching of 0.3 nm of SiO_2 per cycle. The Ar plasma in this process lasts only 1 min, which is on the limits for reaching the self-limiting etching plateau. During this etching plasma, half of the etched amount is removed during the first 15 s.

Same test with 3 s for the purge step was performed at 20 °C. No etching occurs in this case. This proves that the etching achieved at − 90 °C in the same conditions is due to physisorbed species and not from residual C_4F_8 in the chamber. It also shows that no sputtering occurs during the Ar plasma.

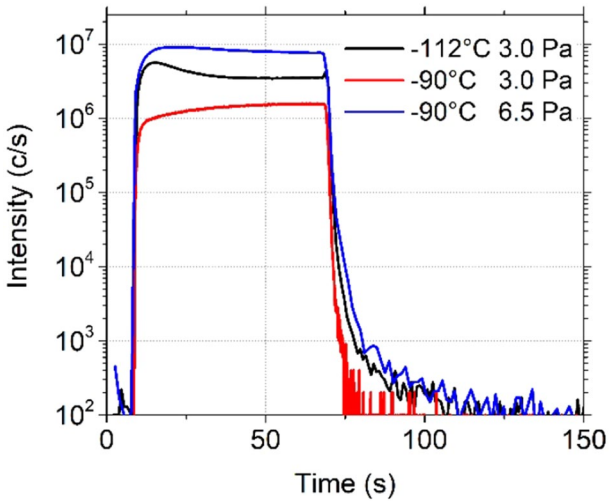

Figure 10. C_4F_8 physisorption on SiO_2 depending on pressure and temperature and monitored by QMS by following $C_2F_4^+$ ion peak intensity evolution versus time. (Experimental conditions: T = − 90 °C and − 112 °C, C_4F_8 flow: 1 min followed by a pumping).

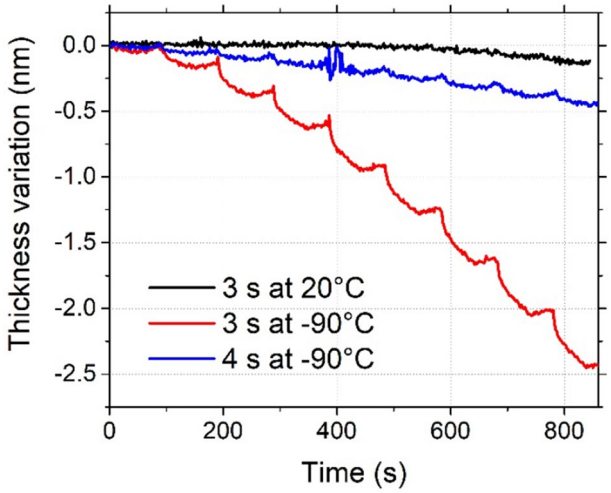

Figure 11. 8 ALE cycles performed on SiO_2 with the thickness variation followed by ellipsometry. (Experimental conditions: T = 20 °C/ − 90 °C, C_4F_8 flow: 20 s, 6 Pa, Ar purge: 3 s/3 s/4 s, < 1 Pa, Ar plasma: 1 min, 3 Pa, Psource = 400 W, Vbias = − 20 V, pumping: 15 s, $< 1.0 \times 10^{-3}$ Pa).

Etch cycles repeatability. It is essential in the nanotechnology industry to be able to run processes without drifts. To check the repeatability and robustness of the process presented in Fig. 11, 150 cryo-ALE cycles have been performed on SiO_2 at − 90 °C and monitored by ellipsometry as shown in Fig. 12a. Relying on observations from Fig. 11, the Ar plasma step time for this process has been reduced to 15 s instead of 1 min, in order to reduce the process time. Figure 12b is an inset showing that it takes about 16 cycles before the process reaches a constant etching amount per cycle. Indeed, during those first cycles, the EPC is first close to 0.05 nm/cycle and increases until it becomes stable at 0.13 nm/cycle, until the end of the process (Fig. 12c). The steady etch amount per cycle is in fact reached after having etched 0.5 nm, which corresponds to approximately one monolayer of SiO_2. During those first cycles, the surface is being modified to form a SiOCF like layer[4,17]. As the temperature is higher than in the previous processes, − 90 °C instead of − 120 °C, less C_4F_8 is adsorbing per cycle, and consequently, more cycles are needed before reaching a quasi-steady surface state. Once the first monolayer, which is also expected to be contaminated by carbon[7], is removed, the surface modification remains the same at the beginning of all the cycles: the SiO_2 layer should contain the same amount of active sites for C_4F_8 physisorption. Moreover, the absence of drift supports that processes based on physisorption at low substrate temperature limit reactor wall contamination and hence the occurrence of drifts. The surface roughness remains the same before and after etching and is close to 0.40 nm for the Root Mean Square roughness (Rq).

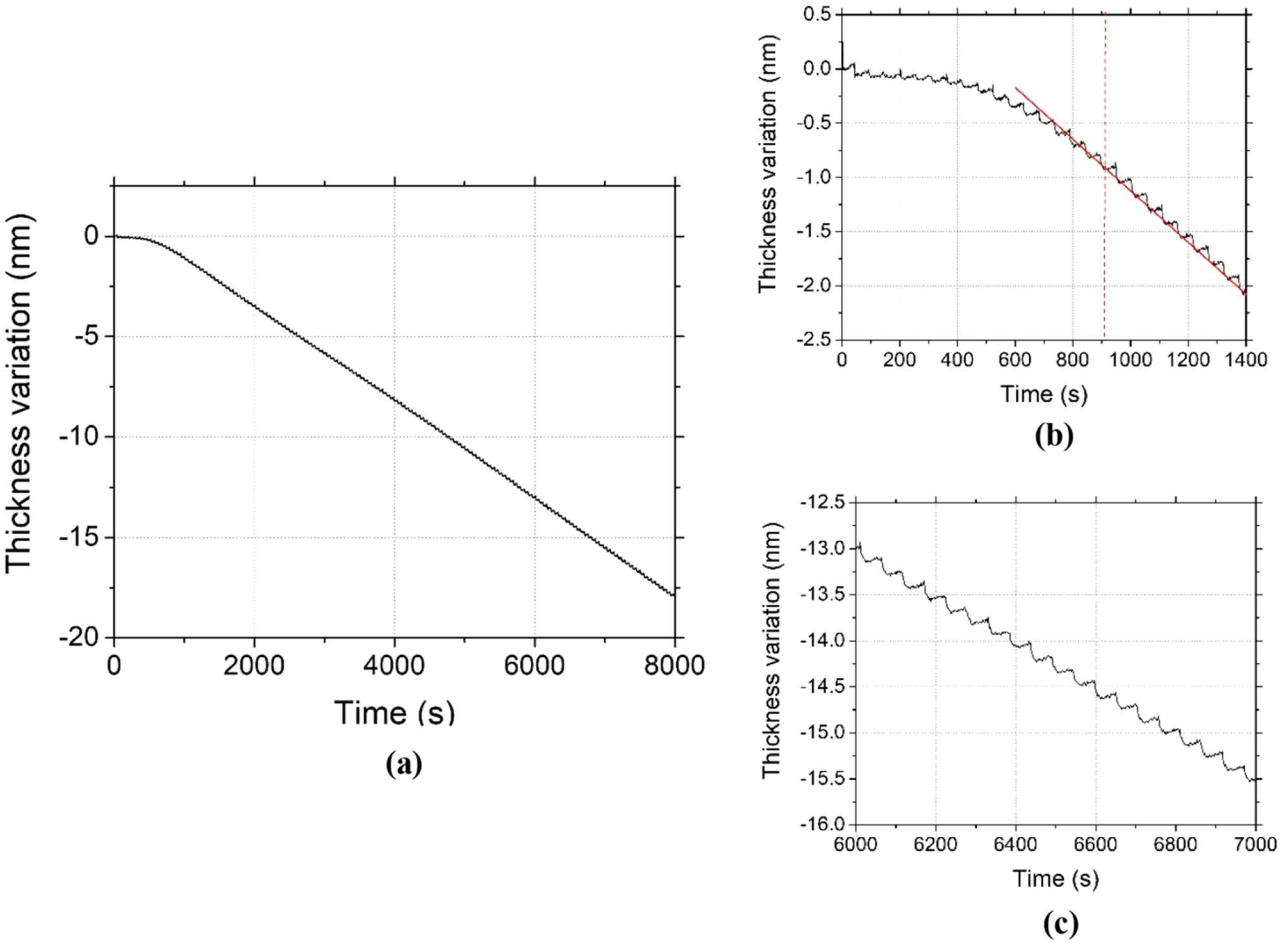

Figure 12. (**a**) 150 ALE cycles performed on SiO_2, (**b**) zoom on the beginning of the process, (**c**) zoom close to the end of the process. (Experimental conditions: T = − 90 °C, C_4F_8 flow: 20 s, 5.5 Pa, Ar purge: 3 s, < 1 Pa, Ar plasma: 15 s, 3 Pa, Psource = 400 W, Vbias = − 20 V, pumping: 15 s, $< 1.0 \times 10^{-3}$ Pa).

Conclusion

The proposed cryogenic Atomic Layer Etching of SiO_2 is a process based on a first injection of C_4F_8 gas without plasma, followed by argon plasma to activate chemical reactions between physisorbed molecules and SiO_2 at the surface. QMS and spectroscopic ellipsometry were used to better understand the parameters affecting physisorption and desorption. The increase of residence time of C_4F_8 molecules at the surface when decreasing the setpoint temperature was clearly observed by mass spectrometry. At higher pressure, desorption takes more time due the higher amount of physisorbed molecules. Consequently, the thickness of adsorbed molecules does not reach a plateau as observed at higher temperatures (between − 90 and − 120 °C). From these observations, the operating process temperature has been increased from − 120 to − 90 °C. To this end, the pressure has also been raised from 3 to 6 Pa and the purge step time was decreased to prevent the desorption of all the physisorbed molecules. QMS tests also enabled to monitor the etching and predict reaching of the self-limiting etching by following the SiF_3^+ signal.

Finally, a remarkably linear etching has been observed when performing 150 cryo-ALE cycles at − 90 °C. The absence of a process drift shows, that contamination of the reactor wall remains very low in these cryogenic process conditions.

Received: 15 September 2020; Accepted: 8 December 2020
Published online: 11 January 2021

References

1. Gasvoda, R. J., Verstappen, Y. G. P., Wang, S., Hudson, E. A. & Agarwal, S. Surface prefunctionalization of SiO_2 to modify the etch per cycle during plasma-assisted atomic layer etching. *J. Vac. Sci. Technol. A* **37**, 051003 (2019).
2. Wang, M., Ventzek, P. L. G. & Ranjan, A. Quasiatomic layer etching of silicon oxide selective to silicon nitride in topographic structures using fluorocarbon plasmas. *J. Vac. Sci. Technol. Vac. Surf. Films* **35**, 031301 (2017).
3. Li, C., Metzler, D., Lai, C. S., Hudson, E. A. & Oehrlein, G. S. Fluorocarbon based atomic layer etching of Si_3N_4 and etching selectivity of SiO_2 over Si_3N_4. *J. Vac. Sci. Technol. Vac. Surf. Films* **34**, 041307 (2016).
4. Metzler, D. *et al.* Characterizing fluorocarbon assisted atomic layer etching of Si using cyclic Ar/C4F8 and Ar/CHF3 plasma. *J. Chem. Phys.* **146**, 052801 (2017).

5. Lin, K.-Y. *et al.* Achieving ultrahigh etching selectivity of SiO_2 over Si_3N_4 and Si in atomic layer etching by exploiting chemistry of complex hydrofluorocarbon precursors. *J. Vac. Sci. Technol. A* **36**, 040601 (2018).
6. Metzler, D., Bruce, R. L., Engelmann, S., Joseph, E. A. & Oehrlein, G. S. Fluorocarbon assisted atomic layer etching of SiO_2 using cyclic Ar/C_4F_8 plasma. *J. Vac. Sci. Technol. Vac. Surf. Films* **32**, 020603 (2014).
7. Kaler, S. S., Lou, Q., Donnelly, V. M. & Economou, D. J. Atomic layer etching of silicon dioxide using alternating C_4F_8 and energetic Ar^+ plasma beams. *J. Phys. Appl. Phys.* **50**, 234001 (2017).
8. Kawakami, M., Metzler, D., Li, C. & Oehrlein, G. S. Effect of the chamber wall on fluorocarbon-assisted atomic layer etching of SiO_2 using cyclic Ar/C_4F_8 plasma. *J. Vac. Sci. Technol. Vac. Surf. Films* **34**, 040603 (2016).
9. Gasvoda, R. J., van de Steeg, A. W., Bhowmick, R., Hudson, E. A. & Agarwal, S. Surface phenomena during plasma-assisted atomic layer etching of SiO_2. *ACS Appl. Mater. Interfaces* **9**, 31067–31075 (2017).
10. Tsutsumi, T. *et al.* Atomic layer etching of SiO_2 by alternating an O_2 plasma with fluorocarbon film deposition. *J. Vac. Sci. Technol. Vac. Surf. Films* **35**, 01A103 (2017).
11. Dallorto, S. *et al.* Balancing ion parameters and fluorocarbon chemical reactants for SiO_2 pattern transfer control using fluorocarbon-based atomic layer etching. *J. Vac. Sci. Technol. B* **37**, 051805 (2019).
12. Dallorto, S. *et al.* Atomic layer etching of SiO_2 with Ar and CHF_3 plasmas: a self-limiting process for aspect ratio independent etching. *Plasma Process. Polym.* **16**, 1900051 (2019).
13. Dussart, R., Tillocher, T., Lefaucheux, P. & Boufnichel, M. Plasma cryogenic etching of silicon: from the early days to today's advanced technologies. *J. Phys. Appl. Phys.* **47**, 123001 (2014).
14. Antoun, G. *et al.* Cryo atomic layer etching of SiO_2 by C_4F_8 physisorption followed by Ar plasma. *Appl. Phys. Lett.* **115**, 153109 (2019).
15. Li, X. *et al.* Properties of C4F8 inductively coupled plasmas. I. Studies of ArÕc-C4F8 magnetically confined plasmas for etching of SiO2. *J. Vac. Sci. Technol. A* **22**, 11 (2004).
16. Basner, R., Schmidt, M., Denisov, E., Becker, K. & Deutsch, H. Absolute total and partial cross sections for the electron impact ionization of tetrafluorosilane (SiF_4). *J. Chem. Phys.* **114**, 1170–1177 (2001).
17. Kanarik, K. J. *et al.* Predicting synergy in atomic layer etching. *J. Vac. Sci. Technol. Vac. Surf. Films* **35**, 05C302 (2017).
18. Brunauer, S., Emmett, P. H. & Teller, E. Adsorption of gases in multimolecular layers. *J. Am. Chem. Soc.* **60**, 309–319 (1938).
19. Kreuzer, H. J. & Gortel, Z. W. *Physisorption Kinetics* Vol. 1 (Springer, Berlin Heidelberg, 1986).
20. Tinck, S., Neyts, E. C. & Bogaerts, A. Fluorine-silicon surface reactions during cryogenic and near room temperature etching. *J. Phys. Chem. C* **118**, 30315–30324 (2014).
21. Unnikrishnan, P. & Srinivas, D. Chapter 3—Heterogeneous Catalysis. In *Industrial Catalytic Processes for Fine and Specialty Chemicals* (eds Joshi, S. S. & Ranade, V. V.) 41–111 (Elsevier, Amsterdam, 2012). https://doi.org/10.1016/B978-0-12-801457-8.00003-3.
22. Kletskii, A. B. & Petric, L. E. Dependence of vapor pressure of perfluorocyclobutane. *Zh. Fiz. Khim.* **41**, 1183–1184 (1967).
23. Stull, D. R. Vapor pressure of pure substances. organic and inorganic compounds. *Ind. Eng. Chem.* **39**, 517–540 (1947).

Acknowledgements

The authors gratefully thank Shigeru Tahara from TEL for all the helpful discussions and also Kumiko Yamazaki and Nagisa Sato from TEL for their support to the project.
This work was supported by the CERTeM 2020 platform, which provides most of the equipment.

Author contributions

G.A., T.T., R.D. wrote the main manuscript text. P.L., J.F. and K.M. helped with the results discussions and choice of figures. All authors reviewed the manuscript.

Competing interests

The authors declare no competing interests.

Additional information

Correspondence and requests for materials should be addressed to G.A. or R.D.

Reprints and permissions information is available at www.nature.com/reprints.

Publisher's note Springer Nature remains neutral with regard to jurisdictional claims in published maps and institutional affiliations.

Résumé de la thèse

Contexte de l'étude

En 1965, Gordon E. Moore, alors directeur du département de recherche et développement chez Fairchild Semiconductor et plus tard co-fondateur d'Intel, publie un article dans *Electronics* sur l'avenir de l'électronique. Il y affirme que l'avenir reposerait sur le développement des circuits intégrés en semi-conducteurs pour concevoir des équipements plus puissants et moins chers. Pour cela, le nombre de composants sur les circuits intégrés doublerait tous les deux ans, le coût de production serait minimisé et le rendement augmenté [1].

Depuis, les industries de l'électronique ont en effet réussi à appliquer cette «loi de Moore» jusqu'à atteindre les domaines appelés «Plus que Moore» ou encore «Au-delà de la loi de Moore», les composants étant désormais conçus à des échelles nanométrique et atomique [2]–[4].

De nos jours, les industries des semi-conducteurs se concentrent sur l'amélioration des composants en créant de nouvelles configurations et en réduisant leur taille jusqu'à l'échelle atomique. Cette miniaturisation rend donc la fabrication des composants très critique, puisque le moindre défaut peut fortement altérer l'efficacité du composant.

Pour éviter ces défauts, la gravure de couches atomiques, aussi appelée « Atomic Layer Etching » (ALE) en anglais, a été proposée comme technique prometteuse pour obtenir des modèles à l'échelle nanométrique.

En 1988, M. Yoder, publie le premier brevet et communication sur l'ALE, qu'il propose comme nouvelle technique pour graver une couche atomique de diamant [5]. Depuis, l'intérêt pour l'ALE et le nombre d'études dessus n'ont cessé d'augmenter, avec un réel gain d'intérêt depuis 2010 [6], [7].

En parallèle de cela, la même année, des études sont publiées par S. Tachi sur la gravure profonde du silicium (Si) à des températures cryogéniques (-130°C à -100°C). Dans cet article, il montre certains avantages des procédés à basse température, comme la sélectivité élevée entre le Si et la photorésine. Mais aussi la gravure du Si en profil anisotrope en utilisant uniquement un plasma SF_6 [8].

Deux ans plus tard, en 1990, la gravure ALE du Si est présentée par Y.Horiike et son équipe. Ils y proposent de refroidir le Si jusqu'à -180°C, puis d'utiliser ensuite des gaz à base fluorée pour les chimisorber ou physisorber sur Si [9], [10]. Ensuite, un bombardement ionique Ar^+ est effectué pour permettre la gravure en surface [10]. Cependant, le traitement à basse température présente certaines contraintes comme la nécessité d'utiliser de l'azote liquide pour refroidir, et par conséquent l'utilisation d'équipements particuliers qui disposent de moyens de refroidissement et sont conçus pour résister à ces conditions. C'est pour ces raisons, que les procédés à température ambiante ont pris de l'avance depuis.

Néanmoins, depuis quelques années, l'intérêt pour les procédés cryogéniques a repris puisqu'ils présentent l'avantage de limiter la contamination des parois du réacteur [11] et la réduction des endommagements des matériaux, par exemple pour la gravure de matériaux Low-k [12].

D'ailleurs, une étude sur la gravure de matériaux low-k à basse température avait été menée dans le cadre d'une collaboration entre les trois entités suivantes : Le laboratoire français *Groupe de Recherches sur l'énergie des Milieux Ionisés* (GREMI), l'institut belge *Institut de Microélectronique Et Composants* (IMEC) et *Tokyo Electron Limited* (TEL), un fournisseur japonais d'équipements de production de semi-conducteurs.

Suite à cette première collaboration, où du C_4F_8 a été utilisé pour physisorber dans les pores des Low-k et les protéger lors de la gravure, un nouveau projet a été développé entre le GREMI et TEL, sur l'étude de la gravure de couche atomique à des températures cryogéniques (Cryo-ALE). Les travaux de cette thèse ont donc été menés dans le cadre de ce projet, au GREMI grâce au soutien financier de TEL.

Dans ce résumé, le principe général de l'ALE par plasma sera présenté. Ensuite, la cryo-ALE qui a fait l'objet de cette thèse sera introduite. Ainsi deux principaux travaux seront présentés. Du fait du caractère confidentiel de cette thèse, le choix a été fait de ne présenter dans ce résumé qu'une partie des travaux effectués.

Introduction à la gravure à échelle atomique par plasma

I. Principe général

L'ALE est un procédé cyclique, où chaque cycle est composé de plusieurs étapes auto-limitantes pour éliminer une à quelques monocouches à la fois. Alors qu'en gravure profonde standard, un précurseur pour modifier la surface et le plasma de gravure sont effectués en une seule et même étape, l'ALE offre la possibilité d'optimiser le procédé en les séparant. La Figure 1 ci-dessous montre les différentes étapes d'un cycle ALE.

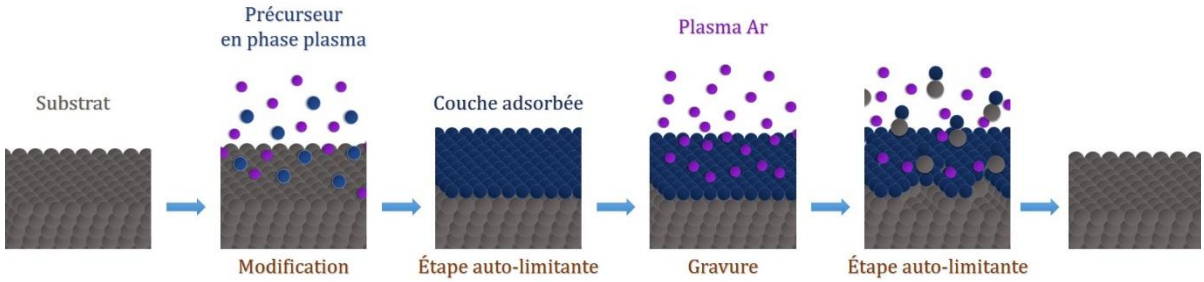

Figure 1. Schéma de principe de l'ALE

La première étape du cycle consiste à exposer la surface du substrat à un gaz réactif, généralement en phase plasma, afin d'adsorber les radicaux en surface, créant une modification de la couche. Le but de cette étape est de créer des liaisons entre les espèces gazeuses et le substrat (E_{ML}) qui nécessitent moins d'énergie pour être rompues que les liaisons entre les atomes du substrat lui-même (E_S), donc $E_{ML} < E_S$. Ainsi, l'objectif principal de cette étape est simplement de modifier la surface du substrat, sans aucune gravure. Par conséquent, l'énergie des ions dans ce plasma doit être faible, ou au moins inférieure à E_{ML} [13]–[15].

Une fois que toute la surface a été modifiée et recouverte avec les espèces du précurseur, plus aucune espèce ne s'adsorbe en surface : c'est pourquoi cette étape est qualifiée « d'auto-limitante ». Une étape de purge ou de pompage peut être réalisée par la suite pour assurer l'évacuation de toutes les espèces non adsorbées en surface, et donc contrôler la quantité d'espèces réactives dans le réacteur.

La troisième étape est l'étape de gravure. Elle consiste à allumer un plasma d'espèces inertes, généralement l'Ar, ayant une faible énergie des ions (E_i) pour éviter la pulvérisation, mais tout en étant suffisamment élevée pour fournir l'énergie nécessaire pour éliminer la couche modifiée [14].

$$E_{ML} < E_i < E_S \qquad \textit{Eq. 1}$$

Il a été montré dans [16], que les ions Ar^+ ne contribuent pas seulement au bombardement ionique mais aident également à la création de nouveaux sites actifs pour la prochaine étape d'adsorption. Selon l'application, cette étape peut être contrôlée pour fournir une gravure isotrope ou anisotrope [17]. Comme dans la gravure continue, les produits de gravure doivent être stables et volatils afin d'éviter toute re-déposition sur le substrat [18]. Cette étape est également auto-limitante puisqu'une fois la couche modifiée épuisée et si $E_i < E_S$, la gravure s'arrête.

Enfin, une autre étape de purge ou de pompage est nécessaire afin d'éliminer tous les produits de gravure de la chambre avant de redémarrer un nouveau cycle [4], [19], [20].

II. Tests caractéristiques d'un procédé de gravure à échelle atomique

Trois principaux tests sont présentés pour définir les caractéristiques d'un procédé ALE.

II.1. La courbe de saturation

Contrairement à la gravure en continu, en ALE, la gravure se produit au début de l'étape de gravure à chaque cycle. Une fois la couche modifiée est enlevée, la gravure s'arrête. Quasi-ALE est un procédé intermédiaire dans lequel la vitesse de gravure diminue de manière significative avec le temps mais ne s'arrête pas. La Figure 2 illustre l'évolution de la gravure par cycle en ALE, quasi ALE et en gravure continue. Il montre que la gravure sature en fonction du temps pour l'ALE puisque cette dernière est auto-limitante. C'est pourquoi un tel tracé est appelé « courbe de saturation ». Ce comportement auto-limitant de la gravure est celui à considérer pour qualifier le procédé d'ALE, plutôt que la quantité de gravure par cycle [6].

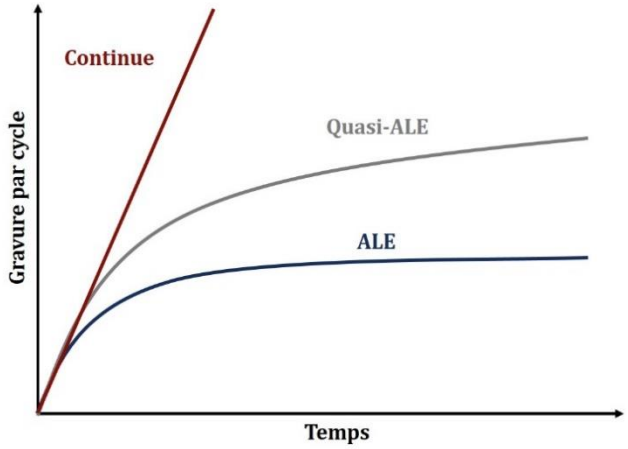

Figure 2. Courbe de saturation

II.2. Le balayage en énergie

Comme mentionné précédemment, l'énergie des ions pendant la gravure du plasma est un paramètre sensible en ALE qui doit être bien défini. Si l'énergie des ions est trop faible, seule une partie de la couche sera gravée, créant une rugosité à la surface et rendant la gravure incontrôlée à mesure que la quantité de couche modifiée augmentera. D'autre part, si l'énergie des ions est trop élevée, le substrat sera gravé par pulvérisation à cause du bombardement ionique. La surface peut donc être endommagée avec, à nouveau, l'augmentation de la rugosité de surface et la gravure ne sera pas auto-limitante. Par conséquent, comme le montre la Figure 3, cela définit une fenêtre pour effectuer de l'ALE où l'énergie des ions est, comme exprimé en Eq. 1, dans la plage souhaitable pour aider à l'élimination complète de la couche modifiée sans gravure par pulvérisation [6], [14], [15].

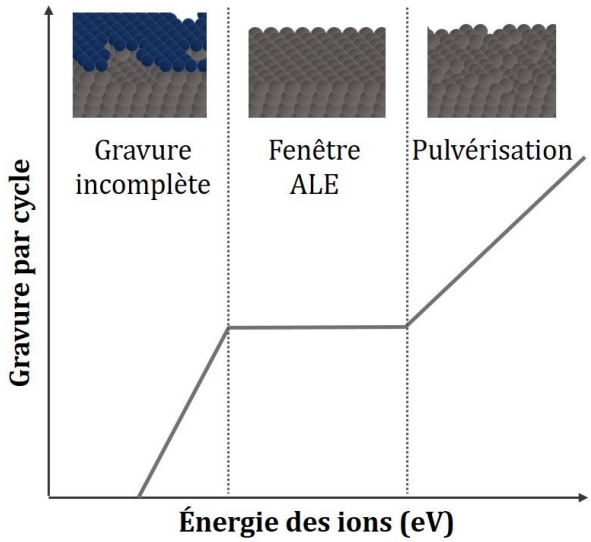

Figure 3. Comportement de la gravure en fonction de l'énergie des ions

II.3. Test de synergie

Pour améliorer le contrôle de la gravure au cours d'un procédé, des tests de synergie peuvent être réalisés. Le but de ces tests est d'identifier toute gravure indésirable. En d'autres termes, comme des espèces réactives sont utilisées dans l'étape de dépôt, une certaine gravure chimique peut se produire même sans assistance par bombardement ionique. De plus, comme expliqué dans la partie précédente, lors de la gravure au plasma, une certaine pulvérisation peut se produire. Les deux phénomènes sont indésirables, car ils empêchent le contrôle de la quantité gravée, et doivent donc être évités. Ainsi, pour identifier leur influence, ces étapes sont effectuées séparément et indépendamment (soit gravure, soit dépôt). Les épaisseurs gravées lors de chaque étape sont ensuite comparées à l'épaisseur gravée lorsque l'on combine les deux réactions dans un procédé global [6], [21], [22] :

$$Synergie\ \%\ (S) = \frac{EPC-(\alpha+\beta)}{EPC} \times 100\% \quad [22] \qquad \text{II.1}$$

Avec α, l'épaisseur gravée lors de l'étape de modification uniquement, β, l'épaisseur gravée uniquement lors de l'étape de gravure et EPC lorsque les deux étapes sont combinées. Les trois entités sont en nm / cycle [22]. Un procédé ALE est considéré comme idéal lorsque sa synergie est proche de 100% [21].

Si une gravure chimique est identifiée lors de l'étape de dépôt, il est suggéré dans [6] de s'en débarrasser en diminuant la température du substrat pour inhiber les réactions chimiques et la gravure spontanée. Les paramètres de ce plasma devront également être revus et optimisés.

En revanche, si une gravure physique est détectée lors de la gravure plasma sans avoir préalablement modifié la surface, l'énergie ionique doit être réduite en dessous du seuil de pulvérisation du matériau gravé [6].

III. Avantages de la gravure à échelle atomique

L'ALE permet une gravure uniforme le long de l'échantillon [13], [20]. Ses réactions étant auto-limitantes permettent de limiter l'effet de charge observé en gravure continue [6].

Ce procédé permet aussi de diminuer la rugosité de surface d'un échantillon. Cela est dû à la faible énergie des ions dans l'étape de gravure, ce qui facilite la diffusion des atomes et par conséquent lisse la surface. L'ALE permet également d'obtenir une sélectivité plus élevée qu'en gravure continue, un fort rapport d'aspect ainsi qu'une diminution des dommages de surface [13], [21], [23].

Cependant, de tels procédés à échelle atomique peuvent connaître des dérives dans le temps, dues à la contamination des parois du réacteur, en particulier lors de l'utilisation des chimies fluorocarbonées [24]–[28]. Pour éviter ces dérives et assurer la reproductibilité, de longues étapes de nettoyage et un conditionnement des parois du réacteur d'environ deux heures peuvent parfois être nécessaires.

Pour surmonter ce problème particulier de dérive, la gravure cryo-ALE a été proposée et a fait l'objet de cette thèse.

Cryo-gravure du SiO_2 par physisorption du C_4F_8

I. Principe général

La Cryo-ALE consiste à graver une à quelques monocouches après avoir baissé la température du substrat en dessous de -40°C. Dans ce chapitre, il est proposé de graver le SiO_2 à l'aide de la physisorption C_4F_8. Le principe est présenté en Figure 4 et peut être comparé au principe général de l'ALE présenté sur la Figure 1. Ainsi, la première étape de ce procédé consiste à refroidir le porte-substrat ainsi que la plaque de SiO_2 sur laquelle les échantillons ont été préalablement collés. Une fois la température de la plaque stabilisée, du C_4F_8 est injecté en phase gazeuse pour se physisorber sur les surfaces refroidies. Les parois du réacteur étant maintenues à température ambiante, aucune adsorption ne se produit dessus. La troisième étape consiste à pomper ou purger la chambre avec de l'argon afin d'éliminer tout le surplus de C_4F_8 qui n'aurait pas physisorbé. Un plasma d'Argon avec polarisation est alors démarré afin d'apporter suffisamment d'énergie aux ions pour faire réagir les CF_x avec SiO_2 et graver une à quelques monocouches du substrat. Cette étape est auto-limitante, puisqu'une fois tous les CF_x consommés, la gravure s'arrête. Elle est donc communément appelée SLE, venant de l'anglais « Self-Limiting Etching ».

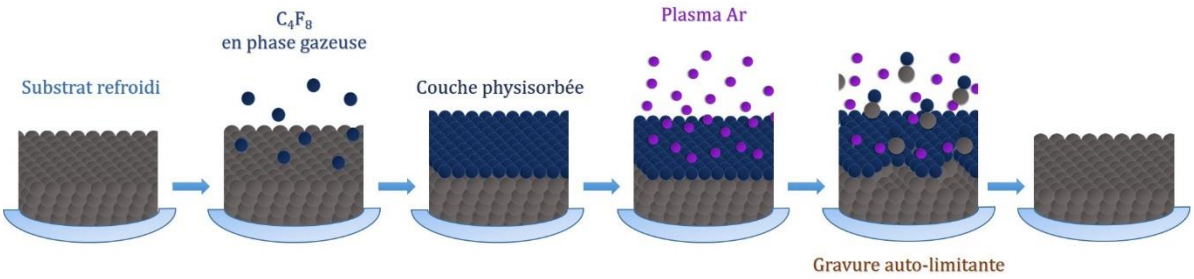

Figure 4. Schéma de principe de la cryo-ALE

II. Méthodes expérimentales

Comme mentionné précédemment, les plaques de support utilisées sont en SiO_2 de 150 mm d'épaisseur sur lesquelles des petits échantillons de SiO_2 sont collés. Les échantillons de SiO_2 sont des substrats de Si (100) avec une couche de SiO_2 de 100 nm d'épaisseur. Pour effectuer le collage des échantillons, une colle spéciale, stable à très basse température, est répartie uniformément sur la face arrière de l'échantillon. Elle permet d'assurer une très bonne conductivité thermique et s'enlève facilement après utilisation.

Les échantillons étant constitués de couches minces de SiO_2 sur Si, ils permettent d'obtenir des résultats très précis par ellipsométrie spectroscopique (SE).

Les échantillons préparés sont ensuite introduits dans un réacteur plasma à couplage inductif : l'Alcatel 601 E. Celui-ci est équipé d'une chambre de diffusion et d'un support de substrat cryogénique. Le porte-substrat peut être refroidi à l'azote liquide et la température est contrôlée et stabilisée à l'aide d'un système PID. Les plaques sont serrées mécaniquement et une pression d'hélium à l'arrière assure un contact thermique optimal avec le porte-substrat. Un schéma du réacteur est présenté sur la figure 1.

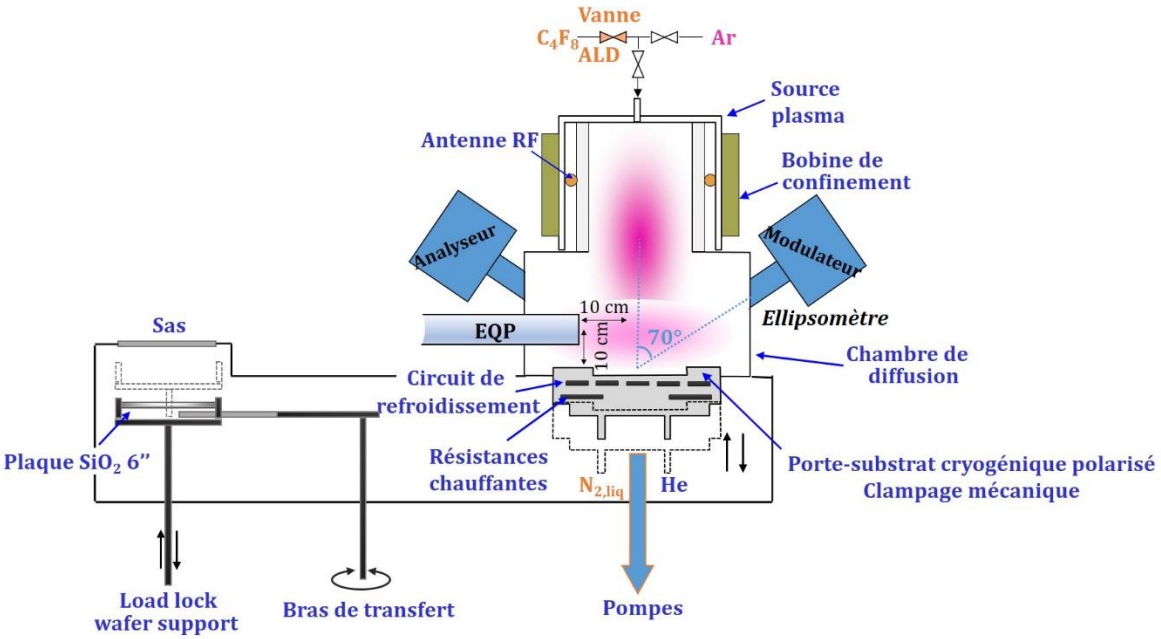

Figure 5. Schéma de l'Alcatel 601 E

Un ellipsomètre spectroscopique : Horiba Jobin Yvon UVISEL est couplé au réacteur à un angle d'incidence de 70° pour caractériser la surface du substrat in-situ. Il permet de suivre la variation d'épaisseur en mode cinétique à la surface de l'échantillon pendant les cycles. L'intervalle d'échantillonnage est fixé à 2 s, avec un temps d'intégration de 0,5 s. Pour chaque point d'acquisition, les spectres sont acquis en utilisant 32 longueurs d'onde de l'UV au visible. Les modèles de Lorentz et Drude ont ensuite été utilisés pour modéliser et ajuster les spectres ellipsométriques.

Bien que tous les résultats ne soient pas présents dans ce résumé, plusieurs autres équipements de caractérisation ont été utilisés au cours de la thèse. Comme, par exemple, un spectromètre de masse (EQP de Hiden Analytical) pour la compréhension du temps de résidence des espèces dans le réacteur. Ou encore, un microscope à force atomique (AFM) pour connaître l'évolution de la rugosité de surface après un procédé.

Des mesures de Spectrométrie photoélectronique X (XPS) en quasi in-situ ont aussi été effectués sur la plateforme OPTIMIST à l'IMN Nantes.

III. Principaux résultats

III.1. Présentation du procédé

Le procédé cryo-ALE, basé sur le principe décrit dans la Figure 4, est présenté dans la Figure 6 ci-dessous. C'est un procédé séquentiel et cyclique.

La première étape d'un cycle est l'injection d'un flux de gaz C_4F_8 pendant 5 à 20 s. La deuxième étape est le pompage de la chambre ou l'injection d'Ar en phase gazeuse pour purger la chambre et éliminer tout le surplus de C_4F_8. La durée de l'étape peut varier entre 3 et 30 s.

La troisième étape est l'allumage du plasma Ar avec une certaine polarisation (entre 0 et -20 V) afin de démarrer la gravure.

La quatrième et dernière étape du cycle est une étape de pompage de 15 s pour éliminer tous les sous-produits gravés.

Ces quatre étapes sont ensuite répétées plusieurs fois et suivies en mode cinétique par ellipsométrie spectroscopique et par spectrométrie de masse si nécessaire (non présenté dans ce résumé).

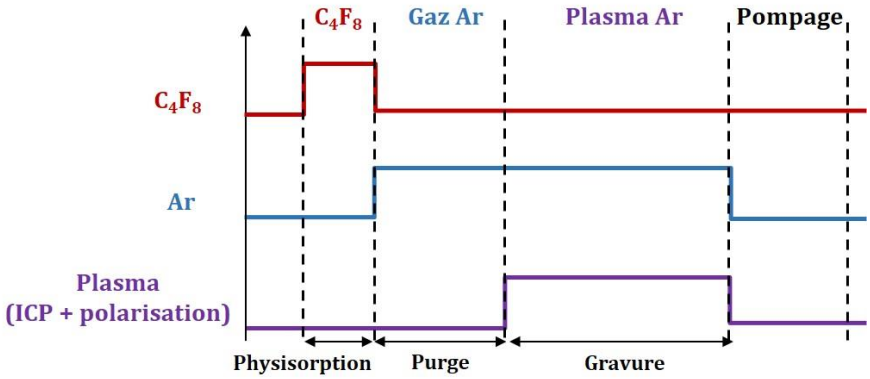

Figure 6. Séquence générale d'un cycle cryo-ALE

III.2. Preuve de principe

Comme il s'agit d'un nouveau procédé, la première étape du projet a été de prouver la faisabilité en injectant le C_4F_8 en phase gazeuse au lieu d'un plasma.

Le procédé a été réalisé sur SiO_2 pendant 8 cycles à deux températures différentes, et suivi par SE in-situ.

À -110 °C, une légère augmentation de l'épaisseur est constatée lors de l'injection de C_4F_8, cependant elle diminue peu de temps après, lors de l'étape de purge. Par conséquent, lors du plasma d'Ar, aucune gravure n'est observée. Cela signifie, d'une part qu'il n'y avait plus de

C_4F_8 présent sur la surface pour permettre la gravure, et d'autre part que l'énergie des ions pendant le procédé est inférieure au seuil de pulvérisation de SiO_2.

Lorsque la température est diminuée à -120°C, environ 8,5 nm sont gravés. Le signal SE est suffisamment précis et permet de différencier toutes les étapes. En effet, en regardant l'encadré de la Figure 7, il est possible de distinguer une augmentation de l'épaisseur lors de l'injection de C_4F_8, puis l'épaisseur diminue un peu avant de se stabiliser lors de l'étape de purge, c'est-à-dire qu'une partie de C_4F_8 se désorbe mais pas la totalité, car l'épaisseur est encore plus élevée qu'avant l'injection de C_4F_8. Enfin, pendant le plasma d'Ar, l'épaisseur ne cesse de diminuer au fur et à mesure que le SiO_2 est gravé, cependant, le SLE n'est pas atteint.

Enfin, cette Figure 7 démontre l'existence d'un seuil de température à partir duquel il sera possible de physisorber une quantité suffisante de C_4F_8 pour permettre la gravure.

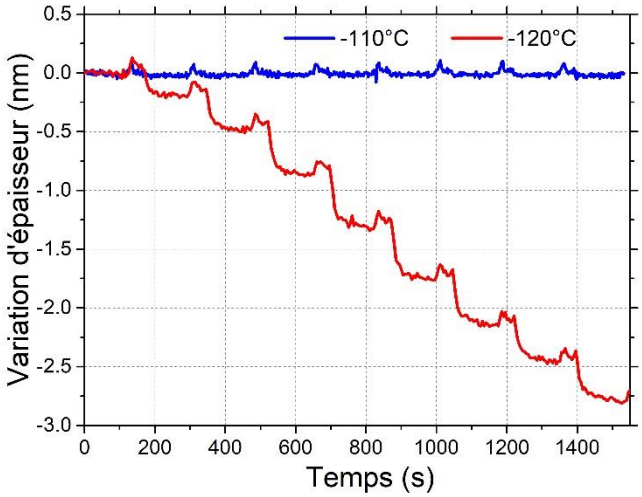

Figure 7. 8 cycles de cryo-ALE faits à -110°C et -120°C

III.3. Amélioration du procédé

Grâce à une étude plus approfondie du procédé, il a ensuite été possible d'augmenter la température à -90°C. Dans la Figure 8 ci-dessous, un long procédé a notamment été effectué pour vérifier la répétabilité à travers les cycles. La courbe globale présente une gravure très régulière, cela signifie qu'aucune dérive due à une contamination des parois du réacteur n'a eu lieu. Mais, lorsqu'on regarde les premiers cycles (environ 16 cycles), entre 0,5 nm et 1 nm d'épaisseur gravée est nécessaire avant d'atteindre une épaisseur gravée par cycle stable. Aux premiers cycles, on observe une gravure d'environ 0,05 nm / cycle. Cela augmente à 0,13 nm / cycle pour les cycles suivants. Cela signifie qu'il faut quelques cycles avant de commencer avec la même surface d'un cycle à l'autre. Cela peut être dû à une certaine contamination au carbone de la surface du substrat qui doit d'abord être éliminée, avant d'atteindre la surface réelle de SiO_2 [29]. Mais cela peut aussi être dû à la formation d'une

couche SiOCF qui met quelques cycles pour atteindre un état stationnaire, étant donné que seulement une petite quantité de C_4F_8 est fournie par cycle pour sa formation [22], [30].

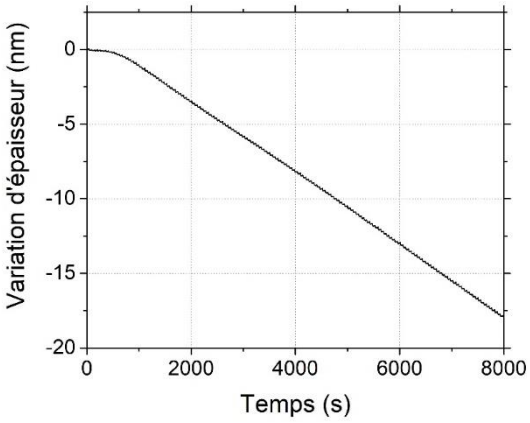

Figure 8. 150 cycles de cryo-ALE effectués à -90°C sur SiO_2

Conclusion

Cette thèse a été effectuée en collaboration avec l'équipementier japonais TEL au sein du laboratoire GREMI à Orléans.

Au cours de cette thèse, une nouvelle approche a été étudiée pour la gravure de couches atomiques (ALE) de matériaux à base de silicium. En effet, il a été testé de refroidir le substrat à graver à des températures entre -120°C et -90°C afin de physisorber dessus une couche de C_4F_8. Puis de démarrer un plasma d'Ar pour activer la gravure. Une étude plus approfondie de la physisorption a ensuite permis d'augmenter la température du procédé en augmentant notamment la pression d'injection du C_4F_8.

Le principal avantage de ce procédé est qu'il permet de limiter la contamination des parois du réacteur par des CF_X, ce qui par conséquent, permet de réaliser de longues gravures sans qu'il n'y est de dérive dans le procédé.

Néanmoins, ce procédé a aussi présenté comme inconvénient le manque de sélectivité. En effet, la vitesse de gravure du Si ou du Si_3N_4 s'est révélée très poche de celle du SiO_2. De plus, alors que la température de procédé souhaitée devant être proche des -50°C, il n'a pas été possible de remonter au-delà des -90°C. C'est pourquoi, bien que le C_4F_8 s'est révélé utile pour l'étude du procédé, il a néanmoins été conclu qu'il n'était pas idéal pour le procédé, et qu'il faudrait donc tester d'autres gaz pouvant se condenser à plus hautes températures et pouvant être plus sélectifs pour la gravure.

Le travail détaillé ici représente à la moitié des travaux effectués durant cette thèse. Une autre approche de cryo-gravure à échelle atomique a aussi été effectuée. Cette technique a permis d'augmenter la température du procédé jusqu'à -60°C, et a permis d'obtenir des sélectivités quasi-infinis de gravure du Si_3N_4 en comparaison avec le Si. Néanmoins, ces travaux n'ont pas été présentés ici pour des raisons de confidentialité.

Références

[1] G. E. Moore, « Cramming More Components Onto Integrated Circuits », *Electronics*, vol. 38, nº 8, p. 82-85, 1965.

[2] C. G. N. Lee, K. J. Kanarik, et R. A. Gottscho, « The grand challenges of plasma etching: a manufacturing perspective », *J. Phys. D: Appl. Phys.*, vol. 47, nº 27, p. 273001, 2014.

[3] K. Ishikawa *et al.*, « Progress and prospects in nanoscale dry processes: How can we control atomic layer reactions ? », *Jpn. J. Appl. Phys.*, vol. 56, nº 6S2, p. 06HA02, 2017.

[4] F. Roozeboom, F. Van Den Bruele, Y. Creyghton, P. Poodt, et W. M. M. Kessels, « Cyclic Etch/Passivation-Deposition as an All-Spatial Concept toward High-Rate Room Temperature Atomic Layer Etching », *ECS J. Solid State Sci. Technol.*, vol. 4, nº 6, p. N5067-N5076, 2015.

[5] M. N. Yoder, « Atomic layer etching », US4756794A, 1988.

[6] K. J. Kanarik *et al.*, « Overview of atomic layer etching in the semiconductor industry », *J. Vac. Sci. Technol. A*, vol. 33, nº 2, p. 020802, 2015.

[7] E. Kessels, « Atomic layer etching turns 32.5 years old! – A good occasion to share an ALE timeline and an animated version of the ALE periodic table », *Atomic Limits*, 2020. https://www.atomiclimits.com/2020/03/02/atomic-layer-etching-turns-32-5-years-old-a-good-occasion-to-share-an-ale-timeline-and-an-animated-version-of-the-ale-periodic-table/ (consulté le mars 26, 2020).

[8] S. Tachi, K. Tsujimoto, et S. Okudaira, « Low-temperature reactive ion etching and microwave plasma etching of silicon », *Appl. Phys. Lett.*, vol. 52, nº 8, p. 616-618, 1988.

[9] Y. Horiike *et al.*, « Digital chemical vapor deposition and etching technologies for semiconductor processing », *J. Vac. Sci. Technol. A*, vol. 8, nº 3, p. 1844-1850, 1990.

[10] H. Sakaue, S. Iseda, K. Asami, J. Yamamoto, M. Hirose, et Y. Horiike, « Atomic Layer Controlled Digital Etching of Silicon », *Jpn. J. Appl. Phys.*, vol. 29, nº Part 1, No. 11, p. 2648-2652, 1990.

[11] R. Dussart, T. Tillocher, P. Lefaucheux, et M. Boufnichel, « Plasma cryogenic etching of silicon: from the early days to today's advanced technologies », *J. Phys. D: Appl. Phys.*, vol. 47, nº 12, p. 123001, 2014.

[12] F. Leroy *et al.*, « Cryogenic etching processes applied to porous low-k materials using SF_6/C_4F_8 plasmas », *J. Phys. D: Appl. Phys.*, vol. 48, nº 43, p. 435202, 2015.

[13] K. J. Kanarik, S. Tan, et R. A. Gottscho, « Atomic Layer Etching: Rethinking the Art of Etch », *J. Phys. Chem. Lett.*, vol. 9, nº 16, p. 4814-4821, 2018.

[14] A. Agarwal et M. J. Kushner, « Plasma atomic layer etching using conventional plasma equipment », *J. Vac. Sci. Technol. A*, vol. 27, nº 1, p. 37-50, 2009.

[15] C. M. Huard, S. J. Lanham, et M. J. Kushner, « Consequences of atomic layer etching on wafer scale uniformity in inductively coupled plasmas », *J. Phys. D: Appl. Phys.*, vol. 51, nº 15, p. 155201, 2018.

[16] S. D. Sherpa, P. L. G. Ventzek, M. Lee, G. S. Hwang, et A. Ranjan, « New insight into desorption step by Ar^+ ion-bombardment during the atomic layer etching of silicon », *J. Vac. Sci. Technol. A*, vol. 36, nº 3, p. 031303, 2018.

[17] M. J. Cooke, « Impact of Atomic Layer Etching on Process Tool Design », *ECS J. Solid State Sci. Technol.*, vol. 4, nº 6, p. N5001–N5004, 2015.

[18] I. L. Berry, K. J. Kanarik, T. Lill, S. Tan, V. Vahedi, et R. A. Gottscho, « Applying sputtering theory to directional atomic layer etching », *J. Vac. Sci. Technol. A*, vol. 36, nº 1, p. 01B105, 2018.

[19] C. T. Carver, J. J. Plombon, P. E. Romero, S. Suri, T. A. Tronic, et R. B. Turkot, « Atomic Layer Etching: An Industry Perspective », *ECS J. Solid State Sci. Technol.*, vol. 4, nº 6, p. N5005-N5009, 2015.

[20] T. Faraz, F. Roozeboom, H. C. M. Knoops, et W. M. M. Kessels, « Atomic Layer Etching: What Can We Learn from Atomic Layer Deposition? », *ECS J. Solid State Sci. Technol.*, vol. 4, nº 6, p. N5023-N5032, 2015.

[21] K. Ishikawa *et al.*, « Rethinking surface reactions in nanoscale dry processes toward atomic precision and beyond: a physics and chemistry perspective », *Jpn. J. Appl. Phys.*, vol. 58, nº SE, p. SE0801, 2019.

[22] K. J. Kanarik *et al.*, « Predicting synergy in atomic layer etching », *J. Vac. Sci. Technol. A*, vol. 35, nº 5, p. 05C302, 2017.

[23] C. M. Huard, Y. Zhang, S. Sriraman, A. Paterson, K. J. Kanarik, et M. J. Kushner, « Atomic layer etching of 3D structures in silicon: Self-limiting and nonideal reactions », *J. Vac. Sci. Technol. A*, vol. 35, nº 3, p. 031306, 2017.

[24] D. Metzler, C. Li, S. Engelmann, R. L. Bruce, E. A. Joseph, et G. S. Oehrlein, « Fluorocarbon assisted atomic layer etching of SiO_2 and Si using cyclic Ar/C_4F_8 and Ar/CHF_3 plasma », *J. Vac. Sci. Technol. A*, vol. 34, nº 1, p. 01B101, 2016.

[25] R. J. Gasvoda, A. W. Van De Steeg, R. Bhowmick, E. A. Hudson, et S. Agarwal, « Surface Phenomena During Plasma-Assisted Atomic Layer Etching of SiO_2 », *ACS Appl. Mater. Interfaces*, vol. 9, nº 36, p. 31067-31075, 2017.

[26] S. Dallorto *et al.*, « Atomic layer etching of SiO_2 with Ar and CHF_3 plasmas: A self-limiting process for aspect ratio independent etching », *Plasma Process Polym*, vol. 16, nº 9, p. 1900051, 2019.

[27] M. Kawakami, D. Metzler, C. Li, et G. S. Oehrlein, « Effect of the chamber wall on fluorocarbon-assisted atomic layer etching of SiO_2 using cyclic Ar/C_4F_8 plasma », *J. Vac. Sci. Technol. A*, vol. 34, nº 4, p. 040603, 2016.

[28] M. Matsui, T. Usui, et T. Ono, « Effect of plasma dissociation on fluorocarbon layers formed under C_4F_8/Ar pulsed plasma for SiO_2 etching », *J. Appl. Phys*, vol. 56, nº 6S2, p. 06HB03, 2017.

[29] S. S. Kaler, Q. Lou, V. M. Donnelly, et D. J. Economou, « Atomic layer etching of silicon dioxide using alternating C_4F_8 and energetic Ar^+ plasma beams », *J. Phys. D: Appl. Phys.*, vol. 50, nº 23, p. 234001, 2017.

[30] D. Metzler, C. Li, S. Engelmann, R. L. Bruce, E. A. Joseph, et G. S. Oehrlein, « Characterizing fluorocarbon assisted atomic layer etching of Si using cyclic Ar/C_4F_8 and Ar/CHF_3 plasma », *J. Chem. Phys.*, vol. 146, n° 5, p. 052801, 2017.

Gaëlle ANTOUN

Cryo-gravure de couches atomiques par plasma : mécanismes et procédés

Cette thèse a été réalisée au GREMI en collaboration avec Tokyo Electron Ltd, qui a également financé le projet. Le but de cette étude était de développer un nouveau procédé de gravure de couche atomique (ALE) à température cryogénique pour la gravure de matériaux à base de silicium.
La Cryo-ALE consiste à graver une ou quelques monocouches après avoir refroidi le substrat. La première étape de ce procédé est l'injection d'azote liquide pour refroidir le porte-substrat et refroidir la plaquette en injectant de l'hélium à l'arrière pour assurer le conductivité thermique. Une fois la température de la plaquette stabilisée, des espèces réactives sont injectées en phase gazeuse pour physisorber sur les surfaces refroidies. Les parois du réacteur étant maintenues à température ambiante, aucune adsorption ne se produit dessus. La troisième étape consiste à pomper ou purger la chambre par de l'argon afin d'éliminer tout le surplus de gaz réactif qui ne s'est pas physisorbé. Un plasma d'argon avec polarisation est alors démarré afin d'apporter suffisamment d'énergie par les ions pour modifier la surface de l'échantillon et graver une ou quelques monocouches du substrat. Cette étape est auto-limitante, car une fois que toute la surface modifiée est enlevée, il n'y a plus de gravure. Pour mener cette étude, un réacteur de recherche cryogénique ICP a été utilisé. Un ellipsomètre spectroscopique in-situ a été couplé pour enregistrer la variation d'épaisseur en temps réel, et un spectromètre de masse a été utilisé pour analyser les espèces présentes dans la chambre du réacteur pendant le procédé et en savoir plus sur les mécanismes. Des analyses par spectroscopie photoélectronique par rayons X quasi in-situ a également été réalisée au laboratoire IMN pour étudier l'évolution de la surface à basse température. Le principal avantage de ce procédé basé sur la physisorption d'espèces réactives, est qu'il permet de limiter la contamination des parois du réacteur et donc d'éviter des dérives au cours du procédé. En parallèle, un deuxième procédé a été développé à des températures cryogéniques mais où l'étape de modification a été réalisée en phase plasma. Ce second procédé a permis d'atteindre une sélectivité élevée entre Si_3N_4 sur Si et SiO_2.

Mots clés : gravure, basse température, échelle atomique

Cryo-Atomic Layer Etching by plasma: mechanisms and processes

This PhD was conducted at GREMI in collaboration with Tokyo Electron Ltd, that has also financed the project. The purpose of this study was to develop a new Atomic Layer Etching (ALE) process at cryogenic temperature for silicon-based materials etching.
Cryo-ALE consists on etching one to few monolayers after decreasing the substrate temperature. The first step of this process is the injection of liquid nitrogen to cool the chuck and cool the wafer by injecting He at its backside to ensure the thermal conductivity. Once the wafer temperature has been stabilized, reactive species are injected in gas phase in order to physisorb on the cooled surfaces. As the reactor walls are kept at room temperature, no adsorption occurs on it. The third step is to pump or purge the chamber by Argon in order to remove all the surplus of the reactive gas that did not physisorb. An argon plasma with bias is then started in order to bring enough energy by the ions to make modify the surface of the sample and etch one to few monolayers of the substrate. This step is self-limited, as once all the modified surface is removed, no more etching occurs. To conduct this study, an ICP cryogenic research reactor has been used. On it an in-situ spectroscopic ellipsometer was coupled to monitor the thickness variation in real time, and an Electrostatic Quadrupole Mass Spectrometer was used to analyze the species present in reactor chamber during the process and know more about the mechanisms. Quasi in-situ X-ray Photoelectron Spectroscopy has also been performed at the laboratory IMN for surface analysis at low temperature. The main advantage of this process based on the physisorption of reactive species, is that it enables to limit reactor walls contamination and hence prevent process drifts. In parallel, a second process was developed at cryogenic temperatures but where the modification step was performed in plasma phase. This second process enabled to achieve high selectivity between Si_3N_4 over Si and SiO_2.

Keywords : etching, low temperature, atomic scale

Groupe de Recherches sur l'Energétique des Milieux Ionisés
14 Rue d'Issoudun BP 6744 45067 Orléans Cedex 2